OPEN ACCESS Freely available online

Polarized Secretion of *Drosophila* EGFR Ligand from Photoreceptor Neurons Is Controlled by ER Localization of the Ligand-Processing Machinery

Shaul Yogev, Eyal D. Schejter, Ben-Zion Shilo*

Department of Molecular Genetics, Weizmann Institute of Science, Rehovot, Israel

Abstract

The release of signaling molecules from neurons must be regulated, to accommodate their highly polarized structure. In the developing *Drosophila* visual system, photoreceptor neurons secrete the epidermal growth factor receptor ligand Spitz (Spi) from their cell bodies, as well as from their axonal termini. Here we show that subcellular localization of Rhomboid proteases, which process Spi, determines the site of Spi release from neurons. Endoplasmic reticulum (ER) localization of Rhomboid 3 is essential for its ability to promote Spi secretion from axons, but not from cell bodies. We demonstrate that the ER extends throughout photoreceptor axons, and show that this feature facilitates the trafficking of the Spi precursor, the ligand chaperone Star, and Rhomboid 3 to axonal termini. Following this trafficking step, secretion from the axons is regulated in a manner similar to secretion from cell bodies. These findings uncover a role for the ER in trafficking proteins from the neuronal cell body to axon terminus.

Citation: Yogev S, Schejter ED, Shilo B-Z (2010) Polarized Secretion of *Drosophila* EGFR Ligand from Photoreceptor Neurons Is Controlled by ER Localization of the Ligand-Processing Machinery. PLoS Biol 8(10): e1000505. doi:10.1371/journal.pbio.1000505

Academic Editor: Konrad Basler, University of Zurich, Switzerland

Received March 18, 2010; **Accepted** August 23, 2010; **Published** October 5, 2010

Funding: This work was supported by US-Israel BSF grant 2005219 to BS, who is an incumbent of the Hilda and Cecil Lewis Molecular Genetics chair. The funders had no role in study design, data collection and analysis, decision to publish, or preparation of the manuscript.

Competing Interests: The authors have declared that no competing interests exist.

Abbreviations: Dac, Dachshund; DN, dominant negative; EGFR, epidermal growth factor receptor; EGUF, Eyeless Gal4 UAS Flip; ER, endoplasmic reticulum; ERG, electroretinogram; GFP, green fluorescent protein; gRho-[number], genomic Rhomboid [number]; Hh, Hedgehog; HRP, Horseradish Peroxidase; ManII, Mannosidase II; PDI, protein disulfide isomerase; RFP, red fluorescent protein; Rho-[number], Rhomboid [number]; RNAi, RNA interference; S, Star; Spi, Spitz; YFP, yellow fluorescent protein.

* E-mail: benny.shilo@weizmann.ac.il

Introduction

Communication between cells and their environment entails the release and reception of signaling molecules. In polarized cells, such as epithelia or neurons, the unique cellular architecture imposes constraints on the precise sites where signal release and reception occur. For example, the distribution of axonal guidance receptors is restricted to specific proximal or distal axon segments [1]. Similarly, secretion of molecules from neurons must be highly polarized for the ligand to propagate in the appropriate receptive field. In some cases, ligand is secreted along the axon, where it interacts with ensheathing glia [2,3], whereas in other cases ligand is secreted locally from cell bodies or growth cones [4–6]. Thus, polarized secretion is an essential aspect of ligand processing in neurons.

An example of ligand secretion from both cell bodies and axonal termini is that of the *Drosophila* epidermal growth factor receptor (EGFR) ligand Spitz (Spi). In the *Drosophila* eye imaginal disc, photoreceptors differentiate in the wake of a progressive morphogenetic furrow, which sweeps from the posterior of the disc to its anterior [7,8]. Secretion of Hedgehog (Hh) from nascent photoreceptor cell bodies promotes the continued movement of the furrow [9,10]. Photoreceptor neurons subsequently secrete the EGFR ligand Spi from their cell bodies, triggering neurogenesis in closely neighboring cells [11,12].

Once specified as neurons, R1–R6 photoreceptor axons grow across the basal surface of the eye disc, funnel through the optic stalk, and reach the lamina, where they locally induce the differentiation of lamina cartridge neurons [13,14]. Secretion of Hh from photoreceptor axon termini triggers an initial phase of neurogenesis in the lamina precursor cells, marked by the expression of Dachshund (Dac) and the EGFR itself [5]. The subsequent phase of lamina neurogenesis requires Spi, which is also locally delivered by the incoming retinal axons. EGFR activation by Spi in the lamina leads to the differentiation of five neurons in each cartridge, which express the pan neuronal marker ElaV [6]. Thus, local secretion of Spi at the two distinct poles of photoreceptor neurons controls neurogenesis in both the eye disc and the lamina. While the mechanisms that regulate Hh delivery to axons have been explored [4], how Spi is secreted from both cell bodies and axonal termini remains unknown.

Spi is the cardinal EGFR ligand throughout *Drosophila* development. It is broadly expressed as an inactive precursor [15]. Spi secretion is dependent on processing by the intramembrane protease Rhomboid-1 (Rho-1) [16]. The inactive Spi precursor is retained in the endoplasmic reticulum (ER) by a COPI-dependent mechanism [17]. Trafficking of Spi from the ER to the Rho-1 compartment requires the type II transmembrane protein Star (S) [18,19]. Upon arrival at this late secretory compartment, Spi is cleaved by the Rho-1 protease and subsequently released to the extracellular milieu.

Rho-1 also cleaves the chaperone S, thereby rendering it incompetent to traffic additional Spi molecules [20]. We have

Author Summary

Cells secrete signaling molecules that trigger a variety of responses in neighboring cells by activating their respective cell-surface receptors. Because many cells in an organism are polarized, regulating the precise location of ligand secretion is important for controlling the position and nature of the response. During the development of the compound eye of the fruit fly *Drosophila*, for example, a ligand of the epidermal growth factor family called Spitz (Spi) is secreted from both the apical and basal (axonal) poles of photoreceptor cells but with different outcomes. Photoreceptor cells are recruited to the developing eye following apical secretion of Spi. Conversely, basal secretion of this same ligand, at a significant distance from the cell body, triggers differentiation of cells in the outer layer of the brain. Although secretion of Spi is known to occur at both poles of the cell, one important question is how Spi and its processing machinery are trafficked throughout the length of the photoreceptor axon to achieve basal secretion. In this study we show that the key to axonal trafficking is the regulated localization of Spi and its processing machinery, including the intramembrane protease Rhomboid, to sites within the endoplasmic reticulum (ER), which extends along the length of the axon. Two different Rhomboid proteins are expressed in photoreceptor cells, but only one of them is localized to the ER. We show that this ER-localized Rhomboid is indeed necessary and sufficient for Spi processing at axon termini. Our work therefore demonstrates how variations in intracellular localization of conserved signaling components can alter signaling outcomes dramatically. It also highlights the importance of the ER in trafficking proteins along the axon.

previously shown that two additional Rhomboid family members, Rho-2 (also called Stet) and Rho-3 (also called Roughoid [Ru]), which are dedicated to oogenesis and eye development, respectively [21,22], localize to the ER, as well as to the late secretory compartment [23]. Although Rho-2 and Rho-3, like Rho-1, promote Spi release from the late compartment, their ER presence attenuates EGFR signaling, primarily because of premature cleavage of S [23]. Thus, in photoreceptor neurons, Spi secretion from cell bodies is promoted by both Rho-1 and Rho-3 acting in the late compartment, with the ER activity of the latter also attenuating the overall levels of secreted ligand.

The presence of ER markers has been observed in axons and dendrites from various neurons [24,25], and the ER has been suggested to be continuous in Purkinje cell axons [26]. However, the traditional role assigned to axonal ER is in localized translation of transported mRNA, rather than translocation of secreted proteins. Recently, a role for the ER in promoting trafficking of NMDA glutamate receptor to dendrites in cultured rat hippocampal neurons has been described [27].

Here we examined the mechanisms that regulate Spi release from axonal termini. We find that, unlike secretion from cell bodies, axonal secretion of Spi relies exclusively on Rho-3. Furthermore, the ability of Rho-3 to promote axonal secretion of Spi stems from its combined ER and late compartment localization. Supplementing an ER presence to Rho-1 or eliminating the ER localization of Rho-3 alternates their potencies vis-à-vis axonal Spi secretion. Our data indicate that the importance of the ER stems from its ability to promote axonal trafficking of Rhomboids, a feature that we suggest is linked to the extension of the ER throughout the axon. Finally, we characterize the apical compartment in which Spi is processed in cell bodies, and suggest that it is also present at axonal termini, where Spi is processed following trafficking along the axon. Our results show that subcellular localization of the EGFR-ligand-processing machinery in photoreceptors dictates the polarity of ligand secretion, and highlight the role of the ER in facilitating protein trafficking from the neuronal cell body to the axon terminus.

Results

EGFR Activation in the Lamina Cartridge Neurons Is Exclusively Mediated by Rho-3

To investigate the requirement for Rho-mediated cleavage in promoting Spi release from photoreceptor axons, we assessed the effect of *rho-1* or *rho-3* mutations on lamina neurogenesis. In late third-instar larvae, EGFR activation by Spi delivered from photoreceptor axons leads to the expression of the pan-neuronal marker ElaV at the posterior part of the lamina (Figure 1A and 1B). Visual systems rendered homozygous for a null *rho-1* allele, using the Eyeless Gal4 UAS Flip (EGUF) system [28], occasionally show some morphological defects, but ElaV expression in the lamina is not perturbed (Figure 1C). Thus, *rho-1* is dispensable for Spi release from photoreceptor axons. We next examined ElaV expression in *rho-3* EGUF clones (Figure 1D) or in homozygous mutant animals (Figure 1H). While ElaV is properly expressed in the eye disc and brain lobula, we could not detect any ElaV expression in the lamina, indicating that *rho-3* is essential for EGFR activation in this tissue. Thus, whereas Rho-1 and Rho-3 can redundantly promote Spi release from cell bodies in the eye disc, only Rho-3 mediates EGFR activation in the lamina.

Since Rho-3 is also involved in photoreceptor neurogenesis, the lack of EGFR activation in the lamina of *rho-3* mutants may be a secondary effect of defective neuronal development or axonal mistargeting. However, *rho-3* mutant photoreceptors properly express the pan-neuronal marker ElaV, as well as markers of specific photoreceptor subtypes (Figure 1D′ and unpublished data; [23]), demonstrating that the general program of photoreceptor differentiation is not perturbed. The only defect we observed at the larval stage is an extra number of neurons, at the expense of non-neuronal cells [23]. Importantly, no overt axonal targeting defects were detected in the mutant, as seen with anti–horseradish peroxidase (HRP) staining (Figure 1D). Furthermore, the normal expression of the Hh target genes *dac* (Figure 1D′′) and *EGFR* (Figure 1E) in the brain reveals that there is no general secretion defect in *rho-3* mutants. It thus appears that the *rho-3* mutant phenotype reflects a specific defect in processing and secretion of Spi from axon termini.

To critically test the functionality of *rho-3* mutant photoreceptors, we performed electroretinogram (ERG) recordings on adult flies (Figure S1). Photoreceptor neurons from wild-type or *rho-3* eyes properly depolarize in response to light. However, "on/off transients," which represent the activity of the post-synaptic lamina neurons [29], are absent in *rho-3* ERG recordings, thus reflecting the defects in lamina neurogenesis. Conversely, "on/off transients" are detected in *rho-1* EGUF clones. Hence, in the absence of Rho-3, Rho-1 facilitates all aspects of photoreceptor development, but not the induction of EGFR activation in the lamina.

Release of Spi from Axon Termini Depends on Cleavage by Rho-3 in Photoreceptor Neurons

Rhomboids promote EGFR signaling by processing the ligand Spi in the signal-sending cell prior to its secretion [30,31]. This suggests that the lack of EGFR activation in *rho-3* mutant laminae

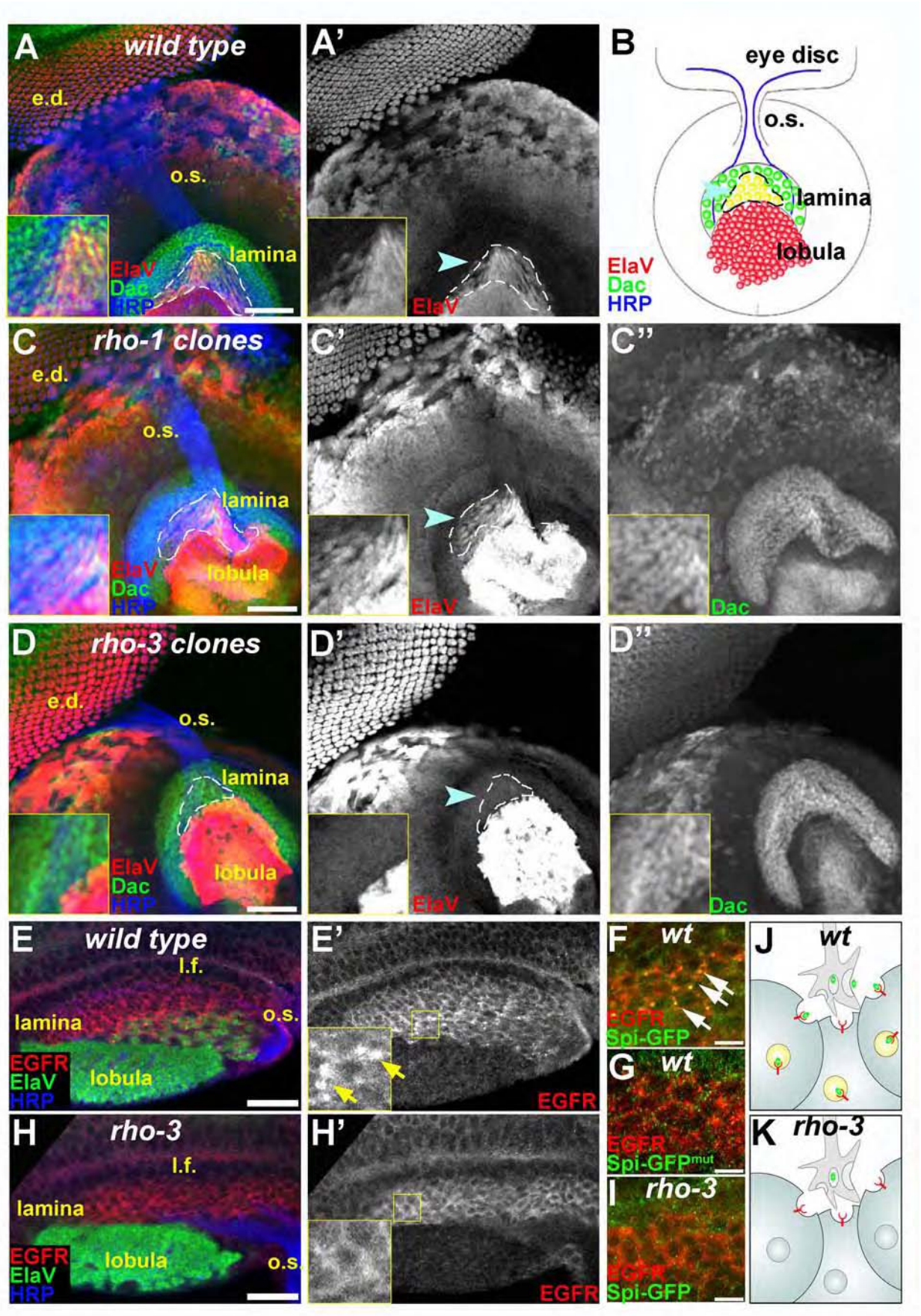
A
wild type
e.d.
o.s.
lamina
ElaV
Dac
HRP
A'
ElaV
B
eye disc
o.s.
lamina
lobula
ElaV
Dac
HRP
C
rho-1 clones
e.d.
o.s.
lamina
lobula
ElaV
Dac
HRP
C'
ElaV
C''
Dac
D
rho-3 clones
e.d.
o.s.
lamina
lobula
ElaV
Dac
HRP
D'
ElaV
D''
Dac
E
wild type
l.f.
lamina
o.s.
EGFR
ElaV
HRP
lobula
E'
EGFR
F
wt
EGFR
Spi-GFP
J
wt
G
wt
EGFR
Spi-GFPmut
K
rho-3
H
rho-3
l.f.
lamina
EGFR
ElaV
HRP
lobula
o.s.
H'
EGFR
I
rho-3
EGFR
Spi-GFP

Figure 1. Rho-3 exclusively mediates Spi secretion from photoreceptor axons. (A–D) Lateral views of developing eye disc and lamina from late third-instar larvae. Photoreceptor cell bodies in the eye disc (e.d.) express the pan-neuronal marker ElaV (red, shown separately in single-primed panels). Photoreceptor axons, marked by HRP (blue), extend from the eye disc through the optic stalk (o.s.) and terminate at the lamina. The posterior lamina, in which ElaV is expressed, is marked by an arrowhead and outlined, and magnified in insets. Dac (green, shown separately in double-primed panels) and ElaV (red) expression in the lamina reflects Hh and Spi secretion from photoreceptor axons, respectively, and the triggering of the signaling pathways in the future lamina cartridge neurons. Scale bar: 40 μm. (A) In wild-type (wt) late third-instar larva, ElaV is expressed in the eye disc and lamina. (B) Schematic of (A). Note the retinotopic projections of photoreceptor axons in the lamina. At this developmental stage, not all photoreceptors have differentiated yet, hence only the posterior part of the lamina is invaded by retinal axons, and ElaV expression (yellow) is detected only there. (C) In eyes bearing large *rho-1* clones, ElaV and Dac are normally expressed in the lamina (inset), despite some morphological abnormalities. (D) Large *rho-3* clones eliminate EGFR activation in the lamina. ElaV expression is missing from the lamina (inset). Note that ElaV is still expressed in the eye disc, indicating that Rho-1 and Rho-3 redundantly mediate Spi secretion from cell bodies. Dac is normally expressed in the lamina, demonstrating that *rho-3* mutants do not suffer from general secretion defects. Anti-HRP staining (blue) shows that *rho-3* axons are correctly targeted to the lamina. (E) Anti-EGFR staining (red) in wild-type lamina shows many endocytic puncta (inset in E′, arrows) at the posterior of the lamina, associated with the ElaV-expressing cells (green). Scale bar: 20 μm. l.f., lamina furrow. (F) Spi–GFP (green) expressed in the eye by GMR–Gal4 is secreted from photoreceptor axons, and co-localizes with EGFR (red) in endocytic puncta (arrows) in lamina cells. Scale bar: 10 μm. (G) Spi–GFP (green) in which the Rhomboid cleavage site was mutated fails to localize with EGFR (red) in the lamina cells. Scale bar: 10 μm. (H) In a lamina from *rho-3* mutants, EGFR distribution (red) shows a reduced number of endocytic puncta (inset in H′), suggesting that the receptor is not engaged by the ligand on the surface of lamina cells. ElaV expression (green) is specifically missing from the lamina. Scale bar: 20 μm. (I) Spi–GFP (green), expressed in the eye of *rho-3* mutants is not secreted from the axons, and does not co-localize with EGFR in lamina cells. Scale bar: 10 μm. (J and K) Schemes of Spi secretion from axons. In wild-type larvae (J), Spi (green ovals) is secreted from axons and co-localizes with EGFR (red) in endocytic puncta in lamina cells. In the absence of cleavage by Rho-3 (K), Spi fails to be secreted from photoreceptor axons, and does not co-localize with EGFR in the lamina, which, in turn, is not internalized.
doi:10.1371/journal.pbio.1000505.g001

stems from a failure in cleavage and secretion of Spi from photoreceptors. To follow Spi processing and secretion, we monitored the localization of Spi–green fluorescent protein (GFP), a biologically active variant of the ligand, tagged by GFP at the extracellular domain [19]. The construct was expressed under the control of GMR–Gal4 [32], to restrict expression exclusively to the eye disc.

Inspection of EGFR distribution in the laminae of wild-type flies reveals many endocytic puncta, which are associated with the ElaV-expressing cartridge neurons (Figures 1E and S1D). We found that Spi–GFP secreted from the eye co-localized in the lamina with EGFR in these puncta, reflecting the release of the ligand from photoreceptor axons and endocytosis of ligand–receptor complexes by lamina cells (Figure 1F and 1J). This co-localization is dependent on cleavage by Rhomboid proteases, since a similarly expressed Spi–GFP construct in which the Rhomboid cleavage site was mutated [33] failed to co-localize with the receptor (Figure 1G and 1K).

We next examined the distribution of EGFR in *rho-3* mutant laminae, and found that it is uniform compared to wild-type, and lacks the bright endocytic puncta (Figures 1H and S1E). In *rho-1* mutant visual systems, the distribution and intensity of laminar EGFR staining were comparable to wild-type (Figure S1F). Furthermore, following expression of Spi–GFP in *rho-3* mutant eye discs, GFP-positive puncta could not be detected in the laminae (Figure 1I and 1K). These results indicate that Rho-3 cleaves Spi within the transmembrane domain in photoreceptor neurons, to promote ligand release from their axons to the lamina.

In summary, our results show that, whereas both Rho-1 and Rho-3 are capable of mediating Spi secretion from cell bodies in the eye disc, only Rho-3 promotes the secretion of Spi from photoreceptor axons to the lamina.

Spi Secreted from R2 and R5 Photoreceptor Axons Patterns the Lamina

Each of the approximately 750 ommatidia in the *Drosophila* eye contains eight photoreceptor neurons of distinct identities. R1–R6 neurons project their axons to the lamina, whereas R7 and R8 project their axons to the medulla. To ask which of these neurons provides Spi for patterning the lamina, we used a repertoire of Gal4 lines to drive Rho-3 expression in different subsets of photoreceptors, and monitored their ability to rescue the *rho-3* mutant phenotype. All Gal4 drivers used are normally expressed in *rho-3* mutant eye discs (unpublished data). As a complementary assay, we expressed Spi–GFP with the same lines, and monitored its co-localization with the internalized EGFR in the signal-receiving lamina neurons. Our findings are summarized in Table 1, showing that Rho-3 acts to promote Spi secretion from the axons of R2 and R5. We note that these axons also play a pivotal role in axonal pathfinding, as their mistargeting can lead to defective guidance of the entire ommatidial fascicle [34]. The concordance between the assays of ElaV induction and Spi internalization in the lamina suggests that the difference between the photoreceptors that do or do not provide the signal lies in their ability to process or secrete Spi, rather than in the capacity of the lamina cells to respond only to Spi that is secreted from distinct photoreceptors.

Table 1. Spi is secreted to the lamina mainly from R2 and R5 photoreceptor axons.

Driver	Expressed in Photoreceptors	Rescue of *rho-3* Phenotype by UAS–Rho-3	Co-localization of Spi–GFP with EGFR in Lamina Cells
GMR–Gal4	R1–R8	+++	+++
MT14–Gal4	R2, R5, R8	+++	+++
Lz–Gal4	R1, R6, R7	+	−
K25–Gal4	R3, R4, R7	−	−
Mδ0.5–Gal4	R4, weak R3	−	−
Sca–Gal4	R8	−	−

Six Gal4 lines, expressed in different combinations of photoreceptor cells, were used to determine which neurons secrete Spi to the lamina. The ability of UAS–Rho-3 to rescue the *rho-3* phenotype and the co-localization of Spi–GFP with EGFR in lamina cells were assayed. Both experiments indicate that mainly R2 and R5 photoreceptor axons are responsible for delivering Spi to the lamina. –, no rescue (no laminar ElaV expression) or no co-localization; +++, full rescue, leading to wild-type ElaV expression, or co-localization of more than 90% Spi–GFP puncta with EGFR. Rescue with Lz–Gal4 (+) yielded ~20% of the wild-type number of ElaV-expressing cells in the lamina.
doi:10.1371/journal.pbio.1000505.t001

The Cytoplasmic Tail and First Intraluminal Loop Mediate Different Subcellular Localizations of Rho-1 and Rho-3

A mechanism that may account for the importance of Rho-3 in promoting Spi secretion from axons is RNA transport and localized translation. However, we have found no *rho-3* RNA in axons, even after Rho-3 overexpression, which rescues the *rho-3* phenotype (Figure S2). We have previously shown that Rho-1 and Rho-3 differ in their subcellular localization within photoreceptor cell bodies. When ectopically expressed with the Gal4–UAS system, Rho-1 localized to apical punctate structures, whereas Rho-3 was localized to the ER, as well as to the apical puncta [23]. We set out to test the hypothesis that the distinct intracellular localizations of Rho-1 and Rho-3 account for the difference in their capacity to trigger Spi processing and secretion in photoreceptor axons.

First, we examined the endogenous localization of the two proteases, without resorting to overexpression. Since antibodies that recognized the endogenous proteins could not be raised, we used recombineering [35] to generate ~45-kb genomic fragments encompassing the *rho-1* or *rho-3* locus that express C-terminally tagged Rho-1–yellow fluorescent protein (YFP) and Rho-3–GFP in patterns and levels identical to the endogenous proteins. Transgenic lines were generated, in which the recombineered genes were inserted at the same chromosomal location. In the eye disc, genomic Rho-1 (gRho-1)–YFP localized exclusively to the apical compartment, whereas gRho-3–GFP was enriched in the ER, with staining also at the apical compartment (Figure 2A and 2B). These distributions demonstrate that despite the caveats associated with overexpression, the localizations obtained previously by the UAS–Gal4 system faithfully reflected the endogenous localization of these proteins.

To identify the sequences mediating the subcellular localization of Rhomboids, we swapped different fragments between Rho-1 and Rho-3. The resulting chimeras were GFP tagged, and transgenic animals were generated. In all cases the constructs were inserted at the same genomic location, to avoid a difference in expression levels. We find that the subcellular localization of Rhomboids depends on their cytoplasmic N terminus and the first intraluminal loop. Replacing these fragments of Rho-1 with the corresponding fragments from Rho-3, to yield GFP–R3L1-R1, relocalized Rho-1 to a Rho-3-like distribution, encompassing the ER and apical compartment (Figure 2C and 2F). Conversely, Rho-3 in which the N terminus and first loop were replaced by those of Rho-1 (GFP–R1L1-R3) retained localization to the apical compartment, but was absent from the ER (Figure 2D and 2E). Importantly, since the active site of the proteases is formed by residues embedded within the fourth and sixth transmembrane helices [36–38], the chimeras uncouple the subcellular localization signal from the catalytic activity. Therefore, the GFP–R1L1-R3 and GFP–R3L1-R1 constructs allow us to specifically define the role of subcellular localization in promoting Spi secretion from axonal termini.

ER Localization of Rho-3 Facilitates Spi Secretion from Axons

Although both Rho-1 and Rho-3 promote Spi secretion from photoreceptor cell bodies, only Rho-3 facilitates Spi secretion from axons. To investigate whether this is due to its ER localization, we assayed the ability of GFP–Rho-1 or GFP–Rho-3 to rescue the *rho-3* lamina phenotype. In addition, we tested a modified Rho-1 targeted to the ER and late compartment (GFP–R3L1-R1) and an ER-excluded Rho-3 (GFP–R1L1-R3) using the same assay. All constructs were shown to be efficient in cleaving Spi in cell culture assays and in vivo (unpublished data). Furthermore, since Rho-1 and Rho-3 are normally expressed at low levels in the eye disc, we inserted all the transgenes into attP18, a genomic landing site that was reported to yield low expression levels [39], and expression was driven in R2, R5, and R8 by MT14–Gal4.

As expected from their in vivo activities, GFP–Rho-3 rescued the *rho-3* mutant lamina phenotype, whereas GFP–Rho-1 did not (Figure 3). Importantly, while GFP–Rho-1 failed to promote Spi secretion from the axons, supplementing it with an ER localization yielded a construct (GFP–R3L1-R1) capable of rescuing the *rho-3* phenotype (Figure 1E and 1F). Conversely, whereas GFP–Rho-3 rescued the *rho-3* phenotype, a Rho-3 version which is not ER localized (GFP–R1L1-R3) failed to do so (Figure 1D and 1F). These experiments show that ER localization is a critical feature that enables Rhomboid proteases to promote Spi secretion from the axons.

We next asked whether intact endogenous Rho-1, which cannot substitute for Rho-3 in Spi processing for axonal release, can facilitate Spi secretion when enriched in the ER. Passage through the ER is an essential step in Rho-1 maturation, as a protein bearing transmembrane domains. We thus attempted to compromise Rho-1 exit from the ER, by removing one copy of the syntaxin *sed5*, which is required for the fusion of ER-derived vesicles with the Golgi [40,41]. When HA-tagged Rho-1 was expressed in *sed5* homozygous mutant clones, its subcellular distribution shifted almost completely to the peri-nuclear ER (Figure 3G and 3H). In *rho-3* mutants in which *sed5* gene dosage was halved, we found that some ElaV expression was restored to the lamina (Figure 3I and 3J). Therefore, when endogenous Rho-1 trafficking out of the ER is compromised, it can substitute for Rho-3 and promote Spi release from axons.

We note here that under strong overexpression conditions, Rho-1 also rescues the *rho-3* phenotype. This may reflect the perdurance of some Rho-1 in the ER when its export machinery is heavily burdened. Indeed, a low endogenous level of ER activity by Rho-1 en route to the apical compartment has been suggested previously [17]. Accordingly, the ER levels of Rho-1–HA in *sed5* heterozygotes were too low to be detected by anti-HA staining, yet restored some laminar ElaV expression to *rho-3* mutants. In summary, our results indicate that the difference in subcellular localization is the cause of the distinct ability of Rho-3, but not Rho-1, to promote Spi processing and secretion from photoreceptor axons.

Spi Processing for Axonal Signaling Does Not Take Place in the ER

The combined ER and secretory compartment localization of Rho-3 is critical for its ability to promote Spi secretion from axons. We next asked whether the ER component of this localization is sufficient for Rho-3 function in lamina induction. We uncoupled the two localizations by tagging Rho-3 with a KDEL sequence at its luminal C-terminus, thereby retaining it in the ER. This construct, as well as a KDEL-tagged Rho-1, were fused at their N-termini to GFP, and inserted into the same genomic landing site as the constructs previously described. Although GFP–Rho-3–KDEL and GFP–Rho-1–KDEL localize to the ER, and efficiently cleave Spi in cell culture assays and in vivo (unpublished data), they could not rescue the *rho-3* lamina phenotype upon expression in the eye by MT14–Gal4 (Figure 4A–4D). This indicates that the ER localization of Rho-3 is not sufficient to promote EGFR signaling in the lamina, and suggests that the active Spi molecules secreted from the axons are not processed in the ER.

Since Spi that is secreted by photoreceptor axons is not cleaved in the ER, we monitored the capacity to traffic the Spi precursor to

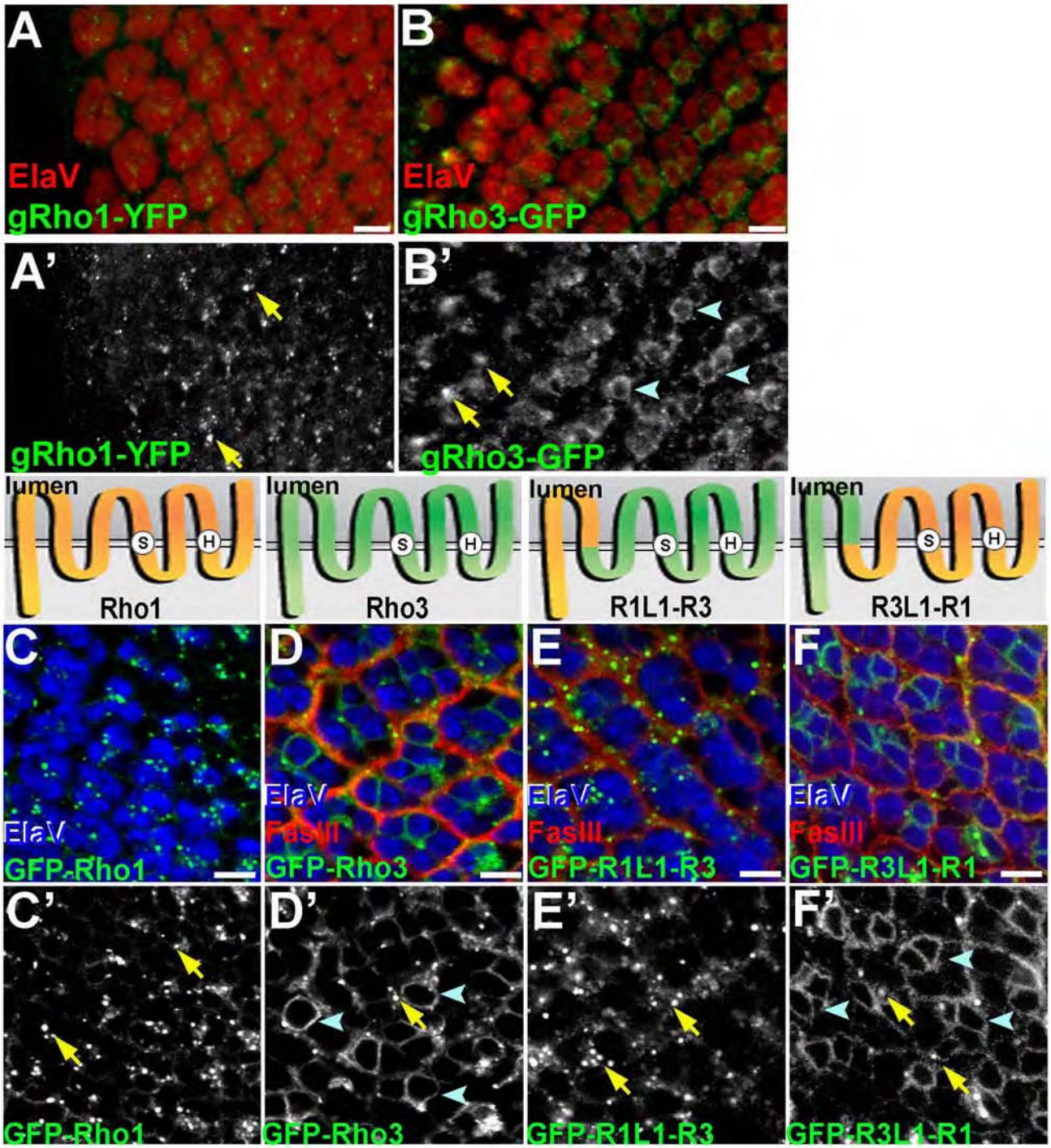

Figure 2. Subcellular localization of Rhomboids is mediated by their cytoplasmic N-termini and first luminal loop. (A) A gRho-1 construct, YFP tagged at the C-terminus (green), localizes to discrete punctate structures (arrows in [A′]). ElaV (red) shows photoreceptor nuclei. The morphogenetic furrow is to the left. Scale bar: 5 μm. (B) Rho-3, expressed from a genomic construct and tagged with GFP at the C-terminus (green) shows both ER (arrowheads in [B′]) and punctate (arrows in [B′]) localization. Like the Rho-1 puncta, Rho-3 puncta are more abundant in apical optical sections (not shown). ElaV (red) shows photoreceptor nuclei. Primed panels show single channels for YFP or GFP. Scale bar: 5 μm. (C–F) Subcellular localization of GFP-tagged Rho-1, Rho-3, R1L1-R3, and R3L1-R1 (green), expressed in the eye disc by GMR–Gal4. ElaV (blue) marks photoreceptor nuclei, and FasIII (red) stains membranes. Primed panels show a single channel for GFP. Scale bar: 5 μm. The schemes at the top of each panel show the topology of the proteases (N-termini are in the cytoplasm; C-termini are luminal; not to scale). Also shown are the positions of the catalytic serine (S) and histidine (H), embedded in the fourth and sixth transmembrane helices, respectively. Rho-1 is orange; Rho-3 is green. (C) GFP–Rho-1 localizes to apical punctate structures (arrows in [C′]). (D) GFP–Rho-3 localizes to the apical structures (arrows in [D′]) and the peri-nuclear ER (arrowheads in [D′]). (E) The N terminus and first luminal loop of Rho-3 were replaced with that of Rho-1. These sequences are sufficient to confer a Rho-1-like localization to GFP–R1L1-R3 (arrows in [E′]). (F) Rho-1 in which these sequences are derived from Rho-3 (GFP–R3L1-R1) is localized to the ER (arrowheads in [F′]) and the apical puncta (arrows in [F′]).
doi:10.1371/journal.pbio.1000505.g002

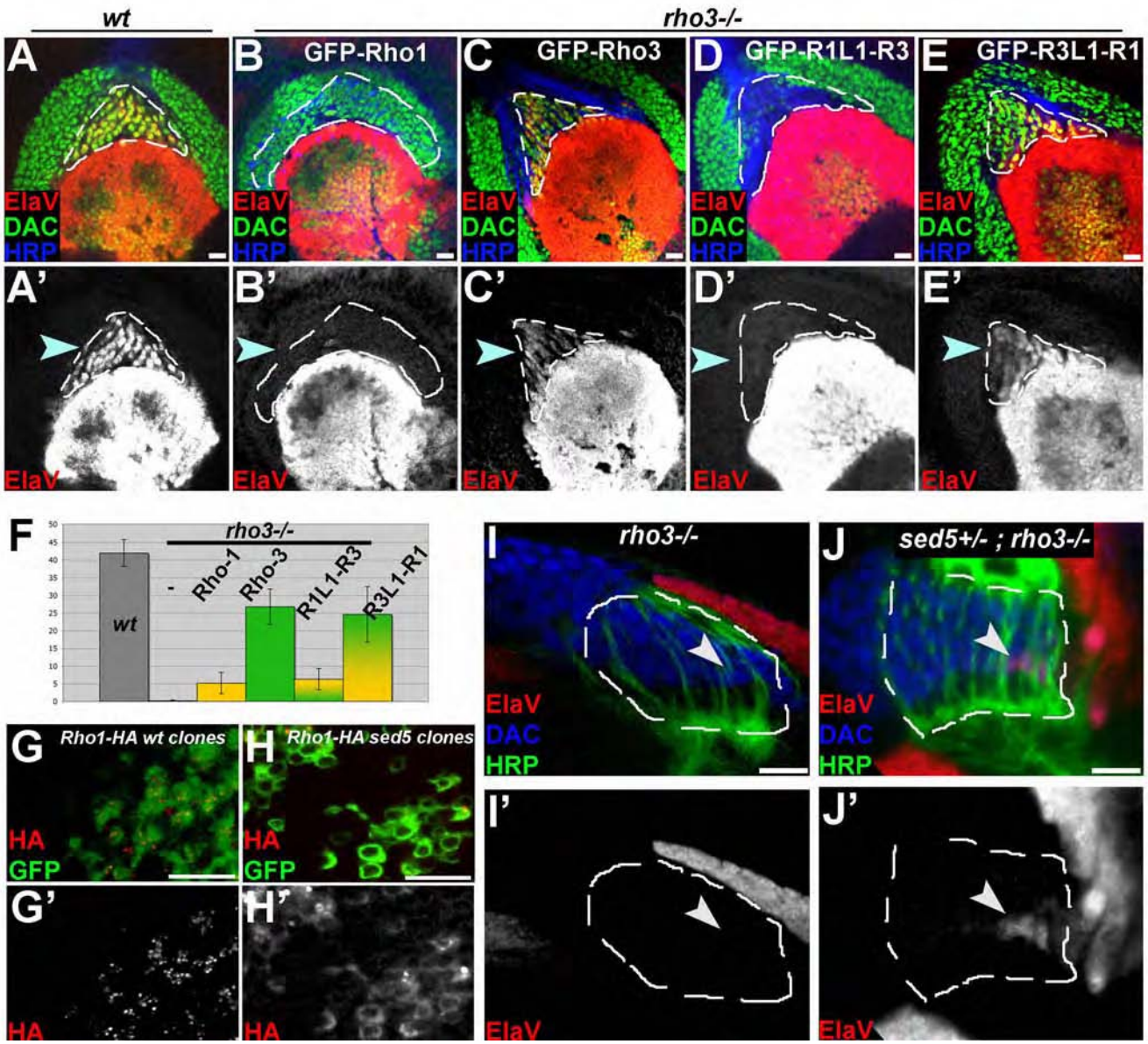

Figure 3. ER localization of Rho-3 facilitates Spi secretion from axons. (A–E) All constructs are GFP tagged at the N-termini, inserted into the same genomic location, and expressed in R2, R5, and R8 by MT14–Gal4. ElaV is red; Dac (green) and HRP (blue) mark photoreceptor axons. (A) Lateral view of a wild-type (wt) lamina from a late third-instar larva, with the typical ElaV triangle at the posterior. (B) GFP–Rho-1, expressed in R2, R5, and R8 fails to rescue the *rho-3* phenotype, as indicated by the lack of ElaV-positive cells within the population of Dac-positive precursors. (C) A GFP–Rho-3 transgene restores ElaV expression to the lamina of a *rho-3* mutant. (D) When Rho-3 is not localized to the ER, as is the case of the GFP–R1L1-R3 chimera, it fails to promote Spi secretion from the axons and induce EGFR activation in the lamina. (E) An ER-enriched Rho-1 (GFP–R3L1-R1) rescues the *rho-3* phenotype. (A′–E′) Single channel for ElaV staining. (F) Quantification of the results from (A–E). ElaV-positive cells in the lamina were counted in 8–10 specimens per genotype. The difference between ER-resident and non-ER-resident proteases is statistically significant (ANOVA). (G) Rho-1–HA (red, shown separately in [G′]) expressed in wild-type MARCM clones (marked by GFP, green) is localized to the typical apical puncta. (H) ER-to-Golgi trafficking is blocked in *sed5* MARCM clones, marked by GFP. Rho-1–HA (red, shown separately in [H′]) expressed in the mutant photoreceptors is retained in the peri-nuclear ER. (I) Horizontal view of a *rho-3* mutant lamina. HRP (green) marks retinal axons and outlines the lamina; Dac is blue. No ElaV-positive cells are seen in *rho-3* mutant lamina (red, shown separately in [I′]). (J) ElaV expression (red, shown separately in [J′]) is restored to a small population of cells at the posterior of the lamina of *rho-3* mutants after elimination of one copy of *sed5*. Scale bars: 10 μm.
doi:10.1371/journal.pbio.1000505.g003

axonal termini. GMR–Gal4-driven expression in a wild-type eye disc of the Spi precursor marked with GFP at the N terminus, gave rise to translocation of the GFP tag across the entire length of the axon bundle (Figure 4E and 4H). However, it is not possible to determine by this assay whether the ligand that reaches the axon termini represents the precursor form or the cleaved ligand. Two lines of evidence suggest that the ligand precursor can be trafficked from the cell body to the axon terminus. First, a non-cleavable form of Spi also reached the axonal growth cones, when expressed in the eye disc (Figure 4F and 4H). Second, expression of mSpi–GFP in a *rho-3* mutant background, in which the precursor does not undergo cleavage in the ER, gave rise to a ligand distribution in axons that was similar to wild-type (Figure 4G and 4H). Taken together, these experiments demonstrate that the Spi precursor

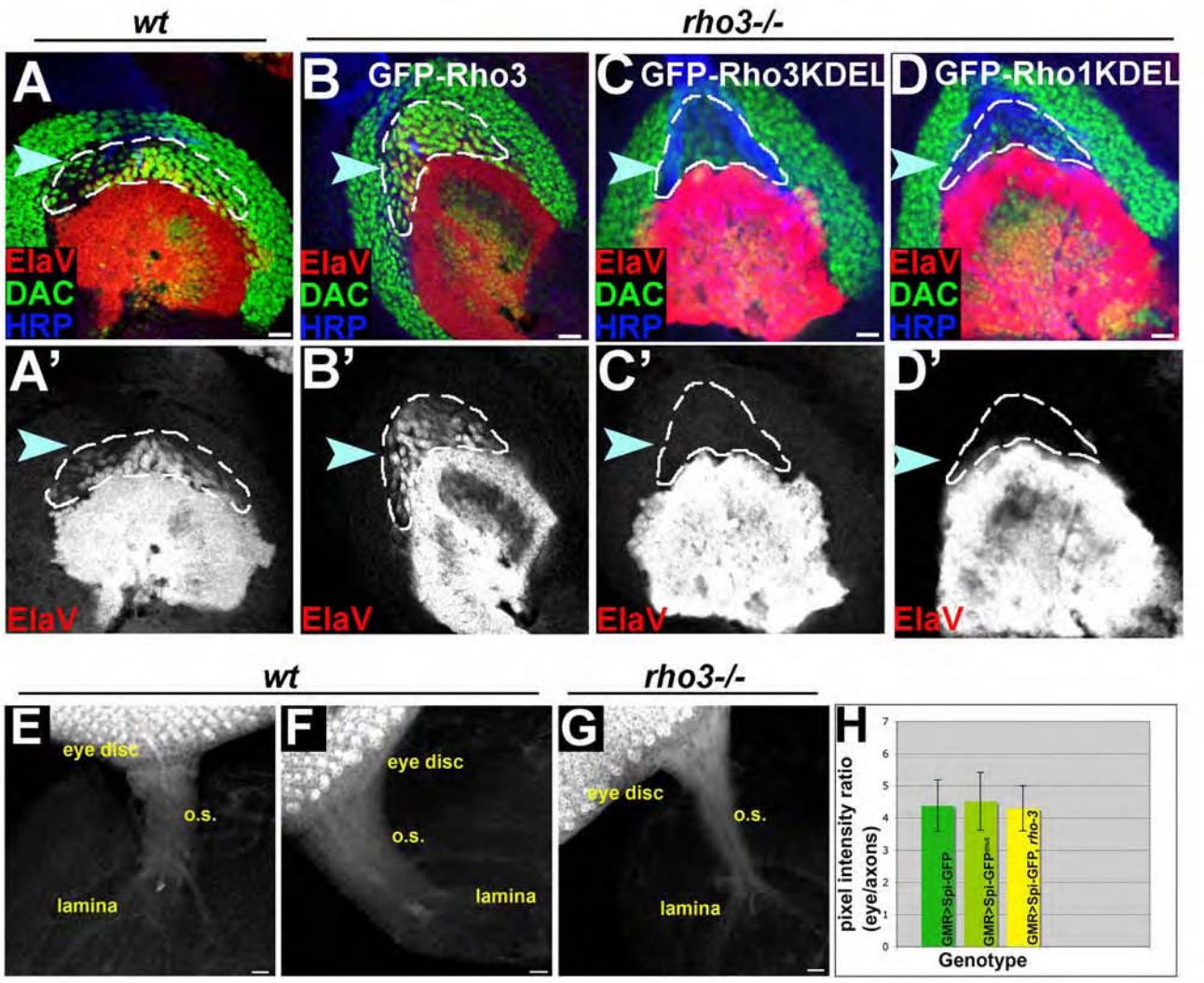

Figure 4. Spi secreted from axons is not processed in the ER. (A–D) Lateral views of late third-instar larva laminae. ElaV (red, shown separately in primed panels), Dac (green), and HRP (blue). The posterior of the lamina, where EGFR activation is evident by ElaV expression, is marked with an arrowhead and is outlined. (A) Wild-type (wt) lamina showing the typical ElaV staining at its posterior. (B) A GFP–Rho-3 transgene, expressed in R2, R5, and R8 by MT14–Gal4 restores ElaV expression in *rho-3* mutants (compare with Figure 3B). (C) When Rho-3 is localized exclusively to the ER by a KDEL tag (GFP–Rho-3–KDEL) it fails to rescue the *rho-3* mutant phenotype. (D) An ER-retained form of Rho-1 (GFP–Rho-1–KDEL) fails to rescue the *rho-3* mutant phenotype. (E and F) Spi does not require cleavage for translocating in the axons. Spi–GFP was expressed in the eye disc by GMR–Gal4, and its distribution in axons in the optic stalk (o.s.) was monitored. (E) Wild-type Spi–GFP expressed in a wild-type genetic background is detected throughout the axons. (F) Mutating the Rhomboid cleavage site in Spi–GFP does not alter its distribution in axons. (G) Cleavage of Spi in the ER does not occur in *rho-3* mutants, yet the distribution of the ligand in axons is similar to wild-type. (H) Quantification of Spi distribution in axons. Mean pixel intensities were determined at the entry point of the optic stalk into the brain, and at the eye disc. A ratio of mean pixel intensity in the eye to mean pixel intensity in the optic stalk was calculated per specimen; 7–10 specimens were used for each quantification. The differences observed are not significant (ANOVA). Scale bars: 10 μm.
doi:10.1371/journal.pbio.1000505.g004

can be trafficked along the axon, and suggest that it is cleaved outside of the ER prior to its secretion.

To support this conclusion, we assayed the ability of a cleaved form of the ligand (cSpi), which is localized to the ER [17], to rescue the *rho-3* phenotype upon expression by MT14–Gal4 in R2, R5, and R8. Biologically active cSpi, tagged with HA or HRP, failed to induce ElaV expression in *rho-3* laminae (Figure S3). This is consistent with the notion that cleavage of Spi in the ER is not the mode by which Rho-3 promotes secretion, and suggests that the importance of the ER to Rho-3 function stems from a different mechanism.

The ER Facilitates Rho-3 Trafficking to Axons

The above experiments demonstrate that while ER localization is crucial for the ability of Rho-3 to promote axonal secretion of Spi, the functional ligand is not cleaved in the ER. We therefore examined whether the ER could promote Rho-3-dependent signaling by facilitating the trafficking of the ligand-processing machinery to axons.

Examination of the endogenous ER markers protein disulfide isomerase (PDI) and BiP reveals that the ER extends throughout the axons of developing photoreceptor neurons (Figure 5A and unpublished data), as does the detection of KDEL-tagged ER

luminal proteins (Figure 5B). ER markers were also observed in axons of adult flies (unpublished data), consistent with previous reports indicating that the ER is continuous in the axons of various neurons [26,42]. We also detected the presence of endogenous ER exit sites (marked by dSec16 [43]) along the axons and at their termini in the lamina (Figure 5C), suggesting that proteins are released from the ER in these locations. Consistently, Golgi outposts (marked by Mannosidase II (ManII)–GFP [44]) were also evident along the entire axon length (Figure 5F). These observations suggest that in photoreceptor axons, the ER can be used by secreted proteins to reach a given exit site, prior to progressing along the secretory pathway.

To further test this idea, we expressed an ER-localized GFP (GFP–KDEL) [45] in the eye disc. GFP immunofluorescence was observed throughout the axons, while *GFP* mRNA was confined to the cell bodies (Figure 5D and 5E). Thus, proteins localized to the ER in the cell body can also reach the axon, by utilizing the extension of the ER to the axon.

Since Rho-3 is ER localized in the cell body, it could use this compartment in a manner similar to GFP–KDEL to move distally. Indeed, whereas *rho-3* mRNA is not detected in the axons (Figure 5G), gRho-3–GFP is found in a continuous distribution in axons (Figure 5H). Conversely, gRho-1–YFP, which is not localized to the peri-nuclear ER, fails to reach the optic stalk (Figure 5I). To examine the possibility that ER localization would promote the axonal delivery of a Rhomboid protease, we generated another gRho-1–YFP construct, with a C-terminal KDEL tag. In contrast to gRho-1–YFP, gRho-1–YFP–KDEL was robustly distributed along the entire length of the axons (Figure 5J).

Taken together, these results imply that the importance of the ER for Spi signaling in this physiological context stems from its ability to promote trafficking to the axons, where Spi processing subsequently occurs.

Co-Trafficking of Spi, S, and Rho-3 Sensitizes EGFR Signaling in the Lamina to S Levels

Besides Rho-3, Spi and S are also localized to the ER in the eye disc. Therefore, the three components could associate in this compartment for joint trafficking to the axons. To test this hypothesis, we examined the co-localization of biologically active, HA-tagged versions of Spi or S with Rho-3–GFP. S–HA co-localizes with Spi–GFP in the axons at the optic stalk (Figure 6B). In photoreceptor cell bodies S was shown to stabilize Spi [46].We observed that S stabilizes Spi in axons, and promotes its trafficking through the axons, as more Spi–GFP molecules arrive at the lamina when co-expressed with S–HA (Figure 6D–6F). S–HA also co-localizes with Rho-3–GFP in the axons. Both the ligand and chaperone thus appear to co-localize with Rho-3–GFP in axons traveling through the optic stalk (Figure 6A and 6C).

We have previously shown that S is a substrate for ER-localized Rhomboid proteases [23], and that cleaved S cannot traffic Spi [20]. ER-based cleavage of S has a functional significance, as it limits the trafficking of the Spi precursor by the S chaperone out of the ER. This results in an increased sensitivity of EGFR signaling to S levels. Indeed, *S* heterozygous flies exhibit reduced EGFR signaling during oogenesis and eye development, where the ER-active Rho-2 and Rho-3 mediate Spi processing, respectively [23]. Thus, a sensitivity to *S* levels is indicative of exposure to Rhomboid-based cleavage in the ER. We find that *S* heterozygous flies show a severe reduction in ElaV expression in the lamina (Figure 6G and 6H). Importantly, the defect in EGFR signaling in the laminae of these flies is significantly more severe than the compromised induction of photoreceptors in the eye disc. This may reflect a longer exposure of S to ER cleavage by Rho-3 during trafficking to the axon termini. Thus, the hypersensitivity of the lamina to *S* gene dosage supports the notion that S and Rho-3 are jointly trafficked through the ER in photoreceptor axons.

Endosomal Trafficking Regulates Spi Secretion

Following its trafficking to the axonal termini, Spi seems to be secreted locally at a precise location [6]. In the eye disc, Spi is also secreted locally, from a late secretory compartment where Rho-1 and Rho-3 reside [23]. To gain insight into the mechanism of Spi release, we set out to identify the "late compartment" in the eye disc. A variety of compartment markers were tested for co-localization with Rho-1–HA expressed in the eye disc (see also [23]), including a collection of YFP-tagged Rab proteins [47]. The only significant co-localization was observed with YFP–Rab4 and YFP–Rab14 (Figure 7A and 7B). This co-localization was also verified in cell culture, where a significant proportion of Rho-1-, Rab4-, and Rab14-positive puncta overlap (Figure S4A). YFP–Rab4 and YFP–Rab14 also co-localize with apical, but not peri-nuclear, Rho-3–HA staining in the eye disc (Figure S5).

Interruption of Rab4 and Rab14 function in photoreceptors by RNA interference (RNAi) or dominant negative (DN) approaches did not result in any discernible phenotypes. However, both Rab proteins interact with effectors of Rab11 [48,49], suggesting a role for this major conserved regulator of endosomal trafficking in Spi exocytosis. Indeed, expression of a DN form of Rab11 in *Drosophila* cell culture disrupted the morphology of Rab4/14 endosomes, marked by Rho-1–red fluorescent protein (RFP) or Spi–HA, when the latter was co-expressed with S (Figure S4). Furthermore, in the eye imaginal disc, Rho-1–GFP, which is normally localized to discrete puncta, is misocalized upon co-expression of Rab11DN by GMR–Gal4 (Figure 7C and 7D). Thus, although Rab11 does not co-localize to the Rho-1-containing endosomes, its function is essential for their correct formation.

We then asked whether EGFR signaling is affected by impairment of the Rab4/14 compartment. Indeed, expression of Rab11DN by GMR–Gal4 led to a reduction in the number of ElaV-expressing cells in the eye disc (unpublished data), as did expression of a Rab11 RNAi construct (Figure 7E). Importantly, there was no alteration of photoreceptor R8 differentiation, which is not dependent upon EGFR signaling. Since this phenotype may reflect a requirement for Rab11 in the signal-receiving cells, downstream to EGFR, we expressed the Rab11DN construct specifically in R8, which is the only photoreceptor that acts exclusively as a signal-emitting cell. Again, EGFR phenotypes such as missing photoreceptors and mis-rotated ommatidia were readily apparent (Figures 7F, S6A, and S6B). This indicates that Rab11 acts non-autonomously in R8, where it is required for EGFR ligand secretion.

When larvae expressing UAS–Rab11DN by GMR–Gal4 in the eye disc were allowed to develop, the resulting adults had very small and rough eyes, as previously reported (Figure 7G; see also [47]). Although Rab11 has pleiotropic functions, this phenotype is at least partly due to a specific failure in EGFR ligand secretion, since co-expression of Rho-1 with Rab11DN considerably ameliorated the phenotype (Figure 7H). We conclude that in the eye disc, Spi is cleaved and secreted from Rab4/14 endosomes, and that the normal function of these endosomes is required for EGFR ligand trafficking and processing.

The requirement for Spi cleavage to take place after ligand is trafficked out of the ER in both the cell bodies and axons, raised the possibility that subsequent trafficking steps also share common features. We therefore sought to determine whether Spi secretion

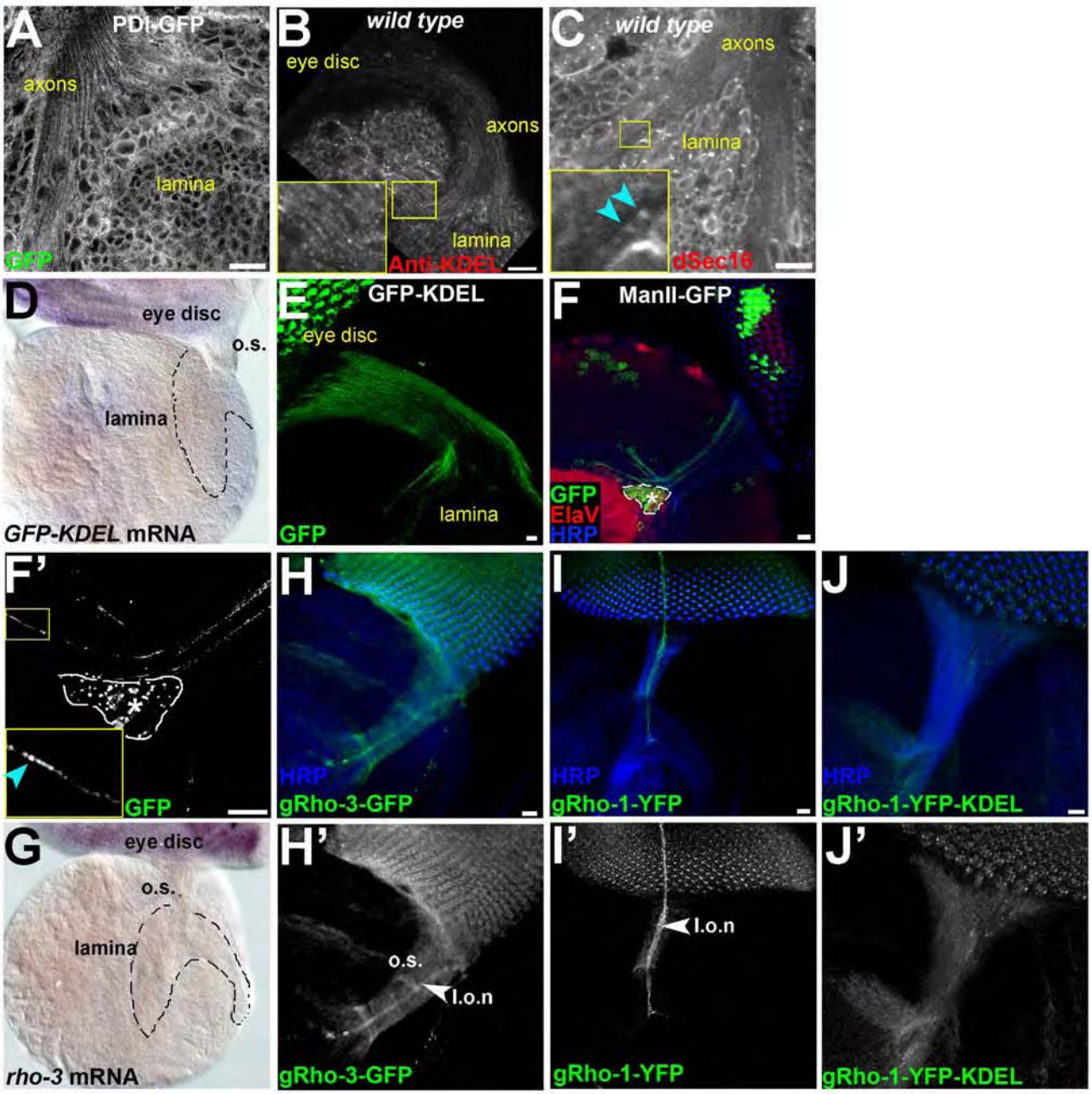

Figure 5. The ER facilitates Rho-3 trafficking to axons. (A–C) Endogenous ER markers are detected throughout the axons of photoreceptor neurons. (A) A GFP gene trap in the endogenous PDI. GFP immunoreactivity is detected along the axons (not shown) and at their termini, as they invade the lamina. (B) ER-retained proteins are revealed by anti-KDEL immunostaining along the length of the axon. The inset shows a magnification of the axonal termini in the lamina. (C) ER exit sites, marked by dSec16, showing a smooth staining and some brighter puncta in the axons and in lamina cells. The inset shows dSec16 puncta (arrowheads) in axons which have reached the lamina. (D and E) Expression of GFP–KDEL in the eye disc by mδ0.5–Gal4. (D) RNA in situ hybridization with a *GFP* probe, showing that *GFP–KDEL* mRNA is restricted to cell bodies in the eye disc. No signal is detected in the optic stalk (o.s.) or the lamina (outlined). (E) GFP–KDEL protein can reach the axon through the ER, and is detected along the entire length of the axon. (F) ManII–GFP (green), expressed in wild-type MARCM clones, is present throughout the axon. The outlined area (asterisk) is a clone in the lamina cells. (F′) shows the ManII–GFP separately, with an enlargement of one fascicle. The Golgi is detected as discrete units (arrowhead), with a ''beads on a string'' appearance. (G) *rho-3* mRNA is confined to cell bodies in the eye disc, and is not detected in the axonal projections into the lamina (outlined). (H) The ER localized gRho-3–GFP (green, and in [H′]) is localized to the eye disc, and is also enriched in axons. Arrowhead in (H′) marks the larval optic nerve (l.o.n.) where nonspecific staining occurs. (I) gRho-1–YFP (green, and in [I′]) is localized specifically to the eye disc, and does not reach the axons. Arrowhead in (I′) marks the larval optic nerve. (J) When gRho-1–YFP is targeted to the ER (gRho-1–YFP–KDEL, green and in [J′]), it is translocated along the axon bundle. Scale bars: 10 μm.
doi:10.1371/journal.pbio.1000505.g005

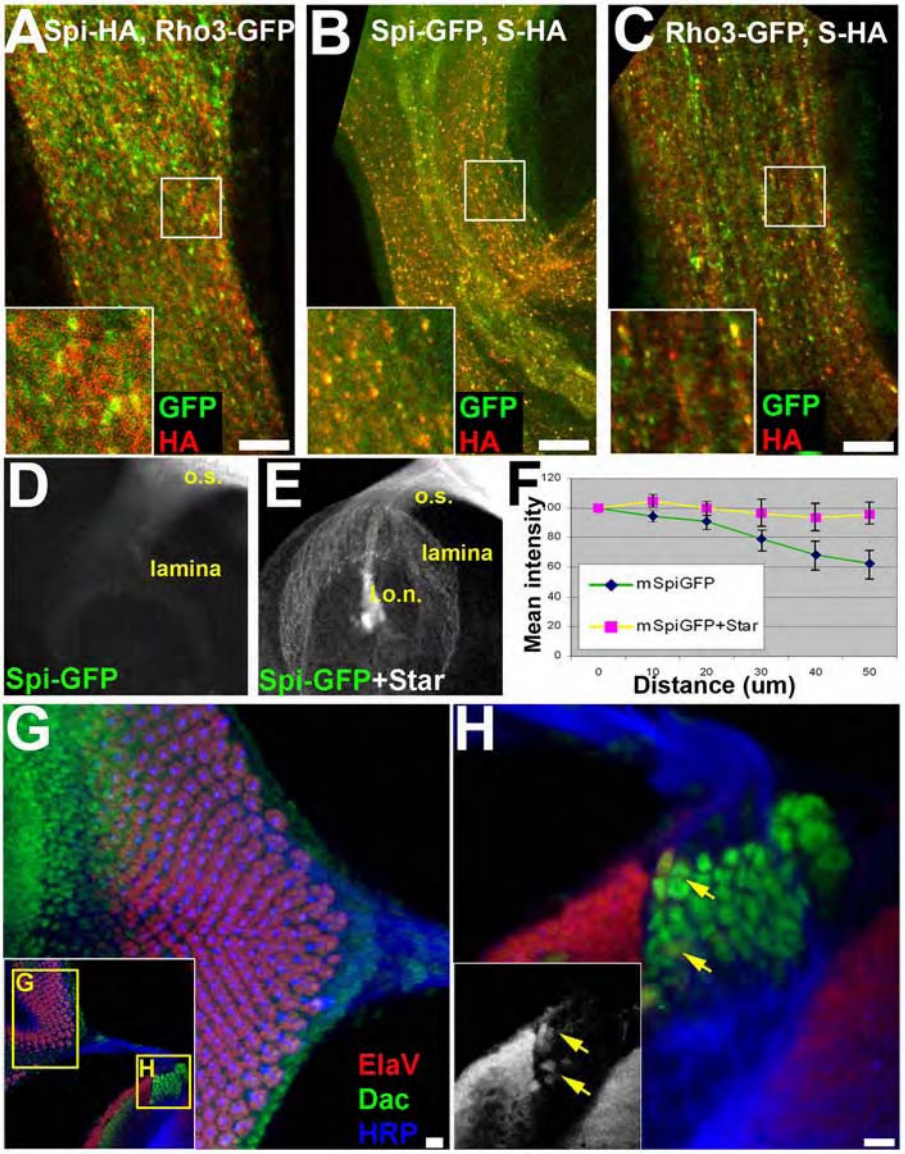

Figure 6. Co-trafficking of Spi, S, and Rho-3 sensitizes EGFR activation in the lamina to *S* gene dosage. (A–C) The localization of Spi, S, and Rho-3 was examined in the optic stalks of specimens expressing HA- (red) or GFP-tagged (green) versions of the proteins in the eye disc by GMR–Gal4. (A) Spi–HA co-localizes with Rho-3–GFP in the axons. (B) Spi–GFP co-localizes with S–HA. (C) S–HA co-localizes with Rho-3–GFP. (D–F) S stabilizes Spi during their joint axonal trafficking. (D) The levels of Spi–GFP (green), expressed on its own in the eye disc, decay along the axons. (E) Co-expression of S–HA with Spi–GFP stabilizes the ligand. l.o.n., larval optic nerve; o.s., optic stalk. (F) Quantification of the effect of S expression on Spi. Mean pixel intensities of Spi–GFP were determined every 10 μm along the optic stalk, from the point where the optic stalk leaves the eye disc (distance = 0). GFP intensity was normalized to 100 at point 0. Seven specimens were examined per genotype. Student's *t*-test shows that the difference at the most distal point is statistically significant. (G and H) EGFR signaling is more sensitive to S levels in the lamina than in the eye. EGFR activation in both tissues is assayed by ElaV expression (red), Dac (green), and HRP (blue). (G) *S* heterozygous eye disc. EGFR phenotypes associated with $S^{+/-}$ (misrotated ommatidia and missing photoreceptors) lead to the slightly abnormal appearance of ElaV staining, but the phenotype is not severe. The inset shows that photoreceptor axons extend normally to the brain. (H) The lamina of the same specimen as in (G) shows a severe reduction in EGFR activation. Only a small number of cells (arrows) at the posterior of the lamina express ElaV, although Dac expression is unperturbed. Scale bars: 5 μm.
doi:10.1371/journal.pbio.1000505.g006

from the axons similarly involves Rab4/14 endosomes, and is dependent upon Rab11 function. Indeed, we found that Rab4 or Rab14, expressed in the eye disc by GMR–Gal4, reached axonal growth cones, as did Rab11. Note that GMR–Gal4 does not drive expression in the lamina ([6] and Figure 4E–4G). As in the eye disc, co-localization between Rho-3–HA and YFP–Rab4 or YFP–Rab14 was observed in axonal termini (Figure S5), but not along the length of the axons in the optic stalk (unpublished data).

Expression of Rab11DN in the eye disc by GMR–Gal4 led to a significant reduction in the number of ElaV-positive cells in the lamina, while Dac expression was normal (Figure 7I). Importantly, expression of Rab11DN in R8, which does not secrete Spi to the lamina, severely impairs EGFR signaling in the eye disc but not in the lamina (Figure S6). To further separate the axonal function of Rab11 from its requirement in photoreceptor differentiation, we expressed Rab11DN by GMR–Gal4 together with RasV12, which

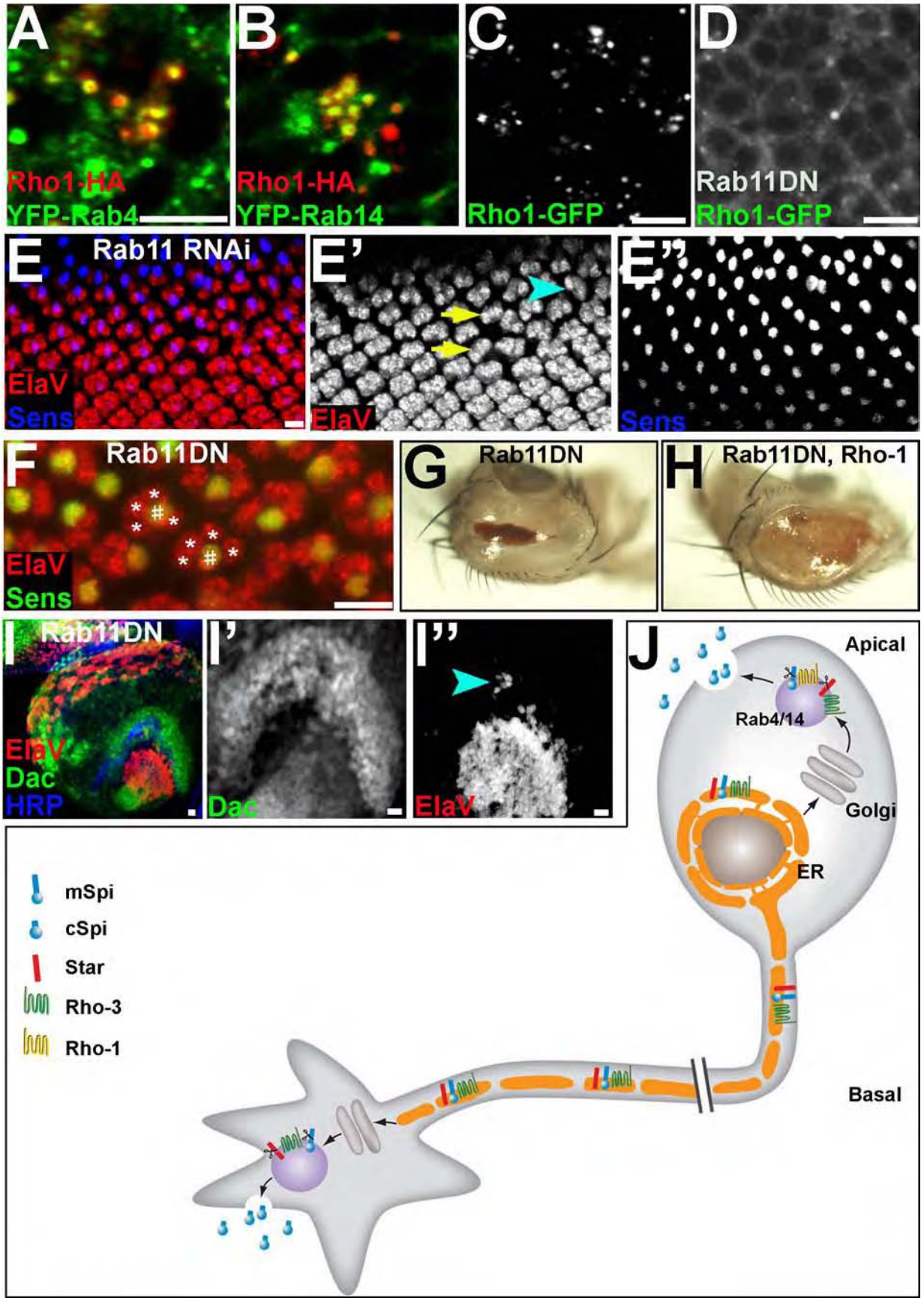
A
Rho1-HA
YFP-Rab4
B
Rho1-HA
YFP-Rab14
C
Rho1-GFP
D
Rab11DN
Rho1-GFP
E
Rab11 RNAi
ElaV
Sens
E'
ElaV
E''
Sens
F
Rab11DN
ElaV
Sens
G
Rab11DN
H
Rab11DN, Rho-1
I
Rab11DN
ElaV
Dac
HRP
I'
Dac
I''
ElaV
J
Apical
Rab4/14
Golgi
ER
Basal
mSpi
cSpi
Star
Rho-3
Rho-1

Figure 7. Regulation of Spi secretion by endosomal trafficking. (A and B) The apical Rho-1 puncta are Rab4/14 endosomes. Rho-1–HA (red), expressed in the eye disc, co-localizes with YFP-tagged Rab4 or Rab14 (green). (A) Co-localization of Rho-1–HA and YFP–Rab4. (B) Co-localization of Rho-1–HA and YFP–Rab14. (C) Rho-1–GFP shows the typical punctate staining of Rab4/14 endosomes when expressed in the eye disc. (D) Upon co-expression of Rab11DN, Rho-1–GFP is mislocalized. Some weak punctate staining is still detectable, but most GFP immunolabeling appears sub-membranal. (E) Expression of Rab11 RNAi in the eye disc by GMR–Gal4 yields EGFR phenotypes such as missing photoreceptors (arrows in [E′]), misrotated ommatidia (arrowhead), and defective ommatidial spacing. Importantly, although ElaV staining (red, and in [E′]) reveals these defects, R8 differentiation (Senseless, blue, and in [E″]) is unaffected. (F) R8-specific expression of Rab11DN by Sca–Gal4 disrupts EGFR signaling in adjacent cells, indicating that Rab11 is involved in ligand secretion. For example, two ommatidia with only four outer photoreceptors (*) and an R8 cell (#) are marked. (G) Adult flies expressing Rab11DN by GMR–Gal4 have small eyes. (H) Co-expression of Rho-1 or Rho-3 (not shown) rescues the defects associated with Rab11DN, suggesting that these defects are partly due to a failure to properly target Rhomboids and secrete Spi. (I) Expression of Rab11DN in the eye also leads to a defect in EGFR signaling in the lamina. ElaV staining in the lamina (red, and in [I″]) is strongly reduced (arrowhead in [I″] shows residual staining), while Dac expression (green, and in [I′]) is not affected. (J) Model. ER-facilitated trafficking of the Spi-processing machinery to axon termini promotes Spi secretion from the axons to the lamina. Scale bars: 5 μm.
doi:10.1371/journal.pbio.1000505.g007

induces massive photoreceptor recruitment ([50] and Figure S7A). In the eye disc RasV12 was epistatic to Rab11DN, where all cells were converted to ElaV-expressing neurons, supporting the notion that Rab11 acts upstream to Ras (Figure S7). Expression of RasV12 in the eye induces an enlarged lamina with extra lamina neurons. Co-expression of Rab11DN attenuated the effects of RasV12 on lamina development in seven of 12 specimens, leading to wild-type or even reduced ElaV expression (Figure S7). In other words, we have uncoupled the requirement for Rab11 for secretion of the ligand in the eye disc and in the lamina by using RasV12 to bypass the requirement for the ligand in the eye disc. Therefore, this effect specifically represents the requirement for Rab11 to allow secretion of the ligand at the axon termini. This is consistent with the notion that after trafficking of mSpi, S, and Rho-3 to the axonal termini, secretion occurs in a similar manner to the eye disc, utilizing a Rab11-dependent mechanism.

Discussion

Axonal Release of Spi Requires the ER Residence of Rho-3

Polarized secretion of ligands from a signal-emitting cell to the appropriate receptive field is crucial for correct intercellular communication. Control over EGFR ligand secretion, and consequently EGFR activation, in *Drosophila* is achieved through trafficking and compartmentalization of the ligand-processing machinery. This work identifies a link between the subcellular localization of the Spi-processing machinery and the polarized release of Spi from axons.

Subcellular localization of Rhomboid proteases, which process the inactive Spi precursor, impinges on ligand secretion [23]. Both Rho-1 and Rho-3 are localized to apical Rab4/14 endosomes, where they are redundant in promoting Spi release from cell bodies. In contrast, only the Rho-3 protease mediates axonal secretion of Spi. This is evident from the *rho-3* mutant phenotype, which shows a complete loss of EGFR activation in the lamina. Since the two proteases are expressed in the neurons which secrete Spi, and share the same substrate specificity, these features cannot account for the specific requirement for *rho-3*. RNA transport and localized translation of Rho-3 are also inconsistent with the following observations: (a) no *rho-3* RNA was detected in axons, (b) gRho-3–GFP, reflecting endogenous expression, is localized throughout the axon, rather than concentrated at a point of localized translation, and (c) Rho-3 cDNA, devoid of 3′ or 5′ UTRs, rescued the mutant phenotype. The RNA of the rescuing construct was also not localized to axons.

Our results indicate that the exclusive requirement for Rho-3 is due to its ER localization. Re-localization of some of the Rho-1 pool to the ER, or removal of Rho-3 from the ER, achieved by swapping specific sequences, alternated their potencies to promote axonal secretion of Spi. Furthermore, when the ER export of endogenous Rho-1 was compromised, EGFR activation was partially restored to the lamina of *rho-3* mutants. Thus, the ER localization of Rho-3 in photoreceptor neurons serves a dual function: it negatively regulates Spi secretion from cell bodies, via premature cleavage of S [23], and positively promotes Spi secretion from the axons to the lamina, by facilitating trafficking of the ligand-processing machinery to axon temini (schematized in Figure 7J).

The ER Promotes Trafficking of the Spi-Processing Machinery to Axons

How does the ER localization of Rho-3 contribute to Spi secretion from axons? The inability of GFP–Rho-3–KDEL or cSpi–HA to rescue the *rho-3* phenotype demonstrates that the axonally secreted Spi is not cleaved in the ER, and prompted investigation into the role of the ER in promoting axonal trafficking.

We have shown that in *Drosophila* photoreceptor neurons, the ER extends throughout the axons. ER exit sites and Golgi outpost markers were also detected in axons. The continuity of the ER was previously demonstrated in Purkinje neurons [26] and in other cell types, including *Drosophila* oocytes [42,51]. This implies that ER-localized proteins could use this compartment to move distally in the axon. Indeed, GFP–KDEL expressed in the eye disc reaches the axonal termini. Furthermore, the ER-localized Rho-3 is enriched in axons, as opposed to Rho-1, which is restricted to endosomes. Importantly, restricting the gRho-1 construct to the ER with a KDEL sequence gave rise to a robust translocation of the protease throughout axons, reaching their growth cones in the lamina.

ER-facilitated trafficking of Rho-3 could occur through diffusion in the ER membrane, with exit and retrieval of ER-derived vesicles being biased distally. Alternatively, and perhaps more likely, the ER presence of Rho-3 could lead it to an exit site localized at the axon base, from which trafficking would be directed towards the growth cones. This would explain the ability of Rho-1 to rescue the *rho-3* phenotype under strong overexpression conditions. Distinction between these possibilities would require co-localization of Rho-3 or Spi immunoreactivity with known compartment markers in axons. So far, and despite a large number of markers examined, we could not detect such co-localization (unpublished data). Since the extension of the ER is correlated with the growth of the axons [52,53], ER-facilitated trafficking also provides a means of ensuring that ligand is released only once the axons have reached their target layer, and ER exit sites and Golgi membranes are set in place.

Spi, S, and Rho-3 are all localized to the peri-nuclear ER in the eye disc. Since all three proteins can interact with one another [19,46], this implies that the processing machinery could assemble in the ER for joint trafficking. Indeed, we found that Spi, S, and Rho-3 also co-localize in photoreceptor axons. Further evidence

for the joint trafficking of S and Rho-3 is the marked sensitivity of EGFR signaling in the lamina to S levels. We have previously shown that S cleavage in the ER leads to compromised EGFR activation phenotypes upon halving *S* gene dosage [23]. The observation that EGFR signaling in the lamina is even more sensitive to *S* gene dosage than in the eye suggests that Rho-3 and S spend a significant time in the ER, where the chaperone is exposed to inactivation by cleavage.

How targeting of Spi–S–Rho-3 complexes to the basally located axons or the apical Rab4/14 endosomes is achieved is unclear. In the case of Hh, the presence or absence of the C-terminal cleavage fragment in the Hh-containing vesicle determines its destination [4]. The Spi C-terminus is not required for axonal targeting, since a Spi–GFP construct lacking most of the C-terminus showed the same distribution as intact Spi–GFP upon expression in the eye (unpublished data). Alternatively, another factor, which would be ER localized, could promote the trafficking of the processing machinery to axons. This factor is also expected to be expressed mainly in R2, R5, and R8, accounting for their importance in Spi secretion to the lamina. In the *Drosophila* oocyte, the polarized ER exit of another EGFR ligand, Gurken, is regulated by Cornichon. Somatic functions for Cornichon and its homolog Cornichon related have also been identified but not thoroughly explored yet [54].

While the presence of ER markers in axons or dendrites has been previously reported [27], the biological significance of such observations, commonly derived from protein localization data in cultured neurons, could only be speculated upon, since no functional readout was examined. The unique properties of photoreceptor axons in *Drosophila*, which not only conduct electrical signals but are also involved in transmitting developmental cues at an earlier phase, have allowed us to functionally demonstrate the essential role of the ER in trafficking the complete EGFR ligand-processing apparatus to axon termini. This mechanism is clearly distinct from the established roles of the axonal ER in allowing local translation of secreted or transmembrane proteins whose mRNAs are enriched at axon termini.

Endosomal Regulation of Spi Secretion

Spi is released to the extracellular milieu following cleavage by Rho-1. Different experimental systems have yielded conflicting reports as to the compartment in which the protease resides [18–20,55]. We now find that in both photoreceptor neurons and Schneider cells, Rho-1 is localized to an endosomal population marked by Rab4 and Rab14. Rab4 localizes to fast recycling endosomes, which mediate the retrieval of endocytosed cargo to the plasma membrane [56,57]. Rab14 mediates trafficking between the Golgi and endosomes [58,59]. Both Rab4 and Rab14 share binding proteins with Rab11 [48,49], a major regulator of vesicle transport.

The role of endosomal dynamics in Spi secretion is manifested by the EGFR phenotypes obtained following expression of Rab11 RNAi or DN constructs. While Rab11 has pleiotropic functions and is not dedicated to EGFR signaling, perturbing Rab11 directly impinges on Spi secretion. This was evident from the mislocalization of Rho-1–GFP in Rab11DN-expressing photoreceptors, and from similar effects in cell culture. This mislocalization is likely the cause of the phenotype, since co-expression of Rho-1 or Rho-3 with Rab11DN abrogated the small eye phenotype associated with Rab11DN expression. Although interfering with endosomal dynamics may also perturb signaling downstream of the receptor, we did not observe a mislocalization of EGFR itself (unpublished data). Furthermore, the expression of Rab11DN in R8 impaired the differentiation of nearby cells into photoreceptor neurons, demonstrating that Rab11 acts non-autonomously upstream of the receptor, consistent with a role in ligand secretion.

Rho-1 and some of the Rho-3 pool are localized to Rab4/14 endosomes. The intracellular route by which they reach these compartments remains to be explored. From the ER accumulation of Rho-1–HA in *sed5* mutant clones, we infer that the proteases do not undertake a Golgi-independent route to the Rab4/14 endosomes [41]. Furthermore, Rab14 mediates trafficking between the Golgi and endosomes [59], and Rab11 endosomes can be reached without passing through the plasma membrane (see for example [60–62]). Therefore, there is no indication that Rhomboids must pass through the plasma membrane to reach the endosomal compartment. Nevertheless, if Spi is secreted by fusion of Rhomboid-containing endosomes with the membrane, then retrieval by endocytosis should play a role in shaping the steady-state distribution of Rhomboids. Accordingly, we have found that upon expression of a DN form of the Dynamin Shibire, Rho-1–HA immunofluorescence is detected on the plasma membrane (unpublished data).

Trafficking of Spi to endosomes also provides an efficient means of disposing of the ligand in cells that do not express a Rhomboid protease, to prevent nonspecific cleavage on the plasma membrane. In this case, the membrane-bound precursor could be sorted to a membrane domain that segregates to multi-vesicular bodies, and then degraded in the lysosome. Accordingly, distinct membrane domains have been described for Rab4 and Rab11 endosomes [63].

Finally, we detected a co-localization between Rab4/14 and Rho-3 at axonal termini, but not in the optic stalk, and found that disrupting Rab11 function in the eye disc compromised EGFR signaling in the lamina. This effect was not due to defects in eye development, as Rab11DN expressed in R8 also impaired eye development but had no effect on the lamina. This finding raises the possibility that the final steps of secretion from axonal termini and cell bodies are regulated in a similar manner, although Rab11 seems to play a more prominent role in secretion from cell bodies. A precedent supporting such a hypothesis is the requirement for Sec15, which interacts with Rab11, for the localization of several molecules at both photoreceptor cell bodies and axonal termini [64].

In summary, our results describe a mechanism of ER-facilitated trafficking of secreted molecules in axons, prior to processing and secretion at the axon tip. This mechanism could also be utilized for other proteins that are secreted in a polarized manner in neurons.

Materials and Methods

DNA Constructs

For the generation of gRho-1–YFP and gRho-3–GFP, 40–45 kb from the *rho-1* or *rho-3* loci, encompassing the ORFs and flanking region, were cloned into P[acman–attB, AmpR] by recombineering-mediated gap repair [35]. The domains extend between 3L:1437674 and 1475379 and 3L:1355719 and 1397235 (release 5.23) for *rho-1* and *rho-3*, respectively. A YFP tag or a YFP–KDEL was inserted at the *rho-1* C-terminus by GalK positive/negative selection [65]. *rho-3* was GFP tagged at the C-terminus using the PL452 C-EGFP tag template vector [66]. Both constructs were injected into VK00005 landing site.

For GFP–Rho-1, GFP–Rho-3, GFP–R1L1-R3, and GFP–R3L1-R1, eGFP was cloned into pUAST–attB at the BglII–EcoRI sites. cDNAs were then cloned using EcoRI and XhoI. All constructs were sequenced, and injected into attP18 lines [39].

cSpiHA contains a triple HA tag from pTWH, inserted after the Spi cleavage site.

mSpi–HA was generated by a site-directed mutagenesis insertion of an XhoI site after T58 of Spi, into which a triple HA tag was subsequently inserted.

mSpi–GFP^{mut} was obtained from S. Urban [33], and cloned into pTWM. Cleavage assays in S2 cells verified that this construct cannot undergo Rhomboid-dependent cleavage (unpublished data).

S–HA is the S cDNA cloned into pTHW. mSpi–GFP and cSpi–HRP were previously described [17,19]. The cleavage activity of all Rhomboid constructs has been tested in cell culture, and the biological activity of all UAS-based constructs was assayed by expression in wing or eye imaginal discs.

Immunohistochemistry

Climbing late third-instar larvae were dissected and fixed in PBS containing 4% PFA. All subsequent washes and antibody incubations were done in PBS with 0.1% Triton X-100.

Primary antibodies used were anti-FasIII (mouse, 1:50), anti-EGFR (rat, 1:1,000), anti-Senseless (guinea pig, 1:2,000; from H. Bellen), anti-dSec16 (rabbit, 1:1,000; from C. Rabouille), anti-Myc (mouse, 1:100; Santa Cruz Biotechnology), anti-GFP (chick, 1:2,000; Abcam), anti-HA (mouse, 1:1,000; Roche), and anti–Troponin H to detect BiP (rat, 1:100; Babraham Bioscience Technologies). Anti-ElaV (rat, 1:2,000, or mouse, 1:500) and anti-Dac (mouse, 1:500) were obtained from the Developmental Studies Hybridoma Bank, University of Iowa. Cy-5-conjugated goat anti-HRP, as well as Cy-2-, Cy-3-, and Cy-5-conjugated secondary antibodies (1:200) were obtained from Jackson ImmunoResearch.

In situ hybridizations using *rho-3* or *GFP* probes were done using standard techniques.

Fly Strains

The following lines were used: GMR–Gal4, Sca–Gal4, m^{TM}–Gal4 (from M. Mlodzik), Lz–Gal4, K25–Gal4, MT14–Gal4 ([34], from I. Salecker), UAS–GFP–KDEL [45], MS1096–Gal4, PDI–GFP [67], *sed5*^{AR113} (From C. Rabouille), *S*^{HN23}, a collection of YFP-tagged, native or DN UAS–Rab transgenes [47], UAS–Rab11DN (from M. Gonzalez-Gaitan), UAS–ManII–GFP (from Y. Jan), and UAS–Rab11–RNAi (VDRC22198). Null alleles of *rho-1* (*rho-1*$^{\Delta p38}$) and *rho-3* (*ru*^{PLL5}) were recombined with *FRT2A*, and crossed to *ey–Gal4,UAS–FLP/Cyo;FRT2a,GMR–hid,l(3)CL–L*^{1}*/TM6B* to generate entirely mutant eyes [28]. To generate *sed5* ^{AR113} MARCM clones expressing Rho-1–HA, *C155–Gal4,UAS–CD8GFP,hsFLP;Gal80, FRT40A* females were crossed to *sed5* ^{AR113}*,FRT40A/+;UAS–Rho-1HA/+* males. Wild-type clones were generated with a chromosome bearing only *FRT40A*. Clones expressing ManII–GFP were induced in animals of the following genotype: *C155–Gal4,hsFLP/+;UAS–ManII–GFP/+;FRT82B*.

UAS–mSpi–GFP^{mut}, UAS–cSpi–HA, UAS–mSpi–HA, UAS–GFP–Rho-1, UAS–GFP–Rho-3, UAS–GFP–R1L1-R3, and UAS–GFP–R3L1-R1 were generated by standard P-element or phi31 germline transformation procedures.

ERG recordings were performed as described in [29].

Supporting Information

Figure S1 *rho-3* mutants have functional photoreceptors but no post-synaptic responses. (A) ERG recording from a wild-type fly shows depolarization of photoreceptors in response to light, as well as "on/off transients" (arrowheads), which represent the post-synaptic response of lamina neurons. (B) *rho-3* mutant photoreceptors depolarize in response to light. The lower amplitude of depolarization probably stems from the disorganization of *rho-3* eyes. Importantly, no "on/off transients" can be detected in the mutant (arrowheads), consistent with a failure in lamina neurogenesis. (C) *rho-1* EGUF clones show a wild-type ERG. (D) EGFR endocytic puncta (arrows in D′) are detected in wild-type lamina. (E) *rho-3* mutants have no endocytic EGFR puncta in the lamina. (F) Lamina from *rho-1* EGUF clones show an EGFR distribution identical to wild-type eyes.
Found at: doi:10.1371/journal.pbio.1000505.s001 (2.92 MB TIF)

Figure S2 *rho-3* RNA is not transported in photoreceptor axons. (A) RNA in situ hybridization with a *rho-3* probe (see also Figure 5G). *rho-3* RNA is localized to the eye disc and is not detected in axons or in the lamina (outlined). (B) A Rho-3–GFP transgene, expressed in the eye disc under the control of the strong promoter GMR–Gal4 fully rescues the *rho-3* mutant lamina phenotype (arrowhead and outline in inset). Importantly, the transgene contains only the cDNA protein coding sequences, and is devoid of 3′ or 5′ UTRs. Anti-HRP staining (blue) shows axons, Dac (green) marks all lamina cells, and ElaV (red, and shown separately in the inset) marks the lamina cartridge neurons. Scale bar: 10 μm. (C) RNA in situ hybridization with a *GFP* probe on a visual system of the same genotype as in (B). RNA of the rescuing transgene is localized exclusively to the eye, and is not detected in the axons or lamina.
Found at: doi:10.1371/journal.pbio.1000505.s002 (3.50 MB TIF)

Figure S3 Cleaved Spi, expressed in the eye disc, does not rescue the *rho-3* phenotype. (A–C) Two independent lines of UAS–cSpi–HA (A and B) or a UAS–cSpi–HRP (C) do not rescue the *rho-3* phenotype in the lamina. All constructs were driven by MT14–Gal4, in a *rho-3* mutant background. ElaV is red, Dac is green, and HRP is blue. Scale bars in the upper panels are 20 μm. The lower panels show enlargements of the lamina. Scale bars are 5 μm. Insets in (A) and (B) show anti-HA staining, demonstrating that the constructs are correctly expressed. (D–F) cSpi–HA (D and E) and cSpi–HRP (F) are biologically active, and are potent activators of the EGFR pathway. The activity of the constructs was assayed by their ability to induce extra vein tissue in wings, following induction in the wing pouch by MS1096–Gal4.
Found at: doi:10.1371/journal.pbio.1000505.s003 (6.10 MB TIF)

Figure S4 Spi is processed in Rab4/14 endosomes in cell culture. (A) Rho-1–GFP (green, and in A′), HA–Rab4 (red, and in A′′), and Myc–Rab14 (blue, and in A′′′) co-localize in S2 cells. Scale bar is 10 μm in all panels. (B) Rho-1–RFP (red) marks endosomes in S2 cells. (C) Expression of Rab11DN led to the accumulation of Rho-1–RFP in enlarged, deformed vesicles (arrows). (D) Spi–HA (red) co-expressed with S is used as a marker for the Rho-1 compartment. (E) Upon expression of Rab11DN, Spi–HA is localized to deformed vesicles of the same morphology as in (C).
Found at: doi:10.1371/journal.pbio.1000505.s004 (1.22 MB TIF)

Figure S5 Rho-3 co-localizes with Rab4 and Rab14 in cell bodies and growth cones. (A) Rho-3–HA (red), YFP–Rab4, or YFP–Rab14 (green) co-localize at the apical-most region of photoreceptor cell bodies (upper panels), but not in the perinuclear ER (lower panels). Scale bar is 5 μm in all panels. (B) At the growth cones, Rho-3–HA is also co-localized with Rab4/14. No co-localization was observed along the axons at the optic stalk (unpublished data). Note that both Rab4 and Rab14 have a cytoplasmic as well as vesicular distribution. The vesicular distribution overlaps with Rho-3–HA (arrows).

Found at: doi:10.1371/journal.pbio.1000505.s005 (2.95 MB TIF)

Figure S6 Rab11 is required non-autonomously in R8 to promote EGFR signaling in the eye but not in the lamina. (A) Rab11DN expressed in R8 cells by Sca–Gal4. Anti-ElaV staining (red, and shown separately) shows defects in photoreceptor recruitment, ommatidial rotation and spacing—phenotypes associated with compromised EGFR signaling. Importantly, the differentiation of R8 cells, marked with Senseless (green, and shown separately), is not perturbed. HRP (blue) marks axons. Scale bar: 5 μm. (A′) shows an enlargement of the boxed area in (A). (B) Rab11DN expression in R8 does not affect EGFR signaling in the lamina. Despite the defects in eye neurogenesis (A and B), ElaV expression in the lamina is indistinguishable from wild-type. ElaV (red, and shown separately) at the posterior part of the lamina is indicated by an arrowhead. Dac (green) and HRP (blue) mark lamina cell and photoreceptor axons, respectively.
Found at: doi:10.1371/journal.pbio.1000505.s006 (6.09 MB TIF)

Figure S7 Rab11 is required for Spi secretion from axons, independently of its function in photoreceptor recruitment. (A) RasV12 expression in the eye disc induces massive photoreceptor recruitment, and an enlarged lamina with extra lamina cartridge neurons. Anti-ElaV staining (red, and shown separately) decorates photoreceptors in the eye disc and lamina neurons. Dac (green) is expressed in non-neuronal cells in the eye, and in lamina precursors. HRP (blue) marks photoreceptor membranes. Scale bar is 10 μm. (B) Co-expression of RasV12 and Rab11DN. In the eye, RasV12 is epistatic to Rab11DN, indicating that Ras function lies downstream from Rab11. In the lamina, the RasV12 hyperactivation phenotype is suppressed by Rab11DN, suggesting that Rab11DN inhibits lamina neurogenesis independently of its effect on photoreceptor development.
Found at: doi:10.1371/journal.pbio.1000505.s007 (4.12 MB TIF)

Acknowledgments

We thank U. Banerjee, H. Bellen, M. Gonzales-Gaitan, Y. Jan, M. Mlodzik, C. Rabouille, I. Salecker, and S. Urban for generously providing reagents. We are grateful to B. Minke and O. Friedman for help in the ERG recordings, and A. Propp for help with Rab11 characterization. We also thank E. Arama, E. Bibi, and O. Schuldiner for critical reading of the manuscript, and the Shilo lab for helpful discussions.

Author Contributions

The author(s) have made the following declarations about their contributions: Conceived and designed the experiments: SY EDS BZS. Performed the experiments: SY. Analyzed the data: SY EDS BZS. Contributed reagents/materials/analysis tools: SY. Wrote the paper: SY EDS BZS.

References

1. Katsuki T, Ailani D, Hiramoto M, Hiromi Y (2009) Intra-axonal patterning: intrinsic compartmentalization of the axonal membrane in Drosophila neurons. Neuron 64: 188–199.
2. Birchmeier C (2009) ErbB receptors and the development of the nervous system. Exp Cell Res 315: 611–618.
3. Michailov GV, Sereda MW, Brinkmann BG, Fischer TM, Haug B, et al. (2004) Axonal neuregulin-1 regulates myelin sheath thickness. Science 304: 700–703.
4. Chu T, Chiu M, Zhang E, Kunes S (2006) A C-terminal motif targets Hedgehog to axons, coordinating assembly of the Drosophila eye and brain. Dev Cell 10: 635–646.
5. Huang Z, Kunes S (1996) Hedgehog, transmitted along retinal axons, triggers neurogenesis in the developing visual centers of the Drosophila brain. Cell 86: 411–422.
6. Huang Z, Shilo BZ, Kunes S (1998) A retinal axon fascicle uses spitz, an EGF receptor ligand, to construct a synaptic cartridge in the brain of Drosophila. Cell 95: 693–703.
7. Doroquez DB, Rebay I (2006) Signal integration during development: mechanisms of EGFR and Notch pathway function and cross-talk. Crit Rev Biochem Mol Biol 41: 339–385.
8. Roignant JY, Treisman JE (2009) Pattern formation in the Drosophila eye disc. Int J Dev Biol 53: 795–804.
9. Heberlein U, Wolff T, Rubin GM (1993) The TGF beta homolog dpp and the segment polarity gene hedgehog are required for propagation of a morphogenetic wave in the Drosophila retina. Cell 75: 913–926.
10. Ma C, Zhou Y, Beachy PA, Moses K (1993) The segment polarity gene hedgehog is required for progression of the morphogenetic furrow in the developing Drosophila eye. Cell 75: 927–938.
11. Freeman M (1996) Reiterative use of the EGF receptor triggers differentiation of all cell types in the Drosophila eye. Cell 87: 651–660.
12. Tio M, Moses K (1997) The Drosophila TGF alpha homolog Spitz acts in photoreceptor recruitment in the developing retina. Development 124: 343–351.
13. Ting CY, Lee CH (2007) Visual circuit development in Drosophila. Curr Opin Neurobiol 17: 65–72.
14. Clandinin TR, Zipursky SL (2002) Making connections in the fly visual system. Neuron 35: 827–841.
15. Shilo BZ (2003) Signaling by the Drosophila epidermal growth factor receptor pathway during development. Exp Cell Res 284: 140–149.
16. Urban S, Lee JR, Freeman M (2001) Drosophila rhomboid-1 defines a family of putative intramembrane serine proteases. Cell 107: 173–182.
17. Schlesinger A, Kiger A, Perrimon N, Shilo BZ (2004) Small wing PLCgamma is required for ER retention of cleaved Spitz during eye development in Drosophila. Dev Cell 7: 535–545.
18. Lee JR, Urban S, Garvey CF, Freeman M (2001) Regulated intracellular ligand transport and proteolysis control EGF signal activation in Drosophila. Cell 107: 161–171.
19. Tsruya R, Schlesinger A, Reich A, Gabay L, Sapir A, et al. (2002) Intracellular trafficking by Star regulates cleavage of the Drosophila EGF receptor ligand Spitz. Genes Dev 16: 222–234.
20. Tsruya R, Wojtalla A, Carmon S, Yogev S, Reich A, et al. (2007) Rhomboid cleaves Star to regulate the levels of secreted Spitz. EMBO J 26: 1211–1220.
21. Wasserman JD, Urban S, Freeman M (2000) A family of rhomboid-like genes: Drosophila rhomboid-1 and roughoid/rhomboid-3 cooperate to activate EGF receptor signaling. Genes Dev 14: 1651–1663.
22. Schulz C, Wood CG, Jones DL, Tazuke SI, Fuller MT (2002) Signaling from germ cells mediated by the rhomboid homolog stet organizes encapsulation by somatic support cells. Development 129: 4523–4534.
23. Yogev S, Schejter ED, Shilo BZ (2008) Drosophila EGFR signalling is modulated by differential compartmentalization of Rhomboid intramembrane proteases. EMBO J 27: 1219–1230.
24. Orso G, Pendin D, Liu S, Tosetto J, Moss TJ, et al. (2009) Homotypic fusion of ER membranes requires the dynamin-like GTPase atlastin. Nature 460: 978–983.
25. Tang BL (2008) Emerging aspects of membrane traffic in neuronal dendrite growth. Biochim Biophys Acta 1783: 169–176.
26. Terasaki M, Slater NT, Fein A, Schmidek A, Reese TS (1994) Continuous network of endoplasmic reticulum in cerebellar Purkinje neurons. Proc Natl Acad Sci U S A 91: 7510–7514.
27. Jeyifous O, Waites CL, Specht CG, Fujisawa S, Schubert M, et al. (2009) SAP97 and CASK mediate sorting of NMDA receptors through a previously unknown secretory pathway. Nat Neurosci 12: 1011–1019.
28. Stowers RS, Schwarz TL (1999) A genetic method for generating Drosophila eyes composed exclusively of mitotic clones of a single genotype. Genetics 152: 1631–1639.
29. Verstreken P, Koh TW, Schulze KL, Zhai RG, Hiesinger PR, et al. (2003) Synaptojanin is recruited by endophilin to promote synaptic vesicle uncoating. Neuron 40: 733–748.
30. Freeman M (2008) Rhomboid proteases and their biological functions. Annu Rev Genet 42: 191–210.
31. Urban S (2006) Rhomboid proteins: conserved membrane proteases with divergent biological functions. Genes Dev 20: 3054–3068.
32. Hay BA, Wolff T, Rubin GM (1994) Expression of baculovirus P35 prevents cell death in Drosophila. Development 120: 2121–2129.
33. Baker RP, Wijetilaka R, Urban S (2006) Two Plasmodium rhomboid proteases preferentially cleave different adhesins implicated in all invasive stages of malaria. PLoS Pathog 2: e113. doi:10.1371/journal.ppat.0020113.
34. Kaminker JS, Canon J, Salecker I, Banerjee U (2002) Control of photoreceptor axon target choice by transcriptional repression of Runt. Nat Neurosci 5: 746–750.
35. Venken KJ, He Y, Hoskins RA, Bellen HJ (2006) P[acman]: a BAC transgenic platform for targeted insertion of large DNA fragments in D. melanogaster. Science 314: 1747–1751.
36. Ben-Shem A, Fass D, Bibi E (2007) Structural basis for intramembrane proteolysis by rhomboid serine proteases. Proc Natl Acad Sci U S A 104: 462–466.
37. Wu Z, Yan N, Feng L, Oberstein A, Yan H, et al. (2006) Structural analysis of a rhomboid family intramembrane protease reveals a gating mechanism for substrate entry. Nat Struct Mol Biol 13: 1084–1091.

38. Wang Y, Zhang Y, Ha Y (2006) Crystal structure of a rhomboid family intramembrane protease. Nature 444: 179–180.
39. Markstein M, Pitsouli C, Villalta C, Celniker SE, Perrimon N (2008) Exploiting position effects and the gypsy retrovirus insulator to engineer precisely expressed transgenes. Nat Genet 40: 476–483.
40. Pelham HR (2001) SNAREs and the specificity of membrane fusion. Trends Cell Biol 11: 99–101.
41. Nickel W, Rabouille C (2009) Mechanisms of regulated unconventional protein secretion. Nat Rev Mol Cell Biol 10: 148–155.
42. Voeltz GK, Rolls MM, Rapoport TA (2002) Structural organization of the endoplasmic reticulum. EMBO Rep 3: 944–950.
43. Ivan V, de Voer G, Xanthakis D, Spoorendonk KM, Kondylis V, et al. (2008) Drosophila Sec16 mediates the biogenesis of tER sites upstream of Sar1 through an arginine-rich motif. Mol Biol Cell 19: 4352–4365.
44. Ye B, Zhang Y, Song W, Younger SH, Jan LY, et al. (2007) Growing dendrites and axons differ in their reliance on the secretory pathway. Cell 130: 717–729.
45. Okajima T, Xu A, Lei L, Irvine KD (2005) Chaperone activity of protein O-fucosyltransferase 1 promotes notch receptor folding. Science 307: 1599–1603.
46. Hsiung F, Griffis ER, Pickup A, Powers MA, Moses K (2001) Function of the Drosophila TGF-alpha homolog Spitz is controlled by Star and interacts directly with Star. Mech Dev 107: 13–23.
47. Zhang J, Schulze KL, Hiesinger PR, Suyama K, Wang S, et al. (2007) Thirty-one flavors of Drosophila rab proteins. Genetics 176: 1307–1322.
48. Eggers CT, Schafer JC, Goldenring JR, Taylor SS (2009) D-AKAP2 interacts with Rab4 and Rab11 through its RGS domains and regulates transferrin receptor recycling. J Biol Chem 284: 32869–32880.
49. Kelly EE, Horgan CP, Adams C, Patzer TM, Ni Shuilleabhain DM, et al. (2009) Class I Rab11-family interacting proteins are binding targets for the Rab14 GTPase. Biol Cell.
50. Yang L, Baker NE (2006) Notch activity opposes Ras-induced differentiation during the Second Mitotic Wave of the developing Drosophila eye. BMC Dev Biol 6: 8.
51. Herpers B, Rabouille C (2004) mRNA localization and ER-based protein sorting mechanisms dictate the use of transitional endoplasmic reticulum-golgi units involved in gurken transport in Drosophila oocytes. Mol Biol Cell 15: 5306–5317.
52. Shim SY, Wang J, Asada N, Neumayer G, Tran HC, et al. (2008) Protein 600 is a microtubule/endoplasmic reticulum-associated protein in CNS neurons. J Neurosci 28: 3604–3614.
53. Aridor M, Fish KN (2009) Selective targeting of ER exit sites supports axon development. Traffic 10: 1669–1684.
54. Bokel C, Dass S, Wilsch-Brauninger M, Roth S (2006) Drosophila Cornichon acts as cargo receptor for ER export of the TGFalpha-like growth factor Gurken. Development 133: 459–470.
55. Urban S, Lee JR, Freeman M (2002) A family of Rhomboid intramembrane proteases activates all Drosophila membrane-tethered EGF ligands. EMBO J 21: 4277–4286.
56. van der Sluijs P, Hull M, Webster P, Male P, Goud B, et al. (1992) The small GTP-binding protein rab4 controls an early sorting event on the endocytic pathway. Cell 70: 729–740.
57. Zerial M, McBride H (2001) Rab proteins as membrane organizers. Nat Rev Mol Cell Biol 2: 107–117.
58. Kitt KN, Hernandez-Deviez D, Ballantyne SD, Spiliotis ET, Casanova JE, et al. (2008) Rab14 regulates apical targeting in polarized epithelial cells. Traffic 9: 1218–1231.
59. Junutula JR, De Maziere AM, Peden AA, Ervin KE, Advani RJ, et al. (2004) Rab14 is involved in membrane trafficking between the Golgi complex and endosomes. Mol Biol Cell 15: 2218–2229.
60. Pelissier A, Chauvin JP, Lecuit T (2003) Trafficking through Rab11 endosomes is required for cellularization during Drosophila embryogenesis. Curr Biol 13: 1848–1857.
61. Ready DF, Hanson TE, Benzer S (1976) Development of the Drosophila retina, a neurocrystalline lattice. Dev Biol 53: 217–240.
62. Satoh AK, O'Tousa JE, Ozaki K, Ready DF (2005) Rab11 mediates post-Golgi trafficking of rhodopsin to the photosensitive apical membrane of Drosophila photoreceptors. Development 132: 1487–1497.
63. Sonnichsen B, De Renzis S, Nielsen E, Rietdorf J, Zerial M (2000) Distinct membrane domains on endosomes in the recycling pathway visualized by multicolor imaging of Rab4, Rab5, and Rab11. J Cell Biol 149: 901–914.
64. Mehta SQ, Hiesinger PR, Beronja S, Zhai RG, Schulze KL, et al. (2005) Mutations in Drosophila sec15 reveal a function in neuronal targeting for a subset of exocyst components. Neuron 46: 219–232.
65. Warming S, Costantino N, Court DL, Jenkins NA, Copeland NG (2005) Simple and highly efficient BAC recombineering using galK selection. Nucleic Acids Res 33: e36.
66. Venken KJ, Kasprowicz J, Kuenen S, Yan J, Hassan BA, et al. (2008) Recombineering-mediated tagging of Drosophila genomic constructs for in vivo localization and acute protein inactivation. Nucleic Acids Res 36: e114.
67. Bobinnec Y, Marcaillou C, Morin X, Debec A (2003) Dynamics of the endoplasmic reticulum during early development of Drosophila melanogaster. Cell Motil Cytoskeleton 54: 217–225.

nature cell biology

The Arp2/3 complex and WASp are required for apical trafficking of Delta into microvilli during cell fate specification of sensory organ precursors

Akhila Rajan[1,5,7], An-Chi Tien[2,6,7], Claire M. Haueter[3], Karen L. Schulze[3] and Hugo J. Bellen[1,2,3,4,8]

Cell fate decisions mediated by the Notch signalling pathway require direct cell–cell contact between adjacent cells. In *Drosophila melanogaster*, an external sensory organ (ESO) develops from a single sensory organ precursor (SOP) and its fate specification is governed by differential Notch activation. Here we show that mutations in *actin-related protein-3 (Arp3)* compromise Notch signalling, leading to a fate transformation of the ESO. Our data reveal that during ESO fate specification, most endocytosed vesicles containing the ligand Delta traffic to a prominent apical actin-rich structure (ARS) formed in the SOP daughter cells. Using immunohistochemistry and transmission electron microscopy (TEM) analyses, we show that the ARS contains numerous microvilli on the apical surface of SOP progeny. In *Arp2/3* and *WASp* mutants, the surface area of the ARS is substantially reduced and there are significantly fewer microvilli. More importantly, trafficking of Delta-positive vesicles from the basal area to the apical portion of the ARS is severely compromised. Our data indicate that WASp-dependent Arp2/3 actin polymerization is crucial for apical presentation of Delta, providing a mechanistic link between actin polymerization and Notch signalling.

Notch signalling is an evolutionarily conserved pathway used by metazoans to control cell fate decisions[1,2]. The Notch receptor and its ligands Delta and Serrate (Jagged in vertebrates) are single-pass transmembrane proteins. Cell–cell communication begins when the extracellular domain of the ligand on the signal-sending cell interacts with the extracellular domain of the Notch receptor on the signal-receiving cell. This interaction triggers a series of proteolytic cleavages that releases the intracellular domain of Notch, which enters the nucleus and functions as a transcriptional regulator[3].

Notch signalling mediates key decisions during nervous system development[4], including patterning and fate specification of the ESOs[5]. Each ESO is composed of four cell types (shaft, socket, sheath and neuron) and is derived from a single cell, the SOP (also called the pI cell), which is selected through Notch-mediated lateral inhibition at about 8–12 h after puparium formation (APF; Fig. 1a). The stage when the SOP has not yet undergone cell division is referred to as the 1-cell stage (15–18 h APF). During the 2-cell stage (~18–18.30 h APF) the SOP undergoes asymmetric cell division to generate the anterior pIIb and posterior pIIa (Fig. 1a). Because of the asymmetric distribution of cell fate determinants such as Numb and Neuralized[6,7], Notch signalling is differentially activated in pIIa and pIIb. The pIIa divides to create the external cells of the ESO, the shaft and socket cells. The pIIb divides twice to create the internal cells of the ESO, the neuron and sheath cell[8]. These four differentiated cells are collectively called the sensory cluster.

Delta and Serrate act redundantly to activate Notch during specification of pIIa and pIIb[9]. Recent studies indicate that endocytosis of Delta in the signal-sending cell is crucial for its ability to activate Notch[10]. An alternative, but not mutually exclusive model, is that ligand endocytosis promotes trafficking of the ligand to an endocytic recycling compartment, resulting in its activation[11,12]. In addition, apical trafficking of Delta seems to be important for proper fate specification in the SOP lineage[13]. However, the nature of ligand activation or the requirement for apical trafficking of the ligand remains unclear.

Here, we report that there is an apical actin-enriched structure in the pIIa and pIIb cells that contains numerous microvilli. The surface area of the actin-rich region and the number of microvilli are markedly reduced in *Arp2/3* complex and *WASp* mutants. More importantly, we found that the Arp2/3 complex and WASp have crucial roles in trafficking of endocytosed Delta vesicles to an apical ARS.

RESULTS

Mutations in *Arp3* result in a pIIa-to-pIIb cell fate transformation in *Drosophila* ESO lineages

Notch loss-of-function results in a pIIa-to-pIIb transformation, leading to loss of bristles[14]. Previous genetic screens based on assaying mitotic clones on the adult *Drosophila* thorax for bristle abnormalities[13,15,16] have

[1]Department of Molecular and Human Genetics, [2]Program in Developmental Biology, [3]Howard Hughes Medical Institute, [4]Department of Neuroscience, Baylor College of Medicine, Houston, TX 77030, USA. [5]Current address: Department of Genetics, Harvard Medical School, Boston, MA 021155, USA.[6]Current address: University of California, San Francisco, CA 94143, USA.
[7]These authors contributed equally to the work.
[8]Correspondence should be addressed to H.J.B. (e-mail: hbellen@bcm.tmc.edu)

Received 9 February 2009; accepted 17 March 2009; published online 21 June 2009; DOI: 10.1038/ncb1888

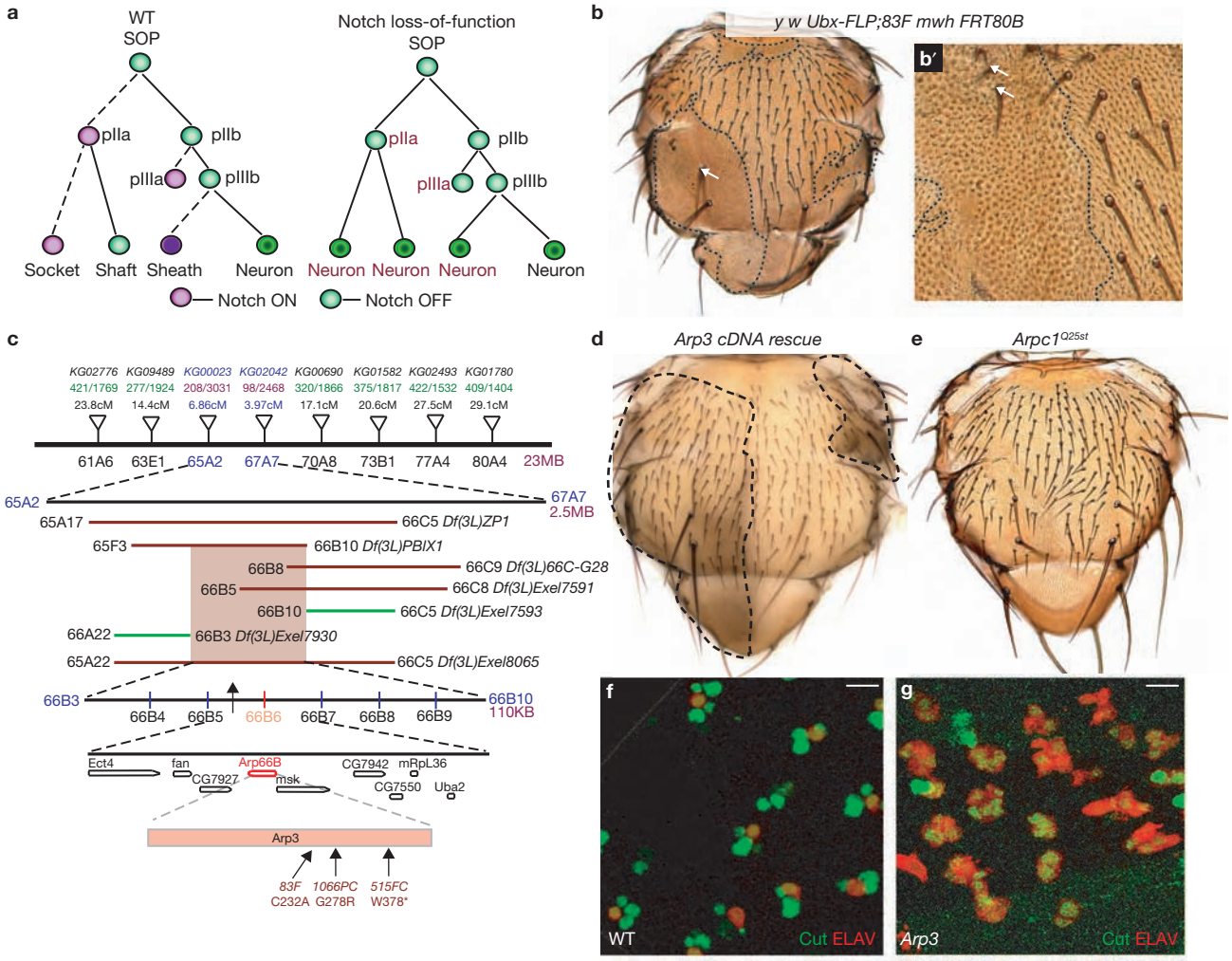

Figure 1 *Arp3* mutations cause a pIIa-to-pIIb transformation in the ESO lineage (**a**) A diagram of the ESO lineage in wild-type (WT) and in *Notch* loss-of-function background. Each cell is represented by a circle; the cells in which Notch is activated are in purple and the signal-sending cells are in green. The dashed lines indicate daughter cells in which Notch is activated. (**b**) Homozygous clones of $Arp3^{83F}$ on an adult thorax induced by *Ubx–FLP*. The clone (dashed lines) is identified by an epithelial cell marker *multiple wing hair (mwh)*, which marks the trichomes (small hair-like structures) on epithelial cells. Mutant clones show loss of external structures, socket and shaft cells, of the microchaetae. Macrochaetae (arrow) sometimes show a double-shaft phenotype in $Arp3^{83F}$ clones. (**b′**) Higher magnification of an $Arp3^{83F}$ clone shows that rarely there are shaft and sockets (arrows) in the mutant clone. Most of the $Arp3^{83F}$ clones show a balding phenotype. (**c**) Schematic representation of the mapping strategy. The inverted triangles represent *P* elements that were used for recombination mapping. Deficiencies represented by lines: those in red failed to complement the alleles, whereas those in green complement our alleles. (**d**) Rescue of the *Arp3* phenotype by overexpression of an *Arp3* cDNA construct in the mutant clones. An image of a pupal notum of an adult thorax which harbours *Arp3* clones; the mutant clones (dashed lines) do not show bristle loss (compare with **b**). (**e**) Flies that harbour clones of $Arpc1^{Q25st}$ show bald patches. The clones were not generated in a *Minute* background and hence appear smaller than *Arp3* clones (compare with **b**). We have not outlined the clones in $Arpc1^{Q25st}$ as they are unmarked clones. (**f**, **g**) A projection of confocal slices show part of the notum at 24–26 h APF stained for ELAV (red) and Cut (green). All cells in the wild-type (**f**) sensory clusters are positive for Cut and one of the cells is ELAV-positive. In *Arp3* (**g**) mutant clones all of the cells in the sensory clusters are positive for Cut and ELAV, indicating the transformation of all SOP progeny to neurons. Scale bar, 10 μm.

identified components in the Notch pathway[14]. We performed a similar F1 mitotic recombination screen on chromosome arm 3L[16] and isolated one complementation group consisting of three homozygous lethal alleles (*83F*, *515FC* and *1066PC*) that cause bristle loss in clones (Fig. 1b, b′). Using a recombination-based mapping strategy[17], the lethality of these alleles was mapped to the 66B cytological region (Fig. 1c). We obtained a *P* element *EP(3)3640* (ref. 18) inserted upstream of the *Arp3* gene that failed to complement our alleles, and identified molecular lesions in *Arp3* for the three alleles (Fig. 1c). Overexpression of the *Arp3* cDNA in *Arp3* mutant clones rescued the lethality and ESO phenotype (Fig. 1d), demonstrating that the observed phenotypes are caused by loss of *Arp3*.

Arp3 is part of the seven-protein Arp2/3 complex, which functions together for polymerization of branched actin filaments[19]. Another component of the Arp2/3 complex, Arpc1, was shown to be involved in ring canal formation during oogenesis in *Drosophila*[18]. As with *Arp3* alleles, $Arpc1^{Q25st}$ clones also cause bristle loss (Fig. 1e)[20]. Bristle loss in *Arp3* clones does not result from a failure to specify SOPs (Supplementary Information, Fig. S1a, a′). To examine whether bristle loss in *Arp3* clones is associated with a *Notch* loss-of-function defect, SOP progeny

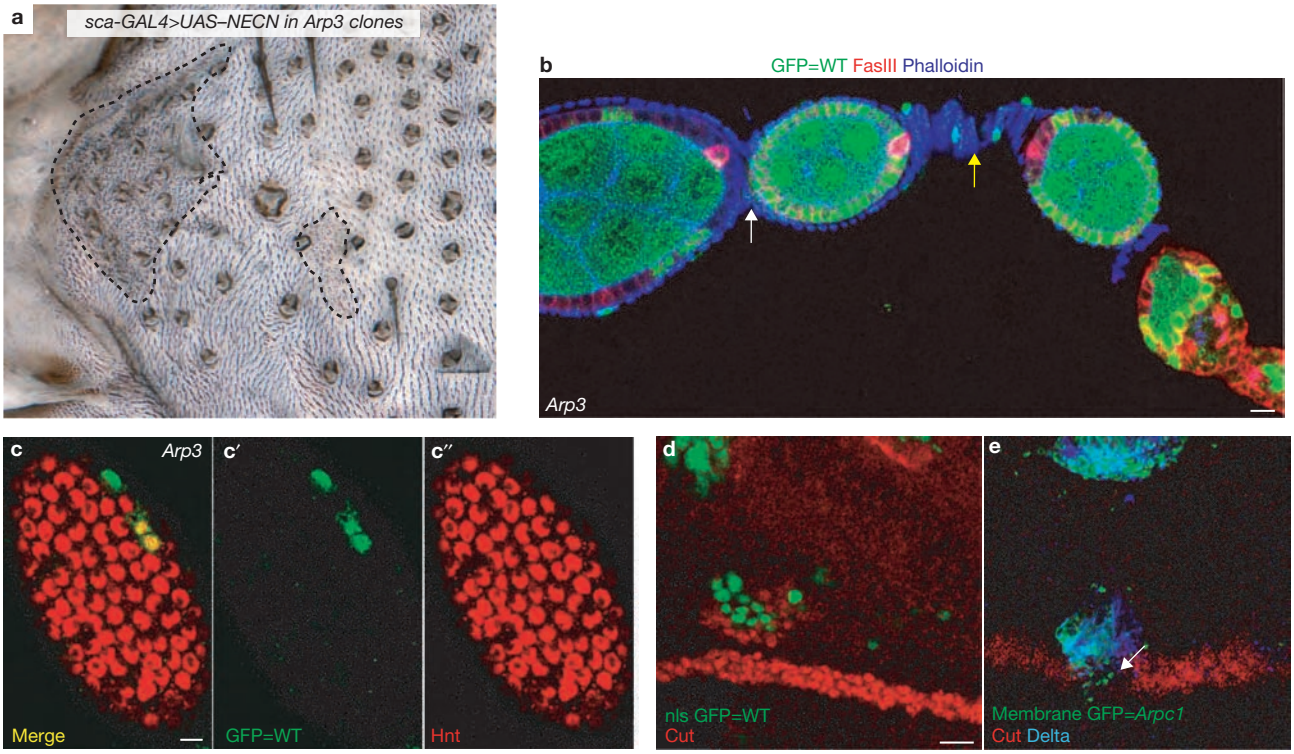

Figure 2 Arp3 is required in the signal sending cells during Notch signalling (**a**) Overexpression of N^{ECN} in wild-type SOPs using the sca^{109-68}-*GAL4* driver results in a multiple socket phenotype in the majority of the sensory clusters. We generated *Arp3* clones (dashed line) using *Ubx–FLP* in this N^{ECN} overexpression background. We did not observe a region of bald cuticle in the *Arp3* clones. (**b**) Clones of $Arp3^{515FC}$ induced by *hs-FLP* in follicle cells are marked by the absence of GFP (green). FasciclinIII (red) marks the follicle cells and is upregulated in polar follicle cells. Phalloidin (blue) marks the membrane of all cells. When polar follicle cells are wild-type (WT), stalk cells (yellow arrow) are formed normally, separating two cysts, whereas, when the polar follicle cells are mutant for *Arp3,* we found a loss of stalk cells between the cysts, resulting in a partial fusion of cysts (white arrow). (**c**–**c**′′) The follicle cells of the cyst harbour mutant clones of *Arp3* induced by *hs-FLP* at stage 7 of oogenesis. *Arp3* mutant clones are marked by the absence of nuclear GFP (green). The cyst was immunostained for Hnt (red), a Notch downstream target gene in the follicle cells. Note that Hnt is still expressed in the *Arp3* mutant follicle cell clones (non-green cells). (**d**) Overexpression of Delta in WT cells (green) near the dorsal-ventral boundary of the wing can induce Cut expression (red) in the adjacent cells near the dorsal-ventral boundary at the dorsal compartment. (**e**) Overexpression of Delta (blue) in *Arpc1* mutant cells (green) cannot induce Cut expression (red) in the adjacent cells near the dorsal-ventral boundary at the dorsal compartment. Note the loss of Cut expression when the clone crosses the dorsal-ventral boundary (arrow). Scale bars, 10 μm (**b**, **d**) and 5 μm (**c**).

at 24 h APF were labelled with differentiation markers. In wild-type sensory clusters, all four cells expressed the homeodomain protein Cut and one expressed the neuronal marker ELAV (Fig. 1f). In contrast, sensory clusters in both *Arp3* and $Arpc1^{Q25st}$ mutant clones contained 4–6 ELAV-positive cells (Fig. 1g and data not shown), suggesting that there is a pIIa-to-pIIb fate transformation.

Although a pIIa-to-pIIb transformation might result from disruption of asymmetric localization of cell fate determinants[6,7], both Neuralized and Numb were asymmetrically localized in *Arp3* mutant SOPs (Supplementary Information, Fig. S1c, e). One of the activators of the Arp2/3 complex, Wiskott-Aldrich syndrome protein (WASp)[21], is also involved in a similar fate specification process in *Drosophila*[22]. Together these observations suggest a specific requirement for WASp-regulated Arp2/3-complex function in Notch signalling.

Arp3 functions in the signal-sending cell during Notch signalling

Is Arp2/3 function required in the signal-sending or the signal-receiving cell during Notch signalling? We first determined the epistatic relationship between *Notch* and *Arp3* with a constitutively active Notch that is independent of ligand activation (N^{ECN})[23]. Expression of N^{ECN} in the ESO lineage causes a *Notch* gain-of-function phenotype, which results in generation of extra socket cells[13]. Overexpression of N^{ECN} in *Arp3* clones, as in wild-type cells, resulted in a *Notch* gain-of-function phenotype, indicating that a ligand-independent form of *Notch* is epistatic to *Arp3* (Fig. 2a). This places the function of Arp3 upstream of Notch activation, possibly in the signal-sending cell.

To gather evidence for a requirement of *Arp3* in the signal-sending cell, we examined its function in oogenesis. Egg chambers are individual units, consisting of germline cells surrounded by somatic follicle cells. The follicle cells can be further divided into three distinct populations: main body follicle cells (phalloidin-positive cells, Fig. 2b), which encapsulate the germline cyst; polar cells, which function as signalling centres (FasIII-positive cells, Fig. 2b); and stalk cells that connect neighbouring cysts (yellow arrow, Fig. 2b). The role of Notch signalling is well-documented in oogenesis[24,25], and signal-sending and receiving cells are spatially well-segregated. *Notch* loss-of-function causes the inability of the follicle cells to encapsulate germline cysts and leads to the formation of giant compound egg chambers[25]. However, *Delta* loss-of-function in follicle cells does not result in an encapsulation defect[25] but rather, loss of stalk cells and partial fusion of the cysts. Delta is required in the anterior polar follicle cells of the posterior egg chamber to specify stalk cells[25,26]. Generating follicle cell clones of *Notch* and *Delta*, therefore, results in

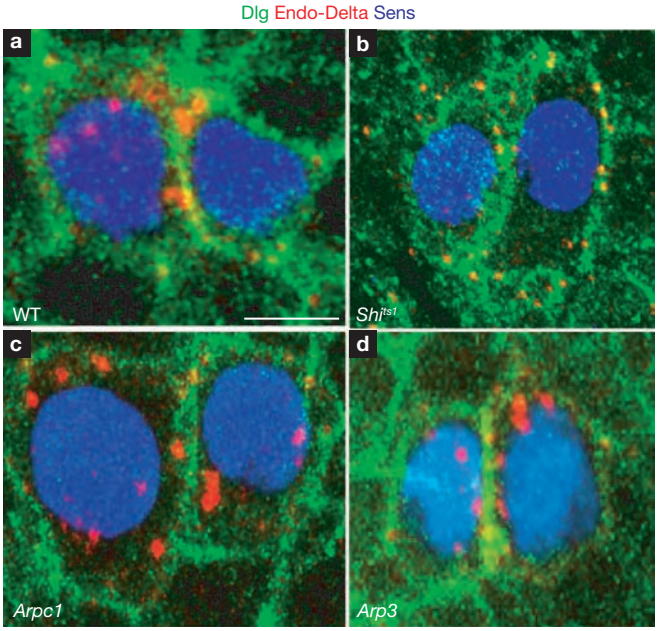

Figure 3 Delta is normally endocytosed in *Arp3* and *Arpc1* mutant pIIa-pIIb. (**a**–**d**) Endocytosis assay for Delta ligand (red) performed at the 2-cell stage in pIIa-pIIb. Sens (blue) labels the nucleus and Dlg (green) marks the sub-apical membrane. A projection of optical slices shows that in the negative control (*shi*^{ts1} (**b**), Delta (red) is found only on the membrane and not in cytoplasmic vesicles between the nucleus and membrane. However, in the wild-type (WT, **a**), *Arpc1* (**c**) and *Arp3* (**d**) pIIa-pIIb, endocytosed Delta vesicles (red) are present in the cytoplasm, indicating that Arp2/3 function is not required for Delta endocytosis. Note small punctae in **b** when Delta is not endocytosed. Scale bar, 5 μm.

distinct phenotypes. We found that loss of *Arp3* phenocopied loss-of-function of *Delta*. Mutant clones of *Arp3* ($n = 14$) in anterior polar follicle cells resulted in loss of stalk cells and partial fusion of adjacent cysts (white arrow, Fig. 2b). At later stages of oogenesis, Delta signals from the germ cells (signal-sending cells) activate Notch in the overlying somatic follicle cells (signal-receiving cells), resulting in expression of a Notch downstream target, Hindsight (Hnt)[27]. Arp3 does not seem to be required in the signal-receiving cell for Notch function, as expression of Hnt was normal in *Arp3* mutant follicle cell clones (Fig. 2c, c′).

To further examine whether Arp2/3 function is required in the signal-sending cell during wing formation, a Delta overexpression assay was performed. During wing development, pre-patterning signals, including Notch, are required to compartmentalize the immature wing imaginal disc at the third-instar larva[28]. Notch signalling is required to activate Cut expression at the dorsal-ventral boundary[29,30]. Previous studies have shown that overexpression of Delta in wild-type clones near the dorsal-ventral boundary results in ectopic Cut expression in the neighbouring cells (Fig. 2d)[11,16,29,30]. However, similar overexpression of Delta in *Arpc1* clones failed to activate Cut expression and resulted in loss of endogenous Cut expression when the clone crossed the dorsal-ventral boundary (Fig. 2e). These data suggest that Arp2/3 complex function is required for the normal function of Delta in the signal-sending cell.

The Arp2/3 complex is not required for Delta endocytosis

Delta must be endocytosed in the signal-sending cell to activate Notch on the receiving cell[6,31]. As Arp2/3 and WASp have been shown to be required for clathrin-mediated endocytosis in yeast[32,33], Arp2/3 might be required for Delta endocytosis during fate specification. However, by performing a Delta endocytosis assay[6] at the 2-cell stage, we found that Delta is endocytosed similarly to wild-type cells (Fig. 3a) in *Arpc1* and *Arp3* mutant tissue (Fig. 3c, d). By contrast, in *shibire* (*Dynamin*) mutant cells kept at the restrictive temperature (Fig. 3b), Delta is not endocytosed[34,35]. This indicates that the Arp2/3 complex is not required for ligand endocytosis during Notch signalling.

A specific ARS forms during fate specification in the ESO lineage

As Arp2/3 is required for polymerization of branched actin filaments[19], we visualized filamentous actin (F-actin) in the ESO lineage with phalloidin. In the wild-type, a prominent apical ARS was present in the pIIa and pIIb (pIIa-pIIb) cells (Fig. 4a, a′′). Co-staining of phalloidin and E-cadherin (*D*E-Cad), which highlights the apical-most stalk region of the pIIb cell that is engulfed by the pIIa cell[36], indicates that the ARS is present in both pIIa-pIIb cells apically (Supplementary Information, Fig. S1f, f′). However, no specialized apical actin enrichment was observed at the earlier 1-cell stage (Supplementary Information, Fig. S1g, g′). In *Arpc1* (yellow arrows, Fig. 4a, a′′), *Arp3* and *WASp* (data not shown) pIIa-pIIb cells, the ARS was formed. However, the apical area of the ARS was markedly reduced in *Arp3* (9.57 ± 5.32 μm^2; mean ± s.e.m, $n = 22$), *Arpc1* (12.25 ± 6.89 μm^2; $n = 19$) and *WASp* (21.86 ± 7.74 μm^2; $n = 19$) pIIa-pIIb cells when compared with the wild-type (43.48 ± 13.79 μm^2; Fig. 4b; $n = 18$). The ARS in wild-type pIIa-pIIb cells formed an umbrella shape along the *xy* axis, whereas in about 50% of the mutant ARS, the stalk of the umbrella was not formed properly (Fig. 4a′′, d).

To test whether the ARS is affected in other mutants, *α-Adaptin*[15] and *numb*[7], which regulate Notch signalling during pIIa-pIIb specification, were examined. In mutant clones of *α-Adaptin* (Fig. 4e) and *numb* (Fig. 4f) the ARS was formed normally, suggesting that the ARS defect is specific to *Arpc1*, *Arp3* and *WASp*. In *neuralized* clones, where both lateral inhibition and fate specification[37] are affected, the ARS was clearly observed in all SOP progeny (Fig. 4 g, g′′). This suggests that most, if not all, SOP progeny at the 2-cell stage are instructed to form an ARS.

To examine whether the Arp2/3 complex colocalizes with the ARS, we overexpressed a GFP-tagged *Arp3* cDNA construct (*UAS–Arp3–GFP)* by *neuralized–GAL4*. We observed that much of the GFP-tagged Arp3 protein colocalized with the ARS (Supplementary Information, Fig. S1h, h′′). The presence of the ARS in the pIIa-pIIb cells during fate specification and the fact that the ARS is morphologically affected in the *Arp3, Arpc1* and *WASp* mutants indicate that it has a role in Notch signal transduction.

Abundant actin-rich microvilli are present at the apical surface of pIIa-pIIb

The ARS was further analysed using TEM to visualize the actin cytoskeleton at the ultracellular level[38]. To distinguish the pIIa-pIIb cell-membrane from that of epithelial cells, HRP was overexpressed in the pIIa-pIIb cells using *neuralized–GAL4* and *UAS–CD2::HRP* (Fig. 5a). On DAB staining, HRP labelling was visualized as a darker cell membrane outline in the SOPs. The serial apical cross-sections (0–2520 nm) of the pIIa-pIIb cells revealed numerous membrane protrusions (Fig. 5b; Supplementary Information, Fig. S2). At high magnification (×10,000), we clearly observed actin bundles within these membranous extensions (Fig. 5c), which was confirmed by immuno-electron microscopy with phalloidin (Fig. 6a, a′). TEM analysis of *Arp3* pIIa-pIIb cells (Fig. 5d–f)

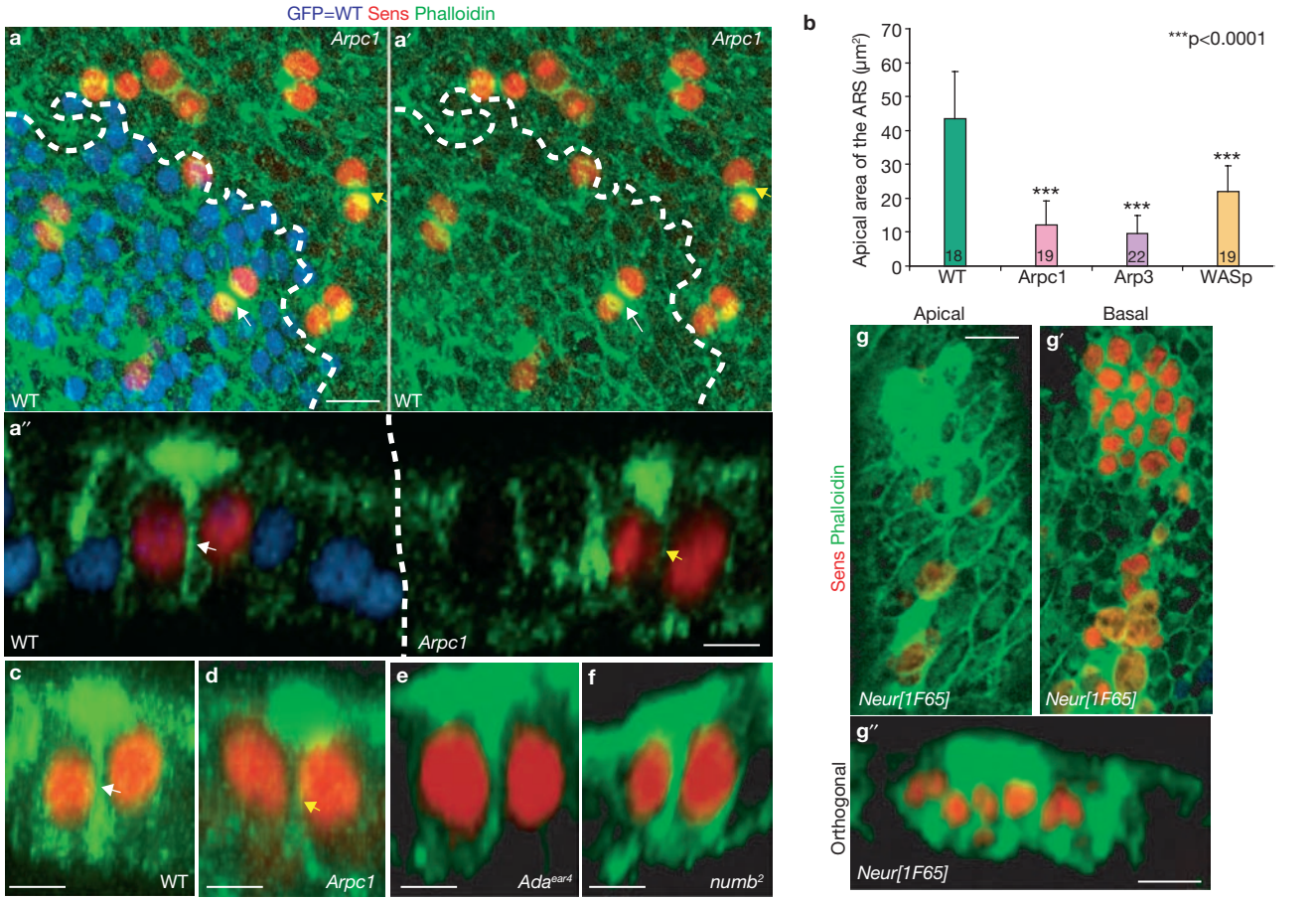

Figure 4 The ARS forms specifically in the pIIa-pIIb progeny and is reduced in *Arp3*, *Arpc1* and *WASp* mutant SOP progeny. (**a**, **a**′) A projection of confocal sections shows that the ARS identified by phalloidin (green) staining is present in both wild-type (WT, white arrow) pIIa-pIIb and *Arpc1* (yellow arrow) mutant pIIa-pIIb cells marked by Sens (red). *Arpc1* homozygous mutant clones (dotted lines) are marked by the absence of nuclear GFP (blue). (**a**′′) An orthogonal confocal section shows that the ARS is quite broad in the WT pIIa-pIIb (white arrow) and has an umbrella-shaped structure, whereas the ARS in the *Arpc1* homozygous clones (yellow arrow) seems compressed and the lateral 'stalk' of the ARS is malformed. (**b**) Quantification of the apical area of the ARS in different genotypes. The ARS area was quantified using the Measure function of ImageJ software. The measurements were analysed using a Student's *t*-test (***P <0.0001). Data are mean ± s.e.m. and the number of SOP progeny pairs used for quantification per genotype is indicated in the bars. (**c**–**g**′′) Pupal nota stained with Sens (red) and phalloidin (green) reveal ARS in pIIa-pIIb. Projections of orthogonal slices show the ARS in WT (**c**, white arrow), *Arpc1* (**d**, yellow arrow), *α-adaptin* (**e**), *numb* (**f**) and *neuralized* (**g**–**g**′′) pIIa-pIIb. An apical section (**g**) reveals apical (0.5 μm) actin enrichment whereas a basal section (**g**′) of the sample (~6 μm) shows the nuclei of the SOP progeny. Scale bars, 10 μm (**a**, **a**′′, **g**, **g**′′) and 5 μm (c–f).

revealed fewer finger-like projections than in wild-type cells (Fig. 5g), consistent with the marked reduction in apical surface area of the ARS in *Arp3*, *Arpc1* and *WASp* mutants (Fig. 4b). Finger-like projections were present on the epithelial cells, but there were fewer and they were markedly shorter (only about 60 nm in length), compared with those of pIIa-pIIb (Supplementary Information, Fig. S3a, c).

The finger-like actin projections on the pIIa-pIIb cells resemble microvilli, which are typically observed to be densely packed in intestinal and kidney epithelial cells[39], and circulating leukocytes[40]. Microvilli on the intestinal and kidney epithelial cells are thought to increase the surface area for absorption, whereas in leukocytes they have been implicated in receptor presentation, which enables leukocyte adhesion[41,42]. To examine whether the finger-like projections are microvilli, the ARS was immunostained with a microvilli marker myosin 1B (Myo1B), which forms lateral tethers between the microvillar membrane and underlying actin filament core[43]. We found that Myo1B is indeed enriched in the apical region of pIIa-pIIb cells (Fig. 6b, b′), specifically at the base of the 'umbrella' region of the ARS (Fig. 6b′′′). This localization of Myo1B was unaffected in *Arp3* mutant pIIa-pIIb cells (Supplementary Information, Fig. S3e, e′). These data indicate that microvilli are present on the apical region of pIIa-pIIb cells.

Delta traffics to the ARS

Intracellular vesicular trafficking of Delta is emerging as a key regulatory step in the activation of Notch[44,45]. We investigated Delta trafficking by co-staining of phalloidin and Delta. In wild-type pIIa-pIIb cells, Delta vesicles colocalized with the apical microvillar region of the ARS (Fig. 7a and transverse section in 7a′). In *Arpc1* (Fig. 7b and transverse section in Fig. 7b′) and *Arp3* (data not shown) pIIa-pIIb, fewer Delta vesicles were colocalized with the ARS. Furthermore, when serial sections were projected to visualize the whole cell (Fig. 7c, c′′), the Delta vesicles were clustered close to the wild-type ARS, whereas the vesicles were widely distributed in the cytoplasm of *Arpc1* pIIa-pIIb cells. The marked reduction of Delta vesicles colocalizing with the ARS in the mutant pIIa-pIIb cells suggests that Arp2/3 has a role in Delta trafficking to the ARS.

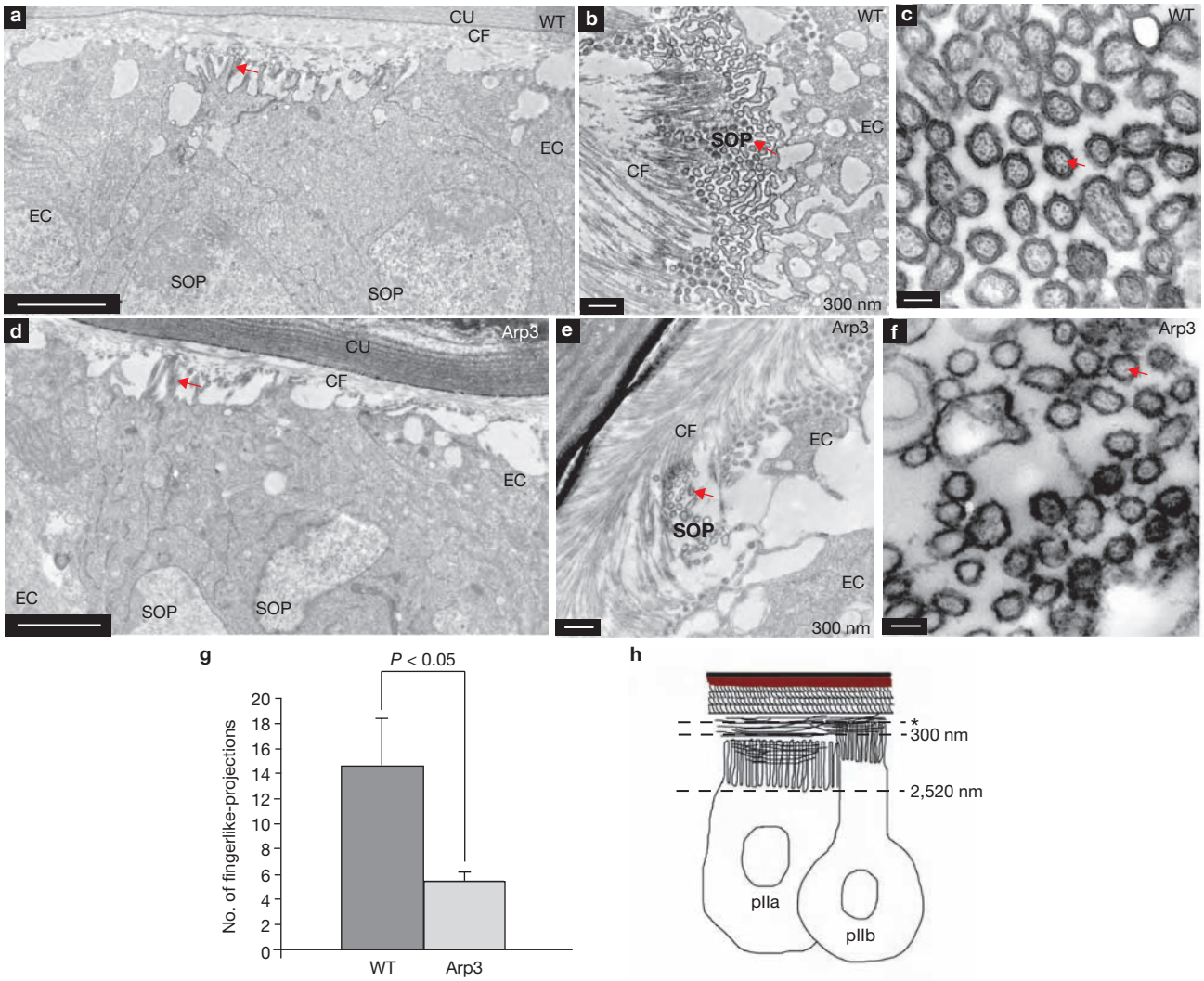

Figure 5 TEM analysis reveals enrichment of actin-filled finger-like projections in pIIa-pIIb cells at 18 h APF. (**a**, **d**) Orthogonal sections of wild-type (WT, **a**) and *Arp3* (**d**) pIIa-pIIb cells show finger-like projections (arrows) at the apical domain of the cells. (**b**–**f**) Cross-section of WT (**b**) and *Arp3* (**e**) pIIa-pIIb cells show finger-like projections (arrows). (**c**, **f**) Higher magnification of the apical surface of WT (**c**) and *Arp3* (**f**) pIIa-pIIb cells shows actin bundles (arrows) inside the finger-like projections. (**g**) Quantification of the number of finger-like projections at the 2-cell stage in WT and *Arp3*. The total number of microvilli in SOP and epithelial cells were quantified using ImageJ. The data are mean ± s.e.m and measurements were analysed using Student's *t*-test. Three SOP progeny pairs were used for this quantification per genotype. (**h**) Schematic representation of pIIa-pIIb in the prepupal thorax epithelium. The asterisk represents the level of the first electron microscopy section at 60 nm. Abbreviations: cuticle (Cu), chitin fibre (CF), epithelial cell (EC), sensory organ precursor cell (SOP). Scale bars, 0.5 μm (**a**, **b**, **d**, **e**) and 0.1 μm (**c**, **f**).

Arp2/3 and WASp are required for trafficking of endocytosed Delta to the apical ARS

To investigate Delta trafficking in *Arp2/3* and *WASp* mutants, we performed pulse-chase labelling experiments[12] to monitor the internalization of Delta in living pupae. Internalization of Delta vesicles with respect to ARS was examined at three different time-points (0, 30 and 60 min). At 0 min Delta vesicles were present apically (~0.5 μm into the sample) and colocalized with ARS in wild-type (Fig. 8a, a′′), *Arp3* (Fig. 8b, b′′), *Arpc1* and *WASp* (data not shown) SOP progeny. At 30 min post-internalization, Delta vesicles were localized basally (~6 μm) in wild-type (Fig. 8c, c′′) and *Arp3* (Fig. 8d, d′′) SOP progeny, indicating that the Delta vesicles had trafficked intracellularly at this time-point. However, 60 min after internalization, localization of Delta vesicles in mutants differed from the wild-type. In the wild-type, about 6–10 Delta-positive vesicles colocalized apically on the ARS (Fig. 8e, e′′), suggesting that endocytosed Delta traffics back to the apical microvilli. In *Arp3* (Fig. 8f, f′′), *Arpc1* (Supplementary Information, Fig. S4a, a′′) and *WASp* (Supplementary Information, Fig. S4b, b′′) mutants, Delta vesicles were not localized apically on the ARS. Instead, they were found basally in the cytoplasm (~6 μm into the cell; Fig. 8f′, f′′; Supplementary Information, Fig. S4a′–b′′), suggesting a defect in Delta trafficking. Indeed, the number of Delta vesicles that traffic to the microvillar region of the ARS at 60 min post-chase was significantly lower in the *Arpc1*, *Arp3* and *WASp* pIIa-pIIb than in wild-type cells (Fig. 8g). However, the total number of internalized Delta vesicles and the intensity of Delta signal in the SOP progeny at 60 min post-chase were very similar in wild-type and mutants (Supplementary Information, Fig. S4c, d). In summary, initially Delta is properly targeted apically at the ARS and endocytosed (Fig. 8a–b′′). Delta traffics basally in both wild-type and mutants (Fig. 8c–d′′) 30

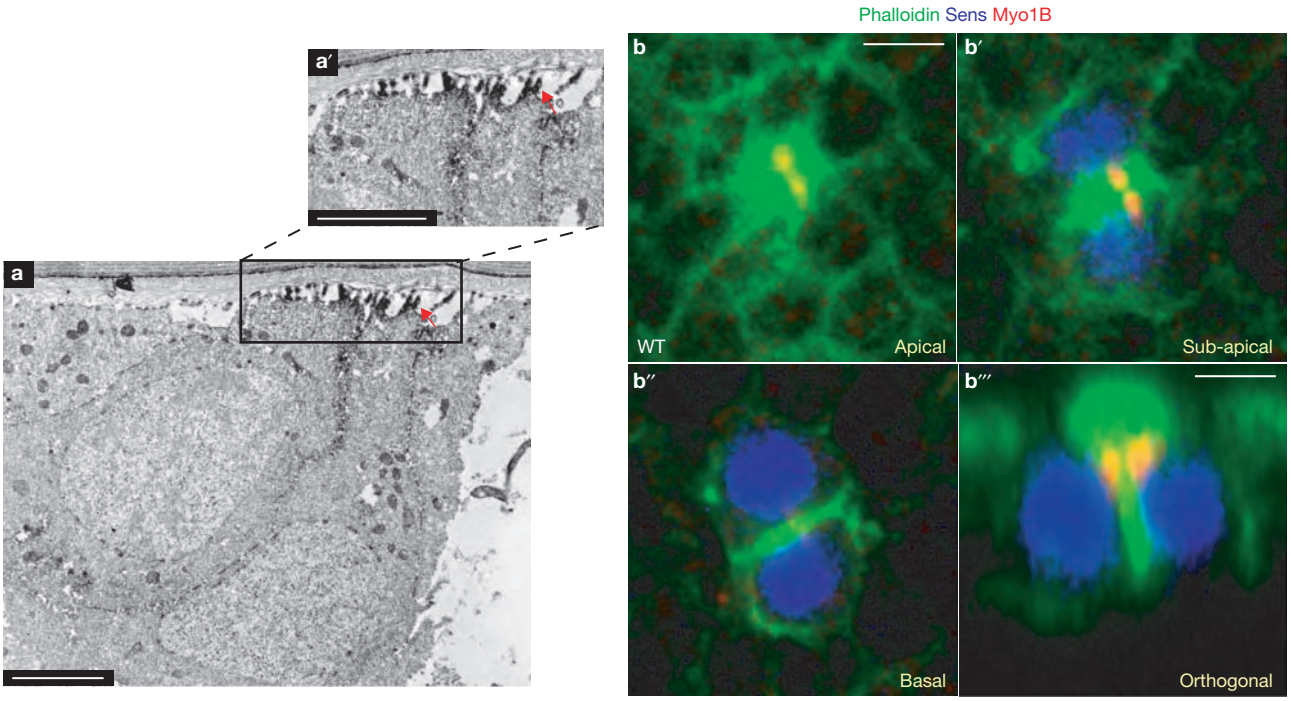

Figure 6 Finger-like projections in pIIa-pIIb cells are enriched with F-actin bundles and are marked by a microvillar marker Myo1B. (**a**, **a**′) Immuno-electron microscopy image of an orthogonal section through the wild-type pIIa-pIIb of a pupal notum shows an enrichment of phalloidin (electron-dense material) in the finger-like projections along the apical region of the ARS. (**a**′) A higher magnification view of the boxed region in **a** is shown in **a**′. The arrow points to the enrichment of phalloidin in the finger-like projections (**b**–**b**‴) Confocal images of single optical (*xy* axis) sections (**b**–**b**″) and orthogonal section (**b**‴) of wild-type (WT) pIIa-pIIb cells immunostained for Myo1B (red), phalloidin (green) and Sens (blue). Scale bars, 0.5 μm (**a**, **a**′) and 5 μm (**b**, **b**‴).

min after internalization. However, endocytosed Delta is not targeted back to the microvillar region in *Arp3*, *Arpc1* and *WASp* SOP progeny 60 min post-chase.

It has been proposed that Delta must be endocytosed and targeted to a specific endosomal compartment to become activated[11], possibly through Rab11-positive recycling endosomes[12,13]. By examining the distribution of the vesicular compartments, we found that the early endosome and the recycling endosome were enriched on the ARS (Supplementary Information, Fig. S4e–h′). Pulse-chase of endocytosed Delta through these compartments (Supplementary Information, Figs S5, S6), showed no significant defects in the localization and abundance of these endosomal compartments or the ability of Delta to traffic through these endosomal compartments in *Arpc1* mutant SOP progeny. The internalized Delta is thought to be proteolytically cleaved in an unknown compartment[11]. We found that Delta processing in *Arp3* mutants is similar to that in the wild-type (Supplementary Information, Fig. S7).

In summary, we surmise that a defect in trafficking of endocytosed Delta to the apical microvillar portion of the ARS leads to a failure in Delta signalling. We conclude that this defect underlies the pIIa-to-pIIb fate transformation phenotype in *Arp3, Arpc1* and *WASp* mutants.

DISCUSSION

Previous reports have suggested that trafficking of a subset of endocytosed Delta to the apical membrane in the pIIb cell is required for its ability to activate Notch in the pIIa cell[12,13]. We have uncovered a highly stereotyped ARS that consists of apical microvilli and a lateral 'stalk' region. In *Arp2/3* and *WASp* pIIa-pIIb cells, the apical surface area of the ARS was significantly reduced and the number of microvilli on the apical region was also reduced. In addition, trafficking of endocytosed Delta to the apical microvilli-rich region of the ARS was severely impaired in *Arp3* mutants. Although numerous studies have focused on the SOP daughter cells, the ARS and the microvilli have not been described previously. These microvillar structures are very different from filopodia[46], which have been reported to have a role in lateral inhibition[47] at an earlier stage. Our data indicate that apical trafficking of Delta to the ARS is required for its ability to signal.

Given the role of Arp2/3 in forming branched actin filaments, one of the primary roles of the Arp2/3 complex and WASp during Notch signalling is probably to form actin networks[48], and to enable and/or to promote the trafficking of Delta vesicles to the ARS (Fig. 8h). This requirement for endocytosed Delta localization to the microvilli during Notch signalling is akin to findings showing that localization of Smoothened to primary cilia is important for its activation during Hedgehog (Hh) signal transduction[49,50]. An interesting study performed in circulating lymphocytes has demonstrated a crucial requirement for microvillar receptor presentation in leukocyte adhesion to the endothelial membrane[41]. In an analogous manner to findings in leukocytes, microvillar presentation of Delta might enhance its ability to contact Notch on the surface of the adjacent cell. As Notch signalling is a major contact-dependent signalling pathway, microvilli might therefore increase the surface area of contact between the signal-sending and receiving cells, enhancing the ability of the ligand to interact with the receptor.

On the basis of the well-characterized role for WASp and Arp2/3 in clathrin-mediated endocytosis[32], it was speculated that Arp2/3 and

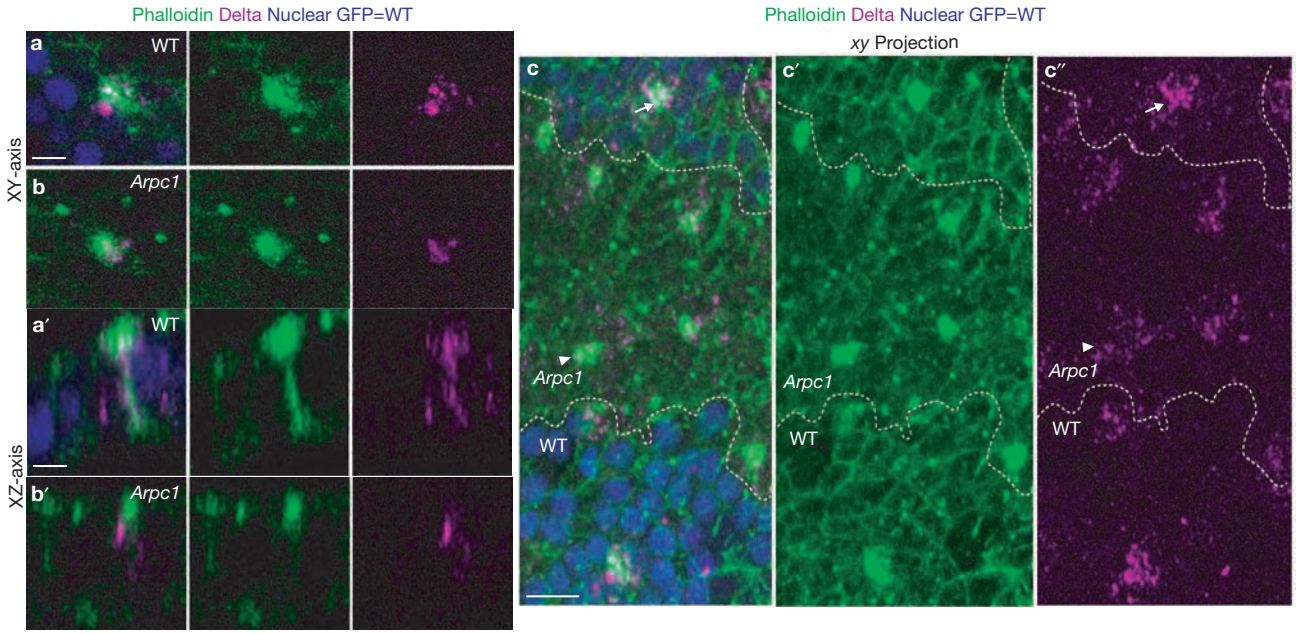

Figure 7 Delta localization to the ARS is reduced in *Arpc1* mutants. (**a**–**c**′′) Pupal wing nota at the 2-cell SOP stage (18.30 h APF) were immunostained with phalloidin (green) and Delta (magenta). *Arpc1* homozygous mutant cells are marked by the absence of GFP (blue). (**a**, **b**) A single section along the *xy* axis through pIIa-pIIb cells shows an enrichment of Delta on the ARS in wild-type (WT, **a**) and this enrichment is much reduced in *Arpc1* (**b**). (**a**′, **b**′) A single section along the *xy* axis of pIIa-pIIb shows that the Delta vesicles colocalize along the lateral stalk of the ARS in WT and in the basal portion of the umbrella region of the ARS (**a**′). In *Arpc1* (**b**′), the lateral stalk of the ARS is malformed and there is a reduction in the number of Delta vesicles that colocalize on the apical portion of the ARS. (**c**–**c**′′) A projection of confocal sections of a pupal notum harbouring an *Arpc1* mutant clone (dashed line). In the WT region, a high density of Delta vesicles are clustered on and around the ARS, whereas in the mutant clones, the Delta vesicles are more widely distributed and do not cluster around the ARS; compare arrowheads (*Arpc1*) with arrows (WT). Scale bars, 5 μm (**a**, **a**′) and 10 μm (**c**).

WASp might be required for endocytosis of Delta and/or Notch during signalling[51]. However, our data indicate that the Arp2/3 complex is not required for Notch in the signal-receiving cell. Our data also indicate that the Arp2/3 complex is not required to endocytose Delta. It is possible that endocytosis of Delta occurs in a clathrin-independent manner[52,53].

The involvement of *WASp* during Notch-mediated fate decisions might have implications for its mammalian homologue in Wiskott-Aldrich syndrome, an X-linked immunodeficiency[54]. Given that Notch signalling is required for proper T-cell development[55] and differentiation of peripheral T-cells[56], defects in Delta trafficking caused by WASp-mediated actin polymerization might underlie the loss and aberrant function of T cells in patients with Wiskott-Aldrich syndrome. Interestingly, microvilli on the surface of lymphocytes might also have a central role in receptor presentation in macrophages and T cells[41,42]. It will be interesting to investigate whether WASp has a role in Notch signalling during T-cell development and activation. □

METHODS

Methods and any associated references are available in the online version of the paper at http://www.nature.com/naturecellbiology/

Note: Supplementary Information is available on the Nature Cell Biology website.

ACKNOWLEDGEMENTS

We are grateful to W. Theurkauf, L. Cooley, E. Schejter, J. Skeath, D. F. Ready, P. Badenhorst, Y. N. Jan, P. Bryant, M. González Gaitán, G. Struhl, E. C. Lai, M. Muskavitch, A. L. Parks, F. B. Gertler, L. M. Lanier, J. Knoblich, F. Schweisguth, R. Dubreuil, W. Sullivan, M. S. Mooseker, G.M. Guild, the Bloomington Stock Center and the Developmental Studies Hybridoma Bank for reagents. We thank G. Emery for advice regarding the Delta endocytosis assay. We would like to thank H. Jafar-Nejad for suggestions and advice during the screen and comments on the manuscript. We thank P. Verstreken and C. V. Ly for their help with the screen, and R. Atkinson for advice on imaging. Confocal microscopy was supported by the BCM Mental Retardation and Developmental Disabilities Research Center. H.J.B. is an investigator of the Howard Hughes Medical Institute.

AUTHOR CONTRIBUTIONS

A.R., A.T. and H.B. conceived the project. A.R. and A.T. carried out the screen, mapped the genes and executed the project. K.S. was involved in the screen and mapping of the genes. C.M.H. in collaboration with A.R. and A.T. designed the TEM experiments and C.M.H. carried out the TEM experiments.

COMPETING INTERESTS

The authors declare that they have no competing financial interest.

Published online at http://www.nature.com/naturecellbiology/Reprints and permissions information is available online at http://npg.nature.com/reprintsandpermissions/

1. Tien, A. C., Rajan, A. & Bellen, H. J. A Notch updated. *J. Cell Biol.* **184 (5),** 621–629 (2009).
2. Bray, S. J. Notch signalling: a simple pathway becomes complex. *Nature Rev. Mol. Cell Biol.* **7,** 678–689 (2006).
3. Schweisguth, F. Regulation of Notch signaling activity. *Curr. Biol.* **14,** R129–138 (2004).
4. Louvi, A. & Artavanis-Tsakonas, S. Notch signalling in vertebrate neural development. *Nature Rev.* **7,** 93–102 (2006).
5. Bray S. Notch signalling in *Drosophila*: three ways to use a pathway. *Sem. Cell Dev. Biol.* **9,** 591–597 (1998).
6. Le Borgne, R. & Schweisguth, F. Unequal segregation of Neuralized biases Notch activation during asymmetric cell division. *Dev. Cell* **5,** 139–148 (2003).
7. Rhyu, M. S., Jan, L. Y. & Jan, Y. N. Asymmetric distribution of numb protein during division of the sensory organ precursor cell confers distinct fates to daughter cells. *Cell* **76,** 477–491 (1994).
8. Gho, M., Bellaiche, Y. & Schweisguth, F. Revisiting the *Drosophila* microchaete lineage: a novel intrinsically asymmetric cell division generates a glial cell. *Development* **126,** 3573–3584 (1999).
9. Zeng, C., Younger-Shepherd, S., Jan, L. Y. & Jan, Y. N. Delta and Serrate are redundant Notch ligands required for asymmetric cell divisions within the *Drosophila* sensory organ lineage. *Genes Dev.* **12,** 1086–1091 (1998).

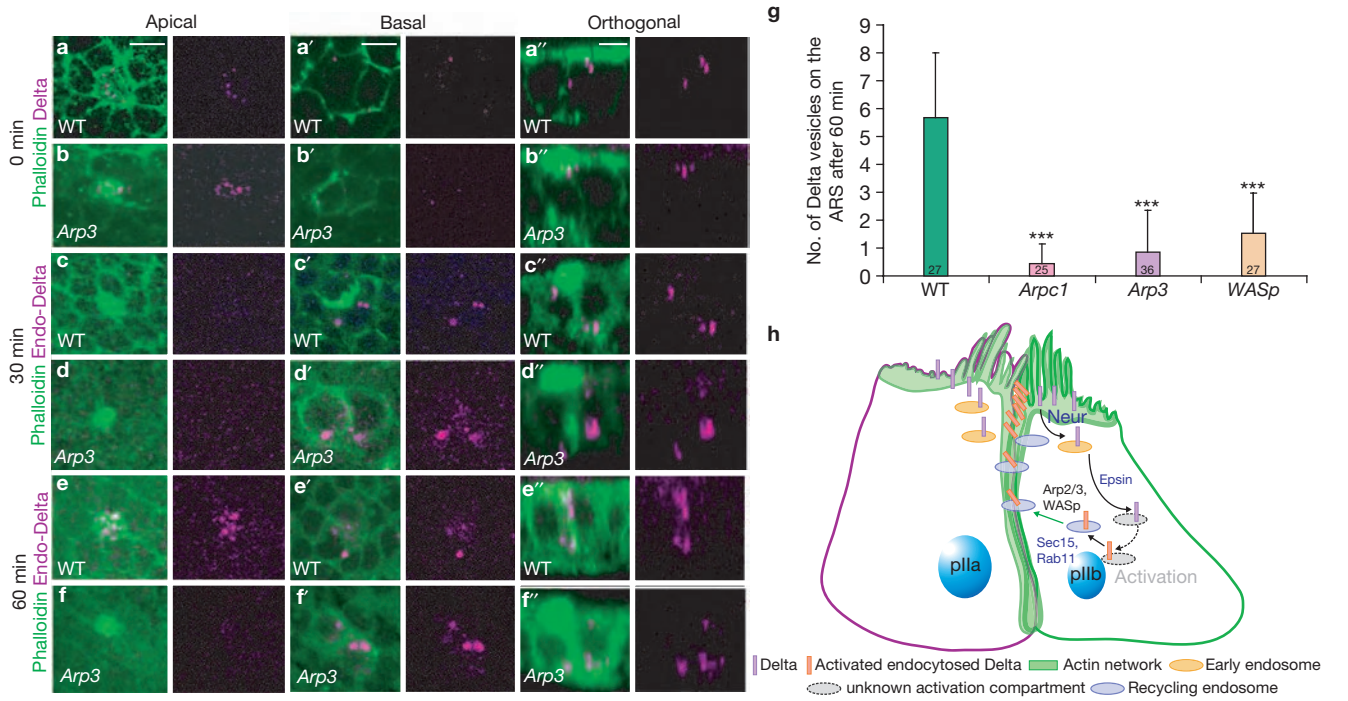

Figure 8 Arp2/3 and WASp are required for trafficking of endocytosed Delta to the apical ARS 1 h post-endocytosis. (**a**–**f**′′) A pulse-chase assay for the trafficking of endocytosed Delta (magenta) at different time-points with respect to the ARS (green) was performed in live pupal nota of wild-type (WT) and *Arp3* mutants. Confocal images show apical (0.5 μm), basal (6 μm) and orthogonal sections of the pIIa-pIIb cells of the WT notum (**a**–**a**′′, **c**–**c**′′, **e**–**e**′′), and *Arp3* mutant clones (**b**–**b**′′, **d**–**d**′′, **f**–**f**′′). The pulse-chase assays for three different time-points, 0 min, 30 min and 60 min, are shown. (**g**) Quantification of the number of internalized Delta vesicles that are present apically and colocalize with the ARS. Measurements of total number of Delta vesicles that traffic to the ARS 1 h after chase were analysed using a Student's *t*-test (***$P < 0.0001$). Data are mean ± s.e.m. and the number of SOP progeny pairs quantified per genotype is indicated in the bars. Note that fewer vesicles that colocalize in mutants when compared with the WT control and the difference is statistically significant. (**h**) Proposed model. In the pIIb cell, Delta is endocytosed by Neuralized (Neur)[6] and trafficked by Epsin[11] to an endocytic compartment where it undergoes activation, probably by a proteolytic cleavage event. It is trafficked back to the membrane in a compartment positive for Rab11 (ref. 12) and the exocyst complex member Sec15 (ref. 13). Arp2/3 and WASp are required for the formation of branched actin networks to form the 'stalk' of the ARS and enables endocytosed vesicles containing activated Delta to traffic back to the dense actin-rich microvilli at the apical membrane of the pIIb cell, where it can signal. Scale bars, 5 μm.

10. Parks, A. L., Klueg, K. M., Stout, J. R. & Muskavitch, M. A. Ligand endocytosis drives receptor dissociation and activation in the Notch pathway. *Development* **127,** 1373–1385 (2000).
11. Wang, W. & Struhl, G. *Drosophila* Epsin mediates a select endocytic pathway that DSL ligands must enter to activate Notch. *Development* **131,** 5367–5380 (2004).
12. Emery, G. *et al.* Asymmetric Rab 11 endosomes regulate delta recycling and specify cell fate in the *Drosophila* nervous system. *Cell* **122,** 763–773 (2005).
13. Jafar-Nejad, H. *et al.* Sec15, a component of the exocyst, promotes notch signaling during the asymmetric division of *Drosophila* sensory organ precursors. *Dev. Cell* **9,** 351–363 (2005).
14. Hartenstein, V. & Posakony, J. W. A dual function of the Notch gene in *Drosophila* sensillum development. *Dev. Biol.* **142,** 13–30 (1990).
15. Berdnik, D., Torok, T., Gonzalez-Gaitan, M. & Knoblich, J. A. The endocytic protein α-Adaptin is required for numb-mediated asymmetric cell division in *Drosophila*. *Dev. Cell* **3,** 221–231 (2002).
16. Tien, A. C. *et al.* Ero1L, a thiol oxidase, is required for Notch signaling through cysteine bridge formation of the Lin12-Notch repeats in *Drosophila melanogaster*. *J. Cell Biol.* **182,** 1113–1125 (2008).
17. Zhai, R. G. *et al.* Mapping *Drosophila* mutations with molecularly defined P element insertions. *Proc. Natl Acad. Sci. USA* **100,** 10860–10865 (2003).
18. Hudson, A. M. & Cooley, L. A subset of dynamic actin rearrangements in *Drosophila* requires the Arp2/3 complex. *J. Cell Biol.* **156,** 677–687 (2002).
19. Machesky, L. M. & Gould, K. L. The Arp2/3 complex: a multifunctional actin organizer. *Curr. Opin. Cell Biol.* **11,** 117–121 (1999).
20. Tal, T., Vaizel-Ohayon, D. & Schejter, E. D. Conserved interactions with cytoskeletal but not signaling elements are an essential aspect of *Drosophila* WASp function. *Dev. Biol.* **243,** 260–271 (2002).
21. Machesky, L. M. & Insall, R. H. Scar1 and the related Wiskott-Aldrich syndrome protein, WASP, regulate the actin cytoskeleton through the Arp2/3 complex. *Curr. Biol.* **8,** 1347–1356 (1998).
22. Ben-Yaacov, S., Le Borgne, R., Abramson, I., Schweisguth, F. & Schejter, E. D. Wasp, the *Drosophila* Wiskott-Aldrich syndrome gene homologue, is required for cell fate decisions mediated by Notch signaling. *J. Cell Biol.* **152,** 1–13 (2001).
23. Struhl, G., Fitzgerald, K. & Greenwald, I. Intrinsic activity of the Lin-12 and Notch intracellular domains *in vivo*. *Cell* **74,** 331–345 (1993).
24. Ruohola, H. *et al.* Role of neurogenic genes in establishment of follicle cell fate and oocyte polarity during oogenesis in *Drosophila*. *Cell* **66,** 433–449 (1991).
25. Lopez-Schier, H. & St Johnston, D. Delta signaling from the germ line controls the proliferation and differentiation of the somatic follicle cells during *Drosophila* oogenesis. *Genes Dev.* **15,** 1393–1405 (2001).
26. Assa-Kunik, E., Torres, I. L., Schejter, E. D., Johnston, D. S. & Shilo, B. Z. *Drosophila* follicle cells are patterned by multiple levels of Notch signaling and antagonism between the Notch and JAK/STAT pathways. *Development* **134,** 1161–1169 (2007).
27. Sun, J. & Deng, W. M. Hindsight mediates the role of notch in suppressing hedgehog signaling and cell proliferation. *Dev. Cell* **12,** 431–442 (2007).
28. de Celis, J. F., Garcia-Bellido, A. & Bray, S. J. Activation and function of Notch at the dorsal-ventral boundary of the wing imaginal disc. *Development* **122,** 359–369 (1996).
29. de Celis, J. F. & Bray, S. Feed-back mechanisms affecting Notch activation at the dorsoventral boundary in the *Drosophila* wing. *Development* **124,** 3241–3251 (1997).
30. Micchelli, C. A., Rulifson, E. J. & Blair, S. S. The function and regulation of cut expression on the wing margin of *Drosophila*: Notch, Wingless and a dominant negative role for Delta and Serrate. *Development* **124,** 1485–1495 (1997).
31. Seugnet, L., Simpson, P. & Haenlin, M. Requirement for dynamin during Notch signaling in *Drosophila* neurogenesis. *Dev. Biol.* **192,** 585–598 (1997).
32. Kaksonen, M., Toret, C. P. & Drubin, D. G. A modular design for the clathrin- and actin-mediated endocytosis machinery. *Cell* **123,** 305–320 (2005).
33. Galletta, B. J., Chuang, D. Y. & Cooper, J. A. Distinct roles for Arp2/3 regulators in actin assembly and endocytosis. *PLoS Biol.* **6,** e1 (2008).
34. Chen, M. S. *et al.* Multiple forms of dynamin are encoded by *shibire*, a *Drosophila* gene involved in endocytosis. *Nature* **351,** 583–586 (1991).
35. van der Bliek, A. M. & Meyerowitz, E. M. Dynamin-like protein encoded by the *Drosophila shibire* gene associated with vesicular traffic. *Nature* **351,** 411–414 (1991).
36. Le Borgne, R., Bellaiche, Y. & Schweisguth, F. *Drosophila* E-cadherin regulates the orientation of asymmetric cell division in the sensory organ lineage. *Curr. Biol.* **12,** 95–104 (2002).
37. Lai, E. C. & Rubin, G. M. neuralized functions cell-autonomously to regulate a subset of notch-dependent processes during adult *Drosophila* development. *Dev. Biol.* **231,** 217–233 (2001).

38. Maupin, P. & Pollard, T. D. Improved preservation and staining of HeLa cell actin filaments, clathrin-coated membranes, and other cytoplasmic structures by tannic acid-glutaraldehyde-saponin fixation. *J. Cell Biol.* **96,** 51–62 (1983).
39. Heintzelman, M. B. & Mooseker, M. S. Assembly of the intestinal brush border cytoskeleton. *Curr. Top. Dev. Biol.* **26,** 93–122 (1992).
40. Majstoravich, S. *et al.* Lymphocyte microvilli are dynamic, actin-dependent structures that do not require Wiskott-Aldrich syndrome protein (WASp) for their morphology. *Blood* **104,** 1396–1403 (2004).
41. von Andrian, U. H., Hasslen, S. R., Nelson, R. D., Erlandsen, S. L. & Butcher, E. C. A central role for microvillous receptor presentation in leukocyte adhesion under flow. *Cell* **82,** 989–999 (1995).
42. Singer, II. *et al.* CCR5, CXCR4, and CD4 are clustered and closely apposed on microvilli of human macrophages and T cells. *J. Virol.* **75,** 3779–3790 (2001).
43. Morgan, N. S., Heintzelman, M. B. & Mooseker, M. S. Characterization of myosin-IA and myosin-IB, two unconventional myosins associated with the *Drosophila* brush border cytoskeleton. *Dev. Biol.* **172,** 51–71 (1995).
44. Le Borgne, R. Regulation of Notch signalling by endocytosis and endosomal sorting. *Curr. Opin. Cell Biol.***18,** 213–222 (2006).
45. Emery, G. & Knoblich, J. A. Endosome dynamics during development. *Curr. Opin. Cell Biol.* **18,** 407–415 (2006).
46. Chhabra, E. S. & Higgs, H. N. The many faces of actin: matching assembly factors with cellular structures. *Nature Cell Biol.* **9,** 1110–1121 (2007).
47. De Joussineau, C. *et al.* Delta-promoted filopodia mediate long-range lateral inhibition in *Drosophila*. *Nature* **426,** 555–559 (2003).
48. Mullins, R. D., Heuser, J. A. & Pollard, T. D. The interaction of Arp2/3 complex with actin: nucleation, high affinity pointed end capping, and formation of branching networks of filaments. *Proc. Natl Acad. Sci. USA* **95,** 6181–6186 (1998).
49. Rohatgi, R., Milenkovic, L. & Scott, M. P. Patched1 regulates hedgehog signaling at the primary cilium. *Science* **317,** 372–376 (2007).
50. Kiprilov, E. N. *et al.* Human embryonic stem cells in culture possess primary cilia with hedgehog signaling machinery. *J. Cell Biol.* **180,** 897–904 (2008).
51. Ilagan, M. X. & Kopan, R. SnapShot: notch signaling pathway. *Cell* **128,** 1246 (2007).
52. Chen, H. & De Camilli, P. The association of epsin with ubiquitinated cargo along the endocytic pathway is negatively regulated by its interaction with clathrin. *Proc. Natl Acad. Sci. USA* **102,** 2766–2771 (2005).
53. Sigismund, S. *et al.* Clathrin-independent endocytosis of ubiquitinated cargos. *Proc. Natl Acad. Sci. USA* **102,** 2760–2765 (2005).
54. Imai, K., Nonoyama, S. & Ochs, H. D. WASP (Wiskott-Aldrich syndrome protein) gene mutations and phenotype. *Curr. Opin. Allergy Clin. Immunol.* **3,** 427–436 (2003).
55. Tanigaki, K. & Honjo, T. Regulation of lymphocyte development by Notch signaling. *Nature Immunol.* **8,** 451–456 (2007).
56. Osborne, B. A. & Minter, L. M. Notch signalling during peripheral T-cell activation and differentiation. *Nature Rev. Immunol.* **7,** 64–75 (2007).

METHODS

***Drosophila* genetics.** Stocks used in this study were: 1) y w; FRT80B (isogenized), 2) y w Ubx–FLP; RpS17[4] Ubi–GFP.nls FRT80B/TM3 Ser, 3) y w hs-FLP; UAS–N[ECN(NEXT)]/CyO; MKRS/TM2 (ref. 57), 4) y w; UAS-Arp3::GFP[58], 5) w; Wsp[3]/TM6B Tb[59], 6) Df(3R)3450/TM6B Tb, 7) y w; Arpc1[Q25St] FRT40A /CyO Kr-GAL4, UAS–GFP[60], 8) y w Ubx–FLP; Ubi–GFP.nls FRT40A/CyO, 9) y w hs-FLP; RpS17[4] Ubi–GFP FRT80B/ TM6B Tb, 10) y hs-FLP tubα1–GAL4 UAS–GFP.nls-6×Myc; tub–GAL80 RpS17[4] FRT80B/TM6B Tb, 11) w*; UAS–CD2::HRP/CyO (Bloomington Stock Center)[61], 12) w[1118]; neur[A101]–GAL4 Kg[V]/TM3 Sb[1] (Bloomington Stock Center)[62], 13) y w; numb[2] ck FRT40A/CyO[63], 14) y w ey-FLP; Ada[ear4] FRT40A/CyO y[+] (ref. 64), 15) w; FRT82B neur[1F65]/TMB6B Tb[65] 16) y w; sca[109–68]-GAL4 (ref. 66).

Rescue experiments were performed using the MARCM technique. Flies of genotype *y hs-FLP tubα1–GAL4 UAS–GFP.nls-6×Myc; UAS–Arp3::GFP/+; tub–GAL80 RpS17[4] FRT80B/ Arp3[515FC] FRT80B* were examined. The homozygous mutant bristles with longer and thicker appearance were differentiated from the short and thin *RpS17[4] (Minute* phenotype) bristles.

Epistasis analysis of *Arp3* with the ligand-independent form of Notch[57], N^{ECN} was performed by examining flies of the genotype *y w Ubx–FLP; sca[109–68]-GAL4/ UAS-N[ECN]; y[+] w[+] FRT80B/mwh Arp3[83F] FRT80B. Arp3* follicle cell clones in egg chambers were generated by heat-shocking virgin females of genotype *y w hs-FLP/+; FRT80B Arp3[515FC]/ RpS17[4] Ubi–GFP FRT80B* for 90 min at 38 °C for 3 consecutive days. Ovaries of heat-shocked females were dissected after 2–3 days of mating on medium supplemented with yeast.

The wing-disc signal-sending cell assay was performed as described previously[67,68] and flies of the genotype *y w hs-FLP UAS–GFP.CD8; tub–GAL80 FRT40A/ Arpc1 FRT40A; tub–GAL4/ UAS-Dl* were examined.

Immunohistochemistry. For conventional immunostaining, ovaries, wing discs from third instar larvae or pupal nota were dissected in PBS and fixed with 4% formaldehyde for 20 min. The samples were then permeabilized in PBS + 0.2% Triton X-100 (PBST) for 20 min and blocked with 5% normal donkey serum in PBST for 1 h. Samples were incubated with primary antibodies at 4 °C overnight. The following primary antibodies were used: chicken anti-GFP (1:2,000, Abcam), mouse anti-Cut (1:500; 2B10; Developmental Studies Hybridoma Bank, University of Iowa (DSHB))[69], rat anti-ELAV (1:200; 7E8A10; DSHB)[70], guinea pig anti-Sens (1:1,000; ref 71), mouse anti-Dl[ECD] (1:1,000; C594.9B; DSHB)[72], guinea pig anti-Delta (1:3,000; M. Muskavitch and A. L. Parks)[73], mouse anti-Fasciclin III (1:10; 7G10; DSHB)[74], mouse anti-Hnt (1:10; 1G9; DSHB)[75], Alexa Fluor 488- and 546-conjugated phalloidin (1 unit per reaction, Invitrogen), rabbit anti-Dlg (1:1,000; P. Bryant)[76], rat anti-Myo1B (1:500; M.S. Mooseker)[77]. The following antibodies were used in the experiments included in the Supplementary Information: rabbit anti-Numb (1:1,000; Y. N. Jan)[78], rabbit anti-Neuralized (1:600; E. C. Lai)[65], rat anti-*D*E-Cadherin (1:1,000, DCAD2, DSHB)[79], rabbit anti-Rab5 (1:200; M. González Gaitán)[80], rabbit anti-Rab11 (1:1,000, D. F. Ready)[81], guinea pig anti-Spinster/Benchwarmer (1:100; G. W. Davis)[82], guinea pig anti-Hrs-FL (1:600; ref. 83).The samples were then incubated with Cy3- and/or Cy5-conjugated affinity purified donkey secondary antibodies (1:500; Jackson ImmunoResearch Laboratories). Images were captured using an LSM510 confocal microscope and Leica TCS SP5 confocal microscope. Images were processed with Amira 5.0.1 and Adobe PhotoShop 7.0.

Transmission electron microscopy (TEM). To identify the pIIa-pIIb cells, we used flies of the following genotype: *UAS–CD2::HRP; neur[A101]-GAL4* (ref. 61). In this genotype the HRP-labelled cell membranes correspond to pIIa-pIIb at the 16–18 h APF time-point, as *neur[A101]-GAL4* drives expression of the CD2::HRP in the SOP and its progeny. To identify the SOP progeny in *Arp3* mutant clones for TEM analysis, we examined the flies with the genotype *y w Ubx–FLP;UAS–-CD2::HRP; Arp3[515FC] FRT80B neur[A101]-GAL4/ arm-lacZ M(3) tub–GAL80 FRT80B* in which the CD2::HRP is activated only in *Arp3* mutant SOP progeny.

HRP label was visualized by TEM as described previously[84] except for the following modifications: the pupal thorax was dissected at 18 h APF. After amplification and visualization of the HRP signal under a dissecting microscope, the tissues were fixed[85] to preserve the actin filament structures. The tissues were then processed for TEM using microwave irradiation with PELCO BioWave equipped with PELCO Cold Spot and Vacuum System. Serial sections (60 nm) were cut and post-stained with Reynold's lead citrate, and examined with a JEOL transmission electron microscope (JEOL 1010). The serial sections were labelled on the basis of their depth from the first electron micrograph that shows the most apical portion of HRP labelled SOP microvilli.

Immunoelectron microscopy of phalloidin. To label actin, the pupal thorax was dissected at 18 h APF, fixed in 1% glutaraldehyde in 0.1M PB pH 7.2 for 1.5 h, permeabilized in 0.1% Triton PBS for 5 min, labelled with biotin-XX phalloidin (3 units; Invitrogen) in PBS for 30–35 min. Samples were then incubated in streptavidin-HRP in TNT buffer (1:100; Sigma). To develop enzyme activity, we used a procedure described previously[84].

Delta endocytosis and pulse-chase assay. The endocytosis and pulse-chase assays were modified from previous reports[86,87]. Pupae were partially dissected in Schneider's medium at 18 h APF by making an incision along the dorsal side, and the internal tissues were washed out. The 'empty' pupal case was incubated with the supernatant of monoclonal antibody mouse anti-Delta[ECD] (1:10; C594.9B; DSHB)[72] for 15–20 min on ice in Schneider's medium supplemented with 25 μg ml^{-1} of 20-hydroxy-ecdysone (Sigma). The tissue was washed three times by medium changes. For the Delta pulse-chase assay the pupal cases were incubated at 25 °C for different time periods (0, 30 and 60 min) in Schneider's medium supplemented with 5 μg ml^{-1} of 20-hydroxy-ecdysone. For the endocytosis assay, the pupal cases were incubated in pre-warmed Schneider's medium supplemented with 5 μg ml^{-1} of 20-hydroxy-ecdysone at 34 °C in a water bath to inactivate the *shibire* gene in the negative control *shi[ts1]*. After incubation at 25 °C (pulse-chase assay) or 34 °C (endocytosis assay), the pupal cases were fixed for 20 min with 4% formaldehyde in Schneider's medium supplemented with 5 μg ml^{-1} of 20-hydroxy-ecdysone. The normal immunostaining protocol was then followed.

The following antibodies were used in the experiments in the pulse-chase co-labelling experiments in the Supplementary Information: rabbit anti-Rab5 (1:200; M. González Gaitán)[80], rabbit anti-Rab11 (1:1,000, D. F. Ready)[81], guinea pig anti-Spinster/Benchwarmer (1:100; G. W. Davis)[82], guinea pig anti-Hrs-FL (1:600; ref. 83).

Statistical analysis. Measurements of total number of Delta vesicles that traffic to the ARS 1 h after chase, and measurements of the total number of Delta vesicles endocytosed were analysed using a Student's *t*-test (***P <0.0001. Measurements of the ARS area were quantified using the Measure function of the ImageJ software. The measurements were analysed using a Student's *t*-test (***P <0.0001). For TEM, measurements of total number of microvilli in SOP and epithelial cells were quantified using ImageJ. The measurements were analysed using a Student's *t*-test (P <0.05).

The measurement of Delta colocalization with Rab5 and Rab11 as well as the determination of Delta, Rab11 and Rab5 signal intensities were quantified using the labelvoxel and materialstatistics functions in Amira 5.0.1. The measurements were analysed using a Student's *t*-test (*P =0.01).

Western blotting. For the Delta western blots, 50 embryos of the appropriate genotypes were collected at 0–13 h AEL and 13–19 hAEL and lysed in ice-cold filtered RIPA buffer (150 mM NaCl, 1.0% NP-40, 0.5% deoxycholic acid, 0.1% SDS, and 50 mM Tris, pH 8.0) with complete protease inhibitor cocktail (Roche). Lysates were suspended in equal volume of 3× Laemmli sample buffer in the absence of reducing agents, and proteins were resolved by SDS–PAGE. Delta was detected on a western blot using anti-Delta (mAb C594.9B) ascites fluid at 1:10,000. HRP-conjugated goat anti-mouse IgG (Jackson ImmunoResearch) was used at 1:10,000 and the blots were developed using Western Lightning chemiluminescent substrate (PerkinElmer LAS).

57. Struhl, G. & Greenwald, I. Presenilin-mediated transmembrane cleavage is required for Notch signal transduction in *Drosophila*. *Proc. Natl Acad. Sci.USA* **98,** 229–234 (2001).
58. Hudson, A. M. & Cooley, L. A subset of dynamic actin rearrangements in *Drosophila* requires the Arp2/3 complex. *J. Cell Biol.* **156,** 677–687 (2002).
59. Ben-Yaacov, S., Le Borgne, R., Abramson, I., Schweisguth, F. & Schejter, E. D. Wasp, the *Drosophila* Wiskott-Aldrich syndrome gene homologue, is required for cell fate decisions mediated by Notch signaling. *J. Cell Biol.* **152,** 1–13 (2001).
60. Zallen, J. A. *et al.* SCAR is a primary regulator of Arp2/3-dependent morphological events in *Drosophila*. *J. Cell Biol.* **156,** 689–701 (2002).
61. Watts, R. J., Schuldiner, O., Perrino, J., Larsen, C. & Luo, L. Glia engulf degenerating axons during developmental axon pruning. *Curr. Biol.* **14,** 678–684 (2004).

DOI: 10.1038/ncb1888

62. Lai, E. C. & Rubin, G. M. neuralized functions cell-autonomously to regulate a subset of notch-dependent processes during adult *Drosophila* development. *Dev. Biol.* **231,** 217–233 (2001).
63. Frise, E., Knoblich, J. A., Younger-Shepherd, S., Jan, L. Y. & Jan, Y. N. The *Drosophila* Numb protein inhibits signaling of the Notch receptor during cell–cell interaction in sensory organ lineage. *Proc. Natl Acad. Sci. USA* **93,** 11925–11932 (1996).
64. Berdnik, D., Torok, T., Gonzalez-Gaitan, M. & Knoblich, J. A. The endocytic protein α-Adaptin is required for numb-mediated asymmetric cell division in *Drosophila*. *Dev. Cell* **3,** 221–231 (2002).
65. Lai, E. C., Deblandre, G. A., Kintner, C. & Rubin, G. M. *Drosophila* neuralized is a ubiquitin ligase that promotes the internalization and degradation of Delta. *Dev. Cell* **1,** 783–794 (2001).
66. Manning, L. & Doe, C. Q. Prospero distinguishes sibling cell fate without asymmetric localization in the *Drosophila* adult external sense organ lineage. *Development* **126,** 2063–2071 (1999).
67. Wang, W. & Struhl, G. *Drosophila* Epsin mediates a select endocytic pathway that DSL ligands must enter to activate Notch. *Development* **131,** 5367–5380 (2004).
68. Tien, A. C. *et al.* Ero1L, a thiol oxidase, is required for Notch signaling through cysteine bridge formation of the Lin12-Notch repeats in *Drosophila melanogaster*. *J. Cell Biol.* **182,** 1113–1125 (2008).
69. Blochlinger, K., Bodmer, R., Jan, L. Y. & Jan, Y. N. Patterns of expression of cut, a protein required for external sensory organ development in wild-type and cut mutant *Drosophila* embryos. *Genes Dev.* **4,** 1322–1331 (1990).
70. Robinow, S. & White, K. Characterization and spatial distribution of the ELAV protein during *Drosophila melanogaster* development. *J. Neurobiol.* **22,** 443–461 (1991).
71. Nolo, R., Abbott, L. A. & Bellen, H. J. Senseless, a Zn finger transcription factor, is necessary and sufficient for sensory organ development in *Drosophila*. *Cell* **102,** 349–362 (2000).
72. Fehon, R. G. *et al.* Molecular interactions between the protein products of the neurogenic loci Notch and Delta, two EGF-homologous genes in *Drosophila*. *Cell* **61,** 523–534 (1990).
73. Parks, A. L., Klueg, K. M., Stout, J. R. & Muskavitch, M. A. Ligand endocytosis drives receptor dissociation and activation in the Notch pathway. *Development* **127,** 1373–1385 (2000).
74. Patel, N. H., Snow, P. M. & Goodman, C. S. Characterization and cloning of fasciclin III: a glycoprotein expressed on a subset of neurons and axon pathways in *Drosophila*. *Cell* **48,** 975–988 (1987).
75. Yip, M. L., Lamka, M. L. & Lipshitz, H. D. Control of germ-band retraction in *Drosophila* by the zinc-finger protein HINDSIGHT. *Development* **124,** 2129–2141 (1997).
76. Woods, D. F. & Bryant, P. J. The discs-large tumor suppressor gene of *Drosophila* encodes a guanylate kinase homolog localized at septate junctions. *Cell* **66,** 451–464 (1991).
77. Morgan, N. S., Heintzelman, M. B. & Mooseker, M. S. Characterization of myosin-IA and myosin-IB, two unconventional myosins associated with the *Drosophila* brush border cytoskeleton. *Dev. Biol.* **172,** 51–71 (1995).
78. Rhyu, M. S., Jan, L. Y. & Jan, Y. N. Asymmetric distribution of numb protein during division of the sensory organ precursor cell confers distinct fates to daughter cells. *Cell* **76,** 477–491 (1994).
79. Oda, H., Uemura, T., Harada, Y., Iwai, Y. & Takeichi, M. A *Drosophila* homolog of cadherin associated with armadillo and essential for embryonic cell–cell adhesion. *Dev. Biol.* **165,** 716–726 (1994).
80. Wucherpfennig, T., Wilsch-Brauninger, M. & Gonzalez-Gaitan, M. Role of *Drosophila* Rab5 during endosomal trafficking at the synapse and evoked neurotransmitter release. *J. Cell Biol.* **161,** 609–624 (2003).
81. Dollar, G., Struckhoff, E., Michaud, J. & Cohen, R. S. Rab11 polarization of the *Drosophila* oocyte: a novel link between membrane trafficking, microtubule organization, and oskar mRNA localization and translation. *Development* **129,** 517–526 (2002).
82. Sweeney, S. T. & Davis, G. W. Unrestricted synaptic growth in spinster-a late endosomal protein implicated in TGF-β-mediated synaptic growth regulation. *Neuron* **36,** 403–416 (2002).
83. Lloyd, T. E. *et al.* Hrs regulates endosome membrane invagination and tyrosine kinase receptor signaling in *Drosophila*. *Cell* **108,** 261–269 (2002).
84. Larsen, C. W., Hirst, E., Alexandre, C. & Vincent, J. P. Segment boundary formation in *Drosophila* embryos. *Development* **130,** 5625–5635 (2003).
85. Maupin, P. & Pollard, T. D. Improved preservation and staining of HeLa cell actin filaments, clathrin-coated membranes, and other cytoplasmic structures by tannic acid-glutaraldehyde-saponin fixation. *J. Cell Biol.* **96,** 51–62 (1983).
86. Le Borgne, R. & Schweisguth, F. Unequal segregation of Neuralized biases Notch activation during asymmetric cell division. *Dev. Cell* **5,** 139–148 (2003).
87. Emery, G. *et al.* Asymmetric Rab 11 endosomes regulate Delta recycling and specify cell fate in the *Drosophila* nervous system. *Cell* **122,** 763–773 (2005).

nature cell biology

DOI: 10.1038/ncb1888

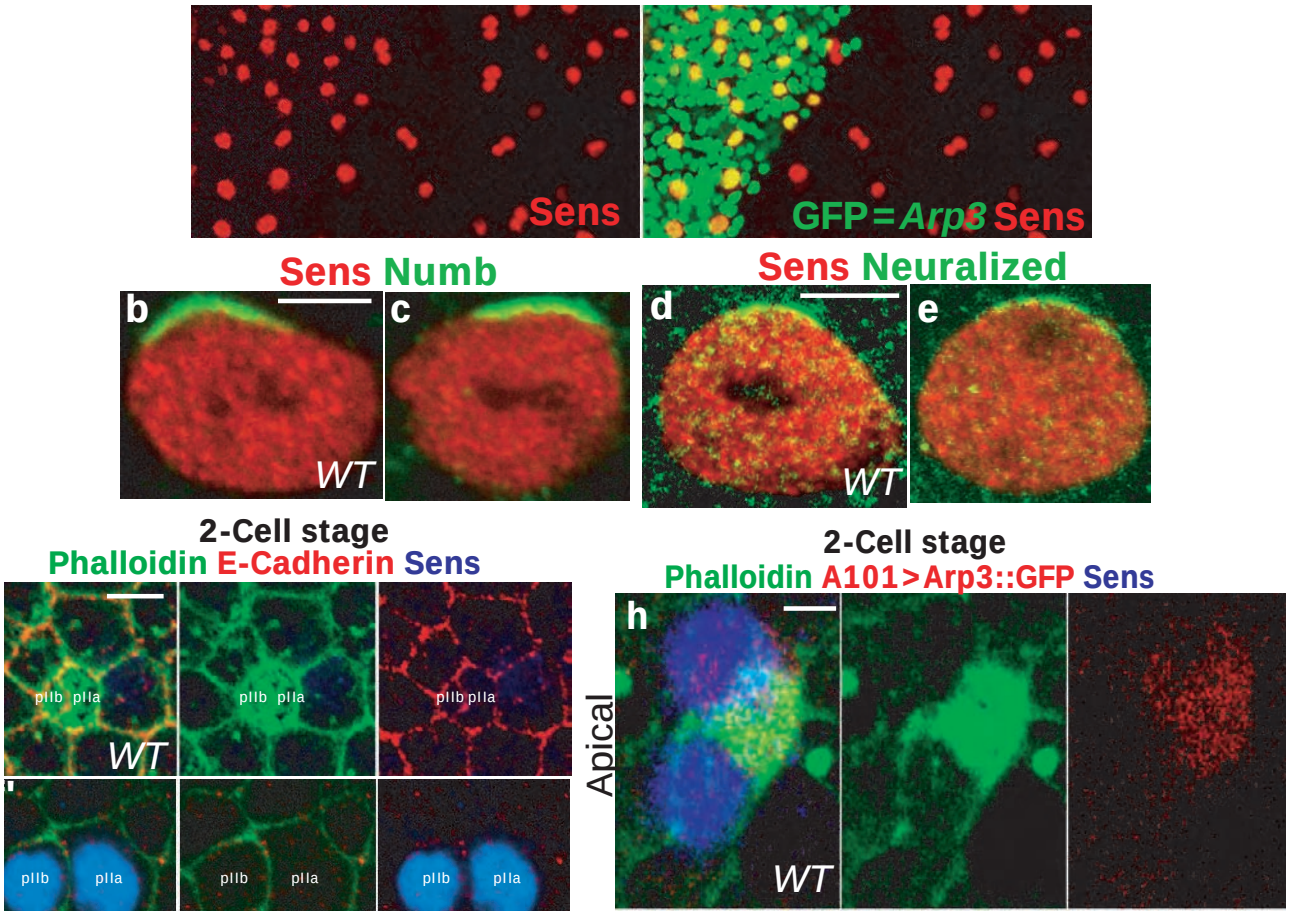

Figure S1 (**a** -**a'**) The SOPs are correctly specified in *Arp3*: (**a**) A projection of confocal sections along the XY-axis of a pupal notum at 17:30hr APF harboring *Arp3* clones marked by the presence of nuclear GFP (green) and immunostained for Sens (red) which marks the SOP and its progeny pIIa-pIIb. Note that SOPs are correctly specified in the mutant clones (green). (**b** -**e**) The segregation of asymmetric fate determinants is normal in *Arp3* mutant SOP: (**b** -**e**) Images showing a single confocal section along the XY-axis of a dividing SOP at 17:30hr APF of a *WT* or an *Arp3* pupal notum stained for asymmetric cell fate determinants (green) and Sens (red). Anterior side of the dividing SOP is oriented upwards in all these images. (**b**, **c**) Numb (green) segregates into the anterior side of the dividing SOP in both *WT* (**b**) and *Arp3* mutant clones (**c**), so that it is inherited into the anterior pIIb daughter. (**d**, **e**) Neuralized (green) segregates into the anterior side of the dividing SOP in both *WT* (d) and *Arp3* mutant clones (**e**), so that it is inherited into the anterior pIIb daughter. (**f** -**g'**) The ARS is formed only in the 2-cell stage: (**f**, **f'**) A confocal image of a single optical section along the XY-axis shows that the ARS forms above the pIIa-pIIb at the 2-cell stage. (**f**) *WT* pupal notum immunostained with phalloidin (green) reveals an apical (0.5 μm) actin enrichment, and this F-actin structure co-localizes with the apical stalk of the pIIa-pIIb cells marked by E-Cad (red). (**f'**) A basal section (~6 μm) of the sample shows the nuclei of the pIIa-pIIb cells marked with Sens (blue). (g, g') A confocal section along the XY-axis, showing immunostaining of *WT* pupal notum at the 1-cell stage with Sens (blue), phalloidin (green) and E-Cad (red). (**g**) The apical section (0.5 μm) reveals that the ARS has not yet formed at 1-cell stage. (**g'**) A basal section (6 μm) shows that the SOP, marked by Sens (blue) has not yet divided. F-actin (phalloidin–green) marks the cell membrane of the epithelial cells and SOP. (**h** -**h"**) Arp3 co-localizes with the ARS: (**h** -**h"**) Confocal images of a single optical section along the XY-axis (**h** -**h'**) and XZ-axis (**h"**) of pupal notum in which *UAS-Arp3-GFP* is expressed under the control of a *neuralized-GAL4* driver *A101-GAL4>Arp3::GFP* (red), immunostained with Sens (blue) and phalloidin (green) at the 2-cell stage. Scale bar: 10 μm in (a), 5 μm in (**f**- **g'**) and 2.5 μm in (**b**, **d**, **h**-**h"**).

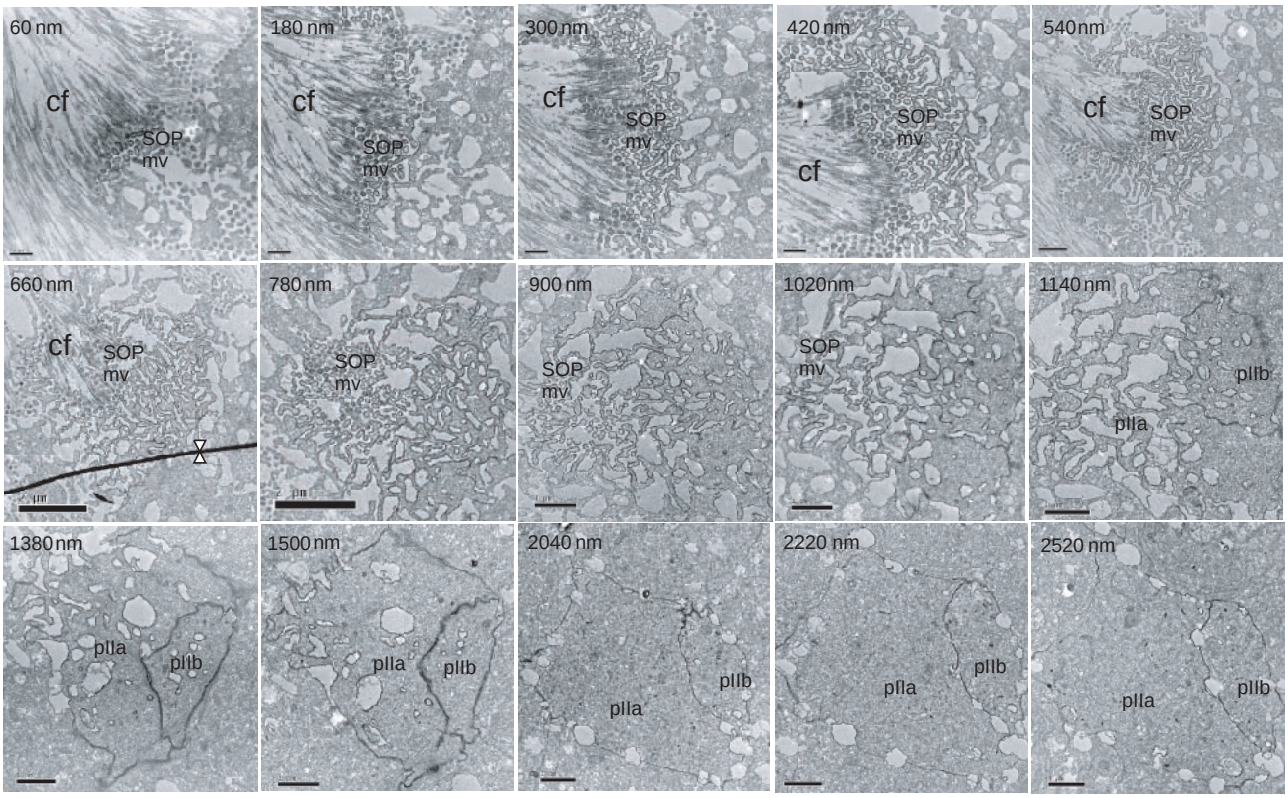

Figure S2 Transmission electron micrographs reveal the presence of finger-like projections on the apical surface of the pIIa-pIIb cells: Serial TEM micrographs of apical cross sections of pIIa-pIIb cells starting at 60 nm of the apical end through 2520 nm (basal end). Serial sections reveal the presence of numerous cross sections of finger-like projections, microvilli (mv) from 60 nm through 1020 nm. Sections from 1500 to 2520 nm show cell membrane outlines of pIIa-pIIb. The chitin fiber (cf) which assembles at the plasma membrane is a part of the apical extracellular matrix (cuticle). The dark line across 660nm with the double arrowhead is a section fold artifact.

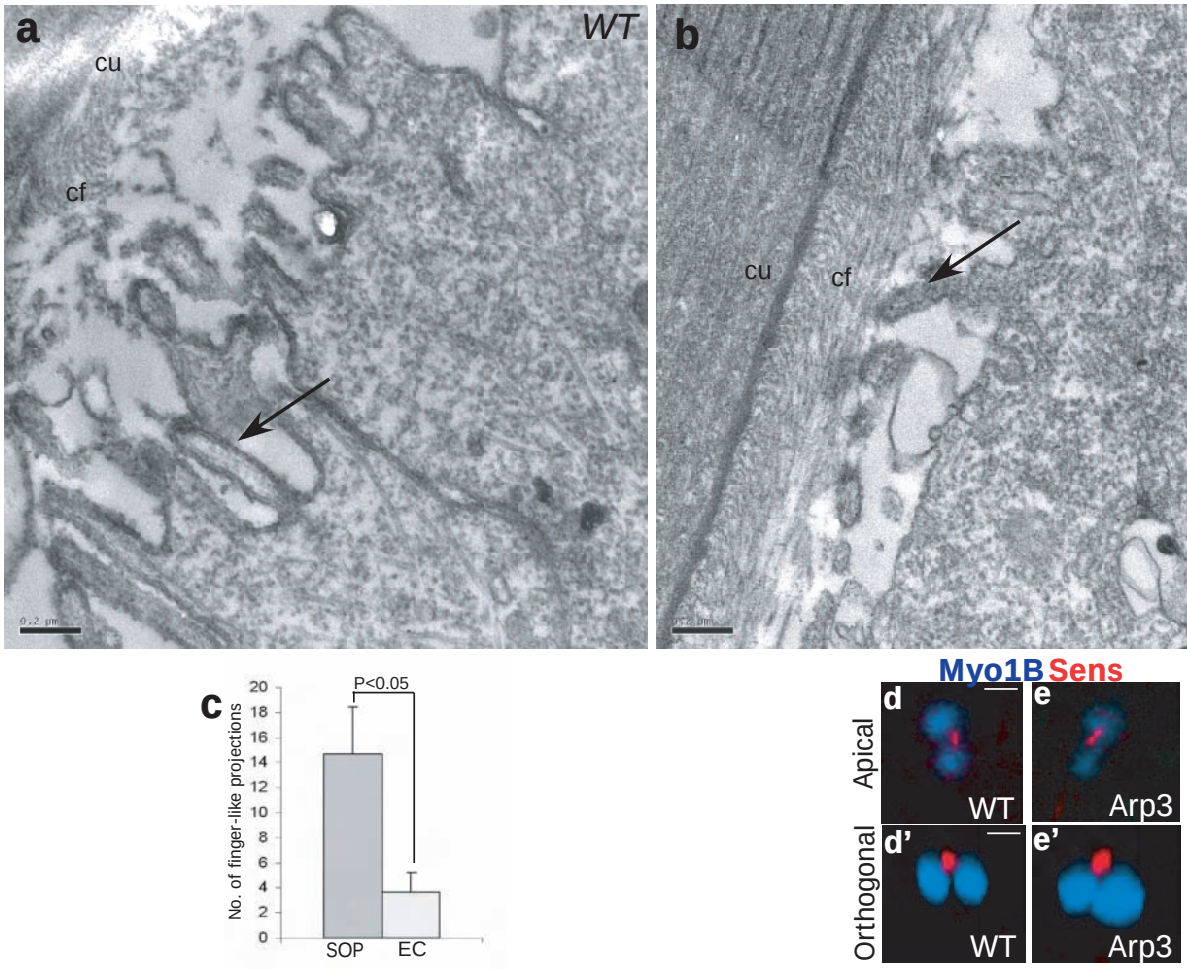

Figure S3 (**a** –**c**) The number of finger-like projections in pIIa-pIIb is significantly higher compared to those on epidermal cells: (**a**) TEM image along the XZ-axis of an SOP and (**b**) Epidermal cells at the 2-cell stage (**c**) A bar graph representing quantification of the number of finger-like projections in the epidermal cells versus the pIIa-pIIb cells. Three *WT* pIIa-pIIb pairs and six *WT* epidermal cells were used for this quantification. Arrows point to the finger-like projections. (**d** -**e'**) Microvilli marker Myo1B is correctly localized in *Arp3* mutant SOP progeny: (**d** -**e'**) Confocal images of single optical sections along the XY-axis (**d**, **e**) and the XZ-axis (**d'**, **e'**) depict immunostainings of *WT* (**d**, **d'**) and *Arp3* (**e**, **e'**) SOP progeny at the 2-cell stage, stained for Myo1B (red) and Sens (blue). Error bars indicate the SEM. Abbreviations: cuticle (cu), chitin fiber (cf). Scale bar: 0.2 μm in (**a**, **b**) and 5 μm in (**d**, **d'**).

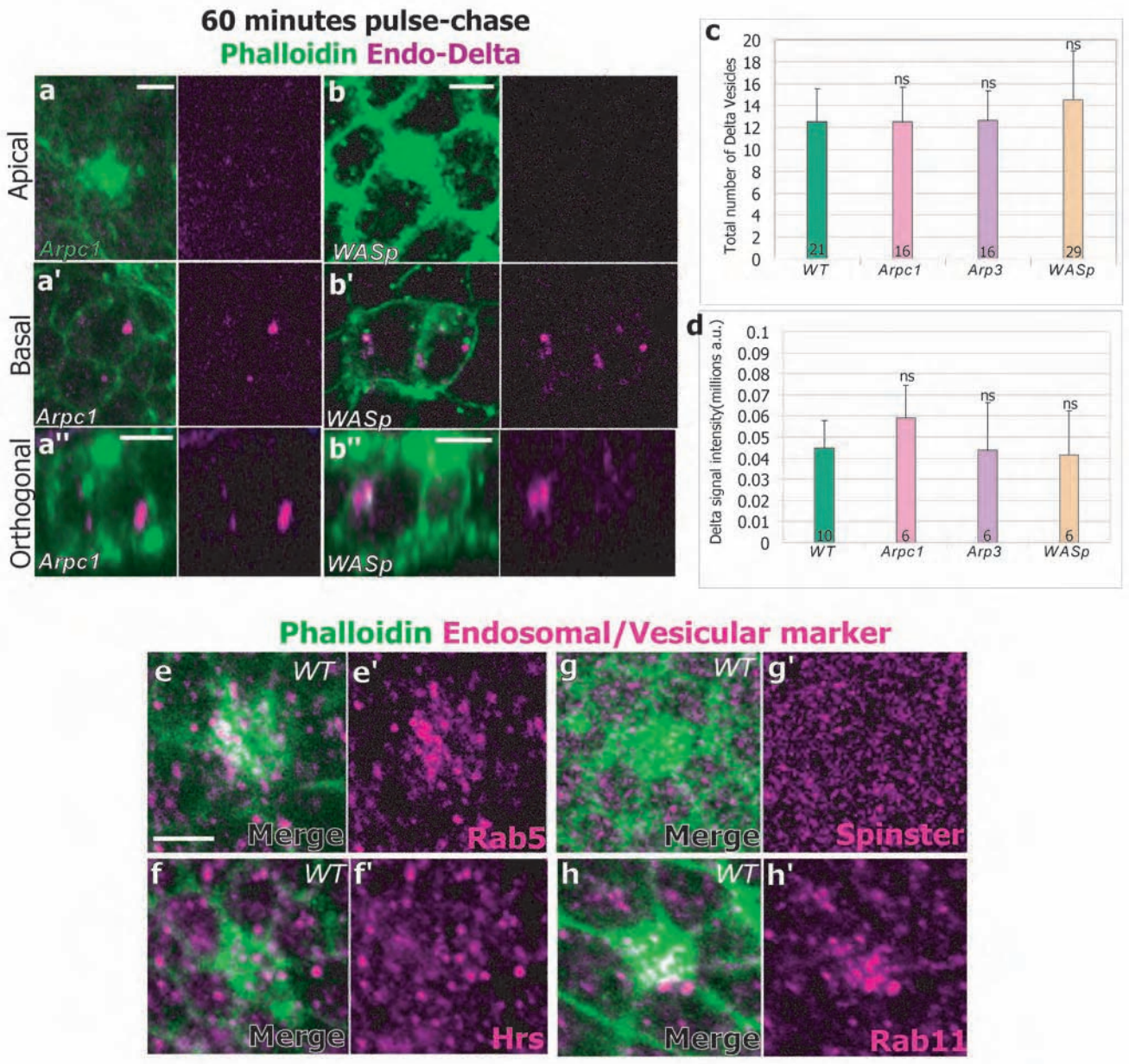

Figure S4 (**a**- **d**) Trafficking of endocytosed Delta traffics apically to the ARS after 60mins chase is compromised in *Arp2/3* and *WASp* mutants: (**a** -**b"**) Confocal images show a single section along the XY-axis (**a**, **a'**, **b**, **b'**) and XZ-axis (**a"**, **b"**) of SOP progeny at the 2-cell stage in *Arpc1* (**a**-**a"**) and *WASp* (**b**-**b"**) mutant during a 60 mins pulse-chase trafficking assay of internalized Delta–anti-Dl^{ECD} vesicles (magenta) with respect to the ARS stained by phalloidin (green). (**c**) A bar graph representing a quantification of the total number of internalized Delta vesicles which are present in the SOP progeny 60 mins after endocytosis. (**d**) A bar graph representing a quantification of the signal intensity of Delta immunostaining in the SOP progeny at 60 min chase. The number of SOP progeny (pIIa-pIIb) quantified per genotype is indicated in the bars. (**e –f'**) Early and recycling endosomes are enriched on the apical region of the ARS during fate specification: (**e** -**f'**) Confocal images of single Z-sections show immunostaining of ARS with phalloidin (green) and endosomal/vesicular markers (magenta) in *WT* pupal nota at the 2-cell stage. (**e**, **e'**) Rab5 (magenta) which marks the early endosome is enriched on the ARS (green). (**f**, **f'**) A subset of late endosomes marked by Hrs (magenta) do not show enrichment with respect to the ARS (green). (**g**, **g'**) The lysosomes marked by Spinster/ Benchwarmer (magenta) do not show enrichment relative to the ARS (green). (**e**, **e'**) Rab11 (magenta) which marks the recycling endosome is enriched with respect to the ARS (green). ns = not statistically significant. Error bars indicate SEM. Scale bar: **5** µm in (**a**, **b**, **a"**, **b"**) and 3.5 µm in (**e**).

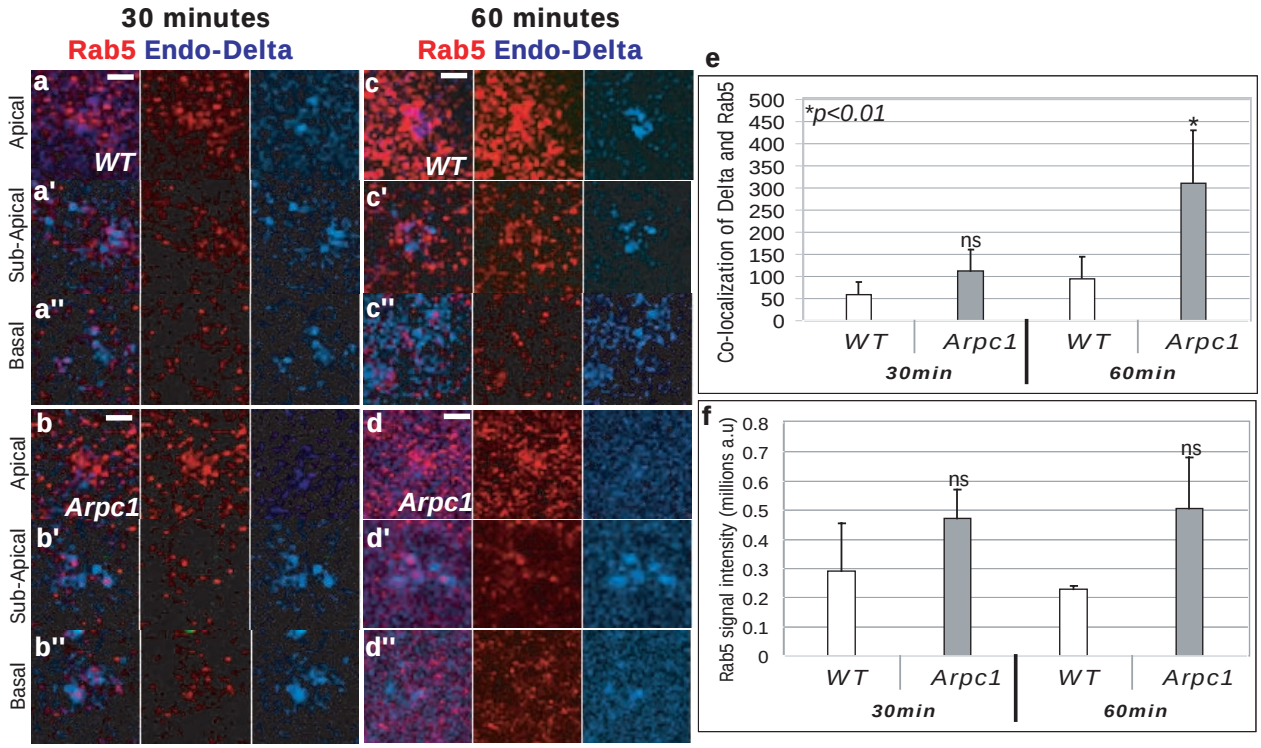

Figure S5 Pulse-chase trafficking of Delta with respect to the early endosomes (EE): Confocal images of single optical sections (**a**-**d”**) of SOP progeny at the 2-cell stage in *WT* (**a**-**a”**, **c**-**c”**) and *Arpc1* (**b**-**b”**, **d**-**d”**) after 30 mins (a-b”) and 60 mins (c-**d”**) pulse-chase trafficking assays of internalized Delta–anti-DI^{ECD} (blue) with respect to the EE stained for Rab5 (red). (**a**-**d**) Apical sections (~0.5 µm) into the sample. (**a’**-**d’**) Sub-apical sections (~3 µm) into the sample. (**a”**-**d”**) Basal sections (~6 µm) into the sample. (**e**) A bar graph depicting co-localization intensity of Delta and Rab5 vesicles in arbitary units (a.u.). The measurements of signal intensities were analysed using a Student’s t-test;*, p=0.01. Seven SOP progeny pairs were quantified per time point per genotype. (**f**) A bar graph depicting signal intensity of Rab5 vesicles in arbitary units (a.u.). The measurements of signal intensities were analysed using a Student’s t-test;*, p=0.01. Seven SOP progeny pairs were quantified per time point per genotype. Abbreviation: ns = not statistically significant. Error bars indicate SEM. Scale bar: 3.5 µm.

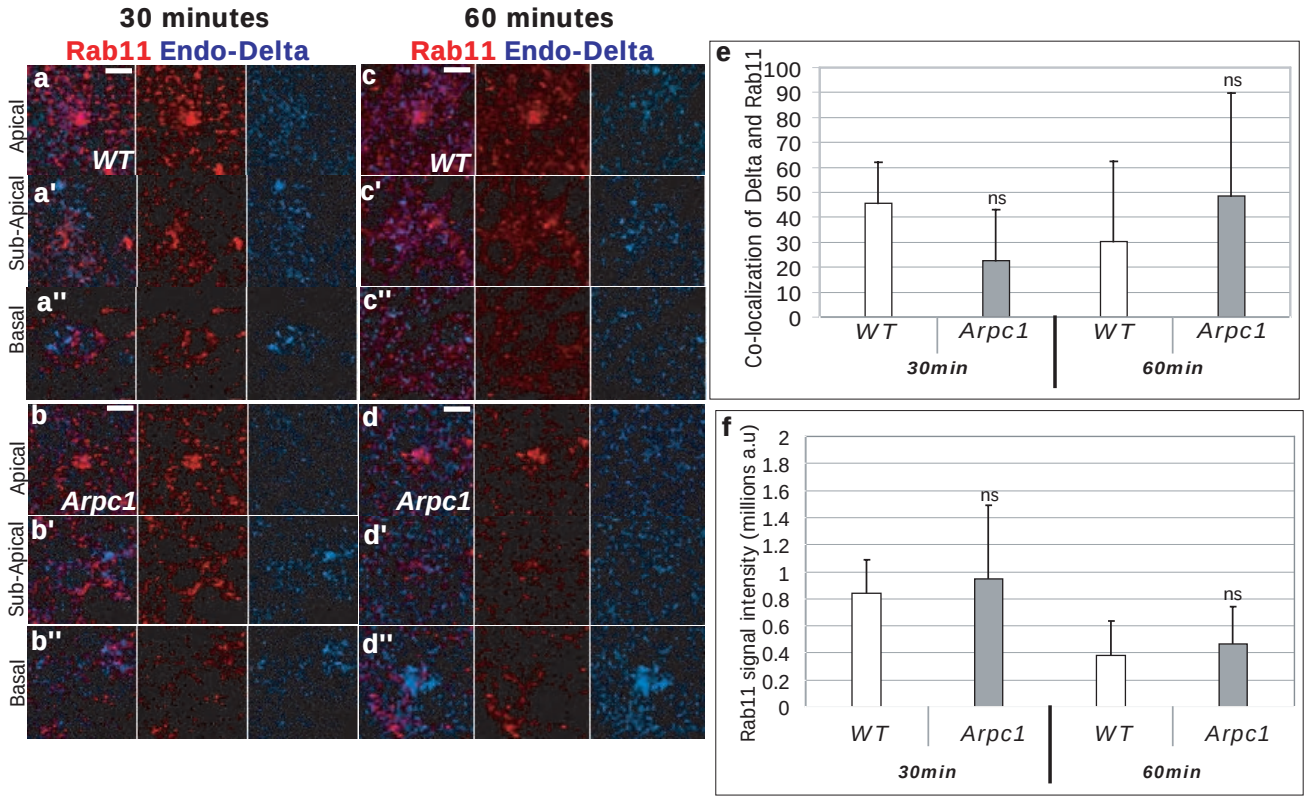

Figure S6 Pulse-chase trafficking of Delta with respect to the recycling endosomes (RE): Confocal images of single optical sections (**a**-**d”**) of SOP progeny at the 2-cell stage in *WT* (**a**-**a”**, **c**-**c”**) and *Arpc1* (**b**-**b”**, **d**-**d”**) after 30 mins (**a**-**b”**) and 60 mins (**c**-**d”**) pulse-chase trafficking assays of internalized Delta–anti-DI^{ECD} vesicles (blue) with respect to the RE stained for Rab11 (red). (**a**-**d**) Apical sections (~0.5 µm) into the sample. (**a’**-**d’**) Sub-apical sections (~3 µm) into the sample. (**a”**-**d”**) Basal sections (~6 µm) into the sample. (**e**) A bar graph depicting co-localization intensity of Delta and Rab11 vesicles in arbitrary units (a.u.). The measurements of signal intensities were analysed using a Student’s t-test;*, p=0.01. Seven SOP progeny pairs were quantified per time point per genotype. (**f**) A bar graph depicting signal intensity of Rab11 vesicles in arbitrary units (a.u.). The measurements of signal intensities were analysed using a Student’s t-test;*, p=0.01. Seven SOP progeny pairs were quantified per time point per genotype. Abbreviation: ns = not statistically significant. Error bars indicate SEM. Scale bar: 3.5 µm.

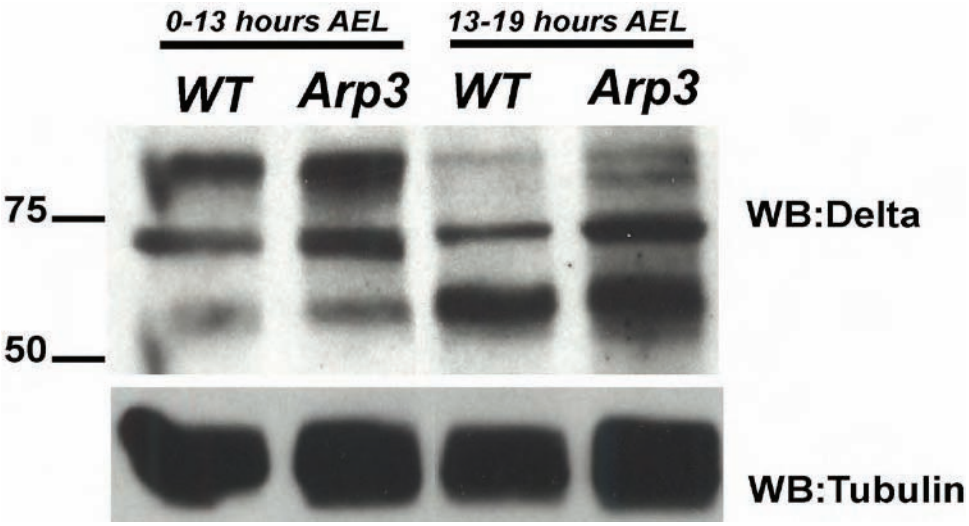

Figure S7 The processing of Delta in *Arp3* mutant embryos is unaffected: Western blotting analysis of *WT* and *Arp3* embryo lysates at 0-13hr AEL and 13-19hr AEL probed with mouse anti-Delta ascites fluid. At 0-13hr AEL note the presence of a 98 kDa band in *WT* and *Arp3* lanes. The Delta S isoform (68 kDa, is present at 0-13hr AEL but is weaker compared to the 98 kDa band. At 13-19hr AEL the 98 kDa band is much reduced in *WT* and *Arp3*. The Delta S isoform (68 kDa, arrow) is highly enriched at the 13-19 hr AEL time point in both *WT* and *Arp3* mutant. In the *Arp3* lane we sometimes observe a doublet at 98 kDa at 13-19hr AEL, but not consistently in various independent trials of the experiment.

Supplementary material:

Results:

Early and recycling endosomes are enriched on the apical region of the ARS during fate specification:

It has been proposed that Delta must be endocytosed and targeted to a specific endosomal compartment to become activated[1], possibly through a Rab11-positive recycling endosomal compartment[2, 3]. Based on our data, the ARS may have a role in these trafficking events. We therefore examined the co-localization of different endosomal compartments with respect to the ARS during cell fate specification. Immunostaining with endosomal and vesicular compartment markers including Rab5 (early endosomes, EE)[4], Rab11 (recycling endosomes, RE)[5], Hrs (late endosomes, LE)[6] and Spinster (lysosomes)[7, 8] revealed that EE and RE are enriched apically where they co-localize with the microvillar region of the ARS in the pIIa-pIIb at the 2-cell stage (Supplementary Fig. 4 e, e', h, h'). However, the LE and lysosomes are not enriched with respect to the ARS (Supplementary Fig. 4 g, g', f, f'). We find the localization of these endosomal and vesicular compartments are similar to *WT* in *Arp3, Arpc1* mutant pIIa-pIIb cells (data not shown).

Endosomal trafficking of Delta through the early endosomes (EE) and recycling endosomes (RE) during pIIa-pIIb fate specification:

To examine if Delta trafficking through the EE and RE is altered in mutants of the Arp2/3 complex, we performed pulse chase assays at 30 mins and 60 mins after

internalization (Supplementary Fig. 5, 6). We focused on these compartments as they were enriched on the ARS at the 2-cell stage (Supplementary Fig. 4 e, e', h, h'). With regard to the Rab5-positive EE compartment we find that there is no statistically significant difference of Delta co-localization with this compartment between *WT* and mutant at 30 mins post-internalization (Supplementary Fig. 5 a-b'', e). However, after 60 mins chase there seems to be a borderline significant increase in Delta vesicle co-localization to the Rab5 compartment (p=0.01, student's two-tailed test) in *Arpc1* mutants compared to *WT* (Supplementary Fig. 5 c-d'', e). We also assayed if the abundance of the EE is altered in the *Arpc1* mutant by quantifying the signal intensity of Rab5 immuno-staining in the *Arpc1* mutant pIIa-pIIb cells, 30 min and 60 mins after internalization, and we find that there is no significant difference (Supplementary Fig. 5 f).

Furthermore, we found that there is not a statistically significant difference of Delta trafficking with respect to the Rab11-positive RE at both 30 mins and 60 mins post internalization (Supplementary Fig. 6 a-d'', e). The distribution and abundance of the Rab11 compartment itself remains largely unaffected in the *Arpc1* mutants (Supplementary Fig. 6 f). In addition, when the pI cell divides, Emery et al (2005) have reported that Rab11 localizes asymmetrically to the pIIb cell[3]. We found that this asymmetric distribution of Rab11 to the pIIb compartment is unaffected in dividing pIs of *Arp3* mutants (data not shown).

Our hypothesis based on these results is that the primary defect in *Arp2/3* mutants is their inability to traffic Delta to the apical region of the ARS, and we consider this increased co-localization of Delta to the Rab5 compartment as a

secondary defect that seems to occur when the Delta vesicles do not arrive at their expected destination. The reason we favor this hypothesis is that the inability of Delta to cluster around the ARS and traffic apically seems to be a highly significant (Fig. 8g) defect as compared to a subtle increase in Delta co-localization to the Rab5 positive compartment (Supplementary Fig. 5e).

Delta processing is unaffected in *Arp3* mutants:

Wang and Struhl[1] have suggested that the internalization of Delta leads to a proteolytic cleavage in an unknown compartment. *Drosophila* full-length Delta (~98 kDa) is proteolytically processed into three different isoforms *in vivo*[9] and the short isoform Delta S (~68 kDa) may correspond to the activated form[1, 9]. During early stages of embryogenesis (0-6 hours after egg laying, hr AEL) the Delta S isoform is not generated[45]. At later developmental stages (13-24hr AEL) full-length Delta is much reduced, but the Delta S isoform is far more abundant[45]. To assay if lack of Arp2/3 function alters Delta processing we prepared lysates from *WT*, *Arp3* and *Arpc1* zygotic mutant embryos at two different developmental time periods, 0-13hr AEL and 13-19hr AEL, for western blot analysis. We find that processing of Delta is largely unaltered in *Arp3* embryos (Supplementary Fig. 7), suggesting that the processing of Delta may not depend on Arp2/3 function.

Developmental Cell
Article

Structural Rules and Complex Regulatory Circuitry Constrain Expression of a Notch- and EGFR-Regulated Eye Enhancer

Christina I. Swanson,[1] Nicole C. Evans,[1] and Scott Barolo[1,*]
[1]Department of Cell and Developmental Biology, University of Michigan Medical School, Ann Arbor, MI 48109, USA
*Correspondence: sbarolo@umich.edu
DOI 10.1016/j.devcel.2009.12.026

SUMMARY

Enhancers integrate spatiotemporal information to generate precise patterns of gene expression. How complex is the regulatory logic of a typical developmental enhancer, and how important is its internal organization? Here, we examine in detail the structure and function of *sparkling*, a Notch- and EGFR/MAPK-regulated, cone cell-specific enhancer of the *Drosophila Pax2* gene, in vivo. In addition to its 12 previously identified protein-binding sites, *sparkling* is densely populated with previously unmapped regulatory sequences, which interact in complex ways to control gene expression. One segment is essential for activation at a distance, yet dispensable for other activation functions and for cell type patterning. Unexpectedly, rearranging *sparkling*'s regulatory sites converts it into a robust photoreceptor-specific enhancer. Our results show that a single combination of regulatory inputs can encode multiple outputs, and suggest that the enhancer's organization determines the correct expression pattern by facilitating certain short-range regulatory interactions at the expense of others.

INTRODUCTION

Enhancers, or *cis*-regulatory elements, are the primary determinants of spatiotemporal patterns of gene expression. In order to properly regulate their target genes, enhancers must perform a number of functions, such as identifying and communicating with the promoter, sometimes over great distances, and triggering transcription in certain cells, but not in others. Many enhancers are capable of driving a heterologous promoter in the proper pattern when removed from their normal genomic context. This autonomy implies that enhancers can assemble a complete set of biochemical activities that together are sufficient for robust, patterned transcriptional activation at a remote promoter. Do different DNA-binding factors recruit distinct types of activation activities, or must the enhancer merely accumulate enough of a single limiting activity to exceed a threshold for activation?

Different types of studies reach widely divergent conclusions about enhancer complexity. For example, Eric Davidson and colleagues, combining reporter assays with affinity purification in an extensive study of *cis*-regulatory logic in the sea urchin *Endo16* gene, identified 55 binding sites for 16 regulatory proteins, which form an intricate regulatory computer spanning 2300 bp of DNA (Davidson, 1999). However, most developmental genetics-based enhancer studies culminate in models requiring no more than three to five different regulators (often only one or two), binding within ~300–1000 bp of DNA, to explain the activity and specificity of a seemingly typical enhancer. In the very rare cases in which the question of sufficiency is addressed in vivo, the defined regulatory sites are generally insufficient to properly reconstitute enhancer function, and an unknown activator, "X," is added to the model (reviewed by Barolo and Posakony, 2002). How many *cis*-regulatory sites are sufficient, when combined, to recapitulate normal enhancer function, in the context of a chromosome in a normal cell?

We have pursued a bottom-up approach to these questions by taking a previously well-characterized developmental enhancer and exhaustively dissecting it in vivo, both to discover the extent of its regulatory complexity and to determine whether different enhancer subelements perform distinct functions. We chose to study the *sparkling* (*spa*) enhancer of the *dPax2* gene, which is necessary and sufficient to specify the cone cell fate in certain multipotent cells in the developing *Drosophila* eye (Fu and Noll, 1997; Fu et al., 1998; Flores et al., 2000; Shi and Noll, 2009). *spa* drives cone cell-specific *dPax2* expression in response to four direct regulators, acting through 12 transcription factor-binding sites (TFBSs): Suppressor of Hairless (Su(H)), under the control of Notch signaling; two Ets factors, the activator PointedP2 (Pnt) and the repressor Yan, both controlled by EGFR/Ras/MAPK signaling; and the Runx-family protein Lozenge (Lz) (Fu et al., 1998; Flores et al., 2000; Tsuda et al., 2002) (Figure 1A). In their report describing the direct regulation of the *spa* enhancer by Su(H), Lz, and Ets factors, Flores et al. (2000) proposed a model in which a combinatorial code, Lz + EGFR/Pnt/Yan + Notch/Su(H), determines the cell-type specificity of *spa* activity. The authors were careful to state that "the model…reflects requirements rather than sufficiency for cell fate specification." Despite this caveat, the Lz + Ets + Su(H) code is now considered to "define the combinatorial input required for cone cell specification" (Voas and Rebay, 2004; see also Pickup et al., 2009; Shi and Noll, 2009).

Because the *spa* enhancer is small (362 bp), and because the known regulatory inputs could, in theory, explain its cell type specificity (Flores et al., 2000), we considered it an ideal test case for a comprehensive structure-function analysis. Here, we

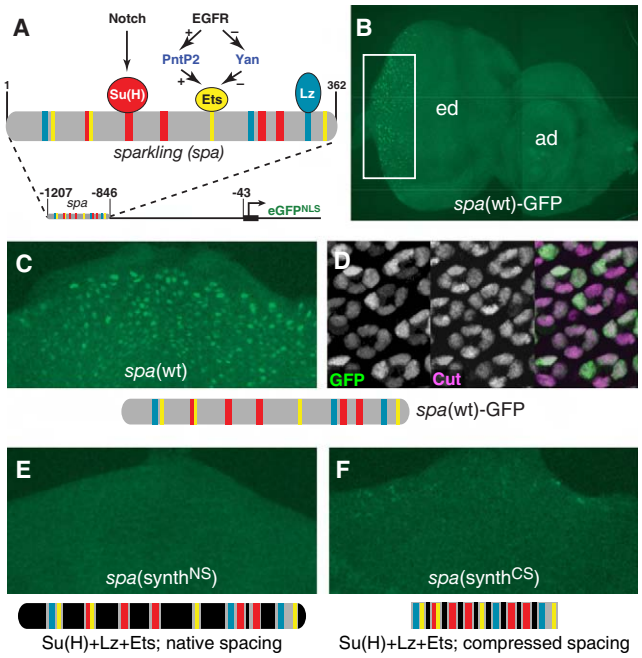

Figure 1. The Known Regulators of *spa* Are Insufficient for Transcription in Cone Cells

(A) Summary of the known regulatory inputs of the *sparkling* (*spa*) cone cell enhancer of *dPax2*. Defined transcription factor-binding sites (TFBSs) are shown as colored bars; uncharacterized sequences are gray. The enhancer is placed 846 bp upstream of the transcription start site in all transgenic constructs, except those in Figure 4.

(B–D) Expression of a GFP transgene under the control of *spa*. (B) Eye-antennal imaginal disc from a *spa*-GFP transgenic larva. (C) The posterior of an eye disc, corresponding approximately to the boxed area in (B). Posterior is oriented toward the top. (D) Eye of a 24 hr pupa carrying *spa*(wt)-GFP, stained with antibodies against GFP (green) and the cone cell nuclear marker Cut (magenta).

(E) *spa*(synth^{NS}), in which the previously uncharacterized sequences have been altered (black), but the 12 defined TFBSs are present in their native arrangement and spacing.

(F) *spa*(synth^{CS}), containing the 12 TFBSs in compressed spacing.

report the results of our initial tests, which reveal several surprising aspects of *spa* enhancer function in vivo.

RESULTS

For our in vivo analysis of the *spa* enhancer, we used a specially built Gateway reporter transgene vector, Ganesh-G1, in which enhancers are placed upstream of a minimal, TATA-containing promoter taken from the *Drosophila Hsp70* gene, driving an EGFP-NLS reporter (Swanson et al., 2008). An important feature of this vector is that the enhancer is placed 846 bp upstream from the transcription start site (Figure 1A), so that in all experiments presented here (except those in Figure 4), the enhancer is forced to act at a moderate distance from the promoter. We do not consider this an unfair test of enhancer activity, given that, in its native genomic context, *spa* is located > 7 kb from the *dPax2* promoter (Fu et al., 1998). We generated at least four independent transgenic lines for each reporter construct. Because line-to-line variability was generally low, we found that examination of 3–5 independently derived lines was sufficient for most constructs. For constructs with more variable expression (usually those with low activity), we examined additional lines (10–14) to ensure that our conclusions were not based on rare insertion effects. Table S1 (available online) lists all transgenic lines and their expression levels.

When placed in Ganesh-G1, *spa* drives cone cell-specific GFP expression in developing retinas of transgenic larvae and pupae (Figures 1B–1D). This and previous work by Flores et al. (2000) demonstrate that the 362 bp *spa* enhancer contains all sequences necessary to (1) activate gene expression in vivo and (2) restrict this activation to developing cone cells.

The (Lz + Pnt + Su(H)) Code Is Insufficient to Specify Cone Cell Expression

All three of the known positive regulators of the *spa* enhancer are required for its activity and cone cell specificity. This suggested a "combinatorial code" model for *dPax2* regulation, in which the combined activities of Lz, Pnt, and Su(H), acting through binding sites in *spa*, cooperatively activate *dPax2* expression specifically in cone cells (Flores et al., 2000; Tsuda et al., 2002; Nagaraj and Banerjee, 2007). We began our analysis by testing the simplest form of such a model, which predicts that the binding sites within *spa* that mediate those three regulatory inputs should suffice, in combination, to drive gene expression in cone cells.

First, we built a synthetic *spa* enhancer construct in which all 12 of the defined binding sites for Lz, Su(H), and Pnt/Yan within *spa* are intact (along with 3–4 flanking base pairs to either side) and are placed in their native arrangement and spacing, but in which all other enhancer sequences are mutated by altering every second base pair. This construct, called *spa*(synth^{NS}) because of the native spacing of its TFBSs, fails to activate gene expression in vivo (Figure 1E). A second version of *spa* (synth^{NS}), in which the opposite set of base pairs was mutated, produced the same result (not shown). We also created *spa* (synth^{CS}), a compressed-spacing construct containing the same 12 sites, in which intersite sequences of > 12 bp have been reduced to 12 bp. *spa*(synth^{CS}) also fails to act as a cone cell enhancer, although weak GFP expression can be detected in a few noncone cells (Figure 1F). Based on these findings, we hypothesized that additional sequences, besides the 12 defined regulatory sites, are necessary for proper transcriptional regulation mediated by *spa*.

Numerous Regulatory Sites within *spa*, in Addition to the Known Binding Sites, Are Required for Cone Cell Activation

In order to pinpoint the regulatory sites within *spa* that make essential contributions to enhancer activity in vivo, we conducted a systematic mutational analysis of all previously uncharacterized sequences within *spa*. These sequences were divided into regions 1–6, and each region was deleted in turn, leaving the known TFBSs intact in all cases (Figure 2A). Of all segments mutated in this manner, only region 3 makes no significant contribution to cone cell expression. Deleting regions 1, 2, 4, or 6 causes total or near-total loss of gene expression in vivo; conversely, deleting region 5 enhances expression in cone cells (Figures 2A–2G).

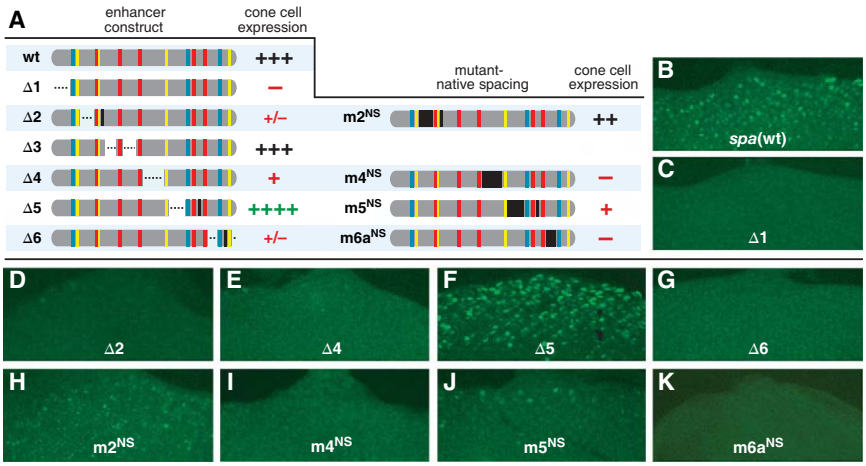

Figure 2. Sequence and/or Spacing Constraints Apply to Multiple Segments of *spa*

(A) Diagrams of *spa* enhancer constructs and summary of their cone cell activity in larval eye discs. Dotted lines indicate deletions; black bars indicate mutations that preserve native spacing (NS). In each case, the 12 known TFBSs are preserved. +++, wild-type levels and pattern of expression in cone cells; ++, moderately reduced expression; +, severely reduced expression; +/–, expression detectable in very few cells; –, no detectable expression; ++++, augmented levels of expression.

(B–K) GFP expression in eye imaginal discs driven by the (B) wild-type *spa* enhancer and (C–K) mutant enhancers carrying deletions or native-spacing mutations in previously uncharacterized sequences, numbered 1–6.

Spacing versus Sequence

Internal deletions of enhancer DNA cause two simultaneous changes: loss of the deleted sequence, and altered relative spacing of the sites to either side. To distinguish between these two types of effects, we made native-spacing (NS) mutations in which a specific sequence was altered, but its length was preserved. In regions 4 and 6, native-spacing alterations and deletions have similar effects, indicating that the sequence content of these regions is functionally significant (Figures 2D, 2G, 2H, and 2K). However, a native-spacing mutation in region 2 has a less severe effect than a deletion (Figure 2H; cf. Figure 2D), from which we infer that much of the regulatory contribution of region 2 can be attributed to its length, rather than its sequence.

Within region 5, deleting the DNA and altering its sequence have opposing effects. Deleting region 5 augments cone cell expression, whereas a native-spacing mutation causes a severe loss of activity (Figures 2F and 2J). The simplest interpretation of these results is that region 5 harbors positive regulatory sequences that are normally required, but that the deletion brings together sites on either side of region 5, increasing synergy between transcription factors and thus compensating for the loss of regulators normally binding to region 5. Consistent with this interpretation is the fact that Pnt and Lz, which bind to either side of region 5, physically interact and synergistically activate transcription, as can mammalian orthologs of these factors (Flores et al., 2000; Behan et al., 2005 and references therein). The fact that multiple smaller-scale native-spacing mutations within region 5 impair *spa* function, while none augment expression (see Figure 3), further supports this conclusion.

spa Is Densely Packed with Regulatory Sites

The analysis described above demonstrates that, in addition to the defined TFBSs, regions 1, 4, 5, and 6 of *spa* (and to a lesser extent region 2) are essential for its proper function. Each of these segments is large enough to contain several protein-binding sites of typical size. To determine what proportion of these sequences has a regulatory role, we made native-spacing mutations to smaller segments (10 bp, on average) within regions 1, 4, 5, and 6. Of these 12 finer-scale mutations, 10 cause severe or total loss of gene expression in cone cells (Figure 3). In addition, results described below indicate the presence of repressive regulatory site(s) within *spa*, but outside of regions 1, 4, 5, and 6. Given that the consensus binding sites for the known regulators of *spa* are < 9 bp in length, there is room for many regulatory sites within these regions. Together, the regulatory sites described here and the previously described TFBSs densely populate *spa*, with apparent "junk" or "spacer" sequences constituting a small proportion of the enhancer.

To investigate the possibility that the regulatory sites in regions 1, 4, 5, and 6 act by facilitating binding of the known activators to nearby binding sites, and the related possibility that these regions contain cryptic or noncanonical binding sites for the known activators, we tested the ability of Lz and Su(H) to bind to sites within *spa* in vitro. In all cases, mutating the newly characterized essential regulatory sequences did not significantly reduce the affinity of Lz or Su(H) for nearby binding sites, as determined by electrophoretic mobility shift assay (EMSA) competition experiments (Table S2). Pnt does not bind in vitro to any sites flanking regions 1, 4, 5, or 6 (Flores et al., 2000). Therefore, in subsequent experiments, we pursued the possibility that the newly characterized regions of *spa* have functions that differ from those of the Lz/Ets/Su(H)-binding sites.

Evidence for a Special Type of Regulatory Site, Specifically Mediating Action at a Distance

The mutational analysis described above defined many regulatory sites of equal importance to the known Lz/Ets/Su(H) sites. We next attempted to isolate and study an important but poorly understood function of the enhancer: activation at a distance. As mentioned above, all of the enhancer constructs described thus far were placed 846 bp upstream of the promoter, thus forcing them to act over a moderate distance. If we could rescue the activity of a mutant enhancer by moving it close to the promoter, we reasoned, the mutated region is likely to specifically mediate remote enhancer-promoter interactions. Conversely, if a mutation cannot be rescued by promoter-proximal placement, it is likely to mediate a different step in gene activation.

The wild-type *spa* enhancer drives the same pattern from −121 bp as from −846 bp (Figure 4A), although activation is noticeably more robust from the more proximal position. A mutant *spa* enhancer lacking region 1 (*spa*(Δ1)), which is

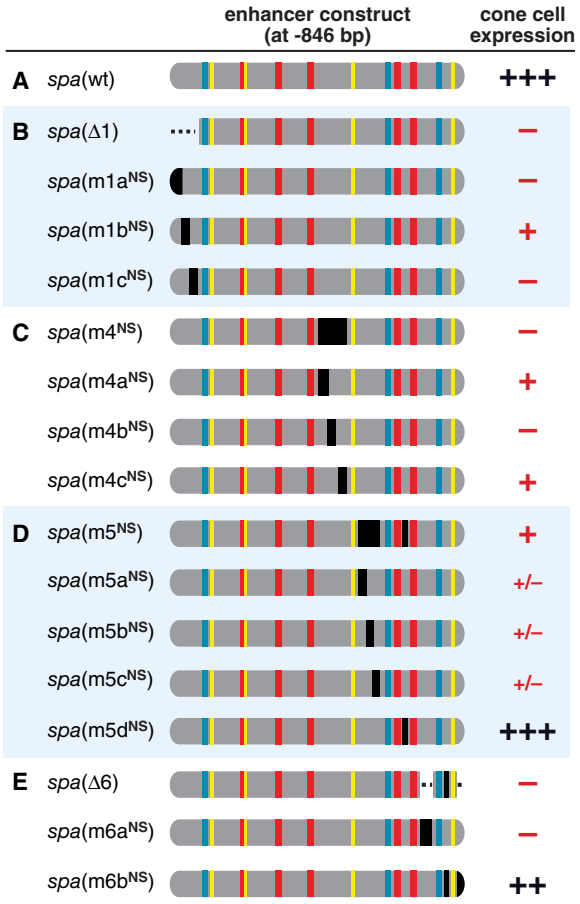

Figure 3. Most of *spa* Is Composed of Critical Regulatory Sequences
(A–E) Diagrams of mutated *spa* enhancer constructs. Blue, yellow, and red bars indicate defined binding sites for Lz, Pnt/Yan, and Su(H), respectively. Dotted lines indicate deletions; black bars indicate mutations that preserve native spacing (NS). GFP expression in larval cone cells is summarized as in Figure 2.

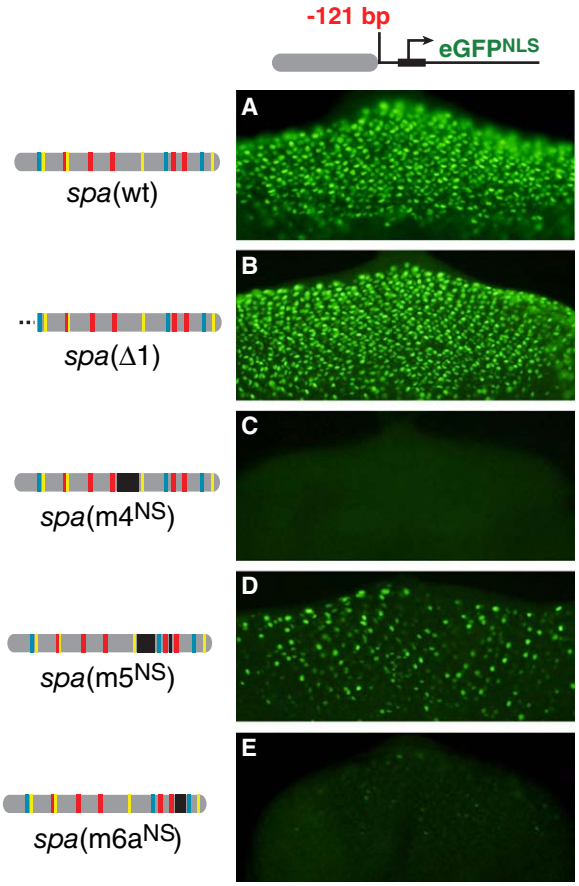

Figure 4. Region 1 Is Required for Activation at a Distance, but Not for Patterning
(A–E) Transgenic larval eye discs. In this figure, all enhancers are proximal to the minimal *Hsp70* promoter, at position −121 from the transcription start site, compared to −846 in all other figures. Because *spa* drives stronger expression from a promoter-proximal position, these images were collected at a lower exposure setting than those in other figures.

transcriptionally dead at −846 bp (Figure 2C), is completely rescued by placement at position −121, driving robust gene expression in the normal pattern (Figure 4B). By contrast, enhancers with mutations in regions 4, 5, or 6a remain unable to drive wild-type levels or patterns of gene expression at −121 (Figures 4C–4E). Interestingly, each of these constructs partially recovers cone cell activity by midpupal stages (not shown), suggesting that these regions may be more critical for the initiation than for the maintenance of gene expression. Similarly, Lz/Pnt/Su(H)-binding sites are required even when *spa* is promoter proximal (Flores et al., 2000). Of all regulatory sites within *spa*, only region 1 is both dispensable for enhancer activity and patterning in a promoter-proximal position, and essential for activation at a distance.

To our knowledge, this is the first case of a regulatory element found within an enhancer that specifically mediates action from a remote position, with no apparent role in patterning of gene expression or other basic activation functions (see Discussion). We therefore refer to region 1 as a "remote control" element to functionally distinguish it from patterning elements within *spa*, which include the defined TFBSs as well as newly mapped patterning sites to be discussed below. Future experiments will test the range, potential promoter preferences, and functional properties of this intriguing regulatory element.

Unlike the Known Transcription Factors, Region 1 Acts Independently of Its Position within *spa*

Having mapped all essential regulatory sites within *spa*, we could then ask whether their linear organization influences gene expression in vivo. First, we tested the structural flexibility of region 1, the remote control element (RCE), by moving it from the 5′ end to the 3′ end of the enhancer. This rearranged enhancer performs normally at −846 bp (Figure 5G), which indicates that the precise position of the RCE, relative to the other regulatory sites within *spa*, is not a critical factor in its remote activation function. Future experiments will determine the distance, relative to the enhancer and to the promoter, over which the RCE can act.

By contrast, the Lz/Ets/Su(H)-binding sites show strong position dependence. We rearranged these sites within *spa*

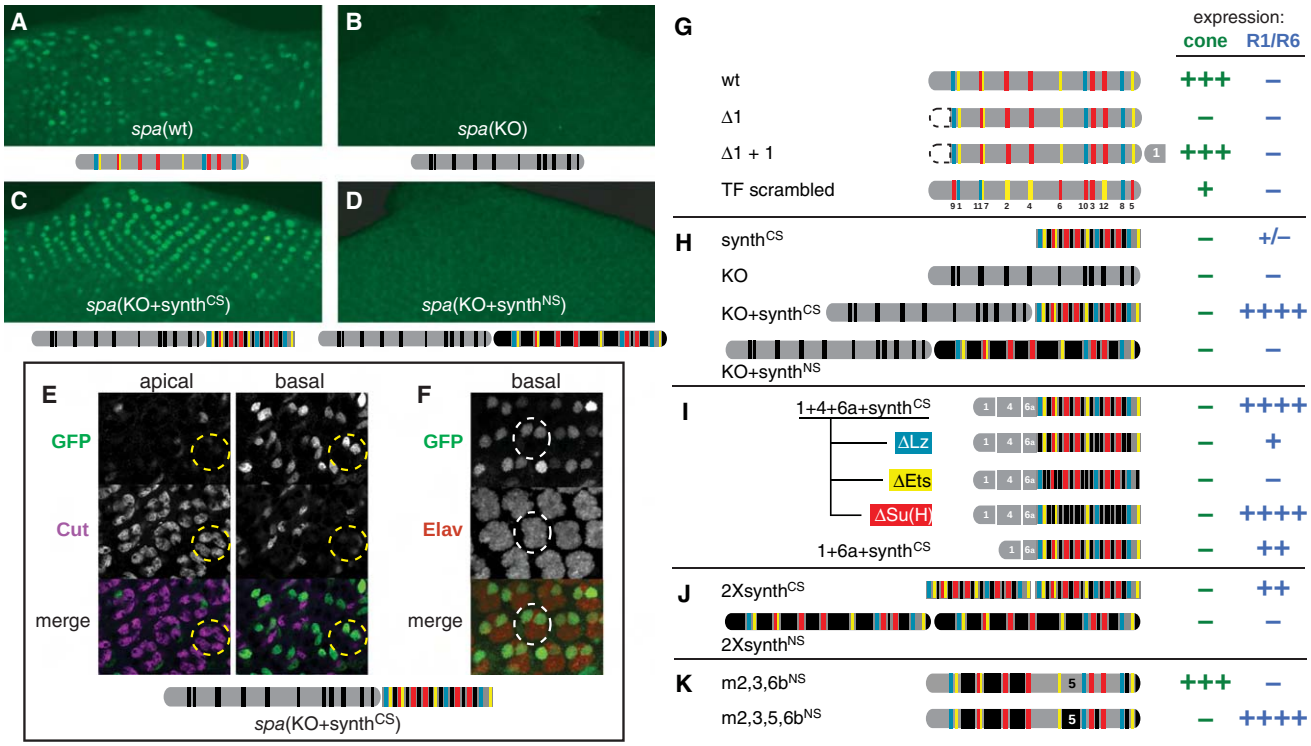

Figure 5. Cell Type Specificity of *spa* Is Controlled by the Arrangement of Its Regulatory Sites

(A–D) GFP expression driven by *spa* enhancer constructs in larval eye discs. All constructs shown here are placed at −846 bp. (A) *spa*(wt). (B) *spa*(KO), in which all 12 Lz/Ets/Su(H) sites are mutated. (C) A rearranged version of *spa*, in which *spa*(KO) is placed next to the 12 TFBSs to create *spa*(KO+synth^{CS}). (D) *spa*(KO+synth^{NS}), in which the TFBSs are placed in their native spacing next to *spa*(KO).

(E and F) *spa*(KO+synth^{CS}) is expressed specifically in photoreceptors (PRs), but not in cone cells, in 24 hr pupae. (E) Confocal images at two different planes, in retinas stained with antibodies against GFP (green) and the cone cell nuclear marker Cut (magenta), show GFP in two nuclei per ommatidium, located basally to cone cells. Posterior is oriented toward the top. (F) GFP driven by *spa*(KO+synth^{CS}) colocalizes with the PR marker Elav (red).

(G–J) Organization of regulatory elements within *spa* is critical for both transcriptional activity and cell type specificity. (G) Effects of relocating region 1 (the remote control element [RCE]), or of scrambling the locations of the known TFBSs, on enhancer function. (H) Rearranging the regulatory sites of *spa* converts its cell type specificity. (I) Creation of a minimal synthetic R1/R6-specific element. (J) 2Xsynth^{CS} and 2Xsynth^{NS}, both of which contain two copies of all known TFBSs.

(K) Region 5 of *spa* mediates repression in PRs, as well as activation in cone cells.

by moving each TFBS (along with flanking sequences) to the position of another, randomly chosen, TFBS. The resultant construct, *spa*(TF scrambled), is only weakly active in cone cells (Figure 5G). Thus, unsurprisingly but in contrast to the RCE, the configuration of the known TFBSs within *spa* plays an important role in enhancer function in cone cells.

Cell Type Specificity Is Controlled by the Structural Organization of *spa*

The diminished activity of *spa*(TF scrambled), along with the altered gene expression resulting from deletions in regions 2 and 5, suggest that the spatial organization of *spa* impacts its transcriptional activity. We next took a different approach to investigate the relationship between structure and function within *spa*.

As we have demonstrated, the 12 defined TFBSs within *spa* are insufficient for cone cell enhancer activity, even when combined. Likewise, when these TFBSs are mutated, the remaining sequences are incapable of driving transcription (*spa*(KO)) (Figure 5B). Because these two constructs, taken together, include all sequences from *spa*, we tested whether combining them would reconstitute enhancer activity. The resultant rearranged *spa* construct, KO+synth^{CS}, drives strong gene expression in the eye (Figure 5C).

Three aspects of this finding are worth noting. First, the activity driven by KO+synth^{CS} is robust, exceeding *spa*(wt) in intensity (Figure 5C; cf. Figure 5A). The defined TFBSs, therefore, are capable of acting synergistically with newly mapped activator sites in *spa*, even when the enhancer is reconfigured. This, combined with the in vitro binding data mentioned above, strongly suggests that the regulatory sites we have identified are not merely extended binding sequences for Lz/Pnt/Su(H).

Second, when the TFBSs adjacent to *spa*(KO) are spread out to mimic their native spacing, gene expression is lost (KO+synth^{NS}, Figure 5D). The activity of *spa* is apparently highly dependent on close proximity, among the known transcription factors and/or between those transcription factors and previously uncharacterized regulatory sites. Because KO+synth^{CS} and KO+synth^{NS} differ by only 29% in total length, and because KO+synth^{NS}, at 730 bp, is not large compared to many enhancers, this extreme dependence on short-range interactions was surprising.

Third, and most importantly, the pattern of gene expression driven by the rearranged enhancer *spa*(KO+synth^{CS}) differs

from that of *spa*(wt)—in fact, the two elements drive completely nonoverlapping expression patterns. Unlike *spa*(wt), whose activity colocalizes with the cone cell marker protein Cut (Figure 1D), KO+synth^{CS}-GFP is expressed only in nuclei located basally to Cut^{+} cells (Figure 5E). KO+synth^{CS} is active in a subset of basal cells expressing Elav, a marker of photoreceptor (PR) cell fate (Robinow and White, 1988). Based on the position of the two GFP^{+} cells within the Elav^{+} PR cluster, *spa*(KO+synth^{CS})'s activity is restricted to PRs 1 and 6 (R1/R6) (Figure 5F). Thus, merely rearranging the regulatory sites within *spa* is sufficient to cleanly switch its cell type specificity in vivo.

Ectopic Photoreceptor-Specific Transcription Depends on Lz and Ets Sites, Multiple Newly Mapped Regulatory Sequences, and Tight Clustering of Regulatory Sites

We next attempted to identify the regulatory sites responsible for ectopic activity of *spa* in PRs. Combining regions 1, 4, and 6a with the known TFBSs (1+4+6a+synth^{CS}) results in strong R1/R6 expression; removing region 4 from this construct weakens its activity (Figure 5I). By selectively mutating TFBSs, we found that R1/R6 expression requires Lz and Ets sites, but not Su(H) sites (Figure 5I). This is consistent with the fact that R1/R6 receive MAPK signaling and express Lz at high levels, but do not respond to Notch signaling (reviewed by Voas and Rebay, 2004).

Based on our remote-versus-proximal enhancer analysis (Figure 4), we hypothesized that different regulatory sequences within *spa* contribute distinct activities to gene activation. If this is so, one type of activity may not be able to functionally substitute for another. We tested this idea by creating tandem repeats of the synth^{CS} and synth^{NS} constructs, which contain two copies of each known TFBS, in compressed or native spacing, respectively. 2Xsynth^{CS} is inactive in cone cells and relatively weakly active in PRs, whereas 2Xsynth^{NS} is inactive in all cell types (Figure 5J). We therefore conclude that the Lz + Ets + Su(H) combination is insufficient for cone cell activation. Furthermore, the fact that additional Lz/Ets/Su(H) sites fail to compensate for the missing sequences adds support to the idea that some parts of the enhancer perform functions in transcriptional activation that are qualitatively distinct from those of the known regulators.

Interestingly, when *spa*(synth^{NS}) is placed at −121 bp, we observe occasional position-effect-dependent activity in cone cells (1 out of 7 lines) or PRs (1 of 7 lines) (Figure S1). The pattern of gene expression in these two lines depends on the site of transgene insertion, which is consistent with the conclusion that Lz + Ets + Su(H) can contribute to gene expression in multiple cell types, but only in combination with additional regulatory inputs.

A Short-Range, Cell Type-Specific Repressor Activity Prevents *spa* Activation in Photoreceptors

In both *spa* constructs driving strong ectopic R1/R6 activity, *spa*(KO+synth^{CS}) and *spa* (1+4+6a+synth^{CS}), the configuration of defined TFBSs differs from wild-type in two respects: their spacing relative to one another is reduced, and their linear order and position relative to the newly mapped regulatory sequences is altered. Ectopic PR expression, then, could have three possible (nonexclusive) causes: (1) tight transcription factor clustering may increase synergy by Lz and Pnt in R1/R6, or altered spacing between transcription factors and newly mapped sites may cause (2) inappropriate synergistic activation and/or (3) weakened repressive interactions in PRs. In order to test these models, and to further explore the role of enhancer structure, we generated compound mutations in multiple regions of *spa*, while keeping the spacing/arrangement of the remaining sequences intact.

First, we simultaneously mutated regions 2, 3, and 6b of *spa*, none of which are essential for cone cell expression. This construct, *spa*(m2,3,6b^{NS}), is comparable to *spa*(wt) in its pattern and levels of expression (Figure 5K). Next, we additionally mutated region 5 in this construct to create *spa*(m2,3,5,6b^{NS}). Remember that when region 5 alone is mutated, cone cell expression is severely reduced, and no ectopic expression is seen (Figures 2J and 3D). However, when region 5 is mutated simultaneously with regions 2, 3, and 6b, a discrete switch from cone cell- to R1/R6-specific expression occurs (Figure 5K). Therefore, region 5 mediates repression in PRs, in addition to activation in cone cells. This repressive activity must be redundant with additional repressor site(s) in regions 2, 3, 6b. It must also have a very limited range of action, because moving Lz and Ets sites to the 3′ end of the enhancer, without altering the repressor sites (KO+synth^{CS}), derepresses *spa* in R1/R6.

spa Enhancer Evolution: Function Is Conserved Despite Rapid Turnover of Regulatory Sequences

Taking this study and previous work into account, *spa* is among the most finely mapped enhancers with respect to regulatory sites essential for function in vivo. We made use of the recent sequencing of multiple *Drosophila* species genomes (Drosophila 12 Genomes Consortium, 2007) to investigate the evolutionary history of *spa*. We will focus on the *D. melanogaster*-*D. pseudoobscura* (*mel-pse*) comparison, which is commonly used to study *cis*-regulatory sequence evolution; the two populations diverged ~25 million years ago (e.g., Ludwig et al., 2005 and references therein). As we will discuss below, blocks of sequence conservation between *melanogaster* and *pseudoobscura spa* are relatively few and short, and most TFBSs and newly mapped regulatory sites were not alignable (Figure 6A). We were therefore surprised to find that a 409 bp *pseudoobscura* sequence we identified as the putative ortholog of *spa* was able to drive cone cell-specific reporter gene expression in transgenic *D. melanogaster*, indistinguishably in pattern and intensity from *melanogaster spa*, even from −846 bp (Figure 6B).

We wish to point out several notable aspects of *spa* sequence evolution. First, its distribution of sequence conservation appears to be unusual among developmental enhancers. When total *mel-pse* sequence identity is considered, *spa* falls only slightly below the range of six well-studied *Drosophila* enhancers we analyzed for comparison (Table S3). However, *spa* is relatively poor in extended blocks of conserved sequence; it contains only one block of 100% conservation of ≥ 10 bp in length (located in region 1, the RCE), constituting 3.9% of the total enhancer sequence. By contrast, in the six reference enhancers, an average of 52% of the sequence lies in perfectly conserved blocks of ≥ 10 bp (range is 37%–75%). Even more strikingly, in the six reference enhancers, an average of one-third of the sequence is in perfectly conserved blocks of ≥ 20 bp, and *spa* has no conserved blocks of this length (Table S3). Lack

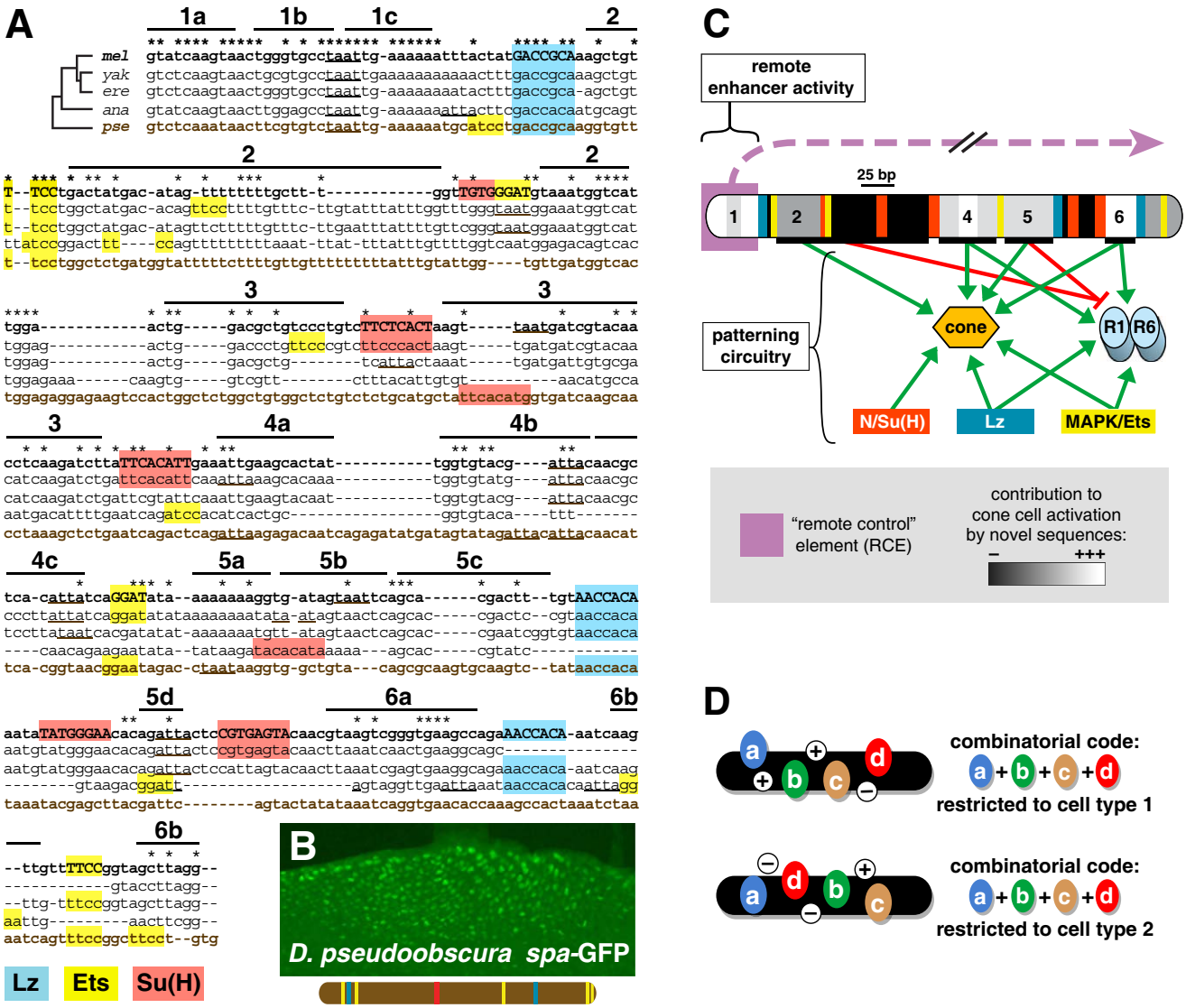

Figure 6. *spa* Enhancer Function Is Evolutionarily Conserved, Despite Rapid Sequence Divergence

(A) Alignment of the *spa* enhancer of *D. melanogaster* (*mel*) and orthologous sequences from *D. yakuba* (*yak*), *D. erecta* (*ere*), *D. ananassae* (*ana*), and *D. pseudoobscura* (*pse*). Binding sites for Lz, Pnt/Yan, and Su(H), and predicted orthologous sites, are highlighted in color. Regions 1–6 are labeled with black bars. TAAT motifs are underlined. Conserved bases are indicated with asterisks.

(B) The 409 bp *D. pseudoobscura* sequence shown in (A) drives robust cone cell-specific gene expression in eye discs of transgenic *D. melanogaster* from −846 bp.

(C) Summary of *spa* regulation: at least two functionally distinct classes of regulatory sites govern the enhancer activity of *spa* in vivo. *spa* requires the presence and proper arrangement of many regulatory subelements for its transcriptional activity and cell type specificity. Region 1 appears to be required for remote enhancer activity, but dispensable for patterning. In addition, proper cell type patterning of *spa* in the developing eye is considerably more complex than previously thought, and it depends on short-range interactions among many regulatory sites. Green arrows indicate activation mediated by sites within *spa*; red bars indicate cell type-specific repression activities.

(D) A simple "combinatorial code" model is insufficient to explain the cell-type specificity of *spa*, as the same regulatory elements can be rearranged to generate transcription in either cone cells or photoreceptors. Thus, any model describing cone cell-specific transcriptional activation by *spa* must also incorporate rules of spatial organization.

of sequence conservation does not appear to result from a reshuffling of regulatory sequences, as *melanogaster* versus *pseudoobscura* dot-plot analysis does not detect any rearrangements within *spa* (data not shown).

Second, of the 12 identified binding sites for Lz, Pnt/Yan, and Su(H), only 3 can be unambiguously aligned with orthologous predicted binding sites in *pseudoobscura*. Four other predicted binding sites for these transcription factors were found in the *pseudoobscura* enhancer, but had no definitive orthologs in *melanogaster spa*, due to significant differences in sequence and/or position (Figure 6A). Overall, *pseudoobscura spa* contains fewer predicted TFBSs than *melanogaster spa*: 1 versus 5 Su(H)

sites, 2 versus 3 Lz sites, and 5 GGAW consensus Ets sites versus 6 in *melanogaster*.

Third, with respect to the previously uncharacterized sequences within *spa*, we do not observe a strong correlation between functional significance and sequence conservation. Of the essential, previously unmapped sequences identified in this report (regions 1, 4, 5abc, and 6a), the total *mel-pse* sequence identity is not greatly higher than that of sequences making little or no contribution to activation (regions 2, 3, 5d, and 6b) (65% versus 58% identity). Thus, in the context of the *spa* enhancer, we find evolutionary sequence conservation to be a poor indicator of functional importance in transcriptional regulation.

DISCUSSION

The goal of this study was to use a well-characterized, signal-regulated developmental enhancer to examine, in fine detail, the regulatory interactions and structural rules governing transcriptional activation in vivo. Taking the elegant work of Flores and colleagues (2000) as a starting point, we have used functional in vivo assays to test the power of the proposed combinatorial code of "Notch/Su(H) + Lz + MAPK/Ets" to explain the activity and cell type specificity of the *spa* cone cell enhancer of *dPax2*. In the course of this work, we have discovered several surprising properties of *spa* that are not accounted for in current models of enhancer function.

The *spa* Patterning Code Is Massively Combinatorial

We chose the *spa* enhancer for our fine-scale analysis because (1) the known direct regulators and their binding sites are well defined, (2) they could, in theory, constitute the sum total of the patterning information received by the enhancer, and (3) the enhancer, at 362 bp, is relatively small, simplifying mutational analyses. To our surprise, a large proportion of the previously uncharacterized sequence within *spa* is vital for normal enhancer activity in vivo, and of that subset, a large proportion directly influences cell type specificity. These findings are summarized in Figure 6C.

Activation in Cone Cells

In addition to necessary inputs from Lz, Pnt, and Su(H), we have identified three segments of *spa*, regions 4, 5, and 6, that make essential contributions to gene expression in cone cells. In addition, region 2 makes a relatively minor contribution. (Region 1, another essential domain, will be discussed separately.) Fine-scale mutagenesis reveals that within regions 4, 5, and 6, very little DNA is dispensable for cone cell activation. The previously uncharacterized regulatory sites in *spa* are very likely bound by factors other than Lz/Pnt/Su(H), for the following reasons: no sequences resembling Lz/Pnt/Su(H)-binding sites reside in these regions; mutations in the newly mapped sites have different effects than removing the defined TFBSs or the proteins that bind them; doubling the known TFBSs fails to compensate for the loss of the newly mapped sequences; and, most importantly, mutating the newly mapped regulatory regions does not significantly affect binding of the known activators to nearby binding sites in vitro (Table S2). We cannot tell whether the proposed novel regulators are cone cell-specific, eye-specific, or ubiquitous in their expression—we only know that the newly mapped sites are necessary both for normal cone cell expression and ectopic PR expression. Cut, Prospero, and Tramtrack are expressed in cone cells, but are thought to act as transcriptional repressors (e.g., Lai and Li, 1999; Cook et al., 2003; Seto et al., 2006). The transcription factor Hindsight is required for *dPax2* expression and cone cell induction, but acts indirectly, activating *Delta* in R1/R6 to induce Notch signaling in cone cells (Pickup et al., 2009).

Unsurprisingly, placing the enhancer closer to the promoter boosts expression of *spa*(wt), as well as some of the impaired mutants (Figure 4). Remember that *spa* is located at +7 kb in its native locus, and that nearly all mutational studies place the enhancer immediately upstream of the promoter. If our entire analysis had been performed at −121 bp, we would have underrated the functional significance of several critical regulatory sequences, and would have dismissed region 1 entirely as nonregulatory DNA. Other well-characterized enhancers, which have been analyzed in a promoter-proximal position only, may therefore contain more critical regulatory sites than is currently realized.

Like many transcriptional activators, all three known direct activators of *spa* (or their orthologs) recruit p300/CBP histone acetyltransferase coactivator complexes (e.g., Kitabayashi et al., 1998; Barolo and Posakony, 2002). Doubling the number of binding sites for these transcription factors (to 6 Lz, 8 Ets, and 10 Su(H) sites) does not suffice to drive cone cell expression in the absence of the newly mapped regulatory regions (Figure 5). It may be, then, that factors recruited to the newly mapped regulatory sites within *spa* employ mechanisms that are distinct from those of the known activators. The remote activity of *spa*, mediated by region 1, appears to be an example of such a mechanism.

Cell Type Specificity

We were able to convert *spa* into a R1/R6-specific enhancer in three ways: (1) by moving the defined TFBSs to one side of the enhancer in a tight cluster; (2) by placing Lz and Ets sites next to regions 1, 4, and 6a; and (3) by mutating regions 2, 3, 5, and 6b within *spa* while maintaining the native spacing of all other sites. From these experiments, we conclude that *spa* contains short-range repressor sites that prevent ectopic activation in PRs by Lz + Pnt + regions 4 + 6a. *spa* contains at least two redundant repressor sites, because both region 5 and regions 2, 3, and 6b must be mutated to attain ectopic R1/R6 expression.

klumpfuss, which encodes a putative transcriptional repressor, is directly activated by Lz in R1/R6/R7, but is also present in cone cells (Wildonger et al., 2005, and references therein), making it an unlikely repressor of *spa*. *seven-up*, another known transcriptional repressor, is expressed in R3/R4/R1/R6 and could therefore act to repress *spa* in PRs (Mlodzik et al., 1990; Cooney et al., 1993). However, we did not identify putative Seven-up-binding sites within *spa*. Phyllopod, an E3 ubiquitin ligase component, represses *dPax2* and the cone cell fate in R1/R6/R7, but the transcription factor mediating this effect is not yet known (Shi and Noll, 2009). Perhaps the best candidate for a PR-specific direct repressor of *spa* is *Bar*, which encodes the closely related and redundant homeodomain transcription factors BarH1 and BarH2. *Bar* expression is activated by Lz in R1/R6 and is required for R1/R6 cell fates (Higashijima et al., 1992; Crew et al., 1997). Furthermore, misexpression of *BarH1*

in presumptive cone cells can transform them into PRs (Hayashi et al., 1998). It is unclear whether Bar-family proteins act as repressors, activators, or both. BarH1/2 can bind sequences containing the homeodomain-binding core consensus TAAT (Noyes et al., 2008), and region 5 of *spa* contains two TAAT motifs (underlined in Figure 6A). Future studies will explore the possibility that Bar directly represses *spa* in PRs.

The combinatorial code of *spa*, then, requires multiple inputs in addition to Lz, MAPK/Ets, and Notch/Su(H). Indeed, our data suggest that the known regulators can contribute to expression in multiple cell types, depending on context. The newly mapped control elements we have identified within *spa* are necessary not only to facilitate transcriptional activation, but also to steer the Lz + Ets + Su(H) code toward cone cell-specific gene expression.

Functional Evidence for a Special Enhancer Regulatory Element, Mediating Remote Interactions, but Not Patterning

Enhancers are often located many kilobases from the promoters they regulate. Enhancer-promoter interactions over such distances are very likely to require active facilitation (Rippe, 2001). Even so, few studies have focused specifically on transcriptional activation at a distance, and the majority of this work involves locus control regions (LCRs) and/or complex multigenic loci, which are not part of the regulatory environment of most genes and enhancers (e.g., Yoshida et al., 1999; Carter et al., 2002; Song et al., 2007). Like *spa*, many developmental enhancers act at a distance in their normal genomic context, yet can autonomously drive a heterologous promoter in the proper expression pattern, without requiring an LCR or other large-scale genomic regulatory apparatus. However, in nearly all assays of enhancer function, the element to be studied is placed immediately upstream of the promoter. In such cases, regulatory sites specifically mediating remote interactions cannot be identified. Because our initial mutational analysis of *spa* was performed on enhancers placed at a moderate distance from the promoter (−846 bp), we were able to screen for sequences required *only* at a distance, by moving crippled enhancers to a promoter-proximal position. Only one segment of *spa*, region 1, was absolutely essential at a distance but completely dispensable near the promoter. This region, which contains the only block of extended sequence conservation within *spa*, plays no apparent role in patterning, or in basic activation at close range. We therefore call this segment of *spa* a "remote control" element (RCE).

The remote enhancer regulatory activity described here differs from previously reported long-range regulatory mechanisms in two important ways. First, the remote function of *spa* does not require any sequences in or near the *dPax2* promoter. This functionally distinguishes *spa* from enhancers in the *Drosophila* Hox complexes that require promoter-proximal "tethering elements" and/or function by overcoming insulators (e.g., Calhoun et al., 2002; Chen et al., 2005; Akbari et al., 2008). This distal activation mechanism also likely differs from enhancer-promoter interactions mediated by proteins that bind at both the enhancer and the promoter, as occurs in looping mediated by ER, AR, and Sp1 (Wang et al., 2005; Williams et al., 2007; Pan et al., 2008). Second, studies of distant enhancers of the *cut* and *Ultrabithorax* genes have revealed a role for the cohesin-associated factor Nipped-B, especially with respect to bypassing insulators (Misulovin et al., 2008, and references therein), but it has not been demonstrated that Nipped-B, or any other enhancer-binding regulator, is required *only* when the enhancer is remote.

To our knowledge, the *spa* RCE is the first enhancer subelement demonstrated to be essential for enhancer-promoter interactions at a distance, but unnecessary for proximal enhancer function and cell type specificity. However, the present work contains only a limited examination of this activity, as part of a broader study of enhancer function. We are currently extending these functional studies, testing for potential promoter preferences and distance limitations, and pursuing the identities of factors binding to the RCE.

Enhancer Structure: Shaped and Constrained by Short-Range Patterning Interactions

As discussed above, it is fairly easy to switch *spa* from cone cell expression to R1/R6 expression (though, curiously, we have yet to generate a construct that is active in both cell types). Our results show that multiple regions of *spa* mediate a repression activity in R1/R6, but not in cone cells. We further conclude that these *spa*-binding repressors act in a short-range manner; that is, they must be located very near to relevant activator-binding sites, because moving Lz and Pnt sites to one side of *spa*, without removing the repressor sites (KO+synth^{CS}), abolishes repression. Despite this failure of repression, synergistic interactions among Lz and Ets sites and the newly mapped sites still occur in this reorganized enhancer—at least in R1/R6 cells. Cone cell-specific expression is lost, however, revealing (along with other experiments) that transcriptional activation in cone cells is highly sensitive to the organization of regulatory sites within *spa*. Slightly wider spacing of regulatory sites (KO+synth^{NS}) kills the enhancer altogether, suggesting that synergistic positive interactions within *spa*, though apparently longer in range than repressive interactions, are severely limited in their range. The structural organization of *spa*, then, appears to be constrained by a complex network of short-range positive and negative interactions (Figure 6D). Activator sites must be spaced closely enough to trigger synergistic activation in cone cells; at the same time, repressor sites must be positioned to disrupt this synergy in noncone cells, preventing ectopic activation.

Recent work by Crocker et al. (2008) has shown that changes to enhancer organization can "fine-tune" the output of a combinatorial code, subtly changing the sensitivity of the enhancer to a morphogen. Given the importance of the structure of the *spa* enhancer for its proper function, we propose that *any* combinatorial code model, no matter how complex, is insufficient to describe the regulation of *spa*, because the same components can be rearranged to produce drastically different patterns.

Conservation of *spa* Function Despite Lack of Sequence Conservation: Insights into Enhancer Structure

One might expect that the regulatory and organizational complexity of the *spa* enhancer, and its extreme sensitivity to mutation, would be reflected in strict evolutionary constraints upon enhancer sequence and structure. Yet, we observe very poor conservation of *spa* sequence, both in the known TFBSs and in most of the newly mapped essential regulatory elements.

The reduced presence of Lz/Ets/Su(H) sites in *D. pse* could potentially be attributed to redundancy of those sites in *D. mel*, or to compensatory gain of binding sites for alternate factors in the *D. pse* enhancer. Perhaps more difficult to understand is the apparent loss of critical regulatory sequences in regions 4, 5, and 6a in *D. pse*; our experiments in *D. mel* suggest that the absence of those inputs would result in loss of cone cell expression and/or ectopic activation. It remains possible that many of these inputs are in fact conserved, but that conservation is not obvious due to binding site degeneracy and/or rearrangement of elements within the enhancer. Fine-scale comparative studies are ongoing.

spa is by no means the first example of an enhancer that is functionally maintained despite a lack of sequence conservation (for a review of this topic, see Wittkopp, 2006). The most thoroughly characterized example of this phenomenon is the *eve* stripe 2 enhancer; its function is conserved despite changes in binding site composition and organization (Ludwig et al., 2000, 2005; Hare et al., 2008). Note, however, that *spa* has undergone much more rapid sequence divergence than *eve* stripe 2 (Figure 6; Table S3), with no apparent change in function. In general, the ability of an enhancer to maintain its function in the face of rapid sequence evolution suggests that enhancer structure must be quite flexible. These observations support the "billboard" model of enhancer structure, which proposes that as long as individual regulatory units within an enhancer remain intact, the organization of those units within the enhancer is flexible (Arnosti and Kulkarni, 2005). Yet, our findings concerning the importance of local interactions among densely clustered, precisely positioned transcription factors are more consistent with the tightly structured "enhanceosome" model (Thanos and Maniatis, 1995). Further structure-function analysis will be necessary to fully understand the players and rules governing this regulatory element.

EXPERIMENTAL PROCEDURES

Generation of Enhancer Constructs

The 362 bp *sparkling* enhancer was amplified from w^{1118} genomic DNA with the following primers: 5′-CACCGGATCCgtatcaagtaactgggtgcctaattg-3′; 5′-GGGTCTAGAcctaagctaccggaaaacaacttg-3′. The 409 bp *D. pseudoobscura spa* enhancer was PCR amplified from genomic DNA with the following primers: 5′-CACCGGATCCgtctcaaataacttcgtgtc-3′; 5′-GGGTCTAGAcacaggaagccggaaactg-3′. The lower-case sequence is homologous to genomic DNA.

Most mutant *spa* constructs were generated by one of three PCR techniques: (1) amplification of *spa*(wt) with tagged primers to create mutations at the 5′ or 3′ end; (2) overlap extension (sewing) PCR to generate internal mutations; or (3) assembly PCR to synthesize enhancers with multiple mutations. See Supplemental Experimental Procedures for complete sequences of all enhancer constructs.

Mutagenesis by Overlap Extension PCR

When targeting mutations in the interior of *spa*, such as in constructs m4A, m4-rs, etc., we separately amplified 5′ and 3′ fragments, by using overlapping tagged primers to integrate mutated sequence, and then joined the fragments by using overlap extension (sewing) PCR (Swanson et al., 2008 and references therein). In our sewing PCR protocol, the 5′ and 3′ fragments (which overlap by 20 bp) were separately PCR amplified and gel purified. We combined 3 μl of each gel-purified fragment with 33.5 μl water, 1.5 μl 10 μm dNTPs, and 5 μl 10× PCR buffer (Roche Expand High Fidelity PCR System). This mix was incubated at 90°C for 10 min, then cooled one degree per min to 72°C. A total of 1 μl polymerase mix (Roche Expand High Fidelity PCR System) was then added, followed by incubation for 10 min at 72°C. Finally, 1.5 μl of each flanking 5′ and 3′ primer (15 pmol each) was added, and the full-length construct was amplified in our standard PCR program (94°C for 2 min; 10 cycles of 94°C for 15 s, 55°C for 30 s, 72°C for 45 s; 20 cycles of 94°C for 15 s, 55°C for 30 s, 72°C for 45 s + 5 s/cycle; 72°C for 7 min).

Assembly PCR

In constructs with extensive mutated sequence (such as *spa*(mut) and *spa*(synth)), constructs were built by annealing overlapping 40 bp oligonucleotides to create the full-length construct by assembly PCR (Swanson et al., 2008 and references therein). We combined 2.5 μl of each flanking primer (10 μM), 1 μl internal primer mix (each primer at 0.25 μM), 1 μl 10 μM dNTPs, and 18 μl sterile water in the template mix. The enzyme mix contained 19.25 μl sterile water, 5 μl 10× PCR buffer, and 0.75 μl DNA polymerase (Roche Expand High Fidelity PCR System). The template mix and enzyme mix were combined immediately before amplification in our standard PCR program (see above).

In mutating previously uncharacterized enhancer sequences, we made noncomplementary transversions to every other base pair. We left 2–4 bp of nonmutated sequence to either side of every TFBS (as defined by consensus sequences), to avoid interfering with transcription factor binding. In mutating TFBSs, we converted Lz sites from RACCRCA to RA**AA**RCA; Ets sites from GGAW to **TT**AW; and Su(H) sites from YGTGDGAA (or related sequence) to YGTGD**C**AA; these changes eliminate transcription factor binding in vitro (Barolo et al., 2000; Flores et al., 2000; references therein).

Enhancer Cloning, Vectors, and Transgenesis

PCR-amplified enhancer constructs were TOPO cloned into the pENTR/D-TOPO vector (Invitrogen). *spa*(synth^{CS}) was created by annealing two complementary oligonucleotides and ligating them into the Gateway donor vector pBS-ENTR-TOPO (Swanson et al., 2008). Subcloned constructs were then Gateway cloned into the Ganesh-G1 GFP reporter vector (Swanson et al., 2008) via LR recombination (Invitrogen), with the following exception: constructs placed at −121 bp from the promoter (Figure 4) were Gateway cloned into Ganesh-G2, which lacks the 0.7 kb spacer sequence between the recombination cloning site and the promoter (Swanson et al., 2008). P element transformation was performed essentially as described by Rubin and Spradling (1982). w^{1118} flies were used for transgenesis.

Tissue Preparation, Staining, and Microscopy

Eye tissues were dissected from transgenic third-instar larvae or 24 hr pupae and fixed in 4% formaldehyde in PBS for 30 min at room temperature. For larval imaginal discs, GFP fluorescence was imaged with an Olympus BX51 microscope and an Olympus DP70 digital camera. Pupal eyes were stained with antibodies to GFP (see below) and imaged with an Olympus IX71 inverted microscope and an Olympus FV500 confocal system. The primary antibodies used included rabbit anti-EGFP (a gift from B. Novitch), diluted 1:100; mouse anti-Cut 2B10 (a gift from K. Cadigan), diluted 1:100; mouse anti-Elav 9F8A9 (Developmental Studies Hybridoma Bank), diluted 1:100.

DNA Sequence Alignment

The *sparkling* multispecies alignment is based on BLASTZ alignments and was taken from the University of California, Santa Cruz genome browser (http://genome.ucsc.edu). Pairwise *mel-pse* enhancer alignments were performed with zPicture (Ovcharenko et al., 2004 [http://zpicture.dcode.org]).

SUPPLEMENTAL INFORMATION

Supplemental Information includes Experimental Procedures (including annotated sequences of all enhancer constructs), one figure, and three tables and can be found with this article online at doi:10.1016/j.devcel.2009.12.026.

ACKNOWLEDGMENTS

This research was supported in part by a Center for Organogenesis Training Grant (5T32HD007505) to C.I.S. and by National Institutes of Health grant GM076509 to S.B. We thank Ying Zhao, Lisa Johnson, Andy Vo, Zeeshaan Bhatti, Iehsus Flores-Pérez, and Trish Hinrichs for research support, and Ben Novitch and Ken Cadigan for sharing reagents. We are grateful to the following people for helpful discussions: Ken Cadigan, Tim Blauwkamp,

Deneen Wellik, Ben Novitch, Doug Engel, Tom Glaser, Trisha Wittkopp, Jim Posakony, Billy Tsai, Albert Erives, Robert Drewell, and many members of the lab.

Received: April 22, 2008
Revised: September 27, 2009
Accepted: December 27, 2009
Published: March 15, 2010

REFERENCES

Akbari, O.S., Bae, E., Johnsen, H., Villaluz, A., Wong, D., and Drewel, R.A. (2008). A novel promoter-tethering element regulates enhancer-driven gene expression at the bithorax complex in the *Drosophila* embryo. Development *135*, 123–131.

Arnosti, D.N., and Kulkarni, M.M. (2005). Transcriptional enhancers: intelligent enhanceosomes or flexible billboards? J. Cell. Biochem. *94*, 890–898.

Barolo, S., and Posakony, J.W. (2002). Three habits of highly effective signaling pathways: principles of transcriptional control by developmental cell signaling. Genes Dev. *16*, 1167–1181.

Barolo, S., Walker, R.G., Polyanovsky, A., Freschi, G., Keil, T., and Posakony, J.W. (2000). A Notch-independent activity of Suppressor of Hairless is required for normal mechanoreceptor physiology. Cell *103*, 957–969.

Behan, K.J., Fair, J., Singh, S., Bogwitz, M., Perry, T., Grubor, V., Cunningham, F., Nichols, C.D., Cheung, T.L., Batterham, P., and Pollock, J.A. (2005). Alternative splicing removes an Ets interaction domain from Lozenge during Drosophila eye development. Dev. Genes Evol. *215*, 423–435.

Calhoun, V.C., Stathopoulos, A., and Levine, M. (2002). Promoter-proximal tethering elements regulate enhancer-promoter specificity in the *Drosophila Antennapedia* complex. Proc. Natl. Acad. Sci. USA *99*, 9243–9247.

Carter, D., Chakalova, L., Osborne, C.S., Dai, Y.F., and Fraser, P. (2002). Long-range chromatin regulatory interactions in vivo. Nat. Genet. *32*, 623–626.

Chen, Q., Lin, L., Smith, S., Lin, Q., and Zhou, J. (2005). Multiple promoter targeting sequences exist in *Abdominal-B* to regulate long-range gene activation. Dev. Biol. *286*, 629–636.

Cook, T., Pichaud, F., Sonneville, R., Papatsenko, D., and Desplan, C. (2003). Distinction between color photoreceptor cell fates is controlled by Prospero in *Drosophila*. Dev. Cell *4*, 853–864.

Cooney, A.J., Leng, X., Tsai, S.Y., O'Malley, B.W., and Tsai, M. (1993). Multiple mechanisms of Chicken Ovalbumin Upstream Promoter Transcription Factor-dependent repression of transactivation by the vitamin D, thyroid hormone, and retinoic acid receptors. J. Biol. Chem. *268*, 4152–4160.

Crew, J.R., Batterham, P., and Pollock, J.A. (1997). Developing compound eye in *lozenge* mutants of *Drosophila*: *lozenge* expression in the R7 equivalence group. Dev. Genes Evol. *206*, 481–493.

Crocker, J., Tamori, Y., and Erives, A. (2008). Evolution acts on enhancer organization to fine-tune gradient threshold readouts. PLoS Biol. *6*, e263.

Davidson, E.H. (1999). A view from the genome: spatial control of transcription in sea urchin development. Curr. Opin. Genet. Dev. *9*, 530–541.

Drosophila 12 Genomes Consortium. (2007). Evolution of genes and genomes on the Drosophila phylogeny. Nature *450*, 203–218.

Flores, G.V., Duan, H., Yan, H., Nagaraj, R., Fu, W., Zou, Y., Noll, M., and Banerjee, U. (2000). Combinatorial signaling in the specification of unique cell fates. Cell *103*, 75–85.

Fu, W., and Noll, M. (1997). The *Pax2* homolog *sparkling* is required for development of cone and pigment cells in the *Drosophila* eye. Genes Dev. *11*, 2066–2078.

Fu, W., Duan, H., Frei, E., and Noll, M. (1998). *shaven* and *sparkling* are mutations in separate enhancers of the *Drosophila Pax2* homolog. Development *125*, 2943–2950.

Hare, E.E., Peterson, B.K., Iyer, V.N., Meier, R., and Eisen, M.B. (2008). Sepsid *even-skipped* enhancers are functionally conserved in *Drosophila* despite lack of sequence conservation. PLoS Genet. *4*, e1000106.

Hayashi, T., Kojima, T., and Saigo, K. (1998). Specification of primary pigment cell and outer photoreceptor fates by *BarH1* homeobox gene in the developing *Drosophila* eye. Dev. Biol. *200*, 131–145.

Higashijima, S., Kojima, T., Michiue, T., Ishimaru, S., Emori, Y., and Saigo, K. (1992). Dual *Bar* homeo box genes of *Drosophila* required in two photoreceptor cells, R1 and R6, and primary pigment cells for normal eye development. Genes Dev. *6*, 50–60.

Kitabayashi, I., Yokoyama, A., Shimizu, K., and Ohki, M. (1998). Interaction and functional cooperation of the leukemia-associated factors AML1 and p300 in myeloid cell differentiation. EMBO J. *17*, 2994–3004.

Lai, Z.C., and Li, Y. (1999). Tramtrack69 is positively and autonomously required for *Drosophila* photoreceptor development. Genetics *152*, 299–305.

Ludwig, M.Z., Bergman, C., Patel, N.H., and Kreitman, M. (2000). Evidence for stabilizing selection in a eukaryotic enhancer element. Nature *403*, 564–567.

Ludwig, M.Z., Palsson, A., Alekseeva, E., Bergman, C.M., Nathan, J., and Kreitman, M. (2005). Functional evolution of a *cis*-regulatory module. PLoS Biol. *3*, e93.

Misulovin, Z., Schwartz, Y.B., Li, X.Y., Kahn, T.G., Gause, M., Macarthur, S., Fay, J.C., Eisen, M.B., Pirrotta, V., Biggin, M.D., and Dorsett, D. (2008). Association of cohesin and Nipped-B with transcriptionally active regions of the *Drosophila melanogaster* genome. Chromosoma *117*, 89–102.

Mlodzik, M., Hiromi, Y., Weber, U., Goodman, C.S., and Rubin, G.M. (1990). The *Drosophila seven-up* gene, a member of the Steroid Receptor gene superfamily, controls photoreceptor cell fates. Cell *60*, 211–224.

Nagaraj, R., and Banerjee, U. (2007). Combinatorial signaling in the specification of primary pigment cells in the *Drosophila* eye. Development *134*, 825–831.

Noyes, M.B., Christensen, R.G., Wakabayashi, A., Stormo, G.D., Brodsky, M.H., and Wolfe, S.A. (2008). Analysis of homeodomain specificities allows the family-wide prediction of preferred recognition sites. Cell *133*, 1277–1289.

Ovcharenko, I., Loots, G.G., Hardison, R.C., Miller, W., and Stubbs, L. (2004). zPicture: dynamic alignment and visualization tool for analyzing conservation profiles. Genome Res. *14*, 472–477.

Pan, Y.F., Wansa, K.D.S.A., Liu, M.H., Zhao, B., Hong, S.Z., Tan, P.Y., Lim, K.S., Bourque, G., Liu, E.T., and Cheung, E. (2008). Regulation of Estrogen Receptor-mediated long range transcription via evolutionarily conserved distal response elements. J. Biol. Chem. *283*, 32977–32988.

Pickup, A.T., Ming, L., and Lipshitz, H.D. (2009). Hindsight modulates Delta expression during *Drosophila* cone cell induction. Development *136*, 975–982.

Rippe, K. (2001). Making contacts on a nucleic acid polymer. Trends Biochem. Sci. *26*, 733–740.

Robinow, S., and White, K. (1988). The locus *elav* of *Drosophila melanogaster* is expressed in neurons at all developmental stages. Dev. Biol. *126*, 294–303.

Rubin, G.M., and Spradling, A.C. (1982). Genetic transformation of *Drosophila* with transposable element vectors. Science *218*, 348–353.

Seto, H., Hayashi, Y., Kwon, E., Taguchi, O., and Yamaguchi, M. (2006). Antagonistic regulation of the *Drosophila* PCNA gene promoter by DREF and Cut. Genes Cells *11*, 499–512.

Shi, Y., and Noll, M. (2009). Determination of cell fates in the R7 equivalence group of the *Drosophila* eye by the concerted regulation of D-Pax2 and TTK88. Dev. Biol. *331*, 68–77.

Song, S.H., Hou, C., and Dean, A. (2007). A positive role for NLI/Ldb1 in long-range β-globin locus control region function. Mol. Cell *28*, 810–822.

Swanson, C.I., Hinrichs, T., Johnson, L.A., Zhao, Y., and Barolo, S. (2008). A directional recombination cloning system for restriction- and ligation-free construction of GFP, DsRed, and lacZ transgenic *Drosophila* reporters. Gene *408*, 180–186.

Thanos, D., and Maniatis, T. (1995). Virus induction of human IFN β gene expression requires the assembly of an enhanceosome. Cell *83*, 1091–1100.

Tsuda, L., Nagaraj, R., Zipursky, S.L., and Banerjee, U. (2002). An EGFR/Ebi/Sno pathway promotes delta expression by inactivating Su(H)/SMRTER repression during inductive Notch signaling. Cell *110*, 625–637.

Voas, M.G., and Rebay, I. (2004). Signal integration during development: insights from the *Drosophila* eye. Dev. Dyn. *229*, 162–175.

Wang, Q., Carroll, J.S., and Brown, M. (2005). Spatial and temporal recruitment of androgen receptor and its coactivators involves chromosomal looping and polymerase tracking. Mol. Cell *19*, 631–642.

Wildonger, J., Sosinsky, A., Honig, B., and Mann, R.S. (2005). Lozenge directly activates *argos* and *klumpfuss* to regulate programmed cell death. Genes Dev. *19*, 1034–1039.

Williams, A.O., Isaacs, R.J., and Stowell, K.M. (2007). Down-regulation of human topoisomerase IIα expression correlates with relative amounts of specificity factors Sp1 and Sp3 bound at proximal and distal promoter regions. BMC Mol. Biol. *8*, 36.

Wittkopp, P.J. (2006). Evolution of *cis*-regulatory sequence and function in Diptera. Heredity *97*, 139–147.

Yoshida, C., Tokumasu, F., Hohmura, K.I., Bungert, J., Hayashi, N., Nagasawa, T., Engel, J.D., Yamamoto, M., Takeyasu, K., and Igarashi, K. (1999). Long range interaction of *cis*-DNA elements mediated by architectural transcription factor Bach1. Genes Cells *4*, 643–655.

Cell, Vol. 103, 75–85, September 29, 2000, Copyright ©2000 by Cell Press

Combinatorial Signaling in the Specification of Unique Cell Fates

Gail V. Flores,[1,7] Hong Duan,[2,5,7] Huajun Yan,[1,7] Raghavendra Nagaraj,[1,7] Weimin Fu,[2,6] Yu Zou,[2] Markus Noll,[2] and Utpal Banerjee[1,3,4]

[1] Department of Molecular, Cell, and Developmental Biology and Molecular Biology Institute
University of California at Los Angeles
Los Angeles, California 90095

[2] Institute for Molecular Biology
University of Zürich
CH-8057 Zürich
Switzerland

[3] Department of Biological Chemistry and Department of Human Genetics
University of California at Los Angeles
Los Angeles, California 90095

Summary

How multifunctional signals combine to specify unique cell fates during pattern formation is not well understood. Here, we demonstrate that together with the transcription factor Lozenge, the nuclear effectors of the EGFR and Notch signaling pathways directly regulate *D-Pax2* transcription in cone cells of the *Drosophila* eye disc. Moreover, the specificity of *D-Pax2* expression can be altered upon genetic manipulation of these inputs. Thus, a relatively small number of temporally and spatially controlled signals received by a set of pluripotent cells can create the unique combinations of activated transcription factors required to regulate target genes and ultimately specify distinct cell fates within this group. We expect that similar mechanisms may specify pattern formation in vertebrate developmental systems that involve intercellular communication.

Introduction

How individual cells within an initially equivalent group acquire a multitude of distinct fates is a fundamental question in developmental biology. Understanding the interplay between intercellular signals and the context in which they are interpreted is the focus of this study. During *Drosophila* eye development, undifferentiated cells are patterned to yield ~800 facets, called ommatidia. Each ommatidium is comprised of eight photoreceptor neurons (R1–R8), four nonneuronal cone cells, three classes of pigment cells, and a bristle complex. Eye morphogenesis initiates during the third larval instar of development as a morphogenetic furrow sweeps across the disc from posterior to anterior (Ready et al., 1976). Cells within the furrow arrest in the G1 phase of the cell cycle (Wolff and Ready, 1991). These cells either emerge from the furrow as five-cell preclusters of R2–R5 and R8, or they undergo a synchronized round of mitosis that creates a new pool of undifferentiated precursors. In a second phase of morphogenesis, these new precursors are recruited into the developing ommatidia as R1, R6, R7, cone, pigment, and bristle cells (Ready et al., 1976; Wolff and Ready, 1991). This study investigates the molecular mechanisms that regulate pattern formation during this second phase of morphogenesis.

Early pioneering work (Ready et al., 1976; Lawrence and Green, 1979; Tomlinson and Ready, 1987) and later molecular analysis (reviewed by Zipursky and Rubin, 1994; Freeman, 1997) showed that the recruitment of ommatidial cells follows a nonclonal mechanism involving extensive cell–cell interactions. The Sevenless (Sev) receptor tyrosine kinase (RTK) signaling cascade was identified as a pathway involved in the determination of a single cell type, R7. This initially suggested that each cell type in the eye may be specified by its own unique signaling mechanism. However, it was later shown that Sev can induce a non-R7 fate when activated in other cells (Dickson et al., 1992), or when the R7 precursor ectopically expresses a transcription factor that specifies R2/R5 fate (Basler et al., 1990; Kimmel et al., 1990). Conversely, an activated version of another RTK, epidermal growth factor receptor (EGFR), can direct an R7 fate in the absence of Sev (Freeman, 1996). These results indicate that while the Sev signal is required as a triggering event in the differentiation of R7, the cell's identity is specified by other mechanisms.

Another signaling cascade, initiated by EGFR, plays many roles during eye morphogenesis. EGFR signaling causes inactivation of the ETS domain repressor Yan and activation of the ETS domain transcriptional activator PntP2 (Brunner et al., 1994; O'Neill et al., 1994; Rebay and Rubin, 1995). In addition to its requirement for the differentiation of all cell types in the eye (Freeman, 1996; Tio and Moses, 1997), the EGFR signal is essential for proper furrow initiation, proliferation, spacing, recruitment, and survival of cells in the eye disc (Baker and Rubin, 1989, 1992; Xu and Rubin, 1993; Freeman, 1996; Tio and Moses, 1997; Domínguez et al., 1998; Kumar et al., 1998; Lesokhin et al., 1999). While the EGFR signal has classically been considered instructive, this multitude of functions suggests that on its own, this pathway does not bear any fate-specifying information.

The Notch (N) signaling pathway also plays many roles in eye development through its activation of the transcription factor Suppressor of Hairless [Su(H)] (reviewed by Artavanis-Tsakonas et al., 1999). This pathway is required for the proper temporal acquisition of several cell fates in the eye (Cagan and Ready, 1989; Fortini et al., 1993), and also functions in proliferation, dorsal–ventral axis establishment, and ommatidial polarity (Domínguez and de Celis, 1998; Go et al., 1998; Papayannopoulos et al., 1998; Cooper and Bray, 1999; Fanto and Mlodzik, 1999). This variety of functions led to the characterization of N as a permissive signal and suggests that, like EGFR and Sev, the N signal alone cannot

[4] To whom correspondence should be addressed (e-mail: banerjee@mbi.ucla.edu).

[5] Present address: Department of Medicine, Division of Cardiology, Albert Einstein College of Medicine, Bronx, NY 10461.

[6] Present address: Department of Neurology, Northwestern University, Chicago, IL 60611.

[7] These authors contributed equally to this work.

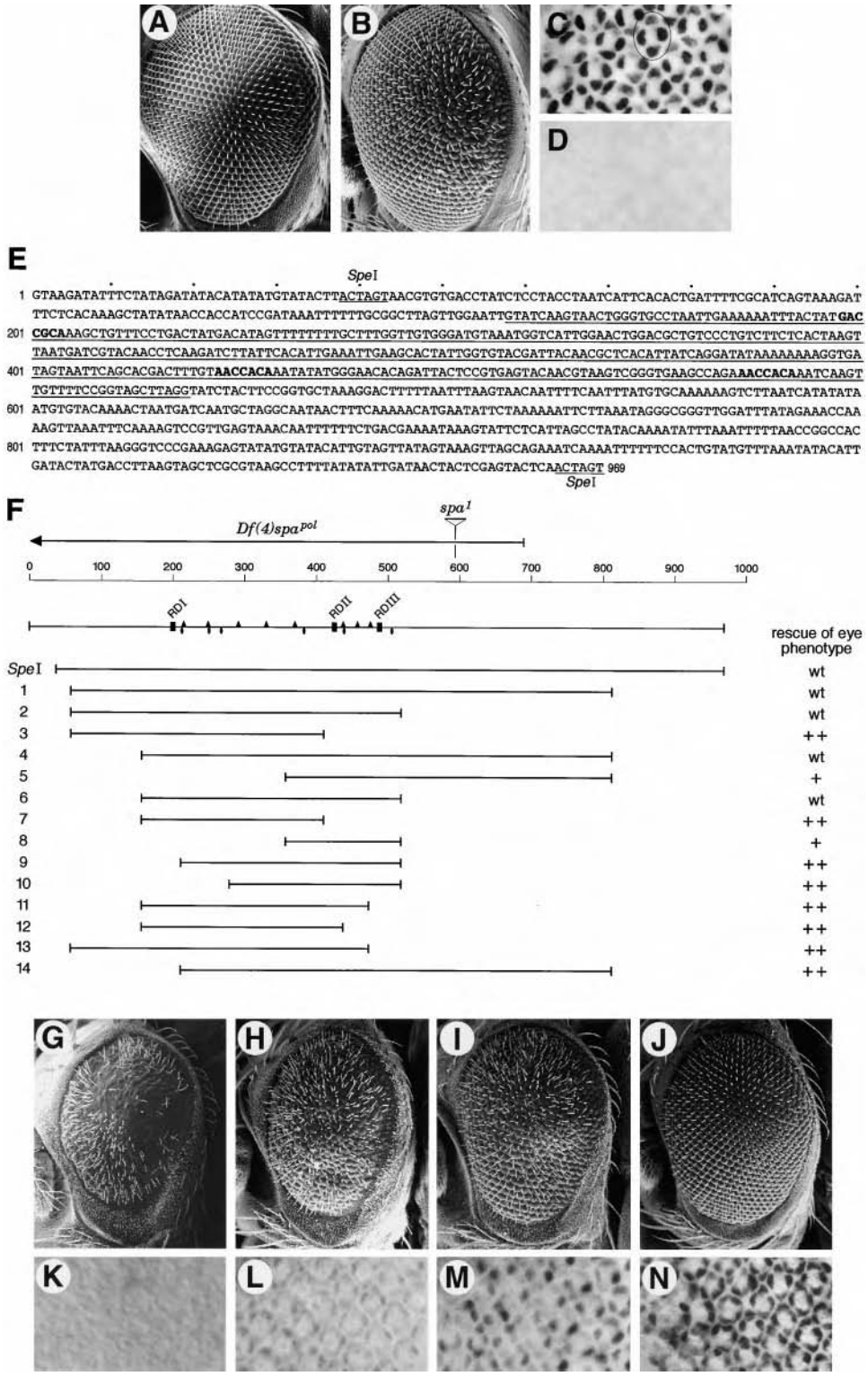

Figure 1. Identification of the Minimal *D-Pax2* Eye-Specific Enhancer and its Potential Lz/Runt Domain Binding Sites

Scanning electron micrographs (SEM) of adult eyes (A, B, and G–J) and immunolocalization of D-Pax2 in late third-instar larval eye discs (C, D, and K–N).

(A) lz^{ts1}/Y flies raised at 25°C. The eye phenotype is wild type.

(B) lz^{ts1}/Y; spa^{pol}/+ flies raised at 25°C. The eye-specific mutation spa^{pol} of *D-Pax2* dominantly enhances the lz^{ts1} phenotype.

(C) Wild type. D-Pax2 is expressed in four cone cell precursors per ommatidium (one example is circled).

(D) lz^{r1}. Note complete loss of D-Pax2 expression in cone cell precursors in this null *lz* allele.

(E) Sequence of *D-Pax2* that includes the eye-specific enhancer at the 5′ end of intron 4. The sequence begins with the splice donor site of

provide the unique information that is necessary to determine a specific cell fate. Each of these signaling cascades must therefore act as a trigger allowing a cell to choose one of several possible fates.

A panoply of transcription factors is expressed in specific cell types in the larval eye disc (reviewed by Freeman, 1997; Kumar and Moses, 1997). During the second phase of recruitment posterior to the furrow, Bar is expressed in R1/R6 (Higashijima et al., 1992), Prospero (Pros) in R7 and cone cells (Kauffmann et al., 1996), and D-Pax2 in cone and primary pigment cells (Fu and Noll, 1997). Combinations of such cell-specific transcription factors ultimately create the differences between cell types. However, their cell-specific expression patterns suggest that the initial discrimination between cell types is established prior to the onset of their expression. To understand cell fate specification, it is therefore important to elucidate the mechanisms involved in generating the unique expression patterns of these proteins. This was lacking in previous studies because controlling regions of these transcription factors had not yet been deciphered.

A first step toward unraveling cell fate specification mechanisms during the second phase of morphogenesis in the eye was the identification of the *lozenge* (*lz*) gene (Daga et al., 1996), which encodes a Runt Domain–containing transcription factor that shares sequences with *Drosophila* Runt and human AML1 (*A*cute *M*yeloid *L*eukemia 1), CBFA1, and CBFA3 (reviewed by Bae and Ito, 1999). Lz regulates the expression of all known cell-specific transcription factors expressed during the second phase of morphogenesis. In *lz* mutants, Bar (Daga et al., 1996; Crew et al., 1997), Pros (Xu et al., 2000 [this issue of *Cell*]), and D-Pax2 (this study) are not expressed, and Seven-up is ectopically expressed in R7 and cone cells (Daga et al., 1996; Crew et al., 1997). Since Lz is expressed in the entire pool of undifferentiated precursor cells posterior to the morphogenetic furrow (Flores et al., 1998), it remained unclear how it causes its target genes to be expressed in a cell-specific manner. Here, we describe results in support of a model for cell fate specification. Its salient feature is the combinatorial use by a cell of a small number of multifunctional signaling pathways controlling the activity of specific transcription factors to activate specific target genes at the appropriate time in development.

Results

Lozenge Directly Regulates *D-Pax2* Expression in Cone Cell Precursors

D-Pax2 is the *Drosophila* homolog of the vertebrate *Pax2* gene (Fu and Noll, 1997; Czerny et al., 1997). This locus is represented by at least two classes of mutant alleles, *shaven* (*sv*) and *sparkling* (*spa*) (Fu et al., 1998; Kavaler et al., 1999). *spa* mutants show cone cell defects resulting from mutations in the fourth intron of the gene, which led to the identification of a 926 bp SpeI fragment within this intron that includes the eye-specific enhancer (Fu and Noll, 1997) (Figure 1F). When combined with its promoter and coding region, this fragment restores wild-type D-Pax2 expression in cone cell precursors of *spa* mutants and rescues the *spa* eye phenotype (Fu et al., 1998).

Enhancement of *lz* eye phenotypes by *spa* alleles has been observed previously (Lindsley and Zimm, 1992; Gupta and Rodrigues, 1995). In addition, two new *spa* alleles were isolated as enhancers of the temperature-sensitive *lz* allele, lz^{ts1} (J. Kaminker, T. Lebestky, and U. B., unpublished data). The strongest eye-specific allele of *D-Pax2*, spa^{pol}, which is not transcribed in cone cell precursors (Fu and Noll, 1997), also enhances lz^{ts1} (Figures 1A and 1B). We found that D-Pax2 is not expressed in cone cell precursors of *lz* mutants (Figures 1C and 1D), which suggests that Lz regulates *D-Pax2* expression. There are three Lz/Runt domain (RD) binding sites (5′-RACCRCA-3′, R = purine; Kamachi et al., 1990) in the *D-Pax2* eye-specific enhancer (RDI–RDIII; Figures 1E and 1F). To determine whether these sites are required for proper *D-Pax2* expression, a series of smaller enhancer fragments derived from the SpeI fragment (1–5 in Figure 1F) was combined with the *D-Pax2* promoter and transcribed region from which introns 1–8 had been removed (see Fu et al., 1998) and tested as transgenes for their ability to rescue spa^{pol} mutants (Figures 1G–1N). There was no loss in rescue efficiency if the truncation did not eliminate any of the three RD binding sites (1, 2, and 4 in Figure 1F). However, if RDI was deleted (5 in Figure 1F), the rescue efficiency (Figure 1H) and D-Pax2 expression in cone cell precursors (Figure 1L) were considerably reduced, and rescue could not be improved by two copies of the transgene (not shown). Similarly, when both RDII and RDIII were removed (3 in Figure 1F), the rescue efficiency (Figure 1I)

intron 4 and ends with the second SpeI site. Runt domain (RD) binding sites are in boldface, and the minimal eye-specific enhancer (SME; positions 158–519 of intron 4) is underlined.

(F) The extent of $Df(4)spa^{pol}$ and the position of the spa^{1} insertion (Fu and Noll, 1997) are mapped relative to the 5′ end of intron 4 whose sequence is shown in (E). In addition to the three RD binding sites, the positions within the SME of eight putative Su(H) (triangles) and six ETS domain (ovals) binding sites are shown. Below, the extent of the 926 bp SpeI fragment of intron 4 and of constructs 1–14 including the entire or truncated forms of the SME are indicated. Transformant lines carrying constructs 1–14 driving D-Pax2 expression were assessed for their efficiency to rescue the spa^{pol} adult eye phenotype. Construct 6 is the smallest enhancer fragment that can fully rescue (wt) spa^{pol}, while constructs 5 and 8 can only weakly rescue (+) and constructs 3, 7, and 9–14 can partially rescue (++) as single-copy transgenes. If homozygous viable, transgenes of constructs 3, 7, and 9–14 can fully rescue the eye phenotype whereas transgenes of constructs 5 and 8 cannot (not shown). The rescue efficiencies (+, ++, wt) indicated on the right are the average of many independent lines of each construct (see Experimental Procedures). Scale indicates distance in bp from the 5′ end of intron 4 of *D-Pax2*.

(G and K) spa^{pol}. Note roughening across entire eye (G) and lack of D-Pax2 expression in cone cell precursors (K).

(H and L) w^{1118}; *P[construct 5-D-Pax2,* w^{+}*]/+*; spa^{pol}. Construct 5, which lacks RDI, can only weakly rescue (+) the spa^{pol} phenotype (H) as well as D-Pax2 expression in cone cell precursors (L).

(I and M) w^{1118}; *P[construct 3-D-Pax2,* w^{+}*]/+*; spa^{pol}. Construct 3, which lacks RDII and RDIII, allows partial rescue (++) of the spa^{pol} phenotype (I) and D-Pax2 expression in cone cell precursors when present as a single copy (M).

(J and N) w^{1118}; *P[construct 6-D-Pax2,* w^{+}*]*; spa^{pol}. Construct 6 is the minimal enhancer fragment (SME) able to completely rescue the spa^{pol} phenotype (J) and D-Pax2 expression in cone cell precursors (N) when driving *D-Pax2* expression as a single-copy transgene.

and expression in cone cell precursors (Figure 1M) were clearly reduced, but rescue to wild type was achieved with two copies of the transgene (not shown). These experiments suggest that the RD binding sites are essential for the control of *D-Pax2* transcription and that omission of RDI has more severe effects than that of RDII and RDIII.

Construct 6, which extends from nucleotides 158–519 and contains all three RD sites (Figures 1E and 1F), is the smallest fragment that can rescue the *spa^{pol}* eye phenotype to wild type (Figure 1J) and D-Pax2 expression in cone cell precursors (Figure 1N) as a single-copy transgene; hence, it was designated as the *spa* minimal enhancer (SME). Any further truncation of this enhancer fragment that removes at least one of the three RD binding sites (7–12 in Figure 1F) destroys its ability to completely rescue the *spa^{pol}* phenotype by a single copy of the corresponding transgene. Eliminating only RDIII (11 and 12 in Figure 1F) or RDII and RDIII (7 in Figure 1F) has similar effects in that the corresponding transgenes in most lines are unable to rescue the *spa^{pol}* eye phenotype completely when present as single copies while the presence of two copies results in a wild-type eye phenotype (not shown). The same result is observed if only RDI is deleted (9 and 10 in Figure 1F). When, in addition, more than half of the SME is removed (8 in Figure 1F), the rescue efficiency is further reduced, which suggests that regulatory elements other than the RD sites are important in the SME. As these sequences are also eliminated in 5 (Figure 1F), it is likely that the reduced rescue efficiency of this fragment is caused by the deletion of sequences in addition to RDI. Sequences outside of the SME are unable to compensate for the loss of regulatory elements within the SME (cf. 13 with 11 or 3 with 7, and 14 with 9 or 5 with 8 in Figure 1F).

Electrophoretic mobility-shift assays (EMSA) demonstrated that in vitro translated Lz can bind specifically to each of the RD binding sites in the SME (Figures 2A–2D). As an in vivo correlate to these experiments, the three RD sites were mutated (5′-RA*AA*RCA-3′) in the context of a transgenic *D-Pax2* rescue construct. Mutation of all three RD binding sites (mRDx3) causes a failure to rescue the *spa^{pol}* eye phenotype (Figure 2E) and D-Pax2 expression in cone cell precursors (Figure 2F). The in vitro and in vivo data together demonstrate that Lz directly regulates *D-Pax2* transcription through the RD binding sites in the SME.

A construct expressing *lacZ* under the control of the SME and the *hsp70* promoter (SME-*lacZ*) faithfully reproduces the wild-type D-Pax2 expression pattern in cone cell precursors (Figure 2G). Mutation of all three RD binding sites in SME-*lacZ* results in the loss of this expression (Figure 2H), further indicating that Lz acts directly through the SME. For the remainder of our analysis, we examined both endogenous D-Pax2 expression as well as SME-*lacZ* expression. In all genetic backgrounds tested, the results obtained in both assays were identical. This suggests that the SME is sufficient for transcriptional regulation of *D-Pax2* in cone cell precursors, and that SME-*lacZ* faithfully reflects this regulation.

The EGFR Pathway Directly Regulates *D-Pax2* Expression in Cone Cell Precursors

In *EGFR^{ts}* third-instar larvae raised at 29°C for 36 hr prior to dissection, D-Pax2 expression is lost in cone cell precursors (Figure 3B). To restrict the loss of EGFR function to the undifferentiated cells posterior to the furrow and cells that acquire their fates during the second phase of morphogenesis, a *lz-Gal4* driver (Crew et al., 1997) was used to express a dominant-negative form of EGFR. In these discs, D-Pax2 expression is lost from cone cell precursors (Figure 3C), while neuronal patterning in the precluster is maintained (Figure 3D). D-Pax2 expression was further examined in mutants of genes encoding the nuclear components of the EGFR signaling pathway, the repressor Yan and the activator PntP2. D-Pax2 expression is also lost in discs in which *lz-Gal4* drives the expression of a nonphosphorylatable form of Yan refractory to the EGFR signal (Figure 3E). Similarly, in the hypomorphic *pnt^{1230}* mutant, a modest reduction of D-Pax2 expression occurs in cone cell precursors (Figure 3F), while a stronger reduction is observed upon expression of a dominant-negative form of PntP2 (Figure 3G). These experiments together suggest that the EGFR signaling pathway activates *D-Pax2* expression in cone cell precursors by relieving Yan-mediated repression and stimulating PntP2 activation.

The above genetic analysis does not address whether the effects of EGFR signaling on *D-Pax2* transcription are direct or indirect. Therefore, we used in vitro mutagenesis to examine potential direct effects. Six ETS domain consensus binding sites (5′-GGAA/T-3′; Nye et al., 1992) were found in the SME (Figure 1F). EMSAs showed that two of these sites (1 and 6, Figures 3H and 3I) are bound by both Yan and PntP2. Yan also binds to two additional sites (2 and 4). All six ETS sites were mutated to 5′-*TT*AA/T-3′ (Wotton et al., 1994) in the context of SME-*lacZ*, and the resulting SME^{mETSx6}-*lacZ* construct was transformed into flies. In these transgenic flies, β-galactosidase expression is lost from cone cell precursors (Figure 3J). Since PntP2 was found to bind only to Ets sites 1 and 6, a SME-*lacZ* construct in which only these sites were mutated (SME$^{mETS(1,6)}$-*lacZ*) was transformed into flies. Figure 3K shows that β-galactosidase expression in cone cells is completely eliminated. These in vitro and in vivo results together demonstrate that PntP2 directly controls *D-Pax2* expression in cone cell precursors by binding to ETS domain sites in the SME. The effect of losing Yan binding in the context of SME^{mETSx6} and SME$^{mETS(1,6)}$ is addressed below.

Notch Signaling Directly Regulates *D-Pax2* Expression in Cone Cell Precursors

In *N^{ts}* third-instar larvae raised at 29°C for 20 hr prior to dissection, D-Pax2 expression is eliminated from cone cell precursors (Figure 4A). Similarly, expression of a dominant-negative form of N under *lz-Gal4* control causes a loss of D-Pax2 expression in cone cell precursors (Figure 4B) without perturbing neuronal development (Figure 4C). D-Pax2 expression is also reduced in discs mutant for *Delta (Dl)* (Figure 4D), which encodes a N ligand. Moreover, expression of a dominant-negative form of Dl (Dl^{DN}) under *lz-Gal4* control causes a loss of D-Pax2 expression in cone cell precursors (Figure 4E), while neuronal patterning occurs in a wild-type fashion (Figure 4F). A further reduction in D-Pax2 expression is seen when Dl^{DN} is driven by *GMR-Gal4* (Figure 4G). A loss of D-Pax2 expression is also seen upon ectopic expression of Hairless (H) (Figure 4H), a direct antagonist of Su(H) function (Brou et al., 1994). These results together suggest that N/Dl signaling via Su(H) is required for proper *D-Pax2* expression in cone cell precursors. This is an inductive rather than lateral inhibitory function

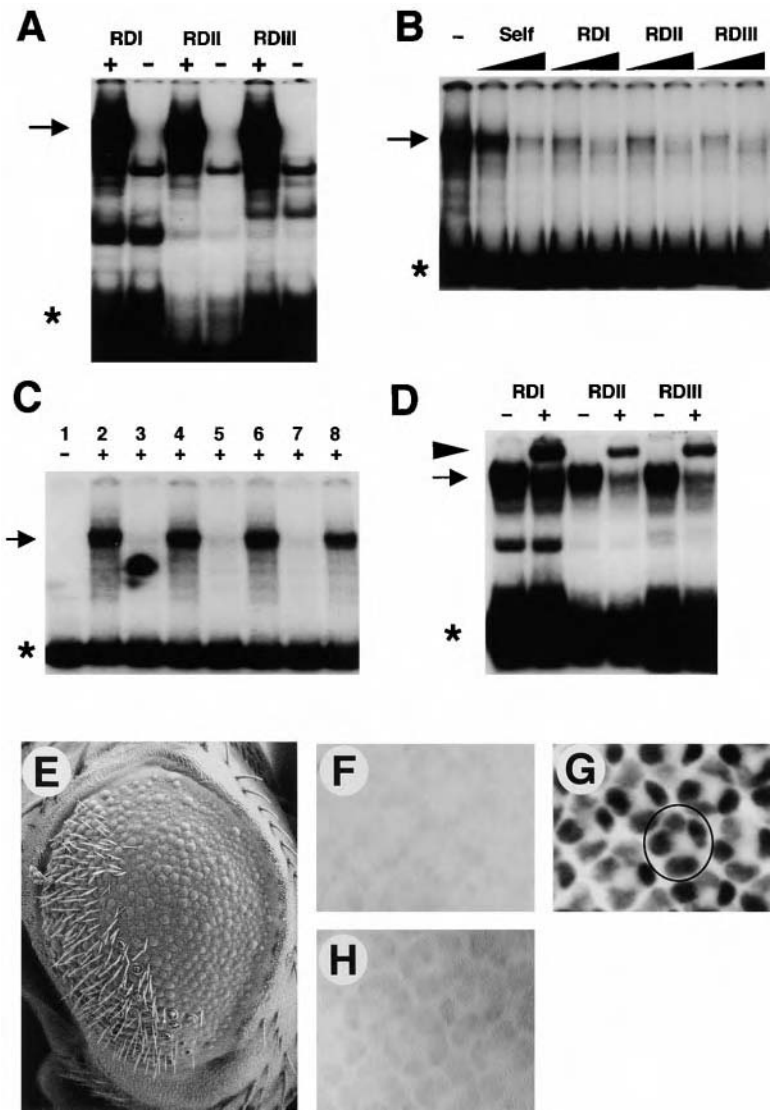

Figure 2. Direct Regulation of *D-Pax2* by Lz

(A–D) Autoradiograms of electrophoretic mobility-shift assays (EMSA). Arrows indicate shifted bands resulting from specific binding of Lz to DNA probes, asterisks mark positions of free probe.

(E) SEM of an adult eye.

(F–H) Immunolocalization of D-Pax2 (F) or β-galactosidase (G and H) in third larval instar eye discs.

(A) EMSA showing binding of Lz to oligonucleotides including one of the three RD binding sites, RDI-RDIII. Lz binds to each oligonucleotide, causing it to migrate more slowly than the free probe. + or − indicates the presence or absence of Lz. Lower molecular weight bands seen in the − lanes are nonspecific.

(B) Competition assay. The probe used for binding in these EMSAs is a SpeI-BglII restriction fragment from the *D-Pax2* eye-specific enhancer (nucleotides 38–320 in Figure 1E) that contains the RDI site. Increased concentrations of cold probe (Self; 10×, 50×) or of oligonucleotides encompassing RDI-RDIII (40×, 200×) efficiently compete with Lz binding.

(C) Competition assays. Cold oligonucleotides including wild-type RDI (lane 3), RDII (lane 5), or RDIII (lane 7) sites, but not oligonucleotides including mutant mRDI (lane 4), mRDII (lane 6), or mRDIII (lane 8) sites, efficiently compete with binding of Lz to the SpeI-BglII probe. + or − indicates presence or absence of Lz. Competitor was omitted in lanes 1 and 2. 200× molar excess of competitor probes was used in lanes 3–8.

(D) Antibody supershift assay. Addition of αLz antibody to the binding reaction of Lz with RD oligonucleotides gives rise to a supershifted band with lower mobility (arrowhead). − or + indicates the absence or presence of αLz antibody.

(E and F) w^{1118}; *P[*mRDx3-*D-Pax2]*; spa^{pol}. In this transformant, all three RD sites in the SpeI fragment are mutated. Neither the spa^{pol} eye phenotype (E) nor D-Pax2 expression in cone cell precursors (F) is rescued (compare with Figures 1G and 1K).

(G) w^{1118}; *P[*SME-*lacZ* w^{+}*]*/+. The expression of the *lacZ* reporter gene under the control of the SME in cone cell precursors (circled) is identical to endogenous wild-type D-Pax2 expression (compare with Figure 1C).

(H) w^{1118}; *P[*SME^{mRDx3}-*lacZ* w^{+}*]*. When the SME is mutated in all three RD sites, expression of β-galactosidase is lost in cone cell precursors.

of the N signaling pathway in cone cell development that has not been previously analyzed with molecular markers. A reporter gene under the transcriptional control of Su(H) binding sites (Go et al., 1998) is expressed in cone cell precursors (Figure 4I), which demonstrates that Su(H) is activated by the N pathway in cone cells.

The Su(H) binding sites in the SME were altered to determine whether the N pathway directly regulates *D-Pax2* transcription. The SME contains eight putative Su(H) binding sites (Figure 1F; 5′-RTGRGAR-3′; Nellesen et al., 1999). EMSAs showed that the Su(H) consensus binding sequence is not strictly followed, since three sites with one mismatch can bind Su(H) (Figure 4J). Su(H) binding is eliminated when the central 5′-GRG-3′ sequence is mutated to 5′-CCC-3′ in all eight sites (Figure 4K). A construct containing these mutations in the context of SME-*lacZ* ($SME^{mSu(H)x8}$-*lacZ*) was transformed into flies. In these transgenic flies, β-galactosidase expression is lost in cone cell precursors (Figure 4L). These in vitro and in vivo results together demonstrate that Su(H) directly controls *D-Pax2* expression in cone cell precursors by binding to the SME.

Single-Cell Clonal Analysis

Mutating Su(H) and ETS binding sites eliminates expression of the target gene in the cone cells, which demonstrates a direct role of these pathways in transcriptional activation of *D-Pax2*. We further used clonal analysis to establish the requirement of the Notch and EGFR pathways in *D-Pax2* expression. Unfortunately, these pathways are necessary for proliferation and have many layers of function (Domínguez et al., 1998, Go et al., 1998). We therefore used a flip-out strategy to inhibit N

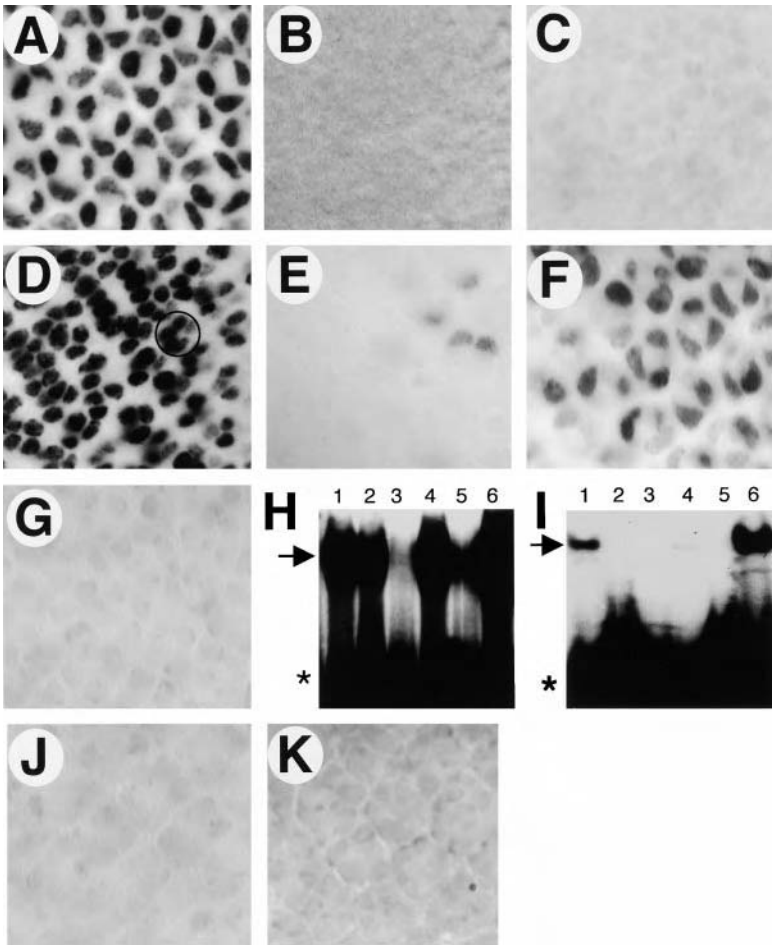

Figure 3. Direct Regulation of D-Pax2 Expression by the EGFR Signaling Pathway

(A–G and J) Immunolocalization of D-Pax2 (A–C and E), ELAV (D), or β-galactosidase (F, G, J, and K) in third larval instar eye discs.

(H and I) EMSA demonstrating specific binding of Yan and PntP2 to the ETS domain binding sites in the SME. Arrows indicate shifted bands caused by binding of ETS domain proteins to DNA probes, asterisks mark free probes.

(A) Wild type. D-Pax2 is expressed in cone cell precursors.

(B) *EGFR^{ts}/EGFR^{top}*. Expression of D-Pax2 is lost from cone cell precursors.

(C) *lz-Gal4:UAS-EGFR^{DN}*. Expression of this dominant-negative form of EGFR under the control of *lz-Gal4* causes a loss of D-Pax2 expression from cone cell precursors.

(D) *lz-Gal4:UAS-EGFR^{DN}*. Expression of the neuronal marker ELAV indicates that neuronal patterning in the precluster (circled) is maintained in the same genotype as in (C).

(E) *lz-Gal4:UAS-yan^{Act}*. Expression of this nonphosphorylatable form of Yan refractory to the EGFR signal leads to a severe reduction of D-Pax2 expression in cone cell precursors.

(F) *pnt^{1230}/pnt^{1230}*; *P[*SME-*lacZ w^{+}]/+*. Expression of SME-*lacZ* in cone cell precursors is reduced in this hypomorphic *pntP2* mutant.

(G) *lz-Gal4:UAS-pntP2^{T151A}*; *P[*SME-*lacZ w^{+}]/+*. Expression of this nonphosphorylatable, dominant-negative form of PntP2 leads to a severe reduction of SME-*lacZ* expression in cone cell precursors.

(H) Yan binds to ETS domain binding sites 1, 2, 4, and 6 within the SME, causing shifted bands.

(I) PntP2 binds to ETS domain binding sites 1 and 6 within the SME, causing shifted bands.

(J) *w^{1118}*; *[*SME^{mETSx6}-*lacZ, w^{+}]*. When the SME is mutated in all six ETS domain binding sites, cone cell expression of the reporter is lost.

(K) *w^{1118}*; *[*SME$^{mETS(1,6)}$-*lacZ, w^{+}]*. When the SME is mutated in PntP2 binding sites 1 and 6, cone cell expression of the reporter is lost. This demonstrates that regulation by PntP2 is direct.

and EGFR function in GFP-labeled single-cell clones (Ito et al., 1997). This was best achieved in clones induced by *GMR-flp*. The GMR enhancer is only active behind the furrow and only a single cell division takes place in this population of cells. As a result, the clone size is very small. In a wild-type background, single cells marked with GFP express D-Pax2 (Figures 5A and 5B). However, when these single cells also express EGFR^{DN} (n = 120 cells in 10 discs; Figures 5C and 5D) or N^{ECN} (n = 150 cells in 12 discs; Figures 5E and 5F), they do not express D-Pax2. Thus, cone cells need functional Notch and EGFR receptors in order to express D-Pax2.

Lz, EGFR, and Notch Restrict *D-Pax2* Expression to Cone Cell Precursors

The results described so far suggest that *D-Pax2* expression is limited to cells which (1) express Lz, (2) receive a sufficiently strong EGFR signal to both alleviate Yan-imposed repression and stimulate PntP2 activation, and (3) receive a N signal able to stimulate Su(H) activation (Figure 5G). The tripartite control of *D-Pax2* expression in the cone cell precursors requires that they receive all three inputs at the proper time in their development. Lz expression in cone cell precursors has been previously demonstrated (Flores et al., 1998). Consistent with their reception of the EGFR signal (Freeman, 1996; Tio and Moses, 1997), activated MAPK is detected in cone cell precursors at the time when they initiate D-Pax2 expression (Figure 5H). We also found that Dl is expressed in developing photoreceptor clusters at the time when the cone cell precursors express D-Pax2 (Figure 5I). Thus, the neuronal clusters signal through an inductive Dl/N pathway to activate *D-Pax2* expression in the neighboring cone cell precursors. These results suggest that, in addition to expressing Lz, the cone cell precursors receive the EGFR and N signals at the time of fate acquisition and D-Pax2 expression. Presumably, at least one of these three activation mechanisms is lacking in cells that do not express *D-Pax2*. This hypothesis was tested through genetic manipulation of the system.

The Absence of EGFR Activation Prevents *D-Pax2* Expression in Undifferentiated Cells

Undifferentiated cells immediately posterior to the furrow receive the N signal (Matsuno et al., 1997) and express Lz, but they do not express D-Pax2. We hypothesized that the absence of D-Pax2 expression in these

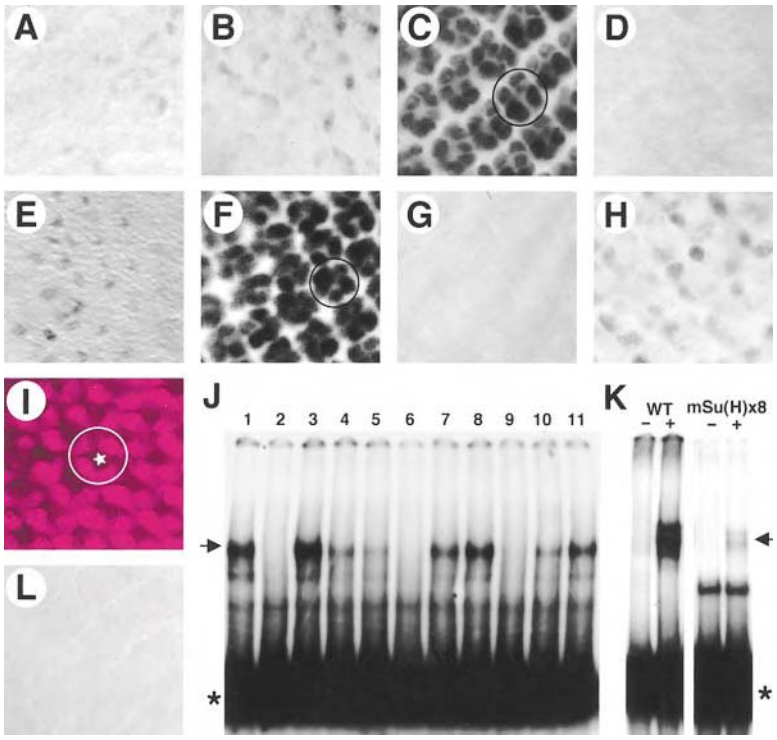

Figure 4. Direct Regulation of D-Pax2 Expression by the N Signaling Pathway

(A–I and L) Immunolocalization of β-galactosidase (A, B, I, and L), ELAV (C and F), or D-Pax2 (D, E, G, and H) in third larval instar eye discs.

(J and K) EMSA demonstrating specific binding of GST-Su(H) to sites in the SME. Arrows indicate shifted bands caused by Su(H) binding to DNA probes, asterisks indicate free probes.

(A) N^{ts1}; *P[*SME-*lacZ* w^+*]/+*. Expression of SME-*lacZ* is lost from cone cell precursors.

(B) *lz-Gal4:UAS-*N^{ECN}; *P[*SME-*lacZ* w^+*]/+*. Expression of this dominant-negative form of N in Lz-expressing cells causes the loss of SME-*lacZ* expression from cone cell precursors.

(C) *lz-Gal4:UAS-*N^{ECN}; *P[*SME-*lacZ* w^+*]/+*. Expression of the neuronal marker ELAV indicates that neuronal patterning in the precluster is maintained (circled) in the same genotype as in (B).

(D) Dl^{B2}/Dl^{R7}. Expression of D-Pax2 is eliminated in cone cell precursors in this heteroallelic *Dl* loss-of-function combination.

(E) *lz-Gal4:UAS-*Dl^{DN}. Expression of this dominant-negative form of Dl causes a reduction of D-Pax2 expression from cone cell precursors.

(F) *lz-Gal4:UAS-*Dl^{DN}. Expression of the neuronal marker ELAV indicates that neuronal patterning in the precluster (circled) is maintained in the same genotype as in (E).

(G) *GMR-Gal4:UAS-*Dl^{DN}. GMR-Gal4 driving the expression of dominant-negative Dl in all cells posterior to the furrow causes a complete loss of D-Pax2 expression.

(H) *lz-Gal4:UAS-H*. Expression of H, an antagonist of Su(H), leads to a reduction of D-Pax2 expression in cone cell precursors.

(I) *12xSu(H)bs-lacZ*. In this construct, twelve copies of Su(H) binding sites control expression of *lacZ*. The observed expression of β-galactosidase indicates that Su(H) functions as a transcriptional activator in cone cell precursors. A single ommatidium is circled showing expression in the four cone cell precursors but not in the neuronal cells (asterisk).

(J) Competition assay. Su(H) binding to the SME in the absence (lane 1) or presence (lanes 2–11) of cold competitors: lanes 2 and 3, wild-type (m4S2) and mutant version (m4S2m) of a known Su(H) binding site, respectively; lanes 4–11, putative Su(H) binding sites found in the SME. Oligonucleotides containing Su(H) sites 2, 3, 4, 6 and 7 (lanes 5, 4, 6, 9, and 10, respectively) efficiently compete for Su(H) binding even though sites 4 and 7 are one nucleotide off the consensus, while site 5 (lane 7; one nucleotide off consensus) and sites 1 and 8 (lanes 8 and 11, respectively; two nucleotides off consensus) do not significantly compete for binding.

(K) Su(H) binding to the SME. − or + indicates absence or presence of Su(H) protein in each assay. Su(H) binds to the wild-type SME (WT). This binding is virtually eliminated when all eight Su(H) binding sites are mutated (mSu(H)x8).

(L) w^{1118}; *P[*$SME^{mSu(H)x8}$*-lacZ,* w^+*]* eye discs. When the SME is mutated in all eight Su(H) binding sites, β-galactosidase expression is lost from the cone cell precursors (compare with Figure 2G), which demonstrates that regulation of D-Pax2 by Su(H) is direct.

cells is caused by a lack of the EGFR signal. This hypothesis is consistent with the observation that EGFR signaling causes these cells to differentiate (Xu and Rubin, 1993; Freeman, 1996; Tio and Moses, 1997). Indeed, D-Pax2 is ectopically expressed in undifferentiated cells that express an activated form of EGFR (Figure 5J). Loss-of-function yan^{e2D}/yan^{pokX8} discs also show ectopic expression of D-Pax2 in undifferentiated cells (Figure 5K). Similarly, in discs expressing SME^{mETSx6}*-lacZ*, in which the six ETS sites in the SME are mutated, β-galactosidase is also expressed in undifferentiated cells (Figure 5L). Presumably, relief of Yan repression is sufficient to activate some *D-Pax2* in undifferentiated cells. In $SME^{mETS(1,6)}$*-lacZ*, where the Pnt binding sites are eliminated but two of the Yan binding sites are still intact, there is no expression of β-galactosidase in the undifferentiated cells (Figure 5M). These results suggest that while the undifferentiated cells posterior to the furrow express Lz and receive the N signal, they fail to express D-Pax2 because they do not receive the EGFR signal and are therefore unable to relieve the Yan-imposed repression of *D-Pax2*.

The Absence of N Activation Prevents *D-Pax2* Expression in R7

The R7 precursors express Lz and receive RTK signals, yet they do not express D-Pax2. We hypothesized that this is due to the lack of the N signal at the time of R7 determination. Indeed, expression of an activated form of N (N^{act}), leads to ectopic D-Pax2 expression in R7 precursors (Figure 5N), which suggests that D-Pax2 is not normally expressed in R7 because this cell does not receive the N signal. These results are consistent with the previous observation that the R7 cell loses its neuronal characteristics upon expression of N^{act} (Fortini et al., 1993).

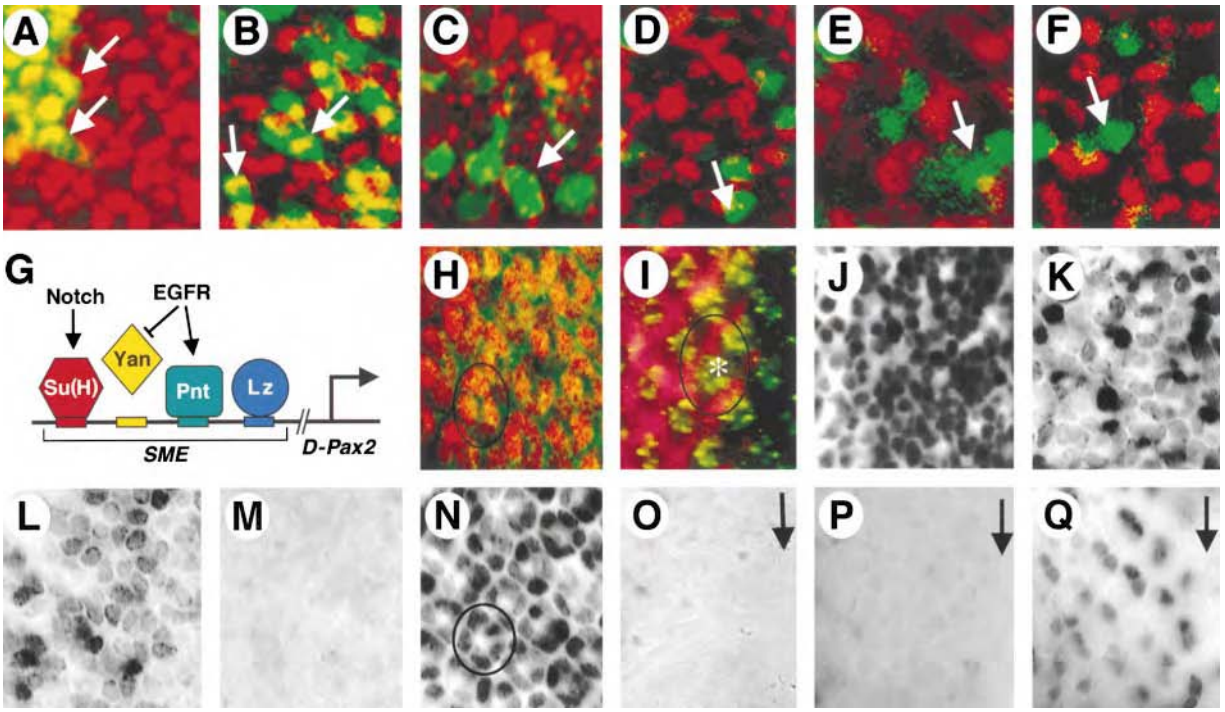

Figure 5. Cell-specificity of D-Pax2 Regulation

(A–F) Clonal analysis of D-Pax2 expression (red) in cone cells. (G) Summary of *D-Pax2* regulation by Lz, EGFR, and N. (H and I) Immunolocalization of β-galactosidase (red) and dpERK (green, H) or Dl (green, I) in third-instar eye discs by confocal microscopy. (J–Q) Immunolocalization of β-galactosidase reporter in third-instar eye discs by light microscopy. Posterior is to the left.

(A) *hsp70-flp*; *Ay-Gal4 UAS-GFP*. Flip-out clone in wild-type eye disc using *hsp*70-*flp*. Cells expressing both GFP and D-Pax2 show yellow nuclei (arrows). Note that GFP (green) is both nuclear and cytoplasmic while D-Pax2 is exclusively nuclear.

(B) *GMR-flp*; *Ay-Gal4 UAS-GFP*. Single-cell flip-out clones in wild-type eye disc (GFP, green) induced by *GMR-flp* and stained with D-Pax2 antibody (red). Cone cells co-expressing GFP and D-Pax2 are yellow (arrows).

(C) *hsp70-flp*; *Ay-Gal4 UAS-GFP*; *UAS-EGFR^{DN}*. Flip-out clones generated at the early third larval instar. No overlap is seen between cells expressing both EGFR^{DN} and GFP (green) and those expressing D-Pax2 (red).

(D) *GMR-flp*; *Ay-Gal4 UAS-GFP*; *UAS-EGFR^{DN}*. Single-cell flip-out clones induced by *GMR-flp* and expressing EGFR^{DN} at the third larval instar. No overlap is seen between cells expressing both EGFR^{DN} and GFP (green) and those expressing D-Pax2 (red). A total of 120 green cells were examined in (C) and (D) at the stage when cone cells develop.

(E) *hsp70-flp*; *Ay-Gal4 UAS-GFP*; *UAS-N^{ECN}*. Flip-out clones generated at the early third larval instar. No overlap is seen between GFP and N^{ECN} expressing cells (green) and D-Pax2 expressing cells (red).

(F) *GMR-flp*; *Ay-Gal4 UAS-GFP*; *UAS-N^{ECN}*. Single-cell flip-out clones induced by *GMR-flp* and expressing N^{DN} at the third larval instar. No overlap is seen between GFP and N^{ECN} expressing cells (green) and D-Pax2 expressing cells (red). A total of 150 green cells were examined in (E) and (F) at the stage when cone cells develop.

(G) Cone cell-specific activation of *D-Pax2* expression is dependent on three inputs: (i) Lz binding to the RD sites in the eye-specific enhancer (SME), (ii) EGFR signal-dependent inactivation of Yan and activation of PntP2, which then binds to ETS domain binding sites in the SME, and (iii) Notch signal-dependent activation of Su(H), which binds to the Su(H) binding sites in the SME.

(H and I) Cone cell precursors receive the proper signals.

(H) SME-*lacZ*. Optical section at the level of cone cell precursors. Activated, phosphorylated MAPK (green) is seen in cone cells, which indicates that these cells receive an RTK signal at the time of SME-*lacZ* (red) expression. Activated MAPK is primarily cytoplasmic; however, small amounts can been seen in nuclei (yellow). A single ommatidium is circled.

(I) SME-*lacZ*. Dl (green) is expressed in photoreceptor clusters (asterisk), but not in cone cells (circled). Expression of this N ligand is downregulated when SME-*lacZ* (red) expression initiates, suggesting transduction of the N signal from the signaling photoreceptor cells to the receiving cone cell precursors.

(J–M) Lack of EGFR signal prevents D-Pax2 expression in undifferentiated cells. The area shown in these three panels is entirely posterior to the furrow.

(J) *lz-Gal4:UAS−λ-topDER*; *P[*SME-*lacZ w^{+}]/+*. Expression of this activated form of EGFR causes ectopic expression of SME-*lacZ* in all of the undifferentiated cells posterior to the furrow.

(K) *yan^{e2D}/yan^{pokx8}*; *P[*SME-*lacZ w^{+}]/+*. SME-*lacZ* is ectopically expressed in undifferentiated cells in this heteroallelic *yan* loss-of-function combination.

(L) *w^{1118}*; *P[*SME^{mETSx6}-*lacZ w^{+}]*. Ectopic expression in undifferentiated cells is evident when all six ETS domain binding sites are mutated in the SME. This demonstrates a direct role for Yan in the negative regulation of *D-Pax2* in the undifferentiated cells.

(M) *w^{1118}*; *P[*SME$^{mETS(1,6)}$-*lacZ w^{+}]*. Ectopic expression in undifferentiated cells is lost when PntP2 binding sites are mutated, but two additional Yan binding sites are maintained. This demonstrates a direct role for Yan in the negative regulation of *D-Pax2* in undifferentiated cells.

(N) Lack of N signal prevents D-Pax2 expression in the R7 precursor. *sev-N^{act}/+*; *P[*SME-*lacZ w^{+}]/+*. Ectopic expression of N^{act} in the R7 precursor leads to expression of SME-*lacZ* in this cell. A representative cluster with five cells expressing β-galactosidase is circled.

(O–Q) Lack of Lz and N signal prevents D-Pax2 expression in the R3/R4 precursors. The furrow is marked with an arrow.

(O) *sev-lz/+*; *P[*SME-*lacZ w^{+}]/+*. Ectopic expression of Lz in the R3 and R4 precursors does not lead to expression of SME-*lacZ* in these cells.

(P) *sev-N^{act}/+*; *P[*SME-*lacZ w^{+}]/+*. Ectopic expression of activated N in the R3 and R4 precursors does not lead to expression of SME-*lacZ* in these cells.

(Q) *sev-lz/+*; *sev-N^{act}/+*; *P[*SME-*lacZ w^{+}]/+*. Coexpression of both Lz and activated N leads to expression of SME-*lacZ* in the R3/R4 precursors (small arrows).

Cell type	Active components			
	N pathway		RTK pathway	
	Lz	Su(H)*	Yan	PntP2*
undiff	Yes	Yes	No	
R3/R4	No	No	Yes	
R7	Yes	No	Yes	
cone	Yes	Yes	Yes	

Figure 6. A Combinatorial Code for Cell Fate Specification

The three components discussed in this paper, Lz, N, and EGFR, can be used to describe the differences between at least four different cell types: cone, R7, R3/R4, and undifferentiated cells. Each of these cell types receives a different combination of signals, which creates the unique set of activated transcription factors that ultimately specify the cell's fate. In such a code, a small number of multifunctional signals such as EGFR and N can be combined to create a large number of distinct cell types (see text for details). Active forms of Su(H) and PntP2 are indicated with an asterisk.

The Absence of N Activation and Lz Prevents *D-Pax2* Expression in R3 and R4

Thus far, this study has focused on cells that express Lz. However, the regulation of *D-Pax2* expression can also be tested in cells that lack Lz, such as the R3/R4 precursors. These cells receive the EGFR signal (Freeman, 1996) but receive the N signal after their initial fate specification, during ommatidial rotation (Cooper and Bray, 1999; Fanto and Mlodzik, 1999). Ectopic expression of either Lz (Figure 5O) or N^{act} (Figure 5P) in the R3/R4 precursors fails to activate *D-Pax2* expression in these cells. However, when Lz and N^{act} are coexpressed in the R3/R4 precursors, D-Pax2 is expressed in these cells (Figure 5Q). These results demonstrate that the lack of both N signaling and Lz during the proper time window prevents R3/R4 cells from expressing *D-Pax2*.

Discussion

In this study, we have examined one example of the complex interplay between multiple signaling pathways during the acquisition of diverse cell fates. We have shown that the nuclear effectors of the EGFR and N signal transduction pathways, Yan, PntP2, and Su(H), and the transcriptional regulator, Lz, act in a combinatorial manner on a tissue-specific enhancer to restrict the expression of *D-Pax2* to the cone cell precursors of the *Drosophila* eye disc. Furthermore, by genetically manipulating these inputs, we observe ectopic expression of *D-Pax2* in specific cell types that do not normally express it. This study provides an exciting example of two multifunctional signaling pathways, EGFR and N, acting together to influence the development of a single cell type. The regulation of *D-Pax2* transcription by each of these inputs is direct, since its expression can be eliminated by mutating the RD, ETS, or Su(H) binding sites in the eye-specific *D-Pax2* enhancer.

The entire code for generating the approximately ten different cell types in the *Drosophila* ommatidium is not yet understood. However, the available data can create a combinatorial code for cell fate specification the use of only three components (Figure 6). In this code, differential activation of the RTK and N signaling cascades creates the unique combinations of activated or inactivated transcription factors that are required for the acquisition of different cell fates. Each of these transcription factors is ubiquitously expressed in the precursor population, but is activated only in cells that receive the proper signals. The model presented in Figure 6 reflects requirements rather than sufficiency for cell fate specification. We anticipate that as additional components are uncovered, the code for the cell types listed in Figure 6 will become complete and that the code for other cell types such as R1/R6 will become evident. In some instances, the regulation of the same target gene may involve different combinations of signals in different cell types. Preliminary data indicate that the combinatorial logic for expression of *D-Pax2* in primary pigment cells is different from that in cone cells in that it requires Su(H) and Lz but not Pnt (G. V. F., R. N., and U. B., unpublished data).

Precise spatial and temporal regulation of the various inputs required for cell fate determination is essential for proper eye patterning. Lz function is restricted to the undifferentiated cells posterior to the furrow by a currently unidentified mechanism. Lozenge might prepare several enhancer regions early, so that they are competent to respond to a later signal. The EGFR ligand, Spitz (Spi), and the N ligand, Dl, are expressed in the previously determined neuronal clusters and act over short extracellular distances at the appropriate time for induction of cone cell fate in the neighboring precursors. Temporal control of the EGFR signal is achieved through the reiterative secretion of Spi as the ommatidium progressively develops (Freeman, 1996; Tio and Moses, 1997). Spi function is spatially restricted by competition with its diffusible antagonist, Argos (reviewed in Freeman, 1997). The N signal is activated early in eye development near the furrow (reviewed in Artavanis-Tsakonas et al., 1999), but this study highlights a late, inductive function of N that is dependent on the temporally controlled expression of Dl in the developing photoreceptor clusters. This N signaling positively influences differentiation and acts in cooperation with, rather than antagonistically to, the EGFR pathway. Tethering of Dl to the membrane allows only adjacent cells to receive this N signal (reviewed in Artavanis-Tsakonas et al., 1999).

Numerous studies involving promoter analysis have established that combinations of multiple transcription factor binding sites are important for gene activation. Comprehensive in vivo studies of the regulatory regions of the sea urchin *Endo 16* gene (Arnone and Davidson, 1997; Yuh et al., 1998) and the *Drosophila even-skipped* (*eve*) stripe 2 enhancer (Arnosti et al., 1996), for example, have convincingly demonstrated the importance of both positive and negative inputs in controlling gene activity. Our studies have focused on the integration of local signaling cascades in the regulation of a target gene. Our aim was to understand the molecular details, in the in vivo context of a developing animal, of how combinatorial signaling can generate fine differences in fate amongst cells that are initially equivalent and that communicate through local cell–cell interactions. Any one signal may not impart fate-specifying information when acting alone, but in combination, different signals can create unique sets of activated transcription factors at

the correct time and in a cell occupying a specific position. Although we have unraveled the molecular mechanisms involved in the regulation of only a single gene, it is likely that the other cell-specific transcription factors expressed in the eye disc and in other contexts will be controlled in a similar manner. Indeed, an example of direct integration of signaling pathways has been observed in muscle differentiation (Halfon et al., 2000 [this issue of *Cell*]). Moreover, analysis of the *pros* enhancer in the *Drosophila* eye suggests that similar combinations of signaling pathways and transcription factors operate in the regulation of this gene in R7 and cone cells (Xu et al., 2000 [this issue of *Cell*]). As additional controlling regions are analyzed, different combinations of signaling systems will undoubtedly be uncovered. Nevertheless, we anticipate that the total number of inputs will not be very large.

Experimental Procedures

Clonal Analysis

Flip out clones expressing *UAS-EGFR*^{DN} or *UAS-N*^{ECN} were generated by the use of the *Ay-Gal4* system (Ito et al., 1997) and marked with *UAS-GFP*, both inserted on the 2nd chromosome. Clones in eye discs were created by *hsp*70-*flp* or *GMR-flp*. *hsp*70-*flp* crosses were maintained at 18°C; early third-instar larvae were heat shocked at 37°C for 20 min to generate small clones.

Constructs Used for Germline Transformation

The 926 bp SpeI fragment of intron 4 of *D-Pax2* (Figure 1E) and its truncated versions were cloned into the BamHI site of the *spa*-PCG2 vector (Fu and Noll, 1997). Fragments 1–14 (Figure 1F) were derived from the SpeI (Figure 1E) fragment by PCR (nucleotide positions in intron 4 are in parentheses): 1 (59–813), 2 (59–519), 3 (59–411), 4 (158–813), 5 (359–813), 6 (158–519), 7 (158–411), 8 (359–519), 9 (213–519), 10 (281–519), 11 (158–474), 12 (158–438), 13 (59–474), and 14 (213–813). Each of the 15 *D-Pax2* transgenes, driven by their own promoter and the 15 different eye enhancer fragments (Figure 1F), were assayed as single copies for rescue of the *spa*^{pol} eye phenotype and D-Pax2 expression in cone cell precursors in several independent transgenic lines. The rescue efficiency of the *spa*^{pol} eye phenotype indicated in Figure 1F is the average of all independent lines of each transgene, which showed the following distributions (numbers indicate number of independent lines with weak (+), partial (++), and full (wt) rescue, respectively). SpeI, constructs 1, 2, 4, and 6: all lines are wt; construct 3: 2, 3, and 1; construct 5: 15, 3, and 0; construct 7: 4, 8, and 3; construct 8 with NotI ends: 6, 2, and 0 (with BamHI ends: 11, 6, and 3); construct 9: 0, 8, and 3; construct 10: 0, 6, and 4; construct 11: 0, 6, and 2; construct 12: 0, 9, and 2; construct 13: 0, 4, and 1; and construct 14: 0, 8, and 0. All homozygous viable ++ lines, but none of the + lines, rescue the *spa*^{pol} eye phenotype when two copies of the transgene are present.

SME-*lacZ*, SME^{mRDx3}-*lacZ*, SME^{mETSx6}-*lacZ*, SME$^{mETS(1,6)}$-*lacZ*, and SME$^{mSu(H)x8}$-*lacZ* were generated by amplifying the appropriate 158–519 fragments and cloning them into PwHZ128, which contains the *hsp70* promoter and the bacterial *lacZ* gene (a gift from A. Courey).

mRDx3 and mETSx6 were generated by site-directed mutagenesis as described (Huang et al., 1993). To generate mSu(H)x8, in vitro mutagenesis for Su(H)3, 6, and 7 was performed as above. The remaining Su(H) sites were altered on the mutated Su(H)3, 6, and 7 template using a PCR-based strategy.

Acknowledgments

We thank H. Wang for extensive help with fly genetics and transformations, J. Jackson and S. Robert for assistance with making constructs, T. Gutjahr for help with SEM, and F. Ochsenbein for help with graphics. We are indebted to R. Carthew for sharing reagents and results prior to publication. We thank S. Artavanis-Tsakonas, N. Baker, R. Carthew, A. Courey, M. Freeman, E. Hafen, Y. Hiromi, C. Klämbt, Z.-C. Lai, M. Mlodzik, K. Moses, M. Muskavitch, J. Pollock, I. Rebay, G. Rubin, D. Yamamoto, L. Zipursky, and K. Matthews and the Bloomington Stock Center for fly stocks and reagents. We thank A. Courey, H. Herschman, M. Levine, S. L. Zipursky, and members of the Banerjee laboratory for critical comments on the manuscript. G. V. F. was supported by a USPHS National Research Service Award (GM07195). This work was supported by the Swiss National Science Foundation (Grant 31-40874.94 to M. N.), the Kanton Zürich, the NIH (Grant # 2R01EY08152 to U. B.), and a McKnight Foundation Investigator Award to U. B.

Received November 29, 1999; revised August 22, 2000.

References

Arnone, M.I., and Davidson, E.H. (1997). The hardwiring of development: organization and function of genomic regulatory systems. Development *124*, 1851–1864.

Arnosti, D.N., Barolo, S., Levine, M., and Small, S. (1996). The *eve* stripe 2 enhancer employs multiple modes of transcriptional synergy. Development *122*, 205–214.

Artavanis-Tsakonas, S., Rand, M.D., and Lake, R.J. (1999). Notch signaling: cell fate control and signal integration in development. Science *284*, 770–776.

Ausubel, F.M., Brent, R., Kingston, R.E., Moore, D.D., Seidman, J.G., Smith, J.A., and Struhl, K., eds. (1991). Current Protocols in Molecular Biology (New York: John Wiley & Sons).

Bae, S.-C., and Ito, Y. (1999). Regulation mechanisms for the heterodimeric transcription factor, PEBP2/CBF. Histol. Histopathol. *14*, 1213–1221.

Baker, N.E., and Rubin, G.M. (1989). Effect on eye development of dominant mutations in the *Drosophila* homologue of the EGF receptor. Nature *340*, 150–153.

Baker, N.E., and Rubin, G.M. (1992). *Ellipse* mutations in *Drosophila* homologue of the EGF receptor affect pattern formation, cell division, and cell death in eye imaginal discs. Dev. Biol. *150*, 381–396.

Basler, K., Yen, D., Tomlinson, A., and Hafen, E. (1990). Reprogramming cell fate in the developing *Drosophila* retina: transformation of R7 cells by ectopic expression of *rough*. Genes Dev. *4*, 728–739.

Brou, C., Logeat, F., Lecourtois, M., Vandekerckhove, J., Kourilsky, P., Schweisguth, F., and Israël, A. (1994). Inhibition of the DNA-binding activity of *Drosophila* Suppressor of Hairless and of its human homolog, KBF2/RBP-J$_K$, by direct protein-protein interaction with *Drosophila* Hairless. Genes Dev. *8*, 2491–2503.

Brunner, D., Dücker, K., Oellers, N., Hafen, E., Scholz, H., and Klämbt, C. (1994). The ETS domain protein Pointed-P2 is a target of MAP kinase in the Sevenless signal transduction pathway. Nature *370*, 386–389.

Cagan, R.L., and Ready, D.F. (1989). *Notch* is required for successive cell decisions in the developing *Drosophila* retina. Genes Dev. *3*, 1099–1112.

Cooper, M.T.D., and Bray, S.J. (1999). Frizzled regulation of Notch signalling polarizes cell fate in the *Drosophila* eye. Nature *397*, 526–530.

Crew, J.R., Batterham, P., and Pollock, J.A. (1997). Developing compound eye in *lozenge* mutants of *Drosophila*: Lozenge expression in the R7 equivalence group. Dev. Genes Evol. *206*, 481–493.

Czerny, T., Bouchard, M., Kozmik, Z., and Busslinger, M. (1997). The characterization of novel *Pax* genes of the sea urchin and *Drosophila* reveal an ancient evolutionary origin of the *Pax2/5/8* subfamily. Mech. Dev. *67*, 179–192.

Daga, A., Karlovich, C.A., Dumstrei, K., and Banerjee, U. (1996). Patterning of cells in the *Drosophila* eye by Lozenge, which shares homologous domains with AML1. Genes Dev. *10*, 1194–1205.

Dickson, B., Sprenger, F., and Hafen, E. (1992). Prepattern in the developing *Drosophila* eye revealed by an activated torso-sevenless chimeric receptor. Genes Dev. *7*, 2327–2339.

Domínguez, M., and de Celis, J.F. (1998). A dorsal/ventral boundary established by Notch controls growth and polarity in the *Drosophila* eye. Nature *396*, 276–278.

Domínguez, M., Wasserman, J.D., and Freeman, M. (1998). Multiple functions of the EGF receptor in *Drosophila* eye development. Curr. Biol. *8*, 1039–1048.

Fanto, M., and Mlodzik, M. (1999). Asymmetric Notch activation specifies photoreceptors R3 and R4 and planar polarity in the *Drosophila* eye. Nature *397*, 523–526.

Flores, G.V., Daga, A., Kalhor, H.R., and Banerjee, U. (1998). Lozenge is expressed in pluripotent precursor cells and patterns multiple cell types in the *Drosophila* eye through the control of cell-specific transcription factors. Development *125*, 3681–3687.

Fortini, M.E., Rebay, I., Caron, L.A., and Artavanis-Tsakonas, S. (1993). An activated Notch receptor blocks cell-fate commitment in the developing *Drosophila* eye. Nature *365*, 555–557.

Freeman, M. (1996). Reiterative use of the EGF receptor triggers differentiation of all cell types in the *Drosophila* eye. Cell *87*, 651–660.

Freeman, M. (1997). Cell determination strategies in the *Drosophila* eye. Development *124*, 261–270.

Fu, W., and Noll, M. (1997). The *Pax2* homolog *sparkling* is required for development of cone and pigment cells in the *Drosophila* eye. Genes Dev. *11*, 2066–2078.

Fu, W., Duan, H., Frei, E., and Noll, M. (1998). *shaven* and *sparkling* are mutations in separate enhancers of the *Drosophila Pax2* homolog. Development *125*, 2943–2950.

Go, M.J., Eastman, D.S., and Artavanis-Tsakonas, S. (1998). Cell proliferation control by Notch signaling in *Drosophila* development. Development *125*, 2031–2040.

Gupta, B.P., and Rodrigues, V. (1995). Distinct mechanisms of action of the *lozenge* locus in *Drosophila* eye and antennal development are suggested by the analysis of dominant enhancers. J. Neurogenet. *10*, 137–151.

Halfon, M.S., Carmena, A., Gisselbrecht, S., Sackerson, C.M., Jimenez, F., Baylies, M.K., and Michelson, A.M. (2000). Ras pathway specificity is determined by the integration of multiple signal-activated and tissue-restricted transcription factors. Cell *103*, this issue, 63–74.

Higashijima, S., Kojima, T., Michiue, T., Ishimaru, S., Emori, Y., and Saigo, K. (1992). Dual *Bar* homeo box genes of *Drosophila* required in two photoreceptor cells, R1 and R6, and primary pigment cells for normal eye development. Genes Dev. *6*, 50–60.

Huang, J.-D., Schwyter, D.H., Shirokawa, J.M., and Courey, A.J. (1993). The interplay between multiple enhancer and silencer elements defines the pattern of *decapentaplegic* expression. Genes Dev. *7*, 694–704.

Ito, K., Awano, W., Suzuki, K., Hiromi, Y., and Yamamoto, D. (1997). The *Drosophila* mushroom body is a quadruple structure of clonal units each of which contains a virtually identical set of neurones and glial cells. Development *124*, 761–771.

Kamachi, Y., Ogawa, E., Asano, M., Ishida, S., Murakami, Y., Satake, M., Ito, Y., and Shigesada, K. (1990). Purification of a mouse nuclear factor that binds to both the A and B cores of the polyomavirus enhancer. J. Virol. *64*, 4808–4819.

Kauffmann, R.C., Li, S., Gallagher, P.A., Zhang, J., and Carthew, R.W. (1996). Ras1 signaling and transcriptional competence in the R7 cell of *Drosophila*. Genes Dev. *10*, 2167–2178.

Kavaler, J., Fu, W., Duan, H., Noll, M., and Posakony, J.W. (1999). An essential role for the *Drosophila Pax2* homolog in the differentiation of adult sensory organs. Development *126*, 2261–2272.

Kimmel, B.E., Heberlein, U., and Rubin, G.M. (1990). The homeo domain protein *rough* is expressed in a subset of cells in the developing *Drosophila* eye where it can specify photoreceptor cell subtype. Genes Dev. *4*, 712–727.

Kumar, J., and Moses, K. (1997). Transcription factors in eye development: a gorgeous mosaic? Genes Dev. *11*, 2023–2028.

Kumar, J.P., Tio, M., Hsiung, F., Akopyan, S., Gabay, L., Seger, R., Shilo, B.-Z., and Moses, K. (1998). Dissecting the roles of the *Drosophila* EGF receptor in eye development and MAP kinase activation. Development *125*, 3875–3885.

Lawrence, P.A., and Green, S.M. (1979). Cell lineage in the developing retina of *Drosophila*. Dev. Biol. *71*, 142–152.

Lesokhin, A.M., Yu, S.-Y., Katz, J., and Baker, N.E. (1999). Several levels of EGF receptor signaling during photoreceptor specification in wild-type, *Ellipse*, and null mutant *Drosophila*. Dev. Biol. *205*, 129–144.

Lindsley, D.L., and Zimm, G.G. (1992). The Genome of *Drosophila melanogaster*. (San Diego: Academic Press).

Matsuno, K., Go, M.J., Sun, X., Eastman, D.S., and Artavanis-Tsakonas, S. (1997). Suppressor of Hairless-independent events in Notch signaling imply novel pathway elements. Development *124*, 4265–4273.

Nellesen, D.T., Lai, E.C., and Posakony, J.W. (1999). Discrete enhancer elements mediate selective responsiveness of *Enhancer of split* Complex genes to common transcriptional activators. Dev. Biol. *213*, 33–53.

Nye, J.A., Petersen, J.M., Gunther, C.V., Jonsen, M.D., and Graves, B.J. (1992). Interaction of murine Ets-1 with GGA-binding sites establishes the ETS domain as a new DNA-binding motif. Genes Dev. *6*, 975–990.

O'Neill, E.M., Rebay, I., Tjian, R., and Rubin, G.M. (1994). The activities of two Ets-related transcription factors required for *Drosophila* eye development are modulated by the Ras/MAPK pathway. Cell *78*, 137–147.

Papayannopoulos, V., Tomlinson, A., Panin, V.M., Rauskolb, C., and Irvine, K.D. (1998). Dorsal-ventral signaling in the *Drosophila* eye. Science *281*, 2031–2034.

Ready, D.F., Hanson, T.E., and Benzer, S. (1976). Development of the *Drosophila* retina, a neurocrystalline lattice. Dev. Biol. *53*, 217–240.

Rebay, I., and Rubin, G.M. (1995). Yan functions as a general inhibitor of differentiation and is negatively regulated by activation of the Ras1/MAPK pathway. Cell *81*, 857–866.

Tio, M., and Moses, K. (1997). The *Drosophila* TGFα homolog Spitz acts in photoreceptor recruitment in the developing retina. Development *124*, 343–351.

Tomlinson, A., and Ready, D.F. (1987). Neuronal differentiation in the *Drosophila* ommatidium. Dev. Biol. *120*, 366–376.

Wolff, T., and Ready, D.F. (1991). The beginning of pattern formation in the *Drosophila* compound eye: the morphogenetic furrow and the second mitotic wave. Development *113*, 841–850.

Wotton, D., Ghysdael, J., Wang, S., Speck, N.A., and Owen, M.J. (1994). Cooperative binding of Ets-1 and core binding factor to DNA. Mol. Cell. Biol. *14*, 840–850.

Xu, T., and Rubin, G.M. (1993). Analysis of genetic mosaics in developing and adult *Drosophila* tissues. Development *117*, 1223–1237.

Xu, C., Kauffmann, R.C., Zhang, J., Kladny, S., and Carthew, R.W. (2000). Overlapping activators and repressors delimit transcriptional response to receptor tyrosine kinase signals in the *Drosophila* eye. Cell *103*, this issue, 87–97.

Yuh, C.-H., Bolouri, H., and Davidson, E.H. (1998). Genomic cis-regulatory logic: experimental and computational analysis of a sea urchin gene. Science *279*, 1896–1902.

Zipursky, S.L., and Rubin, G.M. (1994). Determination of neuronal cell fate: lessons from the R7 neuron of *Drosophila*. Ann. Rev. Neurosci. *17*, 373–397.

LETTER

doi:10.1038/nature09566

Planar polarized actomyosin contractile flows control epithelial junction remodelling

Matteo Rauzi[1]†, Pierre-François Lenne[1] & Thomas Lecuit[1]

Force generation by Myosin-II motors on actin filaments drives cell and tissue morphogenesis[1–15]. In epithelia, contractile forces are resisted at apical junctions by adhesive forces dependent on E-cadherin[16], which also transmits tension[6,17–19]. During *Drosophila* embryonic germband extension, tissue elongation is driven by cell intercalation[20], which requires an irreversible and planar polarized remodelling of epithelial cell junctions[4,5]. We investigate how cell deformations emerge from the interplay between force generation and cortical force transmission during this remodelling in *Drosophila melanogaster*. The shrinkage of dorsal–ventral-oriented ('vertical') junctions during this process is known to require planar polarized junctional contractility by Myosin II (refs 4, 5, 7, 12). Here we show that this shrinkage is not produced by junctional Myosin II itself, but by the polarized flow of medial actomyosin pulses towards 'vertical' junctions. This anisotropic flow is oriented by the planar polarized distribution of E-cadherin complexes, in that medial Myosin II flows towards 'vertical' junctions, which have relatively less E-cadherin than transverse junctions. Our evidence suggests that the medial flow pattern reflects equilibrium properties of force transmission and coupling to E-cadherin by α-Catenin. Thus, epithelial morphogenesis is not properly reflected by Myosin II steady state distribution but by polarized contractile actomyosin flows that emerge from interactions between E-cadherin and actomyosin networks.

The planar polarized remodelling of cell junctions[4,5] that occurs during germband extension (GBE) is shown in Fig. 1a. Myosin II (Myo-II) is concentrated in 'vertical' junctions[4,21] and directs junction shrinkage by increasing junctional tension[7,12]. To understand how Myo-II planar polarity is established, we investigated changes in Myo-II distribution at the onset of GBE. We used a fusion between Myo-II regulatory light chain (MRLC, called Sqh in *Drosophila*) and Cherry (MRLC–Cherry)[15] together with E-cad–GFP to mark adherens junctions (AJs). When the epithelium is formed, MRLC–Cherry is visible in aggregates in the medial region of AJs (Fig. 1b). Subsequently, MRLC–Cherry is also detected at the cortex of AJs of intercalating cells (Fig. 1b). An MRLC–GFP fusion rescuing a null sqh^{AX3} mutant (Fig. 1c) and an antibody against endogenous Myo-II heavy chain (not shown) displayed the same features. Thus two Myo-II populations exist during cell intercalation: a medial and a junctional pool (Supplementary Fig. 1). Labelling of F-actin with Utrophin–GFP (Utr–GFP) shows a network spanning the AJs (Fig. 1d, Supplementary Fig. 1, Supplementary Movie 1a). This network is thin (<500 nm), and contains filaments at low density (mesh size 0.5–2 μm) that overlap and intersect in the form of brighter puncta, which are more apparent in a slightly less apical focal plane intersecting the AJs (Supplementary Movie 1b, Supplementary Fig. 1). Thus, both Myo-II pools are part of a large-scale actomyosin network, spanning multiple cells, which contrasts with previous descriptions focused on junctional actin and Myo-II (refs 4, 5, 7, 12, 18, 21–23).

Live imaging of Utr–GFP and MRLC–GFP indicated complex dynamics (Supplementary Movies 1a, b and 2). The F-actin mesh fluctuated, with the mesh changing size in a few tens of seconds (Fig. 1d and Supplementary Movie 1a, b). Myo-II formed small clusters (presumably Myo-II minifilaments), which coalesced into large (~1 μm) medial aggregates on similar timescales (Fig. 1e, Supplementary Movie 2). Co-imaging of Utr–GFP and MRCL–Cherry revealed

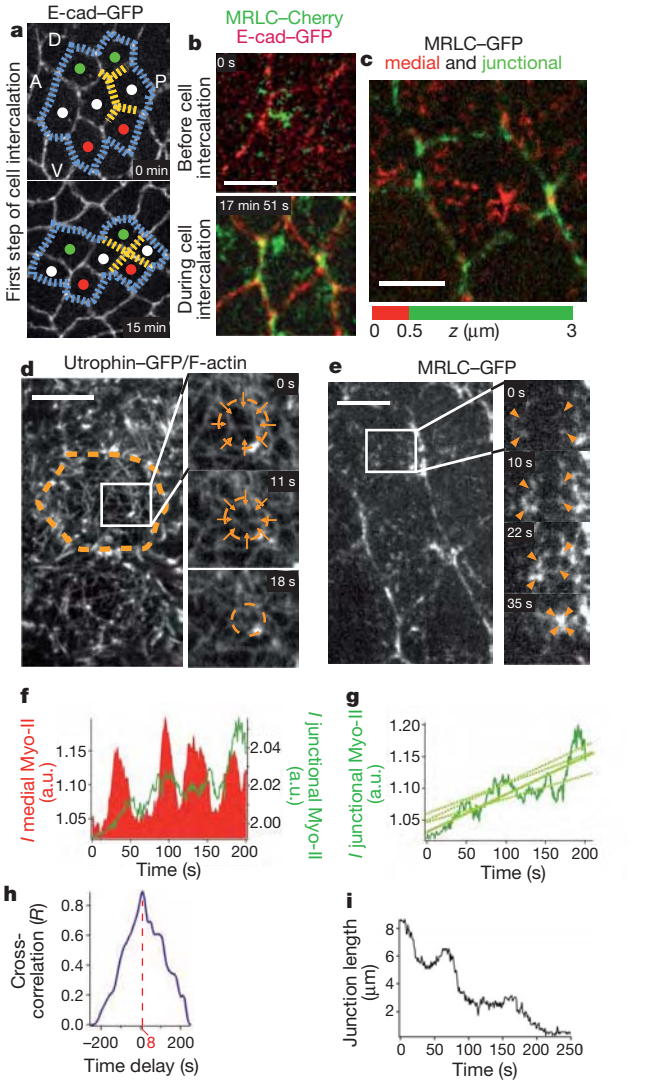

Figure 1 | Two pulsating pools of acto-myosin in intercalating cells. **a**, Polarized junction shrinkage during cell intercalation. A, P, D and V denote respectively dorsal, ventral, anterior and posterior. **b**, Localization of Myo-II and E-cad before and during intercalation. **c**, Respective distribution of medial (red) and junctional (green) Myo-II along the apico-basal (*z*) axis. **d**, **e**, Apical F-actin coalesces locally (**d**, magnified in right panels, arrows), while medial Myo-II clusters (**e**, magnified in right panels, arrowheads). **f**, Myo-II pulses in the medial (red) and junctional (green) regions. **g**, Average junctional Myo-II (dark green) and linear fits for different junctions. **h**, Temporal cross-correlation of the curves in **f**. *R* is the correlation coefficient. **i**, Evolution of junctional length. Scale bars, 5 μm.

[1]IBDML, UMR6216 CNRS-Université de la Méditerranée, Campus de Luminy, case 907, 13288 Marseille Cedex 09, France. †Present address: EMBL, Meyerhofstrasse 1, 69126 Heidelberg, Germany.

that actin and Myo-II coalesce together during aggregation (Supplementary Fig. 2a, Supplementary Movie 3; Methods), reflecting local and transient contractions within the actomyosin network, as also reported in the *Drosophila* mesoderm and the one-cell stage *Caenorhabditis elegans* cortex[15,24].

To further investigate the functions of the medial and junctional Myo-II networks, we monitored their temporal evolution during intercalation (Fig. 1f–i). Both medial and junctional Myo-II, respectively in the vicinity of and at shrinking junctions, fluctuated in intensity (Fig. 1f). In addition to being pulsed, the intensity of junctional Myo-II gradually increased (Fig. 1g). Meanwhile, the changes in 'vertical' junction length are irregular, showing successive steps of shrinkage and arrest (Fig. 1i). In some cases, however, transient relaxation was observed (17.6%, $N = 17$).

To disentangle this complex behaviour and relate contractile dynamics of medial and junctional networks with junction shrinkage, we conducted temporal cross-correlation of fluorescence intensity (Online Methods). Correlation between temporal profiles of MRLC–GFP intensity at the junctions and in the medial regions is high (mean $<R> = 0.86$, Fig. 1h), indicative of similar overall dynamics. Moreover, medial pulses precede junctional pulses by 8 ± 4 s (mean $\pm$ s.d. hereafter, Fig. 1h and Supplementary Fig. 3).

We then compared rates of junction shrinkage with rates of MRLC–GFP intensity changes (Fig. 2a left), which correspond to local accumulations of Myo-II by contraction (Fig. 1e). The maximum of the MRLC–GFP contraction rate in the medial region precedes that of junctional MRLC–GFP by an average of 10.5 ± 2.5 s (Fig. 2b left). Thus contraction of Myo-II occurs in the medial region first and subsequently at junctions (Fig. 2b left, right). Each step of junction shrinkage was associated with tandem medial and junctional Myo-II pulses (Fig. 2a right, horizontal braces). Temporal cross-correlation indicated that the peak rate of junction shrinkage precedes that of junctional Myo-II accumulation by 9 ± 3 s (Fig. 2b left), indicating that junctional Myo-II accumulation cannot cause the shrinkage steps. However, peak junction shrinkage rate temporally coincided with the peak rate of medial Myo-II contraction (Fig. 2b left, right) suggesting a mechanical contribution to shrinkage increments.

To test this, we used laser nanodissection[12] to locally disrupt medial Myo-II clusters at the vicinity of shrinking junctions. Each ablation pulse produced a collapse of the Myo-II pulse and a transient and reversible relaxation of junction length without affecting junctional Myo-II (Fig. 2c left, right, Supplementary Movie 4). Thus, medial Myo-II mechanically causes junction shrinkage. This led us to investigate the function of junctional Myo-II pulses, as previous studies showed it was essential for global junction shrinkage[4,7,12]. Close inspection reveals two situations: (1) in most cases (88%, $N = 17$), medial Myo-II pulses are followed by junctional pulses, and shrinkage steps proceed successfully without relaxation (14/15 cases, Fig. 2a right); (2) occasionally, (12%) medial pulses are not followed by junctional pulses and shrinkage steps relax in all cases (Fig. 2d). Relaxation correlates with failure to sustain junctional Myo-II and with an overall decrease of Myo-II at junctions (Fig. 2d left, right). This suggests that junctional Myo-II stabilizes junction length.

Together these observations point to a mechanical 'division of labour', where medial Myo-II pulses shrink, and sustained junctional Myo-II accumulation stabilizes, junction length. This iterative cycle ensures persistent shrinkage.

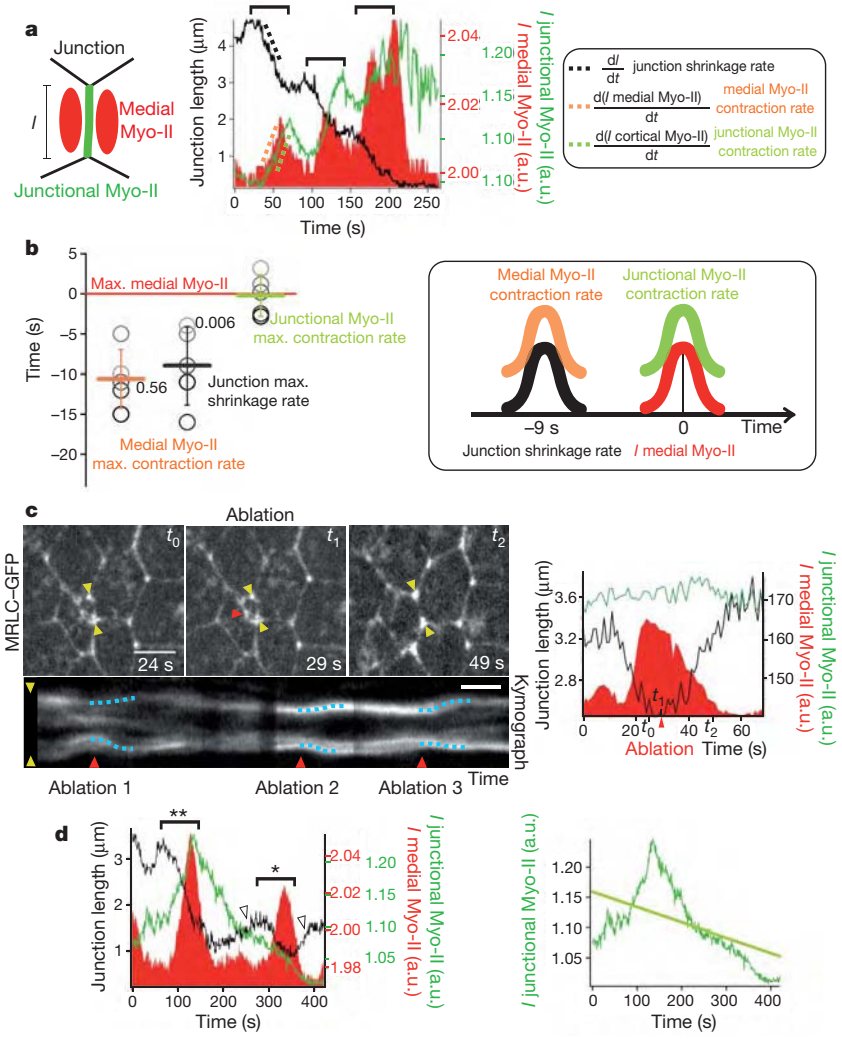

Figure 2 | Medial and junctional Myo-II pools have different mechanical roles. **a**, Left: cartoon depicting a vertical junction (length *l*) and regions where medial and junctional Myo-II are measured. Right: evolution of junction length and Myo-II intensities (*I*). Brackets show clusters of events and dashed lines represent the rates of changes. **b**, Time delays using medial Myo-II intensity maximum as a reference. Mean and s.d. are shown in the left panel. **c**, Left: evolution of a junction (between yellow arrowheads) before (t_0), during (t_1) and after (t_2) focal ablation of a Myo-II pulse (red arrowhead). Bottom, kymograph of the same junction with three ablation events (red arrowheads). Blue dashed lines mark junction relaxation. Scale bar, 25 s. Right: length of junction (from **c**, left) and medial and junctional Myo-II intensity as a function of time. The red arrowhead marks the ablation. **d**, Left: junction relaxation (arrowheads) when a medial pulse is not followed by a junctional pulse (*) or when junctional Myo-II is not sustained (**). Right: junctional Myo-II intensity (dark green) and linear fit (light green). Scale bars in **c**, 5 μm.

These observations suggested that both processes may be spatially coordinated. Indeed, medial pulses show a planar polarized distribution like junctional Myo-II. Defining four quadrants (anterior, A; posterior, P; dorsal, D; and ventral, V; diagram in Fig. 3a right) in the medial region of cells, we determined the integrated intensity ratio of (A+P)/(D+V) MRLC–GFP in time series (Fig. 3a left). Intercalating germband cells exhibit a significant medial Myo-II polarity compared to non-intercalating head cells or to germband cells of *Krüppel*(*Kr*) RNAi embryos where planar cell polarization is affected[4,20] (Fig. 3a left, Supplementary Movie 6).

We next investigated the spatial dynamics of medial and junctional actomyosin networks. Co-imaging of Utr–GFP and MRLC–Cherry and particle imaging velocimetry (PIV) indicated that F-actin and Myo-II have very similar dynamics and that actomyosin clusters flow in the plane of the medial region (Fig. 3b, Supplementary Movie 3). Myo-II was moving slightly (22%) but consistently faster than F-actin (Supplementary Fig. 5), in agreement with the idea that Myo-II is responsible for flow.

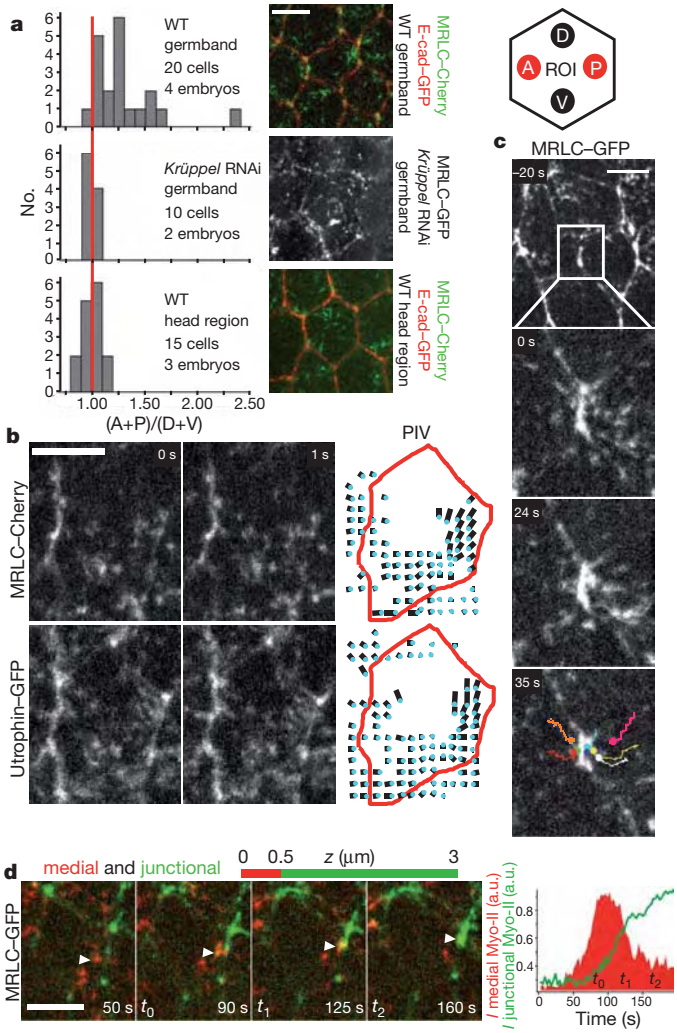

Figure 3 | Medial Myosin-II displays anisotropic flow and feeds 'vertical' junctions. **a**, Left: histograms of medial Myo-II relative intensities in (A+P) regions over (D+V) regions (see diagram at right for nomenclature) in the germband of wild-type (WT) and *Krüppel* (*Kr*) RNAi embryos, and the head of WT embryos. WT/*Kr*RNAi: $P = 0.0007$, WT(germband)/WT(head): $P = 0.001$ (T-student). Right; representative images of cells with MRCL–Cherry and E-cad–GFP. **b**, Comparative PIV of Utr–GFP and MRLC–Cherry in a cell outlined in red. Blue dots mark vector tips. **c**, Medial Myo-II flowing to a vertical junction. Tracking of speckles is showed in coloured lines (right). **d**, Left: a medial cluster (red, arrowhead) flows and fuses to the junctional Myo-II pool (green); right: corresponding quantification. Scale bars, 5 μm.

Tracking of Myo-II speckles (Fig. 3c, Supplementary Movies 2, 5) or of F-actin with Myo-II (Supplementary Fig. 2b) indicated that the polarized distribution of medial Myo-II results from the lateral flow of medial pulses towards 'vertical' junctions. In *Kr*RNAi embryos, this movement occurred randomly (Supplementary Movie 6), consistent with the loss of medial Myo-II polarity (Fig. 3a left).

The polarized flow of Myo-II ($0.11 \pm 0.03\ \mu m\ s^{-1}$) could either reflect a movement of Myo-II minifilaments or the propagation of contractile waves. We tested these alternatives by photobleaching medial MRLC–GFP clusters. The fluorescence recovery in the bleached area (recovery fractions $34 \pm 10\%$ ($N = 5$), $\tau_{1/2} = 4 \pm 1$ s, Supplementary Fig. 6a, b, d) was low compared to the junctions (recovery fractions ~70% (ref. 8), not shown). Moreover, no new cluster appears in the vicinity of bleached pulses, as would be expected for contractile waves (Supplementary Fig. 6a). Together this indicates that medial flows correspond to the movement of relatively stable Myo-II filaments. Fluorescence recovery after photobleaching (FRAP) experiments with Utr–GFP show extensive ($83 \pm 22\%$, $N = 5$) turnover within <3 s (Supplementary Fig. 6c, d), suggesting that the actomyosin flow is mainly determined by Myo-II contractility on a fast-recycling, 'permissive' actin substrate.

We then addressed whether medial pulses are transferred to the junctional cortex and cause the formation of junctional pulses. As medial MRLC–GFP is slightly (500–1,000 nm) more apical than junctional MRLC–GFP, confocal sections distinguished the two pools and showed fusion of medial Myo-II (red) to the cortex and formation of a junctional pulse (green) (Fig. 3d left, right; Supplementary Movie 7). No transfer of medial pulses occurred to the adjacent junction following their ablation (Fig. 2c right). Moreover, photobleaching of MRLC–GFP along a junction (Supplementary Fig. 7a, b; Supplementary Movie 8) indicates two sources of exchange: pre-existing Myo-II patches are rapidly and strongly recovered ($72 \pm 6\%$), consistent with previous reports[7]; new junctional patches form *de novo* where medial Myo-II clusters fuse with junctions.

Junctional Myo-II pulses are delayed by ~8 s relative to medial ones (Supplementary Fig. 3), reflecting a speed of transfer of $\sim 0.125\ \mu m\ s^{-1}$, which is similar to the direct flow speed measurements ($0.11 \pm 0.03\ \mu m\ s^{-1}$).

Thus, medial and junctional actomyosin networks have tightly coordinated and hierarchically organized mechanical functions. Medial pulses flow to and produce steps of shrinkage of the adjacent 'vertical' junctions. They subsequently fuse with junctions and sustain junctional Myo-II accumulation, which stabilizes junction length. This flow and transfer are planar polarized, and drive junctional planar polarity and cell intercalation.

What controls the planar polarized flow of medial Myo-II pulses to vertical junctions? Mechanical anchoring of actomyosin networks at AJs is essential for force production during cell morphogenesis[6,17–19,25]. The medial network is also potentially connected to the apical plasma membrane given its tight apposition (Supplementary Fig. 8). Imaging of the apical plasma membrane with palmitoylated YFP (GAP43–Venus) revealed however a flat apical surface in the medial part of intercalating cells with few, small protrusions (Supplementary Fig. 9, Supplementary Movie 9), unlike apically constricting mesoderm cells where the plasma membrane is strongly ruffled (Supplementary Movie 10). These protrusions display local jitter but no aggregation or flow patterns characteristic of the underlying actomyosin network, suggesting moderate coupling (Supplementary Fig. 9, Supplementary Movie 9). Co-imaging of GAP43–Cherry and Utr–GFP shows that small protrusions and F-actin had un-correlated trajectories (Supplementary Movie 11) or moved at different speeds (Supplementary Movie 12; 3.7-fold reduced lateral dynamics ($0.03 \pm 0.015\ \mu m\ s^{-1}$, Supplementary Fig. 9) compared to MRLC–GFP or Utr–GFP ($0.11 \pm 0.03\ \mu m\ s^{-1}$, Fig. 3c)). Therefore, the apical surface and the medial actomyosin network are in contact but moderately coupled.

This suggested that the anisotropic actomyosin flow may largely depend on the distribution of junctional anchoring points. This requires E-cadherin/β-Catenin complexes at AJs and depends on α-Catenin[18,26]. E-cadherin/β-Catenin/α-Catenin complexes are planar polarized[5] (not shown), such that medial pulses flow towards regions with lower amounts of E-cadherin complexes. The level of E-cadherin along 'vertical' relative to adjacent junctions (E-cadherin anisotropy, Fig. 4a left) is also fluctuating (Fig. 4a middle). Moreover, the onset of medial pulses coincided with the time when E-cadherin anisotropy reached a local maximum (Fig. 4a middle, right) raising the possibility that E-cadherin anisotropy may orient the actomyosin flow. Reduction of E-cadherin by RNAi causes the disappearance of medial Myo-II (Fig. 4b top, c top; Supplementary Movies 13, 14). The junctional Myo-II level is consequently strongly reduced and no longer planar polarized (Fig. 4b bottom, c bottom). We reasoned that reducing the levels of α-Catenin by RNAi should attenuate coupling more subtly. α-Catenin RNAi reduces the number of E-cadherin clusters at AJs and disrupts interactions with junctional F-actin[18]. Moreover, the distribution of E-cadherin is no longer planar polarized in α-CateninRNAi embryos (Fig. 4e, Supplementary Fig. 10). This is associated with a loss of medial (Fig. 4f, Supplementary Movie 15) and junctional (Fig. 4d top, bottom) Myo-II planar polarity. Thus, the planar polarized distribution of E-cadherin/β-Catenin/α-Catenin complexes biases the flow of medial Myo-II and junctional polarization.

In addition to Myo-II contractility, flow requires (1) crosslinkers between filaments to transmit tension within the medial meshwork, and (2) coupling at the cortex to E-cadherin/β-Catenin/α-Catenin complexes. Increased levels of E-cadherin in 'transverse' junctions may change properties of the actin network (for example, crosslinking/viscosity) and inhibit internal transmission of contractile forces and hence prevent D–V oriented flow. To test this, we disrupted the force balance within the medial actomyosin network by focal ablation (Fig. 4g top, bottom), and imaged the redistribution of medial clusters. If increased E-cadherin levels at transverse junctions inhibit tension transmission along the D–V axis, then medial pulses should not flow in this direction following ablation. However, we observed that Myo-II medial clusters flowed radially and away from the point of ablation towards the junctions (velocity $v = 0.05 \pm 0.01\ \mu m\ s^{-1}$) in 100% of cases ($N = 25$), even towards transverse junctions (12/25 cases, Fig. 4g top, bottom; Supplementary Fig. 11; Supplementary Movie 16). Focal ablation of the actin meshwork produces a local hole, which expands radially (Supplementary Movie 17). This argues that transverse

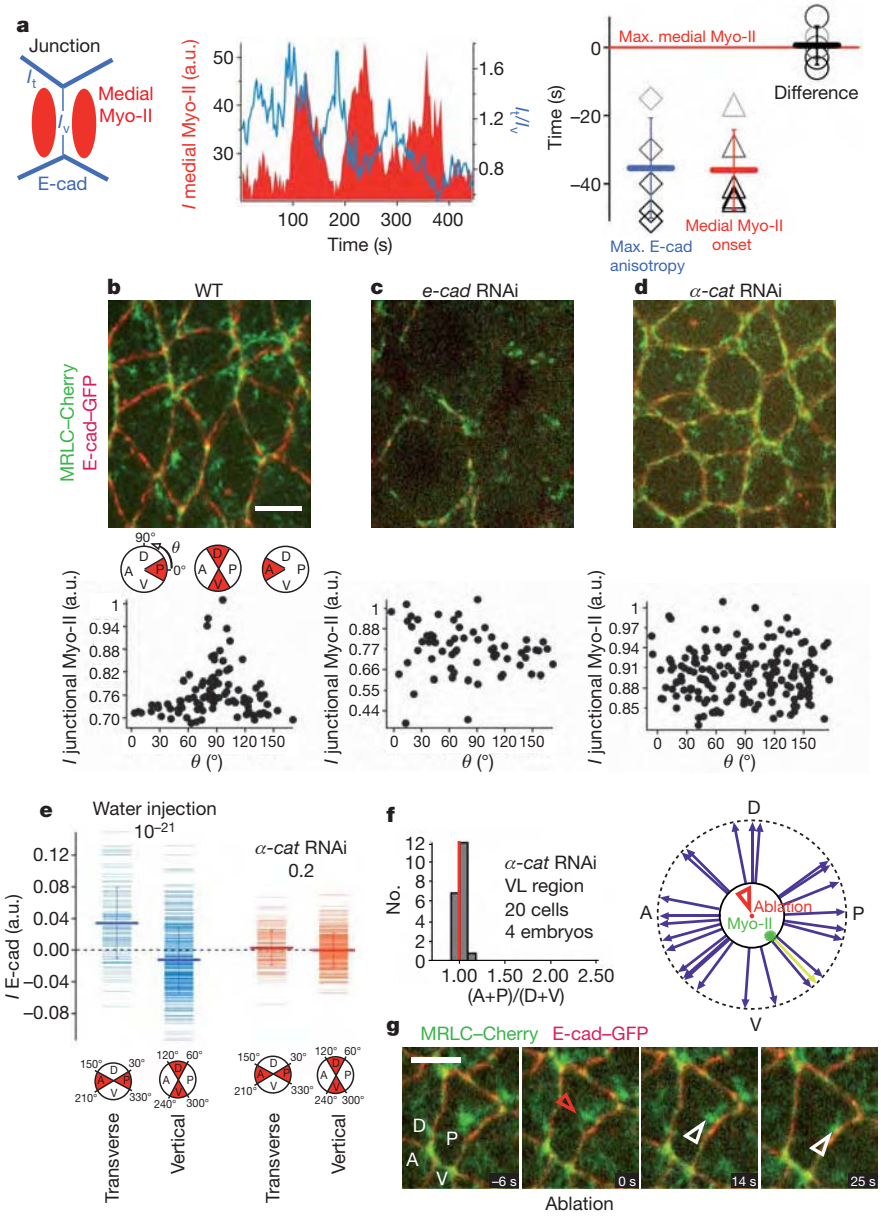

Figure 4 | E-cadherin planar polarity orients medial Myosin-II flow. **a**, Left and middle: medial MRLC–Cherry average intensity (red) and E-cad–GFP polarity (blue) as a function of time. E-cad–GFP polarity is the ratio of its mean intensity in transverse (I_t) and vertical (I_v) junctions. Right: chronology of events taking as a reference medial Myo-II intensity maximum. Delays between events are obtained by correlation; shown are mean and s.d. The difference is in black. **b–d**, Top row: Myo-II and E-cad in control (**b**), *e-cad* RNAi (**c**) and *α-cat* RNAi (**d**) embryos. Bottom row: average intensity of junctional Myo-II as a function of the angle (θ) of the junctions with respect to the A/P axis. **e**, Top: Comparison between normalized E-cad–GFP average intensity ($=(I_j - \bar{I})/\bar{I}$) of transverse versus vertical junctions for water injected (blue) and *α-cat* RNAi embryos (orange); P values are shown (Student's T test). I_j, mean intensity at a junction; $\bar{I}$, mean intensity of all junctions in a cell. Diagram at bottom indicates the angles of vertical and transverse junctions with respect to the A–P axis. **f**, Histogram of average medial Myo-II intensity as in Fig. 2a, right, for *α-cat* RNAi embryos. WT/*α-cat* RNAi: $P = 0.0006$ (Student's T test). **g**, Bottom: movement of a Myo-II cluster (white arrowhead) following nearby focal ablation (red arrowhead). Top right: diagram showing the centrifugal directions of the trajectories followed by Myo-II clusters ($N = 25$). Scale bars, 5 μm.

junctions do not inhibit flow *per se* and that flow directionality emerges from the properties of the actomyosin meshwork integrated over the entire apical surface.

The mechanical properties of the medial actomyosin network are locally defined by Myo-II contractility (concentration, affinity, duty cycle), tension transmission within the network (crosslinking), and viscous resistance to deformations (interactions between filaments)[27,28]. Moreover, these properties fluctuate owing to protein turnover and interactions. E-cadherin is known to anchor[18,26] and modify actin dynamics[29,30]. Our results suggest that the polarized distribution of E-cadherin may control the actomyosin flow pattern by spatially modulating mechanical properties of the actin network.

Current models of epithelial morphogenesis centre on Myo-II steady state distribution and associated contractile forces[1,2,4,5,7,10,12,14,15]. Our data show however that cell deformations cannot be simply derived from the Myo-II distribution itself, but from two central features of actomyosin dynamics, namely concentration (pulses) and movement (flow). Pulsed dynamics defines the rhythm and possibly the speed of deformation. Flow pattern, which in the case of intercalation is anisotropic, dictates the orientation of cell deformation (Supplementary Fig. 12). Flows of Myo-II foci have been reported in the one-cell stage *C. elegans* embryo[22,24], pointing to a more general property of actomyosin networks[15,23]. An important future avenue of research will be to investigate what properties of actin networks control Myo-II flow dynamics in different systems.

METHODS SUMMARY

Mutants and constructs. To visualize Myosin-II we used MRLC fused to eGFP or mCherry and rescuing a protein null sqh^{AX3} mutant. The following stocks were used: sqh^{AX3}*; sqh-MRLC::GFP (II)* and sqh^{AX3}*; ubi-e-cad::GFP, sqh-MRLC::mCherry*. The plasmid coding for the fusion of eGFP and the actin binding domain of human Utrophin was obtained from W. Bement. The Utr–GFP clone was cloned by PCR in a pUASp destination vector (Fig. 1, Supplementary Fig. 1, Supplementary Movies 1a, b) or under the *sqh* promoter (Fig. 3, Supplementary Fig. 2, Supplementary Movie 3). The construct were verified by sequencing. To label the plasma membrane, we used a fusion between the palmitoylated GAP43 protein and YFP/Venus expressed by the GAL4/UAS system with the maternal tubGAL4VP16 driver line. GAP43–Cherry was expressed under the *sqh* promoter.

RNA interference. We generated by PCR dsRNA probes directed against *Krüppel*, *α-catenin* and *e-cadherin* as described in refs 4, 18.

Time-lapse imaging. Embryos were prepared and imaged using a spinning disc confocal system (Perkin Elmer) on an inverted Nikon microscope with 100× oil immersion objective. Nano-ablation was performed using a home-built set-up[12]. Fluorescence recovery after photobleaching (FRAP) measurements were performed as in Supplementary Fig. 6 using a confocal LSM510 (Zeiss) with a Plan-Apochromat 100× oil objective and an argon laser (488 nm).

Image analysis and quantifications. Intensity measurements, cross-correlation analysis, time-delays analysis and PIV analysis are detailed in Online Methods and in Supplementary Figs 3, 4.

Full Methods and any associated references are available in the online version of the paper at www.nature.com/nature.

Received 2 April; accepted 8 October 2010.
Published online 10 November 2010.

1. Lecuit, T. & Lenne, P. F. Cell surface mechanics and the control of cell shape, tissue patterns and morphogenesis. *Nature Rev. Mol. Cell Biol.* **8,** 633–644 (2007).
2. Montell, D. J. Morphogenetic cell movements: diversity from modular mechanical properties. *Science* **322,** 1502–1505 (2008).
3. Hutson, M. S. *et al.* Forces for morphogenesis investigated with laser microsurgery and quantitative modeling. *Science* **300,** 145–149 (2003).
4. Bertet, C., Sulak, L. & Lecuit, T. Myosin-dependent junction remodelling controls planar cell intercalation and axis elongation. *Nature* **429,** 667–671 (2004).
5. Blankenship, J. T., Backovic, S. T., Sanny, J. S., Weitz, O. & Zallen, J. A. Multicellular rosette formation links planar cell polarity to tissue morphogenesis. *Dev. Cell* **11,** 459–470 (2006).
6. Dawes-Hoang, R. E. *et al.* Folded gastrulation, cell shape change and the control of myosin localization. *Development* **132,** 4165–4178 (2005).
7. Fernandez-Gonzalez, R., Simoes Sde, M., Roper, J. C., Eaton, S. & Zallen, J. A. Myosin II dynamics are regulated by tension in intercalating cells. *Dev. Cell* **17,** 736–743 (2009).
8. Hildebrand, J. D. Shroom regulates epithelial cell shape via the apical positioning of an actomyosin network. *J. Cell Sci.* **118,** 5191–5203 (2005).
9. Krieg, M. *et al.* Tensile forces govern germ-layer organization in zebrafish. *Nature Cell Biol.* **10,** 429–436 (2008).
10. Monier, B., Pelissier-Monier, A., Brand, A. H. & Sanson, B. An actomyosin-based barrier inhibits cell mixing at compartmental boundaries in *Drosophila* embryos. *Nature Cell Biol.* **12,** 60–65 (2010).
11. Nishimura, T. & Takeichi, M. Shroom3-mediated recruitment of Rho kinases to the apical cell junctions regulates epithelial and neuroepithelial planar remodeling. *Development* **135,** 1493–1502 (2008).
12. Rauzi, M., Verant, P., Lecuit, T. & Lenne, P. F. Nature and anisotropy of cortical forces orienting *Drosophila* tissue morphogenesis. *Nature Cell Biol.* **10,** 1401–1410 (2008).
13. Skoglund, P., Rolo, A., Chen, X., Gumbiner, B. M. & Keller, R. Convergence and extension at gastrulation require a myosin IIB-dependent cortical actin network. *Development* **135,** 2435–2444 (2008).
14. Landsberg, K. P. *et al.* Increased cell bond tension governs cell sorting at the *Drosophila* anteroposterior compartment boundary. *Curr. Biol.* **19,** 1950–1955 (2009).
15. Martin, A. C., Kaschube, M. & Wieschaus, E. F. Pulsed contractions of an actin-myosin network drive apical constriction. *Nature* **457,** 495–499 (2009).
16. Nishimura, T. & Takeichi, M. Remodeling of the adherens junctions during morphogenesis. *Curr. Top. Dev. Biol.* **89,** 33–54 (2009).
17. Gorfinkiel, N. & Arias, A. M. Requirements for adherens junction components in the interaction between epithelial tissues during dorsal closure in *Drosophila*. *J. Cell Sci.* **120,** 3289–3298 (2007).
18. Cavey, M., Rauzi, M., Lenne, P. F. & Lecuit, T. A two-tiered mechanism for stabilization and immobilization of E-cadherin. *Nature* **453,** 751–756 (2008).
19. Sawyer, J. K., Harris, N. J., Slep, K. C., Gaul, U. & Peifer, M. The *Drosophila* afadin homologue Canoe regulates linkage of the actin cytoskeleton to adherens junctions during apical constriction. *J. Cell Biol.* **186,** 57–73 (2009).
20. Irvine, K. D. & Wieschaus, E. Cell intercalation during *Drosophila* germband extension and its regulation by pair-rule segmentation genes. *Development* **120,** 827–841 (1994).
21. Zallen, J. A. & Wieschaus, E. Patterned gene expression directs bipolar planar polarity in *Drosophila*. *Dev. Cell* **6,** 343–355 (2004).
22. Hird, S. N. & White, J. G. Cortical and cytoplasmic flow polarity in early embryonic cells of *Caenorhabditis elegans*. *J. Cell Biol.* **121,** 1343–1355 (1993).
23. Bertet, C., Rauzi, M. & Lecuit, T. Repression of Wasp by JAK/STAT signalling inhibits medial actomyosin network assembly and apical cell constriction in intercalating epithelial cells. *Development* **136,** 4199–4212 (2009).
24. Munro, E., Nance, J. & Priess, J. R. Cortical flows powered by asymmetrical contraction transport PAR proteins to establish and maintain anterior-posterior polarity in the early *C. elegans* embryo. *Dev. Cell* **7,** 413–424 (2004).
25. Martin, A. C., Gelbart, M., Fernandez-Gonzalez, R., Kaschube, M. & Wieschaus, E. F. Integration of contractile forces during tissue invagination. *J. Cell Biol.* **188,** 735–749 (2010).
26. Yonemura, S., Wada, Y., Watanabe, T., Nagafuchi, A. & Shibata, M. α-Catenin as a tension transducer that induces adherens junction development. *Nature Cell Biol.* **12,** 533–542 (2010).
27. Bendix, P. M. *et al.* A quantitative analysis of contractility in active cytoskeletal protein networks. *Biophys. J.* **94,** 3126–3136 (2008).
28. Koenderink, G. H. *et al.* An active biopolymer network controlled by molecular motors. *Proc. Natl Acad. Sci. USA* **106,** 15192–15197 (2009).
29. Kobielak, A., Pasolli, H. A. & Fuchs, E. Mammalian formin-1 participates in adherens junctions and polymerization of linear actin cables. *Nature Cell Biol.* **6,** 21–30 (2004).
30. Drees, F., Pokutta, S., Yamada, S., Nelson, W. J. & Weis, W. I. α-Catenin is a molecular switch that binds E-cadherin-β-catenin and regulates actin-filament assembly. *Cell* **123,** 903–915 (2005).

Supplementary Information is linked to the online version of the paper at www.nature.com/nature.

Acknowledgements We thank R. Levayer, M. Mavrakis and J.-M. Philippe for making and sharing respectively the utrophin–GFP, GAP43–Venus and GAP43–Cherry transgenic lines. We are grateful to our colleagues for their gifts of reagents: B. Bement, R. Karess, H. Oda, A. Martin and E. Wieschaus. We thank E. Munro and all members of the Lecuit and Lenne groups for discussions, and comments on the manuscript. This work was supported by a Programme Grant from HFSP to T.L, P.-F.L and E. Munro, by the CNRS, the Fondation pour la Recherche Médicale (to T.L), the ANR-Blanc 2005 (to T.L. and P.-F.L), Région PACA and ANR-PCV 2008 (to P.-F.L and T.L.). M.R. was supported by a PhD fellowship by the Région PACA and Amplitude Systems.

Author Contributions M.R. made the original observations of pulsed contractility and flow. M.R. and T.L. planned the project, and analysed the data together with P.-F.L.; M.R. conducted the experiments except for FRAP experiments on MRLC–GFP, which were performed by P.-F.L. and T.L.; P.-F.L. and M.R. developed the nano-ablation system. T.L. and P.-F.L. wrote the manuscript together with M.R. All authors commented on the manuscript.

Author Information Reprints and permissions information is available at www.nature.com/reprints. The authors declare no competing financial interests. Readers are welcome to comment on the online version of this article at www.nature.com/nature. Correspondence and requests for materials should be addressed to T.L. (lecuit@ibdml.univ-mrs.fr) or P.F.-L. (lenne@ibdml.univ-mrs.fr).

METHODS

Fly stocks and constructs. *Drosophila* MRLC is encoded by *spaghetti-squash (sqh)*. All experiments visualizing dynamics of MRLC were looking at MRLC fused to either eGFP or mCherry under the *sqh* promoter and rescuing a protein null sqh^{AX3} mutant[31]. E-cad–GFP was expressed under the ubiquitin promoter *ubi-Ecad::GFP* and rescues a null *e-cad/shotgun* mutant[32].

The following fly stocks were used. Figure 1, Supplementary Fig. 1 and Supplementary Movies 1a, b: matGAL4(67) UASp-Utr–GFP (recombinant on II). sqh^{AX3}*; sqh-MRLC::GFP (II)* (generous gift of R. Karess) and sqh^{AX3}*; ubi-E-cad::GFP, sqh-sqh::mCherry* (recombinant on II). Figure 3, Supplementary Fig. 2, Supplementary Movie 3: sqh^{AX3}*; sqh-MRLC::mCherry, sqh-Utr::GFP* (recombinant on II). *sqh-MRLC::mCherry* (on II) is a gift from A. Martin and E. Wieschaus.

The plasmid coding for the fusion of eGFP and the actin binding domain of human Utrophin was obtained from W. Bement[33]. The Utr–GFP fusion was PCR amplified and inserted in the p221DONR GATEWAY plasmid (Invitrogen). The fusion was recombined in a pUASp GATEWAY destination vector (pPW, from T. Murphy, Carnegie Institute) for expression under the maternal tubGAL4VP16 driver line (67Gal4) in Fig. 1, Supplementary Fig. 1 and Supplementary Movies 1a, b, or expression under the *sqh* promoter in Fig. 3, Supplementary Fig. 2 and Supplementary Movie 3. In the latter case, Utr–GFP expression is lower than under the Gal4 system, hence only reveals brighter structures (puncta) also visible in Supplementary Movie 1a and b and Fig. 1d and not individual filaments contrary to Fig. 1d.

To label the plasma membrane we used a fusion between the palmitoylated GAP43 protein and the YFP variant Venus[34] expressed by the GAL4 UAS system with the maternal tubGAL4VP16 driver line. GAP43–Cherry was constructed similarly and expressed under the *sqh* promoter as in ref. 31.

RNAi interference. We generated by PCR dsRNA probes directed against *Krüppel*, *α-catenin*, and *e-cadherin* using the following primers. The underlined sequence is the T7 promoter. The sequence not underlined corresponds to the template sequence. e-cadherin: 533 nucleotides, between +1475 to +2008 from ATG. E-cad-T7-F, taatacgactcactatagggagaccacgagtctctttgataatggcgagc. E-cad-T7-R, taatacgactcactatagggagaccacggtttccatcgttctggtgaatc. α-catenin: 728 nucleotides, between +81 to +808 from ATG. α-Cat-T7-F, taatacgactcactatagggcac aatgtcagttgaaaaaacacttg. α-Cat-T7-R, taatacgactcactatagggttgggatgactttccttgggc aac. Krüppel: 775 nucleotides, between +491 to +1266 from ATG. Kr-T7-F, taatacgactcactatagggagaccacggagtttcagaccgagatcagca. Kr-T7-R, taatacgactcactat agggagaccacagagctggctccatcttcagaca. Embryos were injected as described in ref. 35.

Time lapse imaging. Embryos were prepared and imaged as detailed in ref. 36, using a spinning disc confocal system (Perkin Elmer) on an inverted Nikon microscope with 100×/1.4 oil immersion objective.

Nano-ablation experiments. We performed nano-dissection experiments with a home-built system. A near-infrared (NIR, 1,030 nm) femtosecond (fs) laser at 50 MHz repetition rate (t-Pulse, Amplitude Systems) was coupled to an inverted microscope (Eclipse TE 2000-E, Nikon). A fast multicolour confocal imaging system, based on the Yokogawa spinning disk (Ultraview ERS, Perkin Elmer), was also mounted at a side port of the microscope. Local ablation and fast fluorescence imaging were thus possible simultaneously. The NIR-fs laser beam is expanded through a ×5 telescope and is aligned with the microscope optical path with a dichroic mirror (FF01-750/SP, Semrock) immediately below the objective lens (×60/1.2, water immersion, Plan Apo VC, Nikon). The collimated beam fills the back aperture of the objective lens which transmits 68% of the incoming NIR light. Nano-dissections of medial Myo-II were performed by exposing this structure to the tightly focused laser during 1–3 ms with an average power of 360 mW at the back aperture of the objective. Exposure time was controlled by an automated 1.5-mm-diameter mechanical shutter (LS2, Uniblitz). The sample was positioned over the tightly focused laser beam thanks to a computer-controlled mechanical stage (Scan IM with a Tango2-Desktop controller, Marzhaüser). A very similar set-up has already been shown to allow sub-cellular ablations[12].

Fluorescence intensity measurements. The intensity of the medial Myo-II is defined as the sum of average intensities of two regions of interest (ROIs) close to the junction (the centre of the elliptical ROIs were ~1 μm away from the junction, Fig. 2a in red). The intensity of the junctional Myo-II is defined as the average intensity of a 500-nm-wide stripe along the junction (Fig. 2a in green). The E-cad anisotropy is the average intensity of a 500-nm-wide stripe along transverse junctions divided by the average intensity measured along the vertical junction (Fig. 4a in blue). Intensity measurements were made by using ImageJ (1.39p version). Analysis were done on time lapse movies (one frame every 1–3 s). For each frame, 6–10 *z*-planes were imaged over 3 μm. For long time lapse imaging (>200 s), bleach correction was performed by using ImageJ.

Cross-correlation analysis. Cross-correlation was performed applying Igor Pro (Wavemetrics) cross-correlation function. This function is given by:

$$C(\tau) = \int_0^T f(t)g(t+\tau)\mathrm{d}t$$

where T represents the overall time over which measurements were made, $f(t)$ and $g(t)$ the two cross-correlated functions (taking f as reference), and τ the time delay.

The basal signal $f_{\min}$ and $g_{\min}$ were subtracted from f and g functions respectively before cross-correlation. The final cross-correlation function was normalized as follows:

$$C_N(\tau) = \frac{\int_0^T (f(t)-f_{\min})(g(t+\tau)-g_{\min})\mathrm{d}t}{\sqrt{\int_0^T (f(t)-f_{\min})^2\mathrm{d}t}\cdot\sqrt{\int_0^T (g(t)-g_{\min})^2\mathrm{d}t}}$$

Time delay measurements. In Fig. 2b all time delays were measured by cross-correlation. Cross-correlation analysis was assessed by performing a measure of delays between peaks for each cluster of events (for example, Fig. 2 shows three clusters of events) (see Supplementary Figs 1 and 2 top middle panel). When correlating with contraction rate functions, curves were smoothed by using a binomial algorithm implemented in Igor Pro software. For this analysis five cases of fully intercalating cells (corresponding to 15 clusters of events) were taken from five different wild-type MRLC–GFP embryos. Time lapse movies were taken at a rate of 1 frame s^{-1}. Each frame consisted in a *z*-stack of 3 μm (images spaced by 500 nm). Time lapse ranged between 200 and 500 s. Time delays in Fig. 4a, right, were determined as follows. The delay between the E-cad anisotropy peak and the medial Myo-II intensity peak was measured by cross-correlation (the medial Myo-II intensity curve was taken as reference). The time onset of medial Myo-II intensity pulses with respect to medial Myo-II intensity peak maxima was determined from the autocorrelation of the medial Myo-II intensity, which provides a measure of the average pulse duration, and therefore a measure of the average delay between pulse onset and pulse intensity peak. Auto-correlation analysis was assessed by performing a measure of delays for each cluster of events (see Supplementary Fig. 2 bottom) as for cross-correlation analysis. For this analysis five cases of intercalating cells were taken from five different wild-type MRLC–Cherry / E-cad–GFP embryos. Time lapse movies (one frame every 3 s) of both MRLC–Cherry and E-cad–GFP were taken. Each frame consisted of a *z*-stack of 3 μm (images spaced by 500 nm). Time lapse ranged between 200 and 500 s. Igor Pro software was used for all time delay measurements.

PIV analysis. PIV was determined with the Mathlab toolbox (procedure MatPIV) developed by J. K. Sveen.

Fluorescence recovery after photobleaching. Fluorescence recovery after photobleaching (FRAP) measurements were performed as in Supplementary Fig. 6 using a confocal LSM510 (Zeiss) with a Plan-Apochromat 100×/1.3 oil objective and an argon laser (488 nm). Before and after photobleaching, images were acquired at low laser power (0.1% AOTF, Acousto Optic Tunable Filter) to avoid bleaching and with a pixel size of 40 nm. Photobleaching was performed for 0.9 s at full laser power over an ROI with 1 μm diameter. Fluorescence recovery was then recorded for 50 s. In Supplementary Fig. 7, we used the photokinesis unit of a Perkin Elmer confocal system for FRAP and the region of interest is a line 5 μm long.

31. Royou, A., Field, C., Sisson, J. C., Sullivan, W. & Karess, R. Reassessing the role and dynamics of nonmuscle myosin II during furrow formation in early *Drosophila* embryos. *Mol. Biol. Cell* **15,** 838–850 (2004).
32. Oda, H. & Tsukita, S. Real-time imaging of cell-cell adherens junctions reveals that *Drosophila* mesoderm invagination begins with two phases of apical constriction of cells. *J. Cell Sci.* **114,** 493–501 (2001).
33. Burkel, B. M., von Dassow, G. & Bement, W. M. Versatile fluorescent probes for actin filaments based on the actin-binding domain of utrophin. *Cell Motil. Cytoskeleton* **64,** 822–832 (2007).
34. Mavrakis, M., Rikhy, R. & Lippincott-Schwartz, J. Plasma membrane polarity and compartmentalization are established before cellularization in the fly embryo. *Dev. Cell* **16,** 93–104 (2009).
35. Pilot, F., Philippe, J. M., Lemmers, C. & Lecuit, T. Spatial control of actin organization at adherens junctions by a synaptotagmin like protein Btsz. *Nature* **442,** 580–584 (2006).
36. Cavey, M. & Lecuit, T. Imaging cellular and molecular dynamics in live embryos using fluorescent proteins. *Methods Mol. Biol.* **420,** 219–238 (2008).

Cell

Control of Chemokine-Guided Cell Migration by Ligand Sequestration

Bijan Boldajipour,[1,4] Harsha Mahabaleshwar,[1,4] Elena Kardash,[1] Michal Reichman-Fried,[1] Heiko Blaser,[1] Sofia Minina,[2] Duncan Wilson,[3] Qiling Xu,[3] and Erez Raz[1,*]
[1]Center for Molecular Biology of Inflammation, Von-Esmarch-Straße 56, D-48149 Münster, Germany
[2]Germ Cell Development, Max Planck Institute for Biophysical Chemistry, Am Fassberg 11, Göttingen, Germany
[3]Division of Developmental Biology, National Institute for Medical Research, The Ridgeway, Mill Hill, London NW7 1AA, UK
[4]These authors contributed equally to this work.
*Correspondence: erez.raz@uni-muenster.de
DOI 10.1016/j.cell.2007.12.034

SUMMARY

Primordial germ cell (PGC) migration in zebrafish is directed by the chemokine SDF-1a that activates its receptor CXCR4b. Little is known about the molecular mechanisms controlling the distribution of this chemoattractant in vivo. We demonstrate that the activity of a second SDF-1/CXCL12 receptor, CXCR7, is crucial for proper migration of PGCs toward their targets. We show that CXCR7 functions primarily in the somatic environment rather than within the migrating cells. In CXCR7 knocked-down embryos, the PGCs exhibit a phenotype that signifies defects in SDF-1a gradient formation as the cells fail to polarize effectively and to migrate toward their targets. Indeed, somatic cells expressing CXCR7 show enhanced internalization of the chemokine suggesting that CXCR7 acts as a sink for SDF-1a, thus allowing the dynamic changes in the transcription of *sdf-1a* to be mirrored by similar dynamics at the protein level.

INTRODUCTION

The generation of positional information during development and adult life is crucial for processes ranging from global patterning of the embryo to building of tissues and organs and their maintenance. Positional information is often established by factors that spread from a defined source, thereby providing the basis for differential cellular response along a gradient. The graded distribution of molecules can dictate different fates in response to the signal level at the position where the responding cells reside (e.g., (Driever and Nüsslein-Volhard, 1988; Ferguson and Anderson, 1992; Nellen et al., 1996)). Alternatively, cells can respond to the distribution of signaling molecules in the environment by migration directed toward or away from the source of an attractant or a repellent, respectively (e.g., (Berg, 1975; Charest and Firtel, 2006; Eisenbach and Giojalas, 2006; Franca-Koh et al., 2006; Raz and Reichman-Fried, 2006; Renault and Lehmann, 2006).

A particularly challenging task is controlling cell migration during early development, a phase during which a large-scale reorganization of embryonic structures results in displacement of sources of guidance cues as well as tissues that serve as substrate on which cells migrate. Determining the strategies that allow cells to reach their target during these stages is thus a major biological question, the answer to which is likely to shed light on the mechanisms governing directed cell migration under less demanding conditions at other time points in the life of the organism.

A useful model for studying guided migration in vivo during early embryogenesis is that of primordial germ cells (PGCs), cells that typically migrate from their site of specification to the position where the gonad develops where they differentiate into gametes (reviewed in Kunwar et al., 2006). PGC migration in zebrafish is well understood, particularly since the guidance cue (the chemokine SDF-1a [Doitsidou et al., 2002]) and its receptor (CXCR4b [Doitsidou et al., 2002; Knaut et al., 2003]) are known. Specifically, the migration route of the PGCs is tightly correlated with dynamic changes in the mRNA expression pattern of the chemoattractant SDF-1a (Doitsidou et al., 2002; Reichman-Fried et al., 2004).

The demonstration that CXCR7 is a receptor for SDF-1 (Balabanian et al., 2005; Burns et al., 2006) ended the seemingly monogamous relationships between this chemokine and its first-to-be-identified receptor CXCR4. In vitro studies aimed at determining the function of CXCR7 yielded conflicting results. Whereas one study suggested that CXCR7 activation promotes cell migration (Balabanian et al., 2005), a more recent study argues that activation of this receptor is not involved in migration. According to the latter work, CXCR7 does not induce calcium mobilization, which normally characterizes the biochemical response to chemokine binding (Burns et al., 2006). Last, in agreement with the results presented above, both CXCR7 ligands, CXCL11 and CXCL12, failed to induce calcium signaling, nor could they promote phosphorylation of either ERK1/2 or Akt/PKB (Proost et al., 2007).

Irrespective of its biochemical activity, CXCR7 function was found to be essential for proper migration of the posterior lateral line primordium, proving that this receptor indeed participates in controlling cell migration in vivo (Dambly-Chaudière et al., 2007; Valentin et al., 2007). Yet, the precise contribution of the receptor to the control of guided cell migration is not known. To determine the role CXCR7 plays in vivo, we examined its function in the context of zebrafish PGC migration.

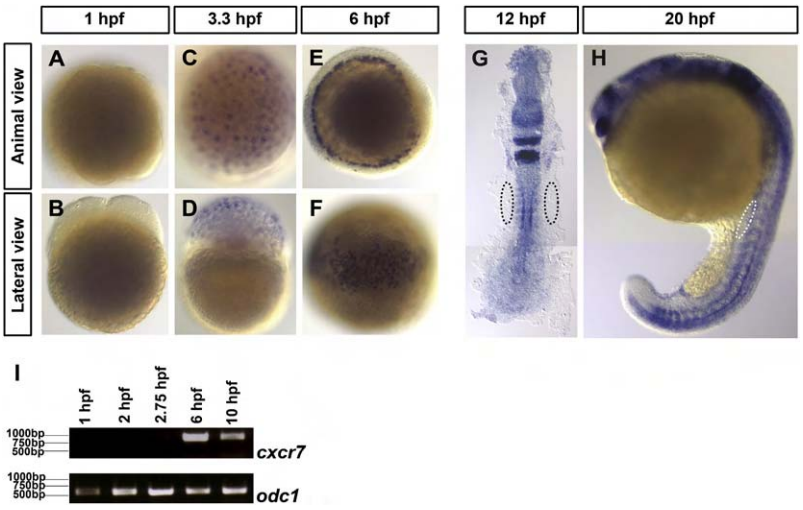

Figure 1. Expression Pattern of *cxcr7*

(A–H) Distribution of *cxcr7* mRNA in wild-type embryos during the first 20 hr of development. In situ hybridization using a *cxcr7*-specific probe shows no staining in four-cell stage embryos (A and B), weak uniform expression at 3.3 hpf (C and D), and enhanced *cxcr7* expression in a ring of deep cells at 6 hpf (E and F). At later stages of development (G and H), uniform *cxcr7* expression with enhanced expression in mesoderm derivatives and in the nervous system is detected, but no expression is observed at the region where the PGCs are located (encircled domains).

(I) Absence of maternally provided *cxcr7* mRNA as determined by RT-PCR at the indicated stages. Control reactions are presented in which primers specific for the maternally provided *ornithine decarboxylase1* (*odc1*) mRNA were used.

In this work we show that in embryos in which CXCR7 function is compromised, PGCs exhibit strongly impaired cell polarity and faulty migration. Strikingly, unlike the other SDF-1a receptor, CXCR4b, whose function is required within the migrating cells, CXCR7 function is exerted primarily in somatic cells. We provide evidence suggesting that CXCR7 effectively reduces the level of SDF-1a available for PGCs by binding and internalizing the chemokine and thus serves to sequester it. In this way, CXCR7 lowers the level of the chemoattractant in the environment, thereby permitting rapid dynamic changes in the distribution of the protein in response to alterations in the transcription pattern of *sdf-1a*.

RESULTS

cxcr7 Is Expressed in Zebrafish Embryos during the Time When PGCs Migrate toward Their Targets

Zebrafish PGCs initiate their active migration toward SDF-1a at 4.5 hr postfertilization (hpf) (Blaser et al., 2005) and reach their final target within the next 15 hr (Weidinger et al., 1999, 2002). In situ hybridization and RT-PCR revealed that *cxcr7* RNA is not provided maternally (Figures 1A, 1B, and 1I) and is transcribed throughout the embryo just before the onset of PGC migration (3.3 hpf, Figures 1C and 1D). During gastrulation stages, the receptor is expressed in a ring of deep cells (6 hpf, Figures 1E and 1F), followed by low-level expression and uniform distribution along with stronger expression in specific structures in the nervous system and in mesodermal derivatives (Figures 1G and 1H). Unlike the distinct expression of *cxcr4b* in PGCs (Doitsidou et al., 2002), we did not observe specific prominent expression of *cxcr7* in migrating PGCs. Thus, while it is possible that *cxcr7* RNA is expressed in PGCs during early stages of development when its expression domain overlaps the location of the PGCs, it is not detectable in the germ cells at later stages (Figures 1G and 1H, encircled domains).

CXCR7 Function Is Essential for Proper PGC Migration

To determine whether CXCR7 plays a role in the migration of PGCs, we have knocked down its activity using morpholino antisense oligonucleotides (Nasevicius and Ekker, 2000) (Figure S1). Strikingly, PGC migration was severely affected in embryos compromised for the receptor function. The CXCR7 loss-of-function phenotype is reminiscent of that of CXCR4b-deficient embryos such that by the end of the first day of development, PGCs failed to form cell clusters at the region where the gonad develops (Figures 2A–2C). This phenotype is likely to reflect defects in cell migration rather than an adverse effect on cell differentiation or survival as the PGCs in manipulated embryos show normal expression of various RNA markers such as *nanos*1 and *h1m* (Köprunner et al., 2001; Müller et al., 2002) (Figure 2C and data not shown). In addition, PGCs in treated embryos were able to protect and translate specific mRNAs (Köprunner et al., 2001) (Figure 2F), formed the typical perinuclear granules (Wolke et al., 2002) (Figure 2F), and exhibited normal proliferation (Figure 2I). Importantly, by reducing the activity of CXCR7, the distribution of *sdf-1a* transcripts was not altered, but the PGCs appeared to be uncharacteristically located outside of the RNA expression domains of the chemokine (Figures 2G and 2H).

To verify that the observed PGC migration phenotype indeed resulted specifically from knockdown of CXCR7 function, we have injected the antisense oligonucleotides, while uniformly coexpressing *cxcr7* mRNA mutated in a way that rendered it resistant to the inhibition. The introduction of *cxcr7* mRNA into embryos by injection could not mimic the endogenous expression pattern or level of the receptor and therefore did not result in a complete suppression of the phenotype. Nevertheless, this treatment led to a dramatic reduction in the severity of the phenotype, demonstrating that the CXCR7 function is required for proper migration of the PGCs (Figures 2K–2L).

CXCR7 Function Is Required in Somatic Cells

The finding that *cxcr7* is not specifically expressed in the PGCs, coupled with the fact that the severity of the knockdown phenotype is significantly reduced by uniform expression of the receptor in the embryo, could indicate that the receptor function is required in the somatic environment rather than in the PGCs themselves. To examine this possibility, we transplanted PGCs

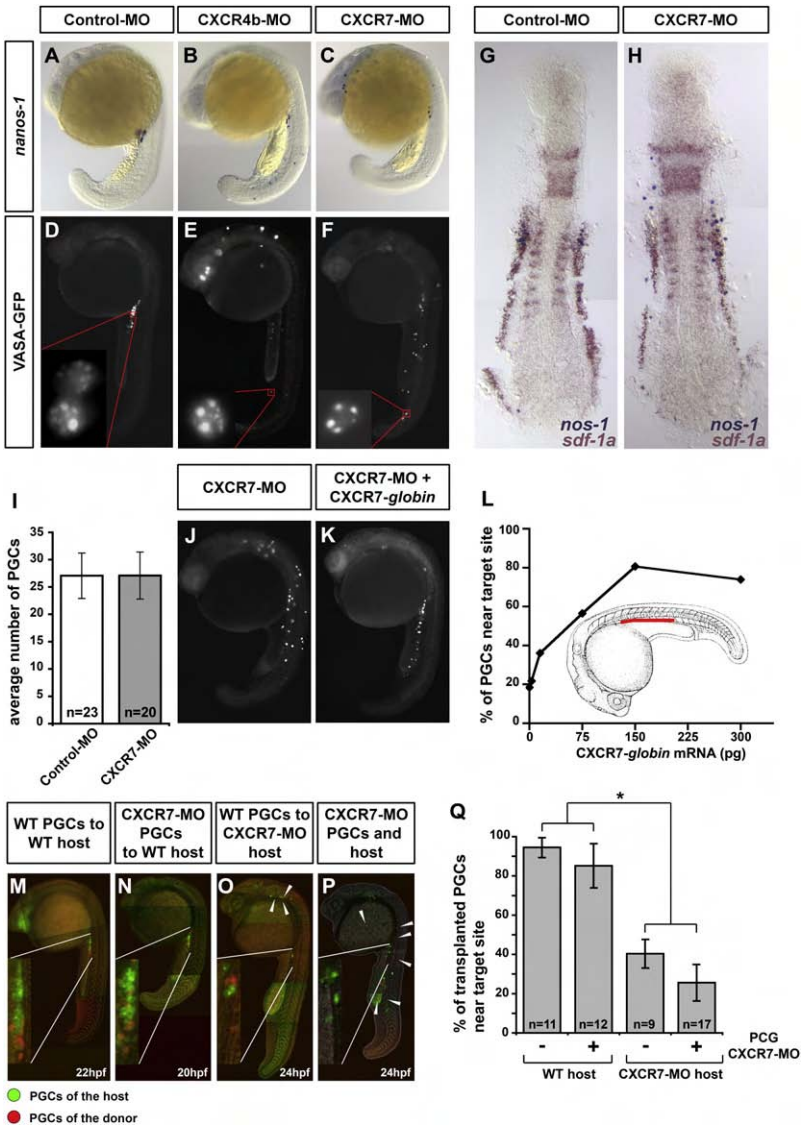

Figure 2. CXCR7 Is Essential for Normal PGC Migration and Is Required in the Somatic Environment of the Embryo

(A–C) Reduction of CXCR7 activity leads to aberrant PGC migration as demonstrated by in situ hybridization using a germ cell-specific *nanos1* probe. PGCs in control embryos cluster at the region where the gonad develops after 20 hr of development (A). Similar to reduction of CXCR4b activity (B), knockdown of CXCR7 results in a pronounced germ cell migration phenotype (C).

(D–F) CXCR7 knockdown does not affect PGC specification. Images of 22 hpf embryos injected with Vasa-GFP-*nos1*-3′UTR mRNA are shown. Germ cell-specific mRNA protection and proper localization of the Vasa-GFP fusion protein to germinal granules is observed in embryos injected with control morpholino (D), CXCR4b morpholino (E), and CXCR7 morpholino (F).

(G and H) General embryonic patterning and expression of *sdf-1a* are not affected by CXCR7 knockdown. Two-color in situ hybridization using *nanos1* (blue) and *sdf-1a* probes (red) of embryos injected with control (G) or CXCR7 (H) morpholino is shown.

(I) CXCR7 knockdown does not affect PGC number as counted at 12 hpf. n signifies the number of embryos examined. Error bars represent standard error of the mean (SEM).

(J–L) The effect of CXCR7 morpholino on PGC migration is reversed by CXCR7 expression. The severe migration phenotype induced by the CXCR7 antisense oligonucleotide (J) is reversed by global expression of RNA encoding CXCR7 (K). A graph demonstrating the dose-dependent rescue of the CXCR7 morpholino-induced phenotype by global expression of CXCR7 (L). For all injections the total amount of injected mRNA was identical (300 pg) by addition of control mRNA (mCherry-F-*globin* mRNA). The red bar indicates the correct target for the migrating PGCs.

(M–Q) PGC migration depends on the activity of CXCR7 in somatic tissues. PGCs expressing DsRedExpress (red) were transplanted into embryos with PGCs expressing EGFP-F (green). Wild-type and CXCR7 knocked-down PGCs arrived at the region of the gonad in wild-type hosts (M and N). A large proportion of wild-type and CXCR7-depleted PGCs does not arrive at the correct target in CXCR7-depleted host embryos (O and P, arrowheads). In (Q), the percent of transplanted PGCs reaching their target after the first day of development is shown. PGCs in CXCR7-depleted hosts embryos show a significant reduction of migration fidelity as compared to PGCs in wild-type hosts ($p < 0.001$, t test, marked with an asterisk). PGCs deficient for CXCR7 do not show a significant difference in arriving at the target as compared to control PGCs ($p > 0.17$, t test). n signifies number of embryos examined. Error bars represent SEM.

from embryos knocked down for CXCR7 into wild-type embryos and compared their ability to reach the target with that of wild-type cells transplanted into CXCR7-depleted embryos. As shown in Figures 2M–2Q, the ability of PGCs to reach their target depends on CXCR7 function in somatic cells. Specifically, PGCs transplanted into a wild-type somatic environment exhibited a high rate of arrival at the target (Figures 2M, 2N, and 2Q). In contrast, most of the PGCs transplanted into a CXCR7-depleted environment failed to reach the region where the gonad develops (Figures 2O, 2P, and 2Q). Importantly, CXCR7 knockdown within PGCs (Figures 2N, 2P, and 2Q) did not significantly affect the efficiency with which they arrived at their target ($p > 0.17$, two-sided t test). Together, these findings support the idea that CXCR7 function is required in somatic cells rather than in the PGCs.

CXCR7 Promotes Internalization of SDF-1a and Clearing of the Chemokine from the Extracellular Space

To determine the role CXCR7 plays in somatic cells, we have studied the subcellular localization of the protein and compared it with that of CXCR4b and SDF-1a. To this end, we have tagged these molecules with fluorescent proteins without affecting their normal activity (see Minina et al., 2007 for CXCR4b, Figure S2 for CXCR7, and Movie S1 for SDF-1a) and followed their distribution within the cells. Interestingly, we found that in contrast to CXCR4b that is largely localized to the plasma membrane (Figure 3A), CXCR7 is enriched in intracellular structures (Figure 3B). These findings raised the possibility that CXCR7 binds SDF-1a and, as a result of internalization, sequesters the chemokine in the cell. CXCR7 could thus affect the shape of

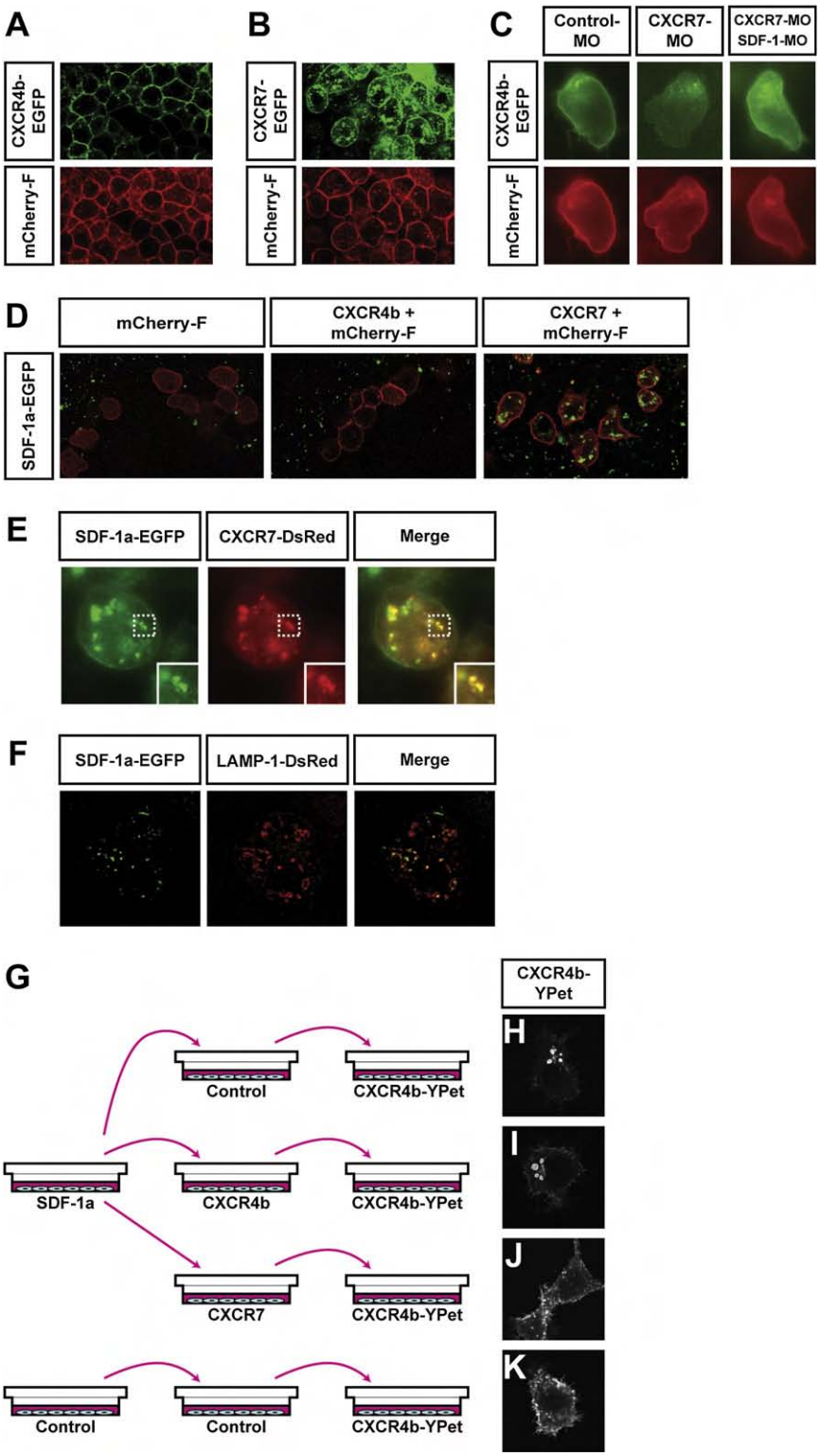

Figure 3. CXCR7 Is an SDF-1a Receptor that Promotes the Internalization of the Chemokine

(A and B) Subcellular localization of CXCR4b and CXCR7 (green) in somatic cells of the embryo. CXCR4b (green) is predominantly found on the membrane of cells (red label of farnesylated mCherry) (A), while CXCR7 (green) is found on the plasma membrane and intracellularly (B).

(C) CXCR7 knockdown increases extracellular SDF-1a levels as judged by internalization of CXCR4b in PGCs. In control embryos (left panel), CXCR4b (green) localizes to the plasma membrane of PGCs (red). CXCR7 knockdown leads to a reduction of CXCR4b on the membrane (middle panel). Membrane localization of CXCR4b in CXCR7 knockdown embryos is restored by SDF-1 knockdown (right panel).

(D) SDF-1a is internalized by CXCR7-expressing cells. Somatic cells (red membrane) expressing CXCR7, CXCR4b, or a control protein were transplanted into host embryos that globally expressed SDF-1a-EGFP. Confocal images were taken 1 hr after transplantation. Transplanted cells (red) expressing either control protein or CXCR4b (left and middle panel, respectively) do not show uptake of SDF-1a (green). In contrast, cells expressing CXCR7 showed intracellular accumulations of SDF-1a protein (right panel).

(E) SDF-1a and CXCR7 colocalize in vesicular structures. Images were taken 1 hr after transplantation of cells expressing CXCR7-DsRedMonomer into SDF-1a-EGFP-expressing hosts. The inset shows a magnification of the dotted box.

(F) SDF-1a accumulates in lysosomes upon CXCR7-mediated internalization. Deconvoluted images were taken 1 hr after transplantation of cells expressing untagged CXCR7 and the lysosomal marker LAMP-1 fused to DsRedMonomer into SDF-1a-EGFP-expressing host embryos.

(G–K) CXCR7-expressing cells reduce extracellular SDF-1a levels. In (G) is a graphic illustration of the experiments designed to examine the depletion of SDF-1a from conditioned medium by CXCR7-expressing cells. The conditioned medium was incubated with cells transfected with the different DNA constructs and subsequently transferred to reporter cultures expressing CXCR4b-EGFP. The extent of CXCR4b-EGFP internalization was then determined. In (H), strong CXCR4b internalization is observed in cells exposed to medium treated with control cells. In (I), medium depleted by CXCR4b-expressing cells induced CXCR4b internalization in 87.5% of all reporter cells, compared to control. CXCR4b internalization was only observed in 56.3% of cells exposed to medium depleted by CXCR7-expressing cells (J). Medium from cells transfected with empty pCDNA3 vector did not induce CXCR4b internalization (K).

the SDF-1a gradient by reducing the level of the chemokine in the extracellular space. We have previously shown that high levels of SDF-1a in the environment trigger the internalization of CXCR4b in germ cells (Minina et al., 2007). Using the subcellular localization of CXCR4b as a measure for the amount of SDF-1a outside of the cells, we determined the distribution of this receptor under conditions where CXCR7 levels were reduced. Indeed, knocking down CXCR7 significantly lowered the level of CXCR4b on the

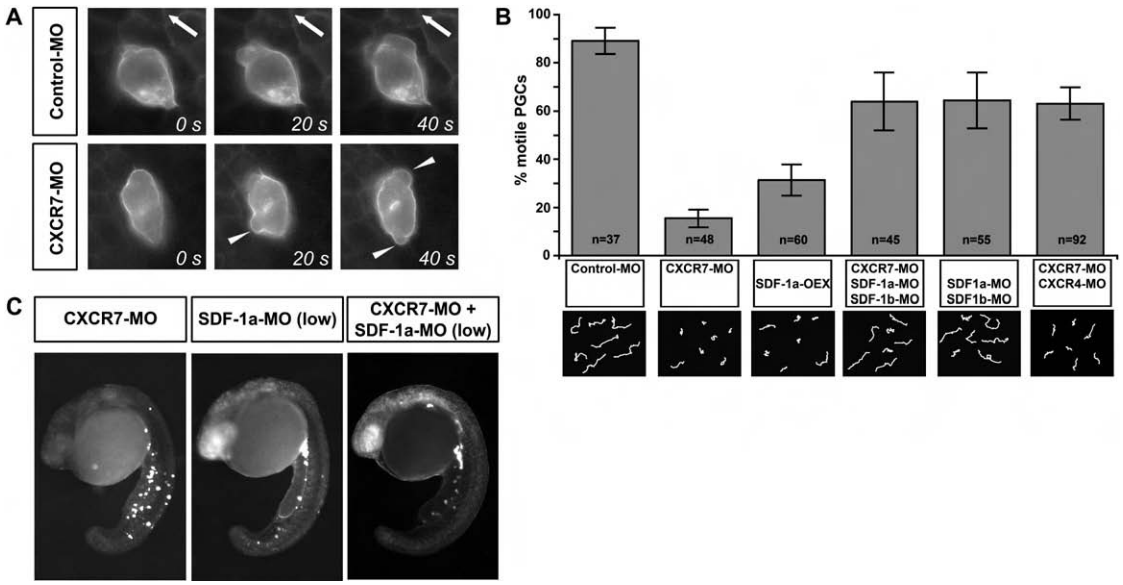

Figure 4. CXCR7 Controls PGC Polarity by Regulating SDF-1 Levels

(A) CXCR7 knockdown reduces the polarity of migrating germ cells. Wild-type PGCs show a typical polarization of the cells with protrusions at the leading edge in the direction of migration (upper panel, arrows). PGCs in CXCR7-depleted embryos exhibit reduced polarity with protrusions extended in opposite directions (lower panel, arrowheads). Cells labeled with EGFP-F.

(B) CXCR7 depletion reduces the motility of PGCs in an SDF-1a-dependent manner. The motility of PGCs was followed in time-lapse movies. Error bars represent SEM. Examples for 70 min long migration paths of germ cells are shown. PGCs in CXCR7 morphants exhibit low motility with short tracks that are reminiscent of PGCs migrating in embryos with high-uniform SDF-1a expression (SDF-1a-OEX). Removal of SDF-1 in CXCR7-depleted embryos restores PGC motility to a level that is similar to that in SDF-1-depleted embryos. Similarly, knocking down CXCR4 restores PGC motility in CXCR7 morphants.

(C) Reduction of SDF-1a expression suppresses the CXCR7 knockdown phenotype. The migration phenotype of embryos knocked down for CXCR7 (left panel, 66.4% ± 3% ectopic cells per embryo, n = 30 embryos) is suppressed by coinjection of low levels (0.02 pmol) of SDF-1a morpholino (middle panel: SDF-1a-MO, 29.4% ± 3% ectopic cells per embryo, n = 22 embryos; right panel: CXCR7-MO and SDF-1a-MO, 36.0% ± 2% ectopic cells per embryo, n = 63 embryos).

plasma membrane (Figure 3C). In addition, introducing antisense oligonucleotides directed against *sdf*-1 reduced the level of CXCR4b internalization observed in CXCR7-deficient embryos (Figure 3C, right panel). These findings support the notion that the enhanced CXCR4b internalization in CXCR7 morphants results from higher levels of extracellular SDF-1. To directly address this idea, we followed the fate of GFP-tagged SDF-1a protein when it encounters cells expressing CXCR7 (Figure 3D). Indeed, a marked internalization of SDF-1a by somatic cells expressing CXCR7 was observed (right panel), whereas nontreated cells or cells overexpressing CXCR4b did not exhibit internalization of the tagged SDF-1a (left and middle panels, respectively). Importantly, in a similar experimental setting, we observed strict colocalization of SDF-1a-EGFP and CXCR7-DsRedMonomer (Figure 3E), supporting the idea that SDF-1a internalization is mediated by CXCR7. To examine the fate of the internalized SDF-1a protein, we compared the localization of the protein with that of the lysosomal marker LAMP-1. For this purpose we transplanted cells expressing CXCR7 and DsRed-tagged LAMP-1 into SDF-1a-EGFP-expressing hosts and detected SDF-1a accumulation in many of the labeled lysosomes (Figure 3F). Similar results were obtained when the lysosomes were labeled using the LysoTracker reagent (Figure S3).

These results suggest that CXCR7 could reduce the time the chemokine is present in the extracellular space, thus permitting the formation of a gradient as well as dynamic alterations in the distribution of the molecule during development. To test this hypothesis more directly, we have assayed the potency of cells expressing CXCR7 in depleting SDF-1a from their environment. In this experiment, SDF-1a-conditioned medium was incubated with human cells expressing zebrafish CXCR7, and the activity level in inducing CXCR4b internalization served as a measure for the remaining amount of the chemokine. Indeed, cells expressing CXCR7 effectively depleted SDF-1a from the medium as compared with the cells transfected with an empty vector or cells expressing CXCR4b (Figures 3G–3K).

CXCR7 Function Is Important for Cell Polarity and Migration

The results presented above suggest that CXCR7 reduces the level of SDF-1a in the embryo allowing proper generation of the chemokine gradient. Detailed morphological analysis of PGCs migrating within the CXCR7-depleted environment strongly supports this idea. Specifically, in contrast with their morphology in wild-type embryos (Figure 4A, upper panels, and Movie S2), PGCs in CXCR7 knocked-down embryos appear less polarized, such that protrusion formation is not focused at the leading edge of the cell, but rather could be observed simultaneously at two opposite sides of the cell (Figure 4A, lower panels, and Movie S3). Further evidence for the reduced polarity

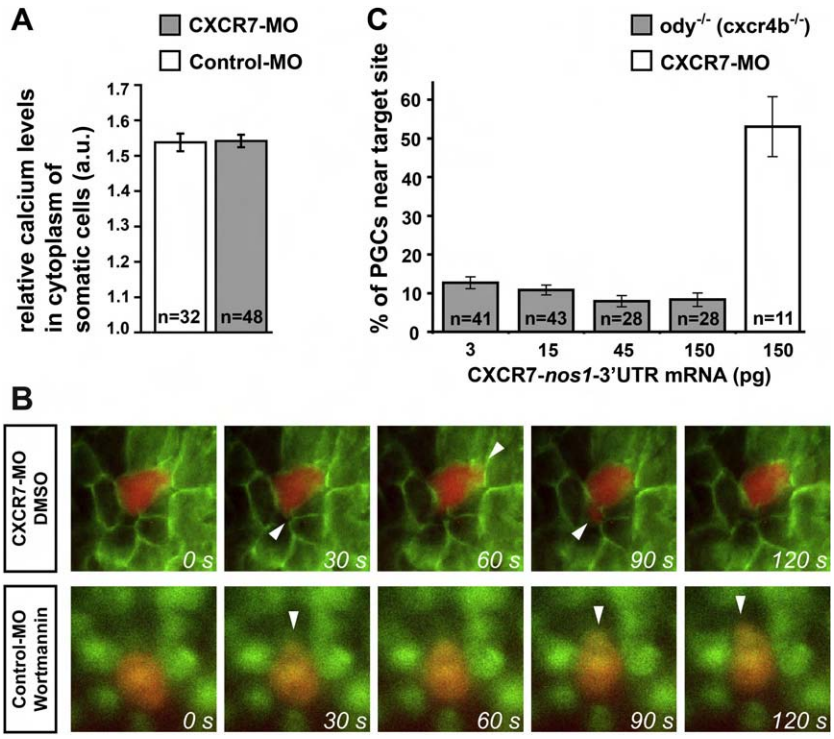

Figure 5. CXCR7 Does Not Activate Major Pathways Downstream to Chemokine Signaling

(A) CXCR7 depletion does not alter calcium levels in the cytosol of somatic cells in control and CXCR7-depleted embryos ($p > 0.1$, t test). n signifies the number of cells examined. Error bars represent SEM. a.u., arbitrary units.

(B) CXCR7 knockdown phenotype is not caused by absence of PI3K function. Shown are PGCs expressing DsRed (red) migrating in embryos globally expressing Akt-PH-EGFP. Migration was monitored in CXCR7-depleted embryos and compared with the migration of PGCs in embryos in which PI3K was inhibited. In CXCR7-depleted embryos PGCs display multiple protrusions in opposing directions (upper panel, arrowheads), typical of CXCR7 inhibition. By contrast, PGCs treated with the selective PI3K inhibitor Wortmannin (25 μM) are polar and migrate with the protrusions, forming in the direction of migration (lower panel, arrowheads). Effective inhibition of PI3K function was monitored by the localization of Akt-PH-EGFP. In DMSO-treated embryos (upper panel), the PH domain localizes to the plasma membrane, whereas PI3K inhibition by Wortmannin induces translocation of the sensor to the cytosol (lower panel). Movies of control cells not treated with the drug and cells in CXCR7-depleted embryos treated with Wortmannin are provided in Movies S8 and S9, respectively.

(C) Germ cell-specific expression of CXCR7 does not substitute for CXCR4b function. CXCR7 expression does not revert the effect of CXCR4b-deficient fish (gray bars), but rescues CXCR7 morpholino-treated embryos (white bar). n signifies the number of embryos examined. Error bars represent SEM.

of PGCs in CXCR7-depleted embryos was obtained by interfering with calcium polarity in the cells. Expressing an activated form of the STIM1 protein in PGCs elevates calcium levels in the rear of migrating cells and challenges their calcium polarity (Blaser et al., 2006). Whereas wild-type PGCs expressing mutated STIM1 are still able to polarize and migrate (Movie S4) (Blaser et al., 2006), a similar manipulation in CXCR7 knocked-down embryos resulted in a dramatic loss of PGC morphological polarity and motility (Movie S5). We consider this finding a further indication for the reduced polarity of PGCs migrating in manipulated embryos.

To validate the notion that the basis for the phenotype of CXCR7 knockdown lies with higher levels of SDF-1 in the environment, we examined PGC behavior in manipulated embryos. PGCs in CXCR7 knocked-down embryos exhibited strong inhibition of motility manifested in short migration tracks (Figure 4B). This phenotype could be mimicked by global SDF-1a expression in otherwise wild-type embryos (Figure 4B). A striking reversal of the CXCR7 knockdown phenotype was observed when CXCR7 and both ligands (SDF-1a and SDF-1b) were simultaneously knocked down; experimental cells exhibited motility similar to cells lacking the guidance cue (Figure 4B) (Doitsidou et al., 2002; Reichman-Fried et al., 2004). Suppression of the CXCR7 phenotype was similarly achieved by concomitant knockdown of CXCR4b (Figure 4B). Although PGCs in these experiments regained motility, they were nevertheless dispersed throughout the embryos (data not shown), since by knocking down CXCR4b or SDF-1 (along with CXCR7), the guidance signal was eliminated. We reasoned that a mild reduction in SDF-1a level might permit cell motility in embryos lacking CXCR7, while preserving the function of the chemokine as a guidance cue. In such a case, one would predict that treating CXCR7 morphants with low levels of *sdf-1a* morpholino should allow many PGCs to reach their target. Indeed, such a manipulation reduced the severity of the migration phenotype observed in 24 hpf embryos (Figure 4C).

To determine whether the effect of CXCR7 on SDF-1a distribution is accompanied by signaling through the ligand-bound receptor, we have tested the possible involvement of two key pathways acting downstream of chemokine receptors, namely elevation in calcium levels and PI3K activation (e.g., Andrews et al., 2007; Blaser et al., 2006; Bleul et al., 1996; Sotsios et al., 1999; Vicente-Manzanares et al., 1999). We found that CXCR7 knockdown had no effect on the level of calcium in somatic cells (Figure 5A). In addition, in embryos in which PI3K activity was inhibited using Wortmannin (as evident by membrane-to-cytoplasm translocation of Akt-PH-EGFP), PGCs maintained their polarity and migrated actively, unlike PGCs in CXCR7 knocked-down embryos, which exhibit defects in motility and cell polarity (Figure 5B and Movies S6 and S7). Last, despite the apparently high-binding affinity of CXCR7 to SDF-1 in the mammalian system (Balabanian et al., 2005), the zebrafish CXCR7 cannot substitute for CXCR4b. Specifically, preferential expression of CXCR7 in PGCs did not suppress the CXCR4b knockdown phenotype (Figure 5C). Consistent with previous findings (Burns et al., 2006; Proost et al., 2007), our results support the idea that at least in the context of PGC migration in zebrafish, CXCR7 is a silent receptor that does not signal.

CXCR7 Affects the Direction of PGC Migration In Vivo

To demonstrate that somatically expressed CXCR7 affects the distribution of SDF-1a in the tissues within which the PGCs migrate, we have generated embryos in which SDF-1a was uniformly expressed and superimposed an uneven distribution of CXCR7 (Figure 6A). We found that the PGCs were preferentially located within domains lacking CXCR7, suggesting that the receptor affected the local SDF-1a concentration, promoting PGC migration toward regions where higher levels of SDF-1a are present (Figure 6B). To visualize the dynamic response of the PGCs to cells expressing CXCR7, we have examined the effect of CXCR7-expressing cells on the migration of PGCs toward an SDF-1a source (Figures 6C and 6D and Movies S10 and S11). PGCs rapidly and effectively migrated toward cells expressing the chemokine, while ignoring control cells transplanted on their way to the source (Figures 6C, upper panels, and 6D, left panel). In a striking contrast, transplantation of CXCR7-expressing cells (red cells in Figure 6C) between the PGCs and the chemokine source (blue cells in Figure 6C) dramatically affected the migration path of the PGCs such that they rarely crossed the CXCR7 expression field (Figures 6C, lower panels, cells 2 and 3, white tracks; and 6D, right panel). Consistently, expression of high levels of CXCR7 in the germ cells themselves affected their migration, presumably by reducing the effective level of SDF-1a around the cells (Figure S4).

To examine the possibility that CXCR7 plays a similar role in other contexts in embryonic development, we investigated the potential function for the gene in the nervous system, where it exhibits a dynamic expression pattern. At 12 hpf *cxcr7* is most prominently expressed in two broad stripes close to the head-trunk border (Figure 1G). Interestingly, the posterior *cxcr7* stripe overlaps with *sdf-1*a, while the anterior *cxcr7* stripe shows a largely complementary pattern with respect to *sdf-1a* (Figure 6E, upper panel). To determine whether the distribution of SDF-1a is altered in a manner that is consistent with the expression pattern of *cxcr7*, we have examined the exact position of PGCs abnormally found in this location in *spadetail* mutants (Weidinger et al., 1999, 2002). This analysis revealed that PGCs were never found in a region where *cxcr7* was expressed (Figure 6E, lower panel). Accordingly, the cells usually ignored the broad *sdf-1a* mRNA expression that is partially overlapping with that of *cxcr7* mRNA (Figure 6E, large brackets) and would settle in an *sdf-1a*-expressing clustering point away from the anterior *cxcr7* stripe (Figure 6E, small brackets).

Together, the results presented in this section are in agreement with the notion that CXCR7 can shape the SDF-1a gradient, thereby affecting the migration path of PGCs within the embryo. As CXCR7 is expressed in a broad range of tissues, it could function in controlling the distribution of SDF-1 in those locations, thereby regulating processes other than PGC migration.

DISCUSSION

During their migration, zebrafish PGCs arrive at locations where *sdf-1*a RNA is expressed (e.g., Figure 2G) (Blaser et al., 2005; Doitsidou et al., 2002; Reichman-Fried et al., 2004). Dynamic alterations in the expression pattern of *sdf-1a* are followed by a rapid migration response of germ cells to maintain their position in close proximity to tissues that express the RNA encoding the chemokine (Figure 7, left panels) (Reichman-Fried et al., 2004). Two processes could account for the observed tight association of PGCs with *sdf-1a*-transcribing cells. First, the responding cells could be capable of detecting minute differences in the level of the attractant and would therefore continuously migrate to remain within domains of *sdf-1a* transcription, where slightly higher levels of the secreted SDF-1a would be found. In addition to the sensitivity and effective response of PGCs to the signal, processes in the environment could cooperate by controlling the shape of the SDF-1a gradient. For example, continuous clearing of the ligand from somatic tissues would constitute a useful mechanism for achieving migration precision. In this study, we provide evidence consistent with the idea that CXCR7 activity is essential for attaining a distribution of SDF-1a that is capable of polarizing the PGCs and directing their migration toward cells expressing the RNA of the attractant. In contrast to CXCR4b, whose internalization regulates the signaling level of the receptor by removing it from the membrane (Minina et al., 2007), CXCR7 regulates the signaling level of CXCR4b by reducing the level of SDF-1a in the extracellular environment. In the absence of CXCR7 activity, an increase in the absolute level of SDF-1a and a decrease in gradient steepness would thus interfere with proper directed migration despite the correct RNA expression pattern (Figure 7, right panels). Whereas anti-SDF-1a antibodies are currently not available, such a reagent would provide interesting insights into the precise effect of CXCR7 loss of function on the distribution of the chemoattractant in the embryo.

While the molecular details differ, a mechanism for controlling cell migration reminiscent to the one proposed here has been suggested to account for guidance of germ cell migration in *Drosophila* (Renault and Lehmann, 2006; Renault et al., 2004). *Drosophila* PGCs are thought to migrate along a gradient of lipid phosphate that acts as a chemoattractant. Analogous to sequestration of SDF-1a, dephosphorylation of the lipid phosphate in specific somatic tissues of the *Drosophila* embryo renders those regions repulsive, thereby directing the migration of the cells toward their target.

The process in which zebrafish PGCs effectively avoid domains where the attractive molecule ceases to be expressed is reminiscent of that observed in the resolution of inflammatory response. In this case, tissue homeostasis depends on migration of cells that were originally attracted to the site of an inflammatory stimulus, away from that location. Different mechanisms that promote clearing of the attractive signal were identified, and these allow efficient resolution and reduction of tissue damage (reviewed in Hansell and Nibbs, 2007; Mantovani et al., 2006; Serhan and Savill, 2005). Of particular relevance for this study is the chemokine depletion without signaling that was proposed to account for the function of the antiinflammatory cytokine IL-10 (D'Amico et al., 2000). In this case, it has been shown that IL-10 maintains the expression of inflammatory chemokine receptors (CCR1, CCR2, and CCR5) on mature dendritic cells (DCs) that act as molecular sinks for the proinflammatory chemokines CCL3 and CCL5. The receptors on the DCs function exclusively in sequestering the chemokine, as they do not induce signaling or chemotaxis. Similarly, CCL3 and CCL5 clearing during the

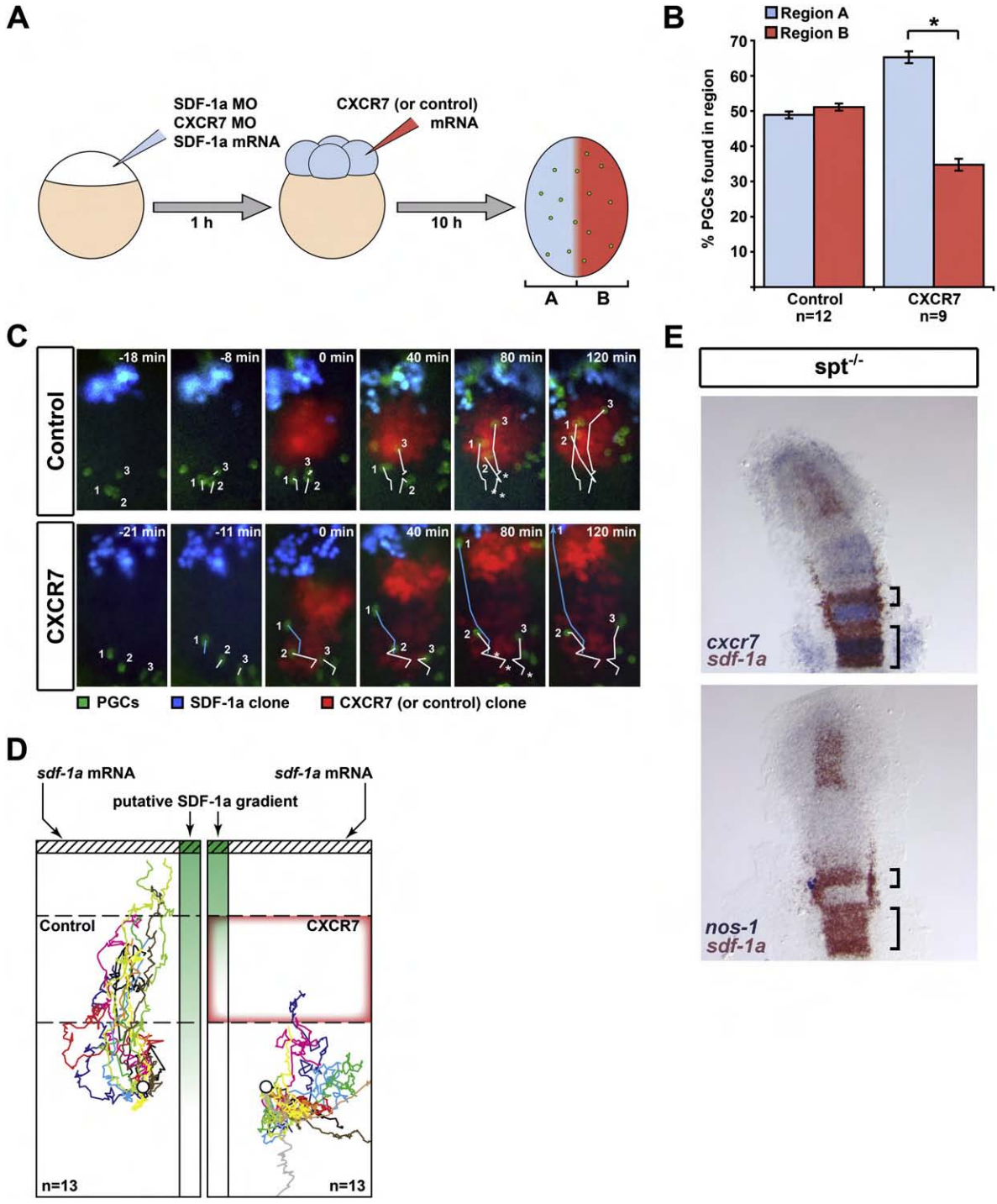

Figure 6. CXCR7 Affects the Direction of Germ Cell Migration In Vivo

(A) A schematic representation of the experimental manipulations generating a CXCR7 expression domain (red, Region A) superimposed on uniform SDF-1a expression (blue, Region B). PGCs are depicted in green.

(B) In contrast to control experiments, PGCs vacated the CXCR7-expressing B region (p value < 0.001, t test). n signifies the number of embryos examined, and error bars represent SEM.

(C) Snapshots of representative time-lapse movies with germ cells (green) migrating toward a transplanted source of SDF-1a (blue) in SDF-1-deficient embryos. A transplant of cells (red) expressing either CXCR7 or control protein was placed at the migration path. In control experiments (upper panel), germ cells (white tracks labeled 1–3) readily traverse the transplant toward the source of SDF-1a. Asterisks denote the starting points. When encountering a CXCR7-expressing transplant

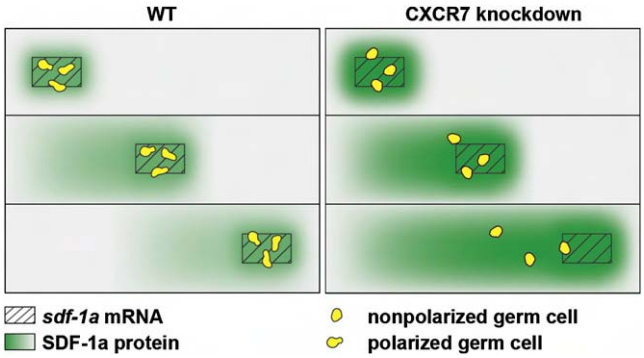

Figure 7. A Model for the Role of CXCR7 in PGC Migration

Morphogenetic movements and changes in expression pattern cause dynamic shifts of *sdf-1a* expression sites (hatched box). CXCR7-mediated removal of SDF-1a facilitates the generation of a sharp gradient (green), allowing the PGCs (yellow) to polarize and migrate toward the site of *sdf-1a* transcription (left panel). In the absence of CXCR7 function (right panel), SDF-1a is not cleared efficiently (extended green gradient), resulting in abnormally high SDF-1a levels and inability of germ cells to establish polarity. Consequently, germ cells lose their close association with *sdf-1a* transcription domains.

resolution of peritonitis depends on their receptor CCR5 that sequesters these chemokines in apoptotic leukocytes (Ariel et al., 2006). As SDF-1 has been implicated in rheumatoid arthritis and in acute lung injury inflammatory responses (e.g., De Klerck et al., 2005; Matthys et al., 2001; Nanki et al., 2000; Petty et al., 2007), it would be interesting to examine whether CXCR7 is involved in regulation of inflammation in these tissues. Furthermore, since the SDF-1/CXCR4 pair is involved in other pathological conditions (in particular cancer, e.g., Muller et al. [2001] and Orimo et al. [2005]) and controls a wide range of developmental and homeostatic activities (e.g., Aiuti et al., 1997; Peled et al., 1999; Zou et al., 1998), examining the role of CXCR7 in these processes would be an important avenue for future research.

Whereas our results provide strong evidence that CXCR7 is a nonsignaling receptor that functions as a sink for SDF-1a in the case of PGC migration, it could be that this molecule functions differently in different contexts. For example, the results of Valentin et al. (2007) are compatible with the idea that in the case of the zebrafish lateral-line primordium, CXCR7 activation plays an instructive role in dictating cell behavior in the posterior part of the migrating organ. The question of whether CXCR7 acts as a professional or a part-time decoy receptor would thus require detailed examination of the biochemical and cellular responses in different settings in which this receptor functions.

Although this study reiterates the central role of SDF-1a and CXCR4b in guiding PGC migration, our results highlight the importance of regulation by other molecules. It would therefore be important to examine additional parameters that could influence SDF-1a function in vivo, especially those relevant for its spread within the embryo. Exploring the role of components of the extracellular matrix that are known to bind SDF-1 as well as enzymes modifying SDF-1 in the extracellular environment would be especially informative in this context.

EXPERIMENTAL PROCEDURES

Zebrafish Strains

Fish of the AB background or transgenic fish carrying the Tol-kop-EGFP-F-*nos1*-3′UTR transgene (Blaser et al., 2006) or a similar line with a Tol-kop-DsRedExpress-F-*nos1*-3′UTR transgene served as wild-type fish. The transgenes direct EGFP-F or DsRedExpress expression to the PGCs. *ody*$^{-/-}$ mutant embryos were used to analyze the migration in the absence of CXCR4b function (Knaut et al., 2003).

Cloning and RT-PCR of *cxcr7*

The zebrafish *cxcr7* open reading frame (accession number XM682279) was amplified from midsomitogenesis cDNA and cloned into expression vectors for expression in germ cells (CXCR7-*nos1*-3′UTR) and for global expression (CXCR7-*globin*).

For RT-PCR, total RNA was isolated from 1 hpf, 2 hpf, 2.75 hpf, 6 hpf, and 10 hpf using TRIZOL (Invitrogen) and cDNA was synthesized using oligo(dT) primers. Primer sequences are provided in the supplemental material.

RNA Expression Constructs and Injections

Capped sense mRNA was synthesized using the mMessageMachine kit (Ambion). RNA was microinjected into the yolk of one-cell stage embryos unless stated otherwise.

A description of the constructs used is provided in the Supplemental Data.

Knockdown of CXCR7, CXCR4b, SDF-1a, and SDF-1b

Knockdown of CXCR7 function was achieved by injection of 1.2 pmol CXCR7-MO morpholino antisense oligonucleotides (5′-ATCATTCACGTTCACACTC ATCTTG-3′) into one-cell stage embryos. A second oligonucleotide (5′-GAA ATCATTCACGTTCACACTCATC-3′) also impaired PGC migration, albeit with lesser effectiveness. Knockdown of CXCR4b and both zebrafish SDF-1 homologs was achieved using 0.4 pmol of either oligonucleotides against *cxcr4b*, *sdf-1a* (Doitsidou et al., 2002), and *sdf-1b* (5′-TTGCTATCCATGCCAAGAGCG AGTG-3′). Control experiments were performed using equal concentrations of irrelevant oligonucleotides.

Fluorescence Microscopy

Epifluorescence images were captured using a Zeiss microscope controlled by the Metamorph Software (Visitron Systems). Time-lapse movies were generated for imaging cell morphology and behavior as well as for track analysis. Frames were captured at 5 s or 10 s intervals for high-magnification movies and at 1 min intervals for low-magnification movies.

Confocal fluorescence images were obtained with the Leica TCS SL confocal microscope.

Measurement of Calcium Levels

Calcium measurements were performed as previously described (Blaser et al., 2006). Somatic cell measurements were performed on the cytosol of cells in the vicinity of migrating PGCs.

Germ Cell Transplantation

Germline chimeras were produced by transplantation of PGCs from Tol-*kop*-DsRedExpress-*nos1*-3′UTR transgenic embryos into Tol-*kop*-EGFP-F-*nos1*-

(lower panel), the migration toward the SDF-1a source is inhibited (cells 2 and 3). Cells that do not encounter CXCR7-expressing cells on their migration path (cell 1) are not affected (blue track).

(D) Multiple migration tracks of germ cells encountering a control transplant (dashed box) or a transplant expressing CXCR7 (red box outline). Tracks have been corrected for morphogenetic movements and were given a common starting coordinate (circle) with the SDF-1a transplant positioned to the top (hatched box). The putative SDF-1a gradient drawn in green. n signifies the number of cells examined. Tracks represent 150 min of PGC migration.

(E) Regions expressing *sdf-1a* fail to attract PGCs if the expression overlaps with that of *cxcr7*. Two-color in situ hybridization on 13 hpf *spt*$^{-/-}$ embryos using *cxcr7* (blue) and *sdf-1a* (red) probes (top panel) and *nanos1* (blue) and *sdf-1a* (red) probes (lower panel).

3′UTR transgenics. CXCR7-depleted donor cells were transplanted into a control morpholino-injected host or vice versa. Control experiments were performed by injecting control or CXCR7 morpholino into both donor and host embryos.

Transplanted cells were obtained from the germ ring of 4 hpf donor embryos and transplanted into embryos of the same stage and their location determined in 24 hpf embryos.

In Vitro SDF-1a Internalization Assays

SDF-1a conditioned media was obtained from HEK293 transfected with pCS2-SDF-1a-FLAG plasmid. Forty-eight hours after transfection, the medium was replaced with a serum-free medium, and SDF-1a conditioned media was collected 48 hr later. The presence of SDF-1a in the medium was confirmed by immunoblotting. For depletion experiments, conditioned medium was subjected to two rounds of 30 min incubation on HEK293 cells transfected with either pCDNA3-CXCR7, pCDNA3-CXCR4b, or with an empty pCDNA3 vector. To check for SDF-1a presence in the treated medium, HEK293 cells were transfected with pCDNA3-CXCR4b-YPet, starved for 48 hr, and stimulated with SDF-1a conditioned media or depleted media at 37°C for 30 min. Cells were washed in PBS and fixed in 4% PFA for confocal microscopy. To quantify the percentage of internalization, 100 cells were counted.

In Vivo SDF-1a Internalization Assays

Cells from 4 hpf embryos injected with 150 pg CXCR7-*globin* and mCherry-F-*globin* mRNA were transplanted into 6 hpf host embryos expressing SDF-1a-EGFP. Following 1 hr incubation, confocal microscopy was performed at an elevated pinhole diameter of 250 nm. As controls, cells expressing 150 pg CXCR4b-*globin* and mCherry-F-*globin* mRNA or only mCherry-F-*globin* mRNA were transplanted.

For colocalization studies, cells from donor embryos that were injected either with CXCR7-DsRedMonomer-*globin* mRNA or with CXCR7-*globin* mRNA and LAMP-1-DsRedMonomer-*globin* mRNA were used. High-magnification epifluorescent Z series were obtained and deconvoluted using the Nearest Neighbor method of the Metamorph software suite.

Mosaic CXCR7 Expression in Zebrafish Embryos

Tol-kop-EGFP-F-nos1-3′UTR transgenic embryos were injected with SDF-1a and CXCR7 morpholino, 30 pg morpholino-resistant SDF-1a-*globin*, and zH1m-GFP-*globin* mRNAs to generate embryos with uniform expression of SDF-1a, uniform nuclear labeling and germ cell-specific membrane labeling. At the four-cell stage, one of the blastomers was injected with CXCR7-*globin* and mCherry-F-*globin* (or with mCherry-F-*globin* alone as control) mRNA. At 11 hpf, the position of the PGCs was determined with respect to the red fluorescent domain that signified CXCR7 expression. Embryos containing five or more labeled germ cells were included in the analysis.

In Vivo Attraction Assays

CFP-labeled, SDF-1a-expressing cells from a 4 hpf donor embryos were transplanted into animal positions of 6 hpf Tol-kop-EGFP-F-nos1-3′UTR embryos in which SDF-1a and SDF-1b were knocked down. After the PGCs initiated directional migration toward the SDF-1a secreting transplant, mCherry-F-labeled, CXCR7-expressing cells from 4 hpf embryos (injected with 150 pg CXCR7-*globin* mRNA at the one-cell stage or mCherry-F alone as a control) were transplanted between the migrating PGCs and the SDF-1a transplant. Cell movement was tracked for up to 150 min using the manual tracking plugin of the ImageJ software. Tracks were corrected for morphogenetic cell movements and aligned into one starting coordinate with the SDF-1a-secreting cells positioned upwards.

Supplemental Data

Supplemental Data include 4 figures, 11 movies, and Supplemental References and can be found with this article online at http://www.cell.com/cgi/content/full/132/3/463/DC1/.

ACKNOWLEDGMENTS

This work was supported by grants from the DFG and funds of the Max-Planck Society to E.R. and a Boehringer Ingelheim Fonds PhD fellowship to B.B. We thank Julia Dörries and Ursula Jahns-Meyer for technical help and Brian Ciruna for suggestions.

Received: June 28, 2007
Revised: September 11, 2007
Accepted: December 10, 2007
Published: February 7, 2008

REFERENCES

Aiuti, A., Webb, I., Bleul, C., Springer, T., and Gutierrez-Ramos, J. (1997). The chemokine SDF-1 is a chemoattractant for human CD34+ hematopoietic progenitor cells and provides a new mechanism to explain the mobilization of CD34+ progenitors to peripheral blood. J. Exp. Med. *185*, 111–120.

Andrews, S., Stephens, L.R., and Hawkins, P.T. (2007). PI3K class IB pathway. Sci. STKE *2007*, cm2.

Ariel, A., Fredman, G., Sun, Y.P., Kantarci, A., Van Dyke, T.E., Luster, A.D., and Serhan, C.N. (2006). Apoptotic neutrophils and T cells sequester chemokines during immune response resolution through modulation of CCR5 expression. Nat. Immunol. *7*, 1209–1216.

Balabanian, K., Lagane, B., Infantino, S., Chow, K.Y., Harriague, J., Moepps, B., Arenzana-Seisdedos, F., Thelen, M., and Bachelerie, F. (2005). The chemokine SDF-1/CXCL12 binds to and signals through the orphan receptor RDC1 in T lymphocytes. J. Biol. Chem. *280*, 35760–35766.

Berg, H.C. (1975). Chemotaxis in bacteria. Annu. Rev. Biophys. Bioeng. *4*, 119–136.

Blaser, H., Eisenbeiss, S., Neumann, M., Reichman-Fried, M., Thisse, B., Thisse, C., and Raz, E. (2005). Transition from non-motile behaviour to directed migration during early PGC development in zebrafish. J. Cell Sci. *118*, 4027–4038.

Blaser, H., Reichman-Fried, M., Castanon, I., Dumstrei, K., Marlow, F.L., Kawakami, K., Solnica-Krezel, L., Heisenberg, C.P., and Raz, E. (2006). Migration of zebrafish primordial germ cells: a role for Myosin contraction and cytoplasmic flow. Dev. Cell *11*, 613–627.

Bleul, C.C., Farzan, M., Choe, H., Parolin, C., Clark-Lewis, I., Sodroski, J., and Springer, T.A. (1996). The lymphocyte chemoattractant SDF-1 is a ligand for LESTR/fusin and blocks HIV-1 entry. Nature *382*, 829–833.

Burns, J.M., Summers, B.C., Wang, Y., Melikian, A., Berahovich, R., Miao, Z., Penfold, M.E., Sunshine, M.J., Littman, D.R., Kuo, C.J., et al. (2006). A novel chemokine receptor for SDF-1 and I-TAC involved in cell survival, cell adhesion, and tumor development. J. Exp. Med. *203*, 2201–2213.

Charest, P.G., and Firtel, R.A. (2006). Feedback signaling controls leading-edge formation during chemotaxis. Curr. Opin. Genet. Dev. *16*, 339–347.

D'Amico, G., Frascaroli, G., Bianchi, G., Transidico, P., Doni, A., Vecchi, A., Sozzani, S., Allavena, P., and Mantovani, A. (2000). Uncoupling of inflammatory chemokine receptors by IL-10: generation of functional decoys. Nat. Immunol. *1*, 387–391.

Dambly-Chaudière, C., Cubedo, N., and Ghysen, A. (2007). Control of cell migration in the development of the posterior lateral line: antagonistic interactions between the chemokine receptors CXCR4 and CXCR7/RDC1. BMC Dev. Biol. *7*, 23.

De Klerck, B., Geboes, L., Hatse, S., Kelchtermans, H., Meyvis, Y., Vermeire, K., Bridger, G., Billiau, A., Schols, D., and Matthys, P. (2005). Pro-inflammatory properties of stromal cell-derived factor-1 (CXCL12) in collagen-induced arthritis. Arthritis Res. Ther. *7*, R1208–R1220.

Doitsidou, M., Reichman-Fried, M., Stebler, J., Koprunner, M., Dorries, J., Meyer, D., Esguerra, C.V., Leung, T., and Raz, E. (2002). Guidance of primordial germ cell migration by the chemokine SDF-1. Cell *111*, 647–659.

Driever, W., and Nüsslein-Volhard, C. (1988). The bicoid protein determines position in the Drosophila embryo in a concentration-dependent manner. Cell *54*, 95–104.

Eisenbach, M., and Giojalas, L.C. (2006). Sperm guidance in mammals - an unpaved road to the egg. Nat. Rev. Mol. Cell Biol. *7*, 276–285.

Ferguson, E., and Anderson, K. (1992). Decapentaplegic acts as a morphogen to organize dorsal-ventral pattern in the Drosophila embryo. Cell *71*, 451–461.

Franca-Koh, J., Kamimura, Y., and Devreotes, P. (2006). Navigating signaling networks: chemotaxis in Dictyostelium discoideum. Curr. Opin. Genet. Dev. *16*, 333–338.

Hansell, C., and Nibbs, R. (2007). Professional and part-time chemokine decoys in the resolution of inflammation. Sci. STKE *2007*, pe18.

Knaut, H., Werz, C., Geisler, R., and Nusslein-Volhard, C. (2003). A zebrafish homologue of the chemokine receptor Cxcr4 is a germ-cell guidance receptor. Nature *421*, 279–282.

Kunwar, P.S., Siekhaus, D.E., and Lehmann, R. (2006). In vivo migration: a germ cell perspective. Annu. Rev. Cell Dev. Biol. *22*, 237–265.

Köprunner, M., Thisse, C., Thisse, B., and Raz, E. (2001). A zebrafish nanos-related gene is essential for the development of primordial germ cells. Genes Dev. *15*, 2877–2885.

Mantovani, A., Bonecchi, R., and Locati, M. (2006). Tuning inflammation and immunity by chemokine sequestration: decoys and more. Nat. Rev. Immunol. *6*, 907–918.

Matthys, P., Hatse, S., Vermeire, K., Wuyts, A., Bridger, G., Henson, G.W., De Clercq, E., Billiau, A., and Schols, D. (2001). AMD3100, a potent and specific antagonist of the stromal cell-derived factor-1 chemokine receptor CXCR4, inhibits autoimmune joint inflammation in IFN-gamma receptor-deficient mice. J. Immunol. *167*, 4686–4692.

Minina, S., Reichman-Fried, M., and Raz, E. (2007). Control of receptor internalization, signaling level, and precise arrival at the target in guided cell migration. Curr. Biol. *17*, 1164–1172.

Muller, A., Homey, B., Soto, H., Ge, N., Catron, D., Buchanan, M.E., McClanahan, T., Murphy, E., Yuan, W., Wagner, S.N., et al. (2001). Involvement of chemokine receptors in breast cancer metastasis. Nature *410*, 50–56.

Müller, K., Thisse, C., Thisse, B., and Raz, E. (2002). Expression of a linker histone-like gene in the primordial germ cells in zebrafish. Mech. Dev. *117*, 253–257.

Nanki, T., Hayashida, K., El-Gabalawy, H.S., Suson, S., Shi, K., Girschick, H.J., Yavuz, S., and Lipsky, P.E. (2000). Stromal cell-derived factor-1-CXC chemokine receptor 4 interactions play a central role in CD4+ T cell accumulation in rheumatoid arthritis synovium. J. Immunol. *165*, 6590–6598.

Nasevicius, A., and Ekker, S.C. (2000). Effective targeted gene 'knockdown' in zebrafish. Nat. Genet. *26*, 216–220.

Nellen, D., Burke, R., Struhl, G., and Basler, K. (1996). Direct and long-range action of a DPP morphogen gradient. Cell *85*, 357–368.

Orimo, A., Gupta, P.B., Sgroi, D.C., Arenzana-Seisdedos, F., Delaunay, T., Naeem, R., Carey, V.J., Richardson, A.L., and Weinberg, R.A. (2005). Stromal fibroblasts present in invasive human breast carcinomas promote tumor growth and angiogenesis through elevated SDF-1/CXCL12 secretion. Cell *121*, 335–348.

Peled, A., Petit, I., Kollet, O., Magid, M., Ponomaryov, T., Byk, T., Nagler, A., Ben-Hur, H., Many, A., Shultz, L., et al. (1999). Dependence of human stem cell engraftment and repopulation of NOD/SCID mice on CXCR4. Science *283*, 845–848.

Petty, J.M., Sueblinvong, V., Lenox, C.C., Jones, C.C., Cosgrove, G.P., Cool, C.D., Rai, P.R., Brown, K.K., Weiss, D.J., Poynter, M.E., and Suratt, B.T. (2007). Pulmonary stromal-derived factor-1 expression and effect on neutrophil recruitment during acute lung injury. J. Immunol. *178*, 8148–8157.

Proost, P., Mortier, A., Loos, T., Vandercappellen, J., Gouwy, M., Ronsse, I., Schutyser, E., Put, W., Parmentier, M., Struyf, S., and Van Damme, J. (2007). Proteolytic processing of CXCL11 by CD13/aminopeptidase N impairs CXCR3 and CXCR7 binding and signaling and reduces lymphocyte and endothelial cell migration. Blood *110*, 37–44.

Raz, E., and Reichman-Fried, M. (2006). Attraction rules: germ cell migration in zebrafish. Curr. Opin. Genet. Dev. *16*, 355–359.

Reichman-Fried, M., Minina, S., and Raz, E. (2004). Autonomous modes of behavior in primordial germ cell migration. Dev. Cell *6*, 589–596.

Renault, A.D., and Lehmann, R. (2006). Follow the fatty brick road: lipid signaling in cell migration. Curr. Opin. Genet. Dev. *16*, 348–354.

Renault, A.D., Sigal, Y.J., Morris, A.J., and Lehmann, R. (2004). Soma-germ line competition for lipid phosphate uptake regulates germ cell migration and survival. Science *305*, 1963–1966.

Serhan, C.N., and Savill, J. (2005). Resolution of inflammation: the beginning programs the end. Nat. Immunol. *6*, 1191–1197.

Sotsios, Y., Whittaker, G.C., Westwick, J., and Ward, S.G. (1999). The CXC chemokine stromal cell-derived factor activates a Gi-coupled phosphoinositide 3-kinase in T lymphocytes. J. Immunol. *163*, 5954–5963.

Valentin, G., Haas, P., and Gilmour, D. (2007). The Chemokine SDF1a Coordinates Tissue Migration through the Spatially Restricted Activation of Cxcr7 and Cxcr4b. Curr. Biol. *17*, 1026–1031.

Vicente-Manzanares, M., Rey, M., Jones, D.R., Sancho, D., Mellado, M., Rodriguez-Frade, J.M., del Pozo, M.A., Yanez-Mo, M., de Ana, A.M., Martinez, A.C., et al. (1999). Involvement of phosphatidylinositol 3-kinase in stromal cell-derived factor-1 alpha-induced lymphocyte polarization and chemotaxis. J. Immunol. *163*, 4001–4012.

Weidinger, G., Wolke, U., Koprunner, M., Klinger, M., and Raz, E. (1999). Identification of tissues and patterning events required for distinct steps in early migration of zebrafish primordial germ cells. Development *126*, 5295–5307.

Weidinger, G., Wolke, U., Koprunner, M., Thisse, C., Thisse, B., and Raz, E. (2002). Regulation of zebrafish primordial germ cell migration by attraction towards an intermediate target. Development *129*, 25–36.

Wolke, U., Weidinger, G., Köprunner, M., and Raz, E. (2002). Multiple levels of post-transcriptional control lead to germ line specific gene expression in the zebrafish. Curr. Biol. *12*, 289–294.

Zou, Y.R., Kottmann, A.H., Kuroda, M., Taniuchi, I., and Littman, D.R. (1998). Function of the chemokine receptor CXCR4 in haematopoiesis and in cerebellar development. Nature *393*, 595–599.

Developmental Cell
Article

Notch Signaling and Morphogenesis of Single-Cell Tubes in the *C. elegans* Digestive Tract

Jeffrey P. Rasmussen,[1,2,3] Kathryn English,[1,2] Jennifer R. Tenlen,[1,2,3] and James R. Priess[1,2,4,*]
[1]Fred Hutchinson Cancer Research Center, Seattle, WA 98109, USA
[2]Howard Hughes Medical Institute
[3]Molecular and Cellular Biology Program
[4]Department of Biology
University of Washington, Seattle, WA 98195, USA
*Correspondence: jpriess@fhcrc.org
DOI 10.1016/j.devcel.2008.01.019

SUMMARY

During organogenesis of the *C. elegans* digestive system, epithelial cells within a cyst-like primordium develop diverse shapes through largely unknown mechanisms. We here analyze two adjacent, dorsal epithelial cells, called pm8 and vpi1, that remodel their shapes and apical junctions to become donut-shaped, or toroidal, single-cell tubes. pm8 and vpi1 delaminate from the dorsal cyst epithelium and migrate ventrally, across the midline of the cyst, on a transient tract of laminin. pm8 appears to encircle the midline by wrapping around finger-like projections from neighboring cells. Finally, pm8 and vpi1 self-fuse to become toroids by expressing AFF-1 and EFF-1, two fusogens that are each sufficient to promote crossfusion between other cell types. Notch signaling in pm8 induces AFF-1 expression, while simultaneously repressing EFF-1 expression; vpi1 expresses EFF-1 independent of Notch. Thus, the adjacent pm8 and vpi1 cells express different fusogens, allowing them to self-fuse into separate, single-cell tubes while avoiding crossfusion.

INTRODUCTION

Epithelia formation is fundamental to the development of all animals. Epithelial cells are polarized, with basolateral domains separated from apical domains by adherens junctions. The adherens junctions contain E-cadherin and other proteins that mediate cell adhesion, and the basal surface typically is associated with a basal lamina. Despite the organization and cohesion of epithelial cells, epithelia can be extensively remodeled in response to developmental signals. Planar epithelia can be remodeled into tubes, and epithelial tubes can develop branches (Lubarsky and Krasnow, 2003). Although oriented cell division or apoptosis can contribute to remodeling (Gong et al., 2004; Schreiber et al., 2005), in many cases remodeling involves nondividing cells that change shape or position. For example, the elaborately branched tracheal tubes of *Drosophila* begin as sacs of epithelial cells that intercalate and change shape without dividing (Casanova, 2007). Epithelia can dissociate during epithelial to mesenchymal transitions (Thiery and Sleeman, 2006), or undergo transient restructuring to allow the passage of migrating cells. Examples of transepithelial migration include *Drosophila* germ cells that migrate through the posterior midgut epithelium to form the gonad (Kunwar et al., 2006), and the passage of human leukocytes through the epithelial lining of blood vessels to reach sites of infection (Petri and Bixel, 2006). These events demonstrate the remarkable ability of epithelial cells to change shapes by altering their adhesiveness.

The *C. elegans* pharynx provides an attractive model system for analyzing molecular mechanisms of epithelial remodeling during organogenesis. The pharynx is essentially a monolayered myoepithelial tube whose anatomy, specification, and gene expression have been compared to the heart of higher animals. For example, the ascidian heart is a simple tube, consisting of a monolayer of myoepithelial cells (Oliphant and Cloney, 1972). The NK homeodomain transcription factors CEH-22 and Nkx2.5 function in nematode pharynx and vertebrate heart development, respectively, and zebrafish Nkx2.5 can rescue *C. elegans* mutants lacking CEH-22 (Chen and Fishman, 1996; Okkema and Fire, 1994; Okkema et al., 1997; Haun et al., 1998). In addition to muscle cells, the pharynx contains glands, neurons, and structural cells called marginal cells. An ultrastructural reconstruction of the adult pharynx showed these individual cells have remarkably complex and reproducible shapes (Albertson and Thomson, 1976). Along the longitudinal axis of the pharynx, muscles and marginal cells are organized into distinct anterior/posterior groups based on region-specific morphologies. For example, the most anterior muscle is shaped like a fenestrated cylinder with openings that are nearly as large as the cell, while the most posterior muscle is a toroid. The pharynx is linked to the intestine through valve cells, the first of which is also a toroid.

Nearly all of the complex changes in pharyngeal cell shape begin within a cylindrical cyst of initially uniform, simple epithelial cells (Leung et al., 1999; Portereiko and Mango, 2001). During early embryogenesis, cells from two separate lineages aggregate to form a primordium that forms the pharynx and valve (reviewed in Mango, 2007). In both lineages, the key step in specifying pharyngeal/valve fate is the expression of *pha-4*, an organ selector gene that encodes a forkhead box transcription factor. PHA-4 is expressed in all pharyngeal and valve cells, and is necessary and sufficient for most early embryonic cells to adopt pharyngeal fates (Horner et al., 1998; Kalb et al.,

1998; Mango et al., 1994). Midway through embryogenesis, cells in the primordium polarize to form an epithelial cyst that is primarily one cell in thickness (Leung et al., 1999). In cross-sections of the cyst, most cells have a simple, wedge-shaped appearance: each cell has a narrow apical tip facing the midline of the cyst, and a broad basal surface associated with a basal lamina.

A complex remodeling of the cyst occurs over the next few hours of embryogenesis (Leung et al., 1999; Mango, 2007). The cylindrical cyst is transformed into a bilobed tubular pharynx that contains a wide diversity of cell shapes and that is partitioned from the adjacent valve cells by a basal lamina. To understand how cell shapes are determined within the cyst, we analyzed here the development of two toroidal, single-cell tubes called pm8 and vpi1. We show that morphogenesis involves Notch signaling, epithelial to mesenchymal transitions, migration through neighboring cells on a transient tract of laminin, and self-fusion. These results reveal numerous interactions that contribute to the final shapes of the cells.

RESULTS

Background

The pharynx is a bilobed myoepithelial tube containing pharyngeal muscles (pm), structural cells called marginal cells (mc), gland cells, and neurons (Figure 1A; see Mango, 2007 for description of pharyngeal anatomy and development). The pharynx connects to the intestine through a multicellular valve (vpi cells for *v*alve *p*harynx/*i*ntestine). The events analyzed here occur in the posterior lobe of the pharynx, called the terminal bulb, and in the adjacent valve cells. Most cells in the pharynx are arranged with 3-fold radial symmetry around the lumenal axis (Figure 1A and Movie S1, see the Supplemental Data available with this article online). Muscles, marginal cells, and valve cells show anterior/posterior differences in cell morphology, creating distinctive groups of one to six cells (groups pm1–8, mc1–3, vpi1–3; Albertson and Thomson, 1976). For example, mc3V is the ventral cell of the three group 3 marginal cells (Figure 1A). Although multiple cells surround the lumen of the pharynx/valve in a typical cross-section, there are two examples of single-cell tubes: pm8, the terminal cell in the pharynx, and vpi1, the first cell in the valve (Figures 1A–1C). Our analysis of pm8 and vpi1 morphogenesis begins at about 6.5 hr after the two-cell stage of embryogenesis, when the primordium of the pharynx/valve is a cylindrical cyst of polarized epithelial cells (Figures 1B and 1D). The apical surfaces of these cells face the midline of the cyst, where the pharyngeal/valve lumen forms, and are outlined by junctional proteins such as AJM-1 (Figures 1D and 1E). The basal surfaces of these cells face the periphery of the cyst and are associated with a basal lamina that contains laminin (Figure 1D).

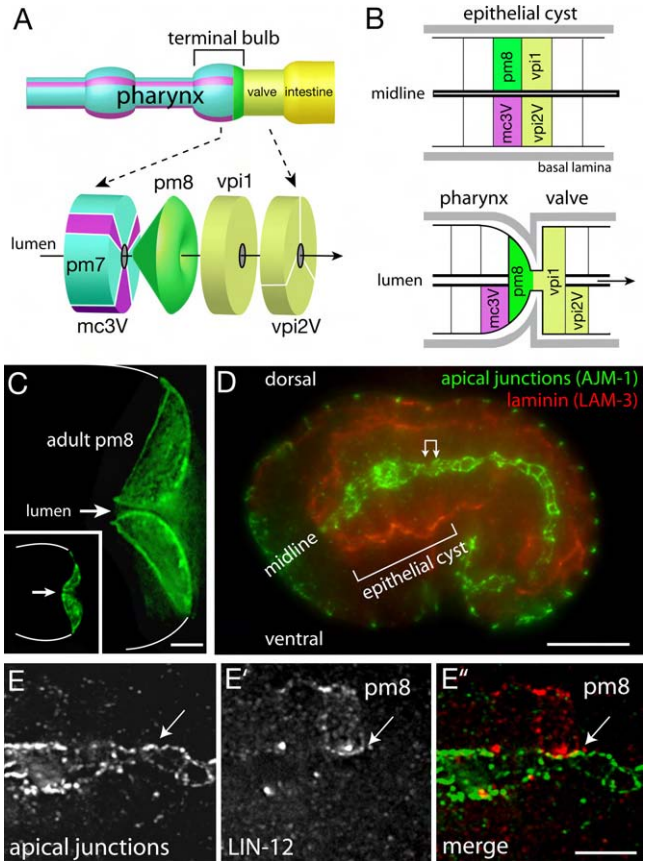

Figure 1. Cell Morphology and Polarity in the Pharynx/Valve

(A) Diagram of some of the cells in the terminal bulb of the pharynx and in the valve. The three group 3 marginal cells are shown in purple, and names of the principle cells mentioned in the text are indicated.

(B) Diagram of cell positions in the cyst (top) and pharynx/valve (bottom). Note the reorientation of the basal lamina-associated, basal surfaces of pm8 and vpi1.

(C) pm8 in an adult and newly hatched larva (inset) visualized by *ref-1*::GFP-PM; white lines indicate perimeter of terminal bulb.

(D) Optical longitudinal section through the middle of an embryo showing the epithelial cyst (bracket).

(E–E″) High magnification of region corresponding to double-headed arrow in (D) after immunostaining for apical junctions (AJM-1) and LIN-12/Notch to visualize pm8 (see also Figure 3D). Note that pm8 contacts, but does not cross, the midline (arrow). Polygonal shapes are the apical surfaces of various cells in the cylindrical array around the midline. Bars = 2 μm (C), 10 μm (D), and 2.5 μm (E–E″).

Notch Signaling Regulates Gene Expression in pm8

Several genes have been described that are expressed in multiple or all pharyngeal and valve cells, however, the *ceh-24* gene is expressed uniquely in pm8 (Harfe and Fire, 1998). CEH-24 is an NK transcription factor related to CEH-22 (see Introduction), and previous studies identified a 117 bp enhancer from *ceh-24* that promotes pm8-specific expression (Harfe and Fire, 1998). We noticed that this enhancer contained a conserved GTGGGAA sequence that is a predicted binding site for LAG-1/CSL, the core DNA-binding protein in the Notch signaling pathway (Figure S1A; see Greenwald, 2005 and Bray, 2006 for reviews on Notch). We found that LAG-1/CSL bound the wild-type enhancer in vitro, and that binding was dependent on the GTGGGAA sequence (Figure S1B). Transgenic *ceh-24*::GFP reporters constructed with either the wild-type enhancer sequence, or with a GTGGGAA to GAGGCAA mutation, were expressed in head neurons outside the pharynx, but only the wild-type enhancer drove robust expression in pm8 (Figure 2C and Figure S1D; Table 1). Expression was dependent on Notch activity, as *lin-12 glp-1* double mutants that lack both of the *C. elegans* Notch proteins, LIN-12 and GLP-1, either did not express *ceh-24*::GFP (18/20 embryos)

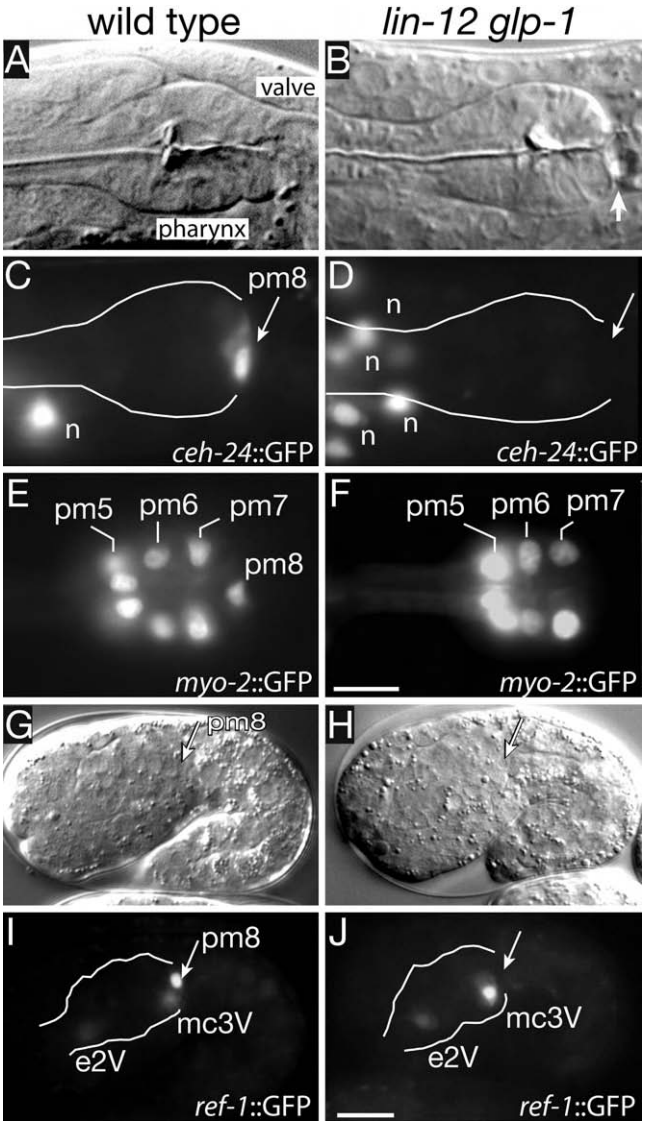

Figure 2. Notch-Dependent Gene Expression in pm8

The columns show wild-type (left) and *lin-12 glp-1* mutant (right) animals either after hatching at 14 hr (A–F), or at 7 hr in embryogenesis (G–J). Transgenic reporters are as listed; white lines indicate perimeter of the pharynx (C and D) or epithelial cyst (I and J). Nuclei labeled "n" in (C) and (D) are neurons outside the pharynx that express *ceh-24*::GFP. Bars = 5 μm (A–F), and 10 μm (G–J). Embryos are approximately 50 μm in length.

or showed only weak expression (2/20 embryos; Figure 2D; Table 1).

REF-1 is a *C. elegans* bHLH transcription factor that is distantly related to *Drosophila* E(spl) (Alper and Kenyon, 2001; Neves and Priess, 2005). The *ref-1* gene is a direct target of Notch signaling in several interactions in the early embryo, but is expressed in other cells independent of Notch (Neves and Priess, 2005). In the wild-type epithelial cyst, we found that *ref-1*::GFP was expressed in pm8 and in the sister cells e2V and mc3V (Figure 2I and data not shown). *lin-12 glp-1* double mutants showed expression in e2V and mc3V, but not in pm8 (Figure 2J; Table 1). Additional experiments showed that pm8 expression required

Table 1. Transgene Expression in pm8

Reporter	Genotype	pm8 Expression % (n)[a]
ceh-24*::GFP*	*WT*	100 (50)
	lin-12(n676n930ts)	52 (72)
	lin-12(n941)glp-1(q46)	10 (20)
ceh-24$^{(-CSL)}$*::GFP*	WT	15 (38)[b]
ref-1$^{(1.8kb)}$::REF-1::GFP	*WT*	100 (60)
	lin-12(n941)glp-1(q46)	0 (83)
	lin-12(n941)	2 (64)
ref-1$^{(600bp)}$::GFP	*WT*	100 (35)
	lag-1(q385)/+	100 (18)
	lag-1(q385)	0 (10)
	lag-2(q411)	100 (15)
	lag-2(q420ts)	100 (20)
	apx-1(zu347ts)	100 (21)
	lag-2(q387)[c]	0 (12)
ref-1$^{(1.8\ -CSL)}$::REF-1::GFP[d]	*WT*	0 (25)
myo-2::GFP	WT	100 (110)
	lag-2(q420ts)	100 (36)
	lin-12(n941)/+	100 (44)
	lin-12(n941)	36 (78)
	lin-12(n941)glp-1(q46)[e]	45 (206)[f]
	lag-1(q385)	3 (89)
aff-1::GFP[g]	WT	96 (67)
	lag-1(q385)	2 (62)[h]

[a] Expressing cells at or near the normal position of pm8 were scored as positive; this includes cases where the expressing cell was in the valve. For example, 9/93 *myo-2*::GFP-expressing nuclei in *lin-12(n941)glp-1(q46)* were in the valve adjacent to the pharynx.

[b] Expression was weak and in two cases a comparable signal was observed in vpi1.

[c] *lag-2(q387)* is a small deficiency that deletes both *lag-1* and *apx-1*, but removes several additional genes.

[d] This reporter lacks all eight CSL sites (Neves and Priess, 2005).

[e] These animals showed a strong correlation between *myo-2*::GFP expression and whether or not the pm8 nucleus was in the ventral side of the terminal bulb; 38/57 of expressing pm8 cells were ventral.

[f] The myogenesis defect in *lin-12 glp-1* double mutants is significantly less than in *lag-1* mutants. Additional experiments ruled out the possibility that the candidate pm8 muscle was a different cell that normally undergoes apoptosis (see analysis in Figure S2). Because the homozygous *lin-12 glp-1* larvae were derived from heterozygous parents, perdurance of maternally-provided *lin-12* and/or *glp-1* might contribute to the phenotype. However, the phenotype of the double mutant was not enhanced by *lin-12(RNAi)*, and it is not possible to remove maternal *glp-1* without severely disrupting embryogenesis (data not shown; Priess, 2005).

[g] Because this reporter transgene is not integrated into a chromosome, and can be lost spontaneously, only those animals with expression in the pm3 and pm5 muscle groups of the pharynx were scored for pm8 expression.

[h] The single positive animal had expression throughout the valve.

LAG-1/CSL, and appeared to involve either of the Notch ligands LAG-2/Delta or APX-1/Delta (Table 1 and see below).

The *myo-2* gene encodes a pharyngeal-specific myosin; the *myo-2* promoter lacks predicted LAG-1/CSL binding sites, and thus is unlikely to be a direct target of Notch signaling (data

not shown). We generated an integrated transgenic strain expressing a nuclear-localized *myo-2*::GFP reporter (J. Gaudet, unpublished data), and found that wild-type larvae reproducibly showed expression in each of the expected 13 muscle nuclei in the terminal bulb (6 pm5 + 3 pm6 + 3 pm7 + 1 pm8; Figure 2E; Table 1). Notch mutant larvae had defects in pm8 myogenesis (Figure 2F and Figure S2B); for example, 97% of *lag-1* mutant larvae contained only 12 *myo-2*::GFP-expressing cells in the terminal bulb, and specifically lacked expression at the normal position of pm8 (Table 1). We conclude that Notch signaling induces the expression of a least two transcription factors in pm8, CEH-24 and REF-1, and is required for pm8 myogenesis.

Notch Mutants Are Defective in Both pm8 and vpi1 Morphogenesis

lag-1 mutant larvae usually lacked a nucleus in the normal position of the pm8 nucleus, suggesting that Notch mutants have a defect in pm8 morphogenesis that is at least partially separate from the myogenesis defect. We used light and electron microscopy to compare the pharynx and valve in newly hatched, wild-type larvae with Notch mutant larvae. In newly hatched, wild-type larvae, the first valve cell (vpi1) forms a cup-like enclosure over the posterior end of pm8 (Figures S3A and S3C); in live animals, pm8 and vpi1 appear tightly adherent and show no visible separation during body locomotion (unpublished data). pm8 and vpi1 make a small direct contact near their apical surfaces, but are otherwise separated by a prominent basal lamina that almost completely separates the pharynx from the valve (Figure S3C). In Notch mutant larvae, cells at the pharynx/valve interface had several morphological defects including large gaps between cells (arrow in Figure 2B), broad contacts between pharyngeal cells and valve cells without an intervening basal lamina (Figure S3B and data not shown), and abnormal patterns of apical junctions (see Figures 4H and 4I). We were unable to identify cells with the normal morphology of pm8 or vpi1 in the mutant larvae, although other cells such as the pm6 and pm7 muscles appeared well differentiated (n = 12; Figure S3B). Thus, these results suggest the Notch pathway has a role in the differentiation or morphogenesis of pm8, vpi1, and possibly other valve cells.

Notch Is Activated in the Postmitotic pm8 Cell

To determine when and where Notch interactions occurred, we first sought to identify the relevant ligand-expressing cells through laser-killing experiments. We found that descendants of the embryonic cell MSaapa that were not previously known to function in Notch signaling expressed the ligand LAG-2/Delta (Figure 3A) and were required for Notch-dependent *ref-1*::GFP expression in pm8 (Figure 3B). In immunostaining experiments, the first apparent contact between MSaapa descendants expressing *lag-2*::GFP and cells that express the receptor LIN-12/Notch occurred after the birth of pm8, approximately 6 hr after the two-cell stage. A clone of four LIN-12-expressing cells is located in the left dorsal quadrant of the epithelial cyst; the most posterior cell in this group is pm8 (Figures 3C and 3D). At this stage, vpi1 is in the right dorsal quadrant of the cyst and does not express detectable levels of LIN-12; the receptor GLP-1/Notch was not detectable in vpi1 or pm8 (Figure 3C and data not shown). MSaapa descendants within the cyst express LAG-2/Delta, and one or two of these cells contact pm8 directly (Figure 3C). Lateral views of embryos at approximately the same stage showed Notch-independent expression of *ref-1*::GFP in the pharyngeal cells e2V and mc3V, but no other pharyngeal or valve cells (Figure 3D′). However, pm8 showed strong *ref-1*::GFP expression about 30 min later (Figure 3E′). These results suggest that Notch signaling is activated in the postmitotic pm8 cell, but not in vpi1 or any other valve cell, and that Notch thus has an indirect role in valve differentiation or morphogenesis.

pm8 and vpi1 Morphogenesis

The initial stages of wild-type pm8 morphogenesis were visualized by immunostaining for LIN-12/Notch. For subsequent stages, we used the *ref-1* promoter to drive expression of a plasma membrane-localized GFP (*ref-1*::GFP-PM). pm8 initially is a wedge-shaped epithelial cell on the dorsal, left side of the cyst, and has a broad, midline-facing apical surface similar to other cyst cells (Figures 1E and 3D). Shortly thereafter, pm8 nearly detaches from the dorsal basal lamina, and its apical surface is remodeled into a lamella that invades the ventral side of the cyst (Figures 3E, 4A, and 4B; data not shown). Both the pm8 nucleus and bulk cytoplasm cross into the ventral side, leaving only a thin connection to the dorsal perimeter of the cyst (Figures 4A–4D). pm8 invades the ventral side of the cyst to the left of the midline, but gradually spreads across the entire cross section of the cyst (Figure 4F and Movie S1).

vpi1 morphogenesis was examined by electron microscopy and expression of *eff-1*::EFF-1::GFP (see below). Similar to pm8, vpi1 initially is a wedge-shaped dorsal cell that extends a lamellar process into the ventral side of the cyst; the vpi1 lamella is closely associated with the posterior surface of the migrating pm8 cell body (Figure 4E and Figure S3D). In contrast to pm8, the nucleus and bulk cytoplasm of vpi1 remain on the dorsal side of the cyst. Both pm8 and vpi1 appear to redistribute cytoplasm throughout their respective cell bodies during late embryogenesis, becoming symmetrical tubes centered on the midline of the cyst (Figure 1C, inset, and data not shown).

pm8 and vpi1 Migrate within the Cyst on a Transient Path of Laminin

In all embryos analyzed, pm8 and vpi1 migrated into the ventral side of the cyst specifically at the lateral interface between the ventral cells mc3V and vpi2V (see Figure 1B). In some examples of transepithelial migration in other systems, cells in the target epithelium disassociate prior to the arrival of migrating cells, thus creating openings for migration (Kunwar et al., 2006). Electron micrographs of the epithelial cyst before or during pm8 migration did not show obvious gaps between any ventral cells (data not shown). A second possibility is that the mc3V/vpi2V interface provides a guidance cue for pm8 migration. Consistent with this hypothesis, we found that a transient tract of laminin appears in the ventral cyst shortly before pm8 migration (Figures 5A and 5D), and disappears after pm8 migration (Figure 5E). Heterotrimeric laminin in *C. elegans* is composed of either of two α chains (EPI-1 and LAM-3), a β chain (LAM-1), and a γ chain (LAM-2) (Kramer, 2005). An antiserum specific for LAM-3 stained the tract in wild-type embryos, but not in *lam-3* mutant embryos (data not shown). In time-lapse movies of *lam-1*::LAM-1::GFP, the laminin tract appeared to spread inward from the ventral perimeter of the cyst over a 20 min interval (Movie S2) before regressing. In later

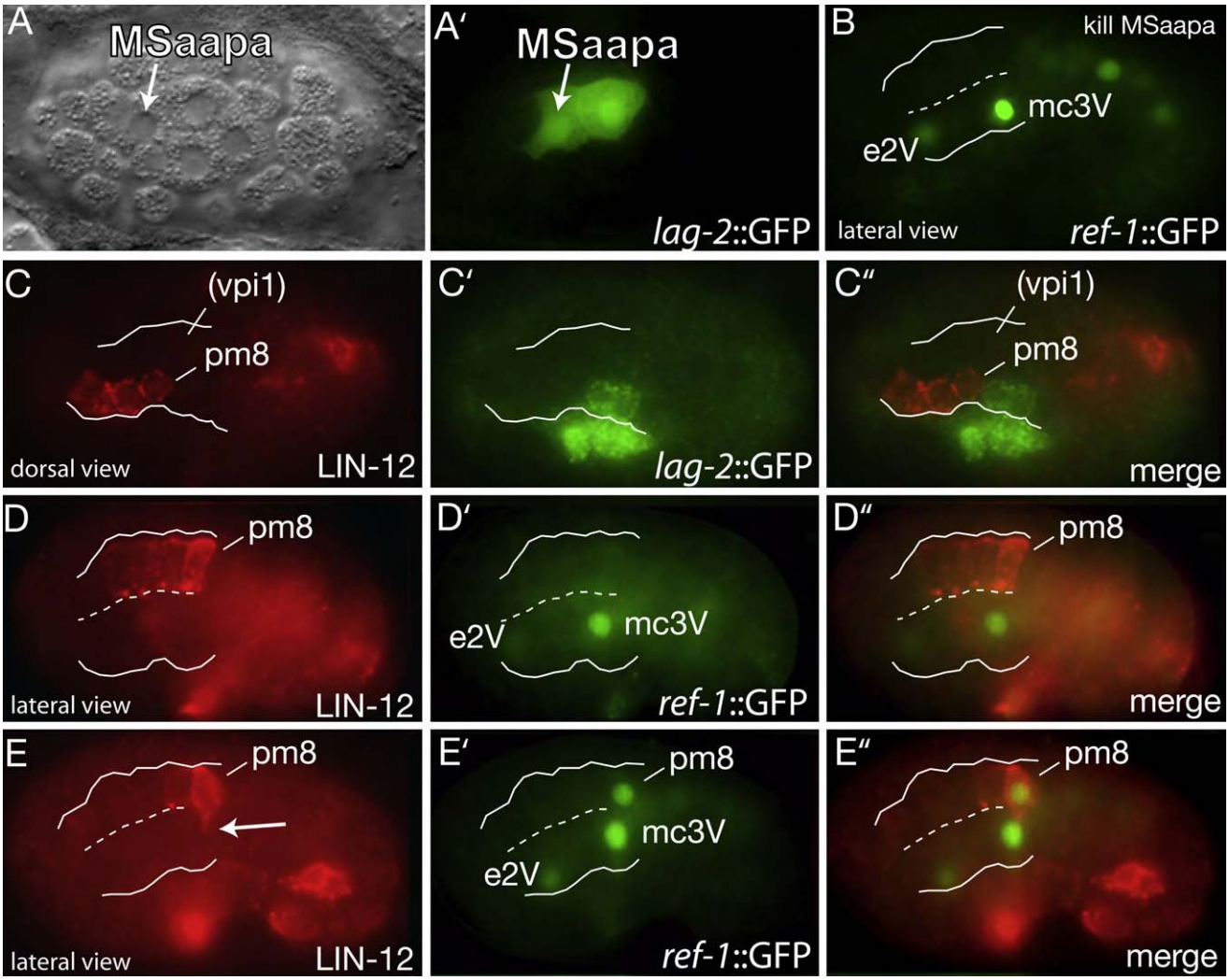

Figure 3. Notch Signaling in the Epithelial Cyst

(A–A′) Ventral view of an embryo before formation of the cyst showing *lag-2* expression in MSaapa.

(B) *ref-1*::GFP expression in a cyst-stage, wild-type embryo after killing MSaapa; embryo shown is the same stage and orientation as in Figure 2I. *ref-1*::GFP expression in pm8 was observed after killing the following cells: MS (0/4 embryos), MSaa (0/4- MS and MSaa are precursors of pm8), MSap (6/6), MSaap (0/4), MSaapa plus MSaapp (0/3), MSaapp (5/5),and MSaapa (4/4 when the ablated cell entered the body cavity, 0/3 when it remained outside).

(C–C″) Dorsal view of a 6 hr embryo immunostained for GFP (*lag-2*::GFP) and LIN-12/Notch; white lines indicate boundary of epithelial cyst. The approximate position of vpi1 is indicated based on light microscopy of living embryos at this stage and orientation.

(D–D″) Lateral view of embryo at about the same stage as (C); *ref-1*::GFP is expressed in the Notch-independent cells e2V and mc3V, but not in pm8.

(E–E″) Embryo approximately 20 min later than in (D) showing *ref-1*::GFP in pm8. Note lamella from pm8 (arrow in [E]) extending ventrally across the midline of the cyst (dashed line).

embryogenesis, a different and permanent zone of laminin appears along the posterior surface of pm8 that is part of the basal lamina between pm8 and vpi1 (Figure 5F and Figure S3C). Using *ref-1*::GFP to identify both mc3V and pm8, we found that the transient laminin tract appeared specifically at the mc3V/vpi2V interface, and that the tract disappeared concomitant with the ventral migration of pm8 (Figures 5G–5I). The laminin tract was present at the mc3V/vpi2V interface in *lin-12 glp-1* mutants, indicating that it is specified independent of Notch signaling. Indeed, the tract persisted in 7.5 hr-old *lin-12 glp-1* mutant embryos (Figure 5B) long after it disappears from wild-type embryos (Figure 5E).

An antiserum against EPI-1 stained the tract, indicating that it contains both laminin α chains, LAM-3 and EPI-1. We found that *lam-3* and *epi-1* single mutants appeared to have normal pm8 migration (data not shown). However, pm8 was unable to migrate ventrally in *lam-3; epi-1* double mutants, and instead remained primarily on the dorsal side of the cyst (Figure 5J). Cell migration on laminin surfaces can involve the major laminin receptor, integrin. In *C. elegans*, *ina-1* is one of two genes encoding the α subunit of heterodimeric integrin, and *pat-3* encodes the sole β subunit (Kramer, 2005). *pat-3(RNAi)* embryos had severe developmental defects that complicated an analysis of pm8 migration. However, most *ina-1* mutants were able to

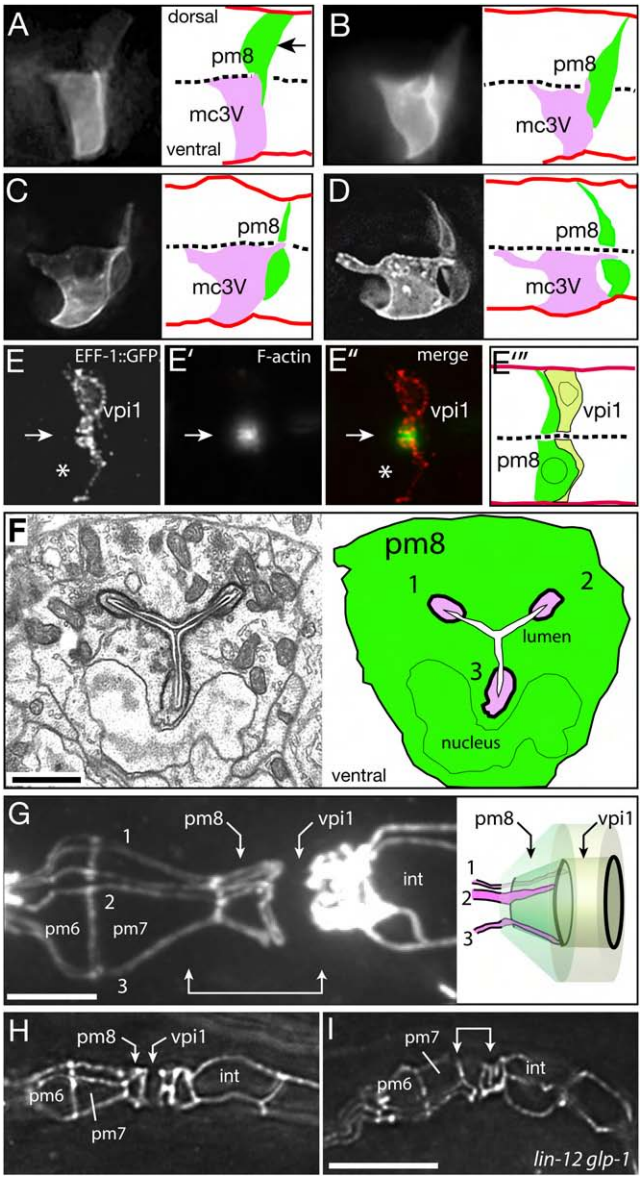

Figure 4. Ventral Migration and Lumen Formation in pm8 and vpi1

(A–D) *ref-1*::GFP-PM expression in pm8 and the group 3 marginal cell mc3V in successively older embryos. Images are optical sections through the midline of the cyst; a complete image series corresponding to (D) is shown in Movie S4.

(E–E″) vpi1 expressing *eff-1*::EFF-1::GFP and stained with phalloidin to visualize F-actin at the midline (arrow); note relative absence of actin in pm8 (asterisk indicates position of pm8 nucleus).

(E‴) Diagram of vpi1 with the approximate position of the pm8 cell body included for reference (see Figure S3D).

(F) Electron micrograph and diagram of a cross-section through pm8 in an embryo near hatching. The three marginal cell fingers (numbered 1–3) are evident in the Y-shaped lumenal channel (white) of pm8.

(G) Apical junctions in a wild-type, third stage (L3) larva; cells in the pharynx and valve do not divide during larval development, but increase in size and allow better visualization of apical junctions. Apical surfaces of cell like pm7 resemble broad triangles, while the group 3 marginal cells (numbered 1–3) have long, thin apical surfaces (see also Movie S1). Note how fingers from the marginal cells extend through the apical surface of pm8. The region indicated by the double-headed arrow is diagrammed to show a superposition of the pm8 and vpi1 cell bodies on their apical surfaces; apical junctions are drawn in black. (H and I) Same region as in (F) in wild-type (H) and *lin-12 glp-1* mutant (I) embryos near hatching. Bars = 1 μm (F) and 5 μm (G–H).

complete embryogenesis and hatch as deformed larvae. We found that *ina-1* mutants showed severe defects in pm8 migration (Figure 5K). In many larvae, pm8 appeared to have migrated abnormally into the region normally occupied by valve cells and anterior intestinal cells (Figure 5K). The pm8 cell body was closely apposed to the basal lamina surrounding the valve and intestine, suggesting that pm8 might extend along basal laminae associated with these surfaces rather than the normal mc3V/vpi2V interface.

Tubulogenesis and Self-Fusion

A single-cell tube such as pm8 or vpi1 might, in principle, be either a toroid or a C-shaped cell. The apical surfaces of both types of tubes have circular intercellular junctions at each end of the cell, but only the C-shaped cell has an autocellular apical junction (Figure 6A). pm8 and vpi1 have been shown to be toroids, rather than C-shaped cells, in adult *C. elegans* (Albertson and Thomson, 1976). We found that in 7.5 hr embryos pm8 and vpi1 had the apical junction pattern expected for toroidal cells (two unconnected circles; Figure 6B), and confirmed by electron microscopy that both cells are toroids (Figure S4). Although an epithelial cell can roll up into a C-shape, a toroid has a distinct topology that requires at least one self-fusion event. *C. elegans* development provides multiple examples where adjacent cells fuse together into a multinucleate syncytium, and most of these fusions require the *eff-1* gene (Mohler et al., 2002). EFF-1 acts homotypically to induce fusion; it is sufficient to promote fusion of heterologous cells that each express EFF-1 (Podbilewicz et al., 2006). Recent studies in *C. elegans* have identified a second fusogen, AFF-1, with a similar ability to fuse heterologous cells (Sapir et al., 2007). We found that *eff-1*::EFF-1::GFP was expressed at high levels in vpi1 beginning at about 7 hr (Figure 6B′), but was never expressed in pm8. In 7.5 hr *eff-1* mutant embryos, vpi1 had a novel, autocellular junction as characteristic of a C-shaped cell, while pm8 retained the wild-type, toroidal pattern of intercellular junctions (Figure 6B, inset). Conversely, *aff-1*::GFP was expressed in the wild-type pm8 beginning at about 7.2 hr, but was never expressed in vpi1 (Figure 6C′). In 7.5 hr *aff-1* mutant embryos, pm8 had a novel autocellular junction, while vpi1 retained the wild-type, toroidal pattern of intercellular junctions (Figure 6B, inset). These results suggest that in normal development both pm8 and vpi1 adopt C-shapes before self-fusing through AFF-1 and EFF-1 activities, respectively.

Because cells in the approximate positions of pm8 and vpi1 have highly abnormal patterns of apical junctions in Notch mutants, we examined EFF-1 expression in these embryos. Although *eff-1*::EFF-1::GFP is expressed only in vpi1 in wild-type embryos, in *lag-1* mutant embryos the reporter was expressed in two adjacent cells at this position (Figures 6D and 6E), or in a single, abnormally large binucleate cell (Figure 6F). We identified one of the cells that expressed *eff-1*::EFF-1::GFP as pm8 based on its contact with group 7 muscle cells (data not shown). Conversely, neither pm8 nor vpi1 expressed *aff-1*::GFP in *lag-1* mutants (Table 1). We conclude that Notch has two roles in pm8 and vpi1 tubulogenesis. First, Notch is required for pm8 to express AFF-1, allowing pm8 to self-fuse. Second, Notch is

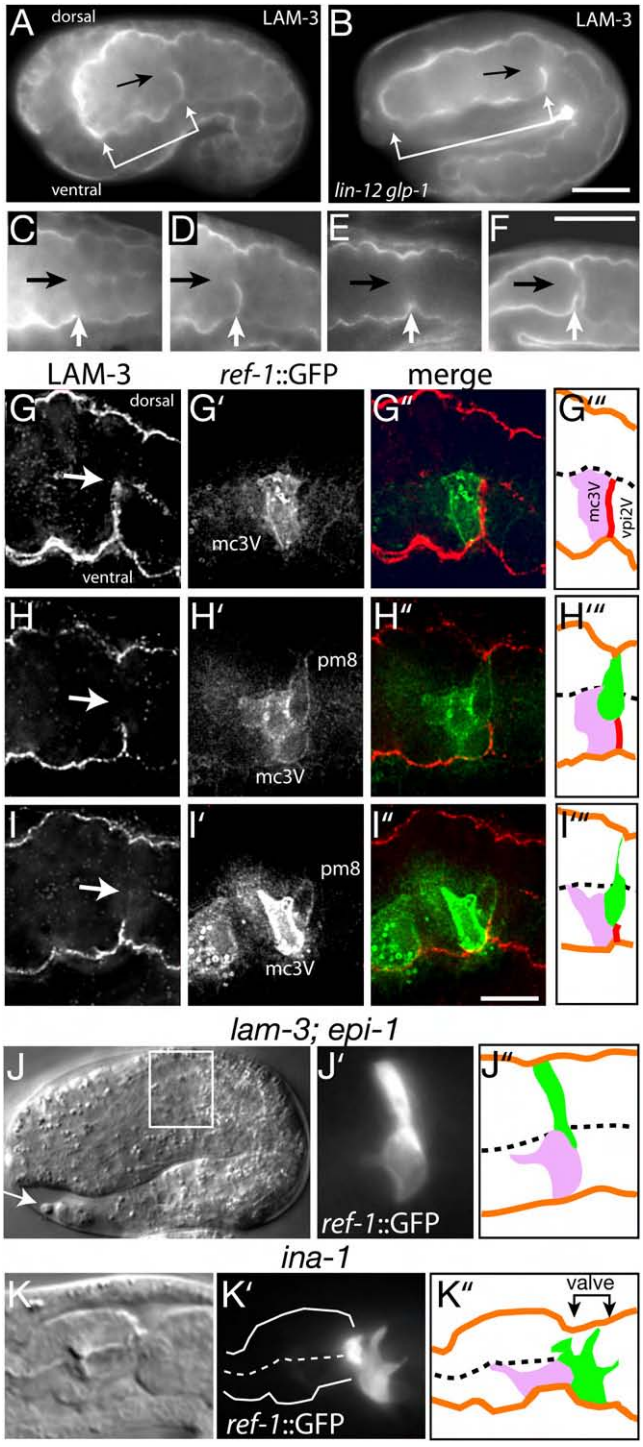

Figure 5. pm8 Migrates Ventrally on a Laminin Tract

(A) Optical longitudinal section through the middle of a 7 hr embryo stained for laminin. Laminin is present in the basal lamina surrounding the cyst (bracket). A transverse tract of laminin is evident in the posterior ventral half of the cyst (arrow indicates the cyst midline).

(B) *lin-12 glp-1* embryo at 7.5 hr.

(C–F) Sequence of successively older wild-type embryos showing the appearance (D) and disappearance (E) of the laminin tract, followed by the deposition of laminin on the posterior surface of pm8 after morphogenesis (F).

(G–I) Single embryos immunostained for LAM-3 and GFP (*ref-1*::GFP-PM) before (G), during (H), and near the completion (I) of pm8 migration. Arrows indicate the midline of the cyst. The fixation required for LAM-3 staining compromises GFP-PM localization in pm8 (compare with Figures 4A–4D).

(J) *lam-3; epi-1* double mutant at about 9 hr; pm8 has failed to migrate to the ventral side. This embryo has a shape similar to younger, 7.5 hr wild-type embryos because of defects in body morphogenesis, but has the well-formed tail spike (arrow) characteristic of wild-type 9 hr embryos.

(K) *ina-1* mutant larva showing pm8 extension into the valve/anterior intestine; similar defects occur in 74% of the hatched animals (n = 46). Bars = 10 μm (A–F) and 5 μm (G–I).

required to prevent pm8 from expressing EFF-1, thereby preventing pm8 from crossfusing with the EFF-1-expressing vpi1 cell.

Formation of the Intracellular Lumen in pm8 and vpi1

If pm8 and vpi1 normally become C-shaped cells that then self-fuse into toroids, how are their C-shapes determined? Three group 3 marginal cells are immediately anterior to pm8 during pm8 and vpi1 morphogenesis, and one of these (mc3V) expresses the same *ref-1*::GFP-PM reporter as pm8 (see Figures 1A and 3E′). In analyzing pm8 morphogenesis, we discovered that all three marginal cells extend a finger-like process posteriorly along the midline of the cyst during pm8 and vpi1 morphogenesis (Figures 4A–4D, and 4F, Figure S4A, and Movie S3). Thus, as the pm8 cell body moves into the left ventral side of the cyst, then spreads across the entire cross-section of the cyst, it wraps around the three marginal cell fingers (Movie S4). The fingers appeared to stop at, or extend slightly beyond, the posterior surface of pm8, where they would presumably contact the thin, ventral lamella from vpi1; vpi1 showed a strong enrichment of filamentous actin at the midline during formation of its lumen that was not apparent in pm8 (Figure 4E). Previous studies have shown that the pharyngeal lumen begins as small opening along the midline of the epithelial cyst; as the lumen expands it acquires a Y-shape when viewed in cross-section (Leung et al., 1999). The three marginal cell fingers remained in the center of pm8 during lumenal expansion, moving apart to occupy the three tips of the Y-shaped lumen (Figure 4F). The marginal cell fingers formed apical junction connections with the apical face of pm8, but not vpi1, and persisted in the pm8 cell body throughout larval development. Thus, while the cylindrical apical surface of pm8 initially has only two circular intercellular junctions (Figure 6B), in late embryos and larvae there are an additional three paired lines of junctional material across this surface that correspond to the three fingers (Figure 4G and 4H). An intriguing possibility is that the marginal cells fingers template the lumenal channel through pm8, and possibly vpi1, as pm8 and vpi1 remodel their apical surfaces. However, we have not yet been able to test this hypothesis by removing all three marginal cells simultaneously; pm8 formed an abnormally shaped lumen when only mc3V was killed with a laser microbeam (2/2 embryos), or when the fate of mc3V was transformed by the *glp-1(e2072)* mutation (3/3 embryos examined by electron microscopy; see Priess et al., 1987).

DISCUSSION

Establishment of the Pharynx/Valve Boundary

We here analyzed the morphogenesis of pm8 and vpi1, two adjacent, single-cell tubes in the *C. elegans* digestive tract. pm8

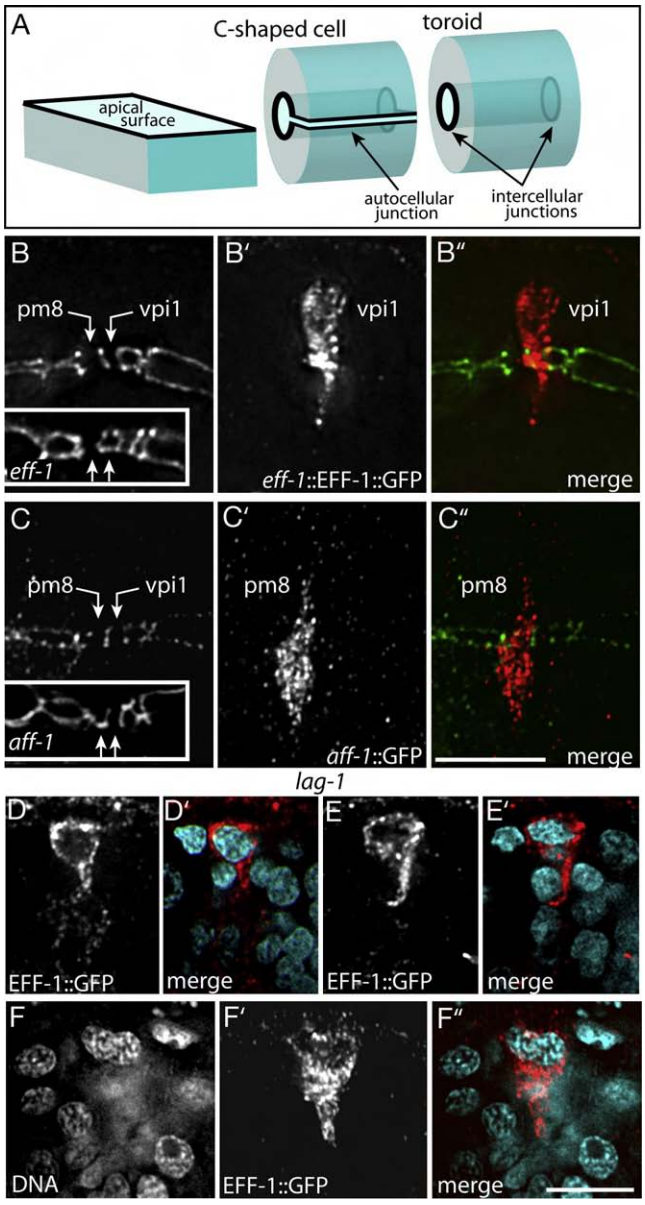

Figure 6. Self-Fusion of pm8 and vpi1

(A) Diagram comparing (1) a box-like cell with a simple, flat apical surface, (2) a topologically equivalent C-shaped cell, and (3) a topologically distinct toroid with a cylindrical apical surface; apical junctions are shown as bold lines.

(B–B″) Apical junctions at the pharynx/valve boundary in a 7.5 hr wild-type embryo stained for the apical junction marker AJM-1 (B) and for *eff-1*::EFF-1::GFP (B′). In this longitudinal view, the intercellular junctions at the ends of pm8 and vpi1 appear as vertical lines (B). The inset in (B) shows the same region in an *eff-1* mutant with an autocellular junction linking the intercellular junctions in vpi1, but not pm8.

(C–C″) Same region and stage as in (B), showing *aff-1*::GFP expression in pm8 and an autocellular junction in pm8 in an *aff-1* mutant (inset).

(D and D′) *lag-1* embryo showing a mononucleate cell expressing *eff-1*::EFF-1::GFP.

(E and E′) Different focal plane of the same embryo in (D) showing a second *eff-1*::EFF-1::GFP-expressing cell. Note that both cells have a ventral-directed process but neither cell extends completely through the cyst.

(F–F″) *lag-1* embryo with binucleate cell expressing *eff-1*::EFF-1::GFP.

Bars = 2.5 μm (B–F).

and vpi1 differentiate within a cyst of initially similar epithelial cells that all express PHA-4. The morphogenetic events that define the pm8/vpi1 boundary compartmentalize the cyst into the functionally distinct organs of the pharynx and valve. Cells throughout the epithelial cyst initially have radially oriented apicobasal axes, and most cells retain this polarity after morphogenesis. For example, pharyngeal muscles have single sarcomeres, and in most of these muscles the myofilaments are oriented radially, extending from the pharyngeal lumen to the peripheral basal lamina. In contrast, the apicobasal axes of pm8 and vpi1 are reoriented during morphogenesis. The basal surfaces of pm8 and vpi1 shift to face each other, and presumably form the basal lamina that nearly separates the two cells. This shift in polarity allows pm8 to have obliquely oriented myofilaments; similar myofilaments occur at the terminus of the pharynx in diverse groups of nematodes and are believed to function in moving foodstuffs during feeding (Doncaster, 1962; Mapes, 1965). We speculate that it is advantageous for pm8 and vpi1 to be toroids, rather than simply C-shaped cells, because toroids present a symmetrical pm8/vpi1 interface for cell attachment and basal lamina deposition (see Figure 6A).

Formation of a toroid requires at least one fusion event; thus, pm8 and vpi1 must self-fuse, but not crossfuse. We have shown that pm8 and vpi1 self-fuse by expressing different fusogens, an elegant solution to the problem of creating linked, single-cell tubes. vpi1 expresses a fusogen, EFF-1, that is sufficient to fuse heterologous cells that each express EFF-1 (Podbilewicz et al., 2006). We have shown that in *eff-1* mutants vpi1 is a C-shaped cell with an autocellular junction, indicating that EFF-1 normally promotes the self-fusion of vpi1. pm8 does not express EFF-1, but instead expresses a second fusogen, AFF-1, and requires *aff-1* activity to become a toroid. Thus, AFF-1 and EFF-1 cause self-fusion in pm8 and vpi1, in addition to promoting crossfusion between other types of embryonic cells.

Epithelial to Mesenchymal Transition

pm8 and vpi1 are wedge-shaped, dorsal epithelial cells prior to becoming C-shaped cells and self-fusing. To form a C-shape around the cyst midline, both pm8 and vpi1 invade between cells in the ventral side of the cyst. Although vpi1 extends only a lamellar process through ventral cells, the nucleus and most of the pm8 cell body enter the ventral side. Notch activity appears to be involved in pm8 delamination from the dorsal basal lamina; pm8 normally detaches from the dorsal perimeter at about the same time as Notch target genes are expressed in pm8, but does not appear to detach in Notch mutant embryos. The delamination and migration of pm8 can be considered an epithelial to mesenchymal transition (EMT). In most animals, EMT is a fundamental and widely used morphogenetic program that functions in gastrulation, and tissue and organ development. EMT also occurs in pathological states during wound healing and in tumor progression (Thiery and Sleeman, 2006). A well-documented role for EMT occurs in the development of the vertebrate heart (Eisenberg and Markwald, 1995). Within the primitive heart tube, epithelial (endocardial) cells that contribute to valve development and heart septation break adherens connections to their neighbors and invade the surrounding extracellular matrix (cardiac jelly). Notch signaling occurs within the endocardium and is critical for EMT (Timmerman et al., 2004). In contrast to

the prevalence of EMT in other systems, the *C. elegans* literature is almost devoid of examples of EMT. For example, most gastrulating cells in *C. elegans* are not epithelial, and lineage mechanisms ensure that most cells are born in their appropriate positions without extensive tissue remodeling (Nance et al., 2005). Because many basic processes in EMT are poorly understood, such as the restructuring of junctional complexes between cells, pm8 morphogenesis should prove a useful model system for genetic analysis.

Laminin and Intraepithelial Cell Movements

The migration of pm8 and vpi1 between cells in the ventral epithelium of the cyst resembles transepithelial migration in other systems, such as human leukocytes and *Drosophila* germ cells (see Introduction). In all three systems, migration occurs between cells in the target epithelium. These events occur rapidly, requiring about 15 min for pm8 migration and from 5–16 min in some in vitro models of leukocyte invasion (Shaw et al., 2001). In *Drosophila*, the target epithelium appears primed for invasion; apical junctions are remodeled to create intercellular gaps even in the absence of the invading germ cells (Kunwar et al., 2006). In contrast, invading leukocytes can induce junctional remodeling of the target epithelium (Shaw et al., 2001). In our present study, we found (1) that a tract of laminin appears between the ventral cells mc3V and vpi2V prior to pm8 and vpi1 migration, (2) that pm8 and vpi1 migration occurs specifically at the mc3V/vpi2V interface, and is associated with a disappearance of the laminin tract, and (3) that laminin function is essential for pm8 migration (vpi1 was not examined in this experiment). These results suggest that laminin provides a transient path for pm8 migration. We do not yet know whether the formation of the laminin tract is induced by signals from pm8 and/or vpi1, however, the tract forms independent of Notch. Future genetic studies should reveal the laminin receptor(s) involved in pm8 migration. If integrin were the sole receptor for laminin in pm8 migration, we would have expected a lack of migration in integrin mutants, rather than the overmigration, or aberrant migration observed. Interestingly, neurons in α6 integrin null mice show an analogous overmigration phenotype (Georges-Labouesse et al., 1998). Although laminin is often implicated in animal cell migration, we know of no similar example of a transient laminin tract guiding migrating cells through a polarized epithelium. The tract in *C. elegans* forms and disappears within about 30 min, so it is possible similar, transient tracts might have been overlooked in epithelia in other systems. Indeed, we observed additional examples of laminin within *C. elegans* tissues that are not known to contain migratory cells (unpublished data). Thus, it will be interesting to determine whether laminin-dependent, short-range cell movements similar to those of pm8 and vpi1 are a common feature of epithelial remodeling.

Lumen Formation in a Single-Cell Tube

Single-cell tubes are found in diverse animal tissues, including the fine capillaries of the vertebrate vascular system, the termini of the *Drosophila* tracheal system, and the *C. elegans* excretory (renal) system (Lubarsky and Krasnow, 2003). Some of these tubes, such as the fusion cells of the *Drosophila* tracheal system, are toroids like the *C. elegans* pm8 and vpi1 cells (Samakovlis et al., 1996). The lumen in some single-cell tubes is thought to form from the coalescence of cytoplasmic vacuoles (Lubarsky and Krasnow, 2003; Berry et al., 2003; Kamei et al., 2006). In our electron microscopic study, we did not find obvious cytoplasmic vacuoles in pm8 or vpi1 before or immediately after lumen formation (see Figure S3D). pm8 migrates into the ventral side of the epithelial cyst on the left side of the midline, and the pm8 cell body subsequently spreads across the diameter of the cyst. During these events, the three group 3 marginal cells extend fingers posteriorly along the midline. Thus, pm8 must actively or passively wrap around the fingers at the midline. An intriguing possibility is that the fingers play a morphogenetic role in templating the lumenal surface of pm8. However, we have not been able to test this hypothesis by removing all three of the marginal cells simultaneously. If the fingers do not play a direct role in templating the lumen, it is possible they have a mechanical function in holding cyst cells together while pm8 and vpi1 remodel their apical junctions.

Notch Signaling and Tubulogenesis

The Notch pathway is required for proper pm8 and vpi1 tubulogenesis, and appears to have two distinct roles. First, Notch is required for pm8 to express the fusogen AFF-1. Although the presumptive ligand-expressing cells in the cyst appear to contact both pm8 and vpi1 (see Figure 3C), only pm8 expresses LIN-12/Notch, and only pm8 expresses the Notch targets *ceh-24* and *ref-1*. These results suggest that the Notch pathway is activated only in pm8, and that defects in vpi1 morphogenesis in Notch mutants occur indirectly. Second, we have shown that expression of the EFF-1 fusogen is normally restricted to vpi1, but that pm8 and vpi1 both express EFF-1 in Notch mutants and can crossfuse. Crossfusion would prevent a basal lamina from forming between pm8 and vpi1, and thus account for the inappropriate, broad cellular contacts observed between pharyngeal and valve cells in Notch mutant embryos. Future studies should elucidate the transcriptional network linking Notch targets with fusogen expression and myogenesis. The regulatory regions of both *aff-1* and *eff-1* contain candidate LAG-1/CSL binding sites (unpublished data), however, we do not yet know whether either gene is a direct target of Notch. pm8 does not appear to express FOS-1A, a transcription factor that regulates *aff-1* expression in a larval cell called the anchor cell (Sapir et al., 2007, and unpublished data).

We conclude by noting that cells acquire several distinct and reproducible morphologies during the differentiation of the pharynx/valve from an epithelial cyst. The remarkable number of events underlying the development of just two of these cells, pm8 and vpi1, hint at the complexity of organ differentiation. Because only a few postmitotic cells in the cyst express the receptors LIN-12/Notch or GLP-1/Notch, it appears that Notch does not play a major role in the morphogenesis of most other cyst cells. Thus, it is likely that there are several different pathways that specify cell shapes throughout the cyst, and it should be interesting in future studies to identify these pathways and determine how they are coordinated.

EXPERIMENTAL PROCEDURES

Nematodes

Standard techniques were used to maintain and manipulate nematodes (Brenner, 1974). The following extrachromosomal or integrated arrays were created

for this study; details available upon request: *zuEx146*: [*ceh-24* ^{115bp}::GFP (pKG63); *rol-6*], *zuEx165*: [*ceh-24* $^{115bp\ (-CSL)}$::GFP (pKG70); *rol-6*], *zuEx221*: [*ref-1*^{153bp}::GFP-PM (pKG79); *rol-6*], *zuIs190:* [*myo-2*::GFP (pSEM474); *rol-6*]; the plasmid pSEM474 was kindly provided by Jeb Gaudet and Susan Mango. The following transgenes have been described: *zuEx132*: [*ref-1*$^{(600bp)}$::GFP] (Neves et al., 2007); *zuIs104*: [*ref-1*$^{(1.8kb)}$::REF-1::GFP] (Neves and Priess, 2005); *urEx131*: [*lam-1*::LAM-1::GFP] (Kao et al., 2006); *hyEx167*: [*aff-1*::GFP] (Sapir et al., 2007); *zzIs22*: [*eff-1*::EFF-1::GFP] (del Campo et al., 2005); and *syIs123:* [*fos-1a*::YFP::FOS-1A] (Sherwood et al., 2005). Mutant alleles used in this study are described in WormBase (http://www.wormbase.org/): LG1, *lam-3(n2561)*; LG II, *aff-1(tm2214)*, *eff-1(hy21), eff-1(ok1021)*; LG III, *glp-1(q46), ina-1(gm86), lin-12(n941)*; LG IV, *epi-1(rh199)*, *lag-1(q385)*; LG V, *apx-1(zu347ts), lag-2(q387), lag-2(q411)*, *lag-2(q420ts)*. A strain was constructed with the *ref-1*::GFP-PM transgene that was heterozygous for the *lam-3(n2561)* and *epi-1(rh199)* mutations. Approximately 1/16 of the progeny of these animals had a novel and consistent defect in pm8 migration that was not observed in either of the homozygous single mutants; we infer that these embryos are homozygous for both mutations.

Transgenes

Standard techniques were used to manipulate DNA. All transgene constructs were made using PCR fusion techniques (Hobert, 2002). GFP reporter constructs for *ceh-24* and *ref-1* were derived from pAP10 (A. Paulson and S.E. Mango, unpublished data). The *ceh-24* promoter was amplified using PstI linkers and the following forward (F) and reverse (R) genomic sequences: *ceh-24* (F = gagctctttgcatctttttcac, R = gagaagtgttatcagtgttatcc; pKG63). *ref-1*::GFP-PM was constructed by cloning amplified genomic *ref-1* DNA (F = ctcaccaggggttatcaaaccaatatg, R = atcccaatggttcccatcactatc) into the Hind III/Bam H1 sites of pJN152 GFP-PM (J. Nance, unpublished data). Promoter / enhancer mutagenesis was performed using the QuikChange site-directed mutagenesis kit (Stratagene, La Jolla, CA, USA). Predicted start codons were obtained from the WormBase web site (http://www.wormbase.org). Constructs were injected at 40 ng/μl together with *rol-6* DNA, at 100 ng/μl, to generate extrachromosomal arrays (Mello and Fire, 1995). At least two independent lines were analyzed for each transgene, and at least 20 embryos were examined per line. The *myo-2*::GFP array was integrated by γ irradiation (Mello and Fire, 1995).

Electrophoretic mobility shift assays (EMSA) shown in Figure S1 were performed essentially as described (Stroeher et al., 1994), but see the Supplemental Data for details.

Immunofluorescence

The following antibodies/antisera were used: anti-LAM-3, anti-EPI-1 (Huang et al., 2003), mAbGJ1, mAbGJ2 (see Supplemental Experimental Procedures), anti-LIN-12 (gift from Stuart Kim), MH27 (Francis and Waterston, 1991), anti-GFP (Abcam ab6556). Worm and embryo fixation procedures were performed essentially as described (Lin et al., 1998; Leung et al., 1999). Unless stated otherwise, between 5 and 25 embryos were analyzed for all immunofluorescence experiments.

Microscopy

Electron microscopy was performed as described (Costa et al., 1997). Sets of 5–10 thin sections spaced by 0.5–1 micron intervals were taken from plastic-embedded clusters of 25–50 embryos. Embryos with the plane of section though the axis of the pharyngeal lumen were selected for detailed analysis.

Images shown in Figure S4 and Figure 4F were from a set of serial sections through the terminal bulb of the pharynx and valve (J.R.P. and J.N. Thomson, unpublished data). Fluorescence images in Figure 5G and Movies S1, S2, and S4 were collected with a spinning disk confocal system (Yokogawa CSU-10) on a Nikon TE-2000 inverted microscope equipped with a Hamamatsu C-9100 camera, running Volocity 4.1 (Improvision, Lexington, MA).

SUPPLEMENTAL DATA

Supplemental Data include four figures, four movies, and Supplemental Experimental Procedures and can be found with this article online at http://developmentalcell.com/cgi/content/full/14/4/559/DC1/.

ACKNOWLEDGMENTS

We thank Jeremy Nance for advice about laminin localization, an anonymous reviewer for comments about autocellular junctions, A. Chisholm and W. Wadsworth for strains and antisera, and members of the Priess lab for discussion and technical assistance. We thank Jeff Molk for assistance with confocal microscopy. Some of the nematode strains used in this study were provided by the *Caenorhabditis* Genetics Center, which is funded by the NIH National Center for Research Resources. J.P.R. and J.R.T. were supported by National Institutes of Health Developmental Biology Training Grant 5T32 HDO7183. J.R.P. is an investigator with HHMI.

Received: July 23, 2007
Revised: October 22, 2007
Accepted: January 31, 2008
Published: April 14, 2008

REFERENCES

Albertson, D.G., and Thomson, J.N. (1976). The pharynx of *Caenorhabditis elegans*. Philos. Trans. R. Soc. Lond. B Biol. Sci. *275*, 299–325.

Alper, S., and Kenyon, C. (2001). REF-1, a protein with two bHLH domains, alters the pattern of cell fusion in *C. elegans* by regulating Hox protein activity. Development *128*, 1793–1804.

Berry, K.L., Bulow, H.E., Hall, D.H., and Hobert, O. (2003). A *C. elegans* CLIC-like protein required for intracellular tube formation and maintenance. Science *302*, 2134–2137.

Bray, S.J. (2006). Notch signalling: a simple pathway becomes complex. Nat. Rev. Mol. Cell Biol. *7*, 678–689.

Brenner, S. (1974). The genetics of *Caenorhabditis elegans*. Genetics *77*, 71–94.

Casanova, J. (2007). The emergence of shape: notions from the study of the *Drosophila* tracheal system. EMBO Rep. *8*, 335–339.

Chen, J.N., and Fishman, M.C. (1996). Zebrafish *tinman* homolog demarcates the heart field and initiates myocardial differentiation. Development *122*, 3809–3816.

Costa, M., Draper, B.W., and Priess, J.R. (1997). The role of actin filaments in patterning the *Caenorhabditis elegans* cuticle. Dev. Biol. *184*, 373–384.

del Campo, J.J., Opoku-Serebuoh, E., Isaacson, A.B., Scranton, V.L., Tucker, M., Han, M., and Mohler, W.A. (2005). Fusogenic activity of EFF-1 is regulated via dynamic localization in fusing somatic cells of *C. elegans*. Curr. Biol. *15*, 413–423.

Doncaster, C.C. (1962). Nematode feeding mechanisms. I. Observations on Rhabditis and Pelodera. Nematologica *8*, 313–320.

Eisenberg, L.M., and Markwald, R.R. (1995). Molecular regulation of atrioventricular valvuloseptal morphogenesis. Circ. Res. *77*, 1–6.

Francis, R., and Waterston, R.H. (1991). Muscle cell attachment in *Caenorhabditis elegans*. J. Cell Biol. *114*, 465–479.

Georges-Labouesse, E., Mark, M., Messaddeq, N., and Gansmuller, A. (1998). Essential role of α6 integrins in cortical and retinal lamination. Curr. Biol. *8*, 983–986.

Gong, Y., Mo, C., and Fraser, S.E. (2004). Planar cell polarity signaling controls cell division orientation during zebrafish gastrulation. Nature *430*, 689–693.

Greenwald, I. (August 4, 2005). LIN-12/Notch signaling in *C. elegans, WormBook*, ed. The *C. elegans* Research Community, WormBook. doi/10.1895/wormbook.1.10.1. http://www.wormbook.org.

Harfe, B.D., and Fire, A. (1998). Muscle and nerve-specific regulation of a novel NK-2 class homeodomain factor in *Caenorhabditis elegans*. Development *125*, 421–429.

Haun, C., Alexander, J., Stainier, D.Y., and Okkema, P.G. (1998). Rescue of *Caenorhabditis elegans* pharyngeal development by a vertebrate heart specification gene. Proc. Natl. Acad. Sci. USA *95*, 5072–5075.

Hobert, O. (2002). PCR Fusion-based approach to create reporter gene constructs for expression analysis in transgenic *C. elegans*. Biotechniques *32*, 728–730.

Horner, M.A., Quintin, S., Domeier, M.E., Kimble, J., Labouesse, M., and Mango, S.E. (1998). *pha-4*, an HNF-3 homologue, specifies pharyngeal organ identity in *Caenorhabditis elegans*. Genes Dev. *12*, 1947–1952.

Huang, C.C., Hall, D.H., Hedgecock, E.M., Kao, G., Karantza, V., Vogel, B.E., Hutter, H., Chisholm, A.D., Yurchenco, P.D., and Wadsworth, W.G. (2003). Laminin α subunits and their role in *C. elegans* development. Development *130*, 3343–3358.

Kalb, J.M., Lau, K.K., Goszczynski, B., Fukushige, T., Moons, D., Okkema, P.G., and McGhee, J.D. (1998). *pha-4* is *Ce-fkh-1*, a *fork head/HNF-3*α, β, γ homolog that functions in organogenesis of the *C. elegans* pharynx. Development *125*, 2171–2180.

Kamei, M., Saunders, W.B., Bayless, K.J., Dye, L., Davis, G.E., and Weinstein, B.M. (2006). Endothelial tubes assemble from intracellular vacuoles *in vivo*. Nature *442*, 453–456.

Kao, G., Huang, C.C., Hedgecock, E.M., Hall, D.H., and Wadsworth, W.G. (2006). The role of the laminin β subunit in laminin heterotrimer assembly and basement membrane function and development in *C. elegans*. Dev. Biol. *290*, 211–219.

Kramer, J.M. (September 1, 2005). Basement membranes, *Wormbook*, ed. The *C. elegans* Research Community, WormBook. doi/10.1895/wormbook.1.16.1. http://www.wormbook.org.

Kunwar, P.S., Siekhaus, D.E., and Lehman, R. (2006). In vivo migration: a germ cell perspective. Annu. Rev. Cell Dev. Biol. *22*, 237–265.

Leung, B., Hermann, G.J., and Priess, J.R. (1999). Organogenesis of the *Caenorhabditis elegans* intestine. Dev. Biol. *216*, 114–134.

Lin, R., Hill, R.J., and Priess, J.R. (1998). POP-1 and anterior-posterior fate decisions in *C. elegans* embryos. Cell *92*, 229–239.

Lubarsky, B., and Krasnow, M.A. (2003). Tube morphogenesis: making and shaping biological tubes. Cell *112*, 19–28.

Mango, S.E. (January 22, 2007). The *C. elegans* pharynx: a model for organogenesis. *Wormbook*, ed. The *C. elegans* Research Community, WormBook. doi/10.1895/wormbook.1.129.1. http://www.wormbook.org.

Mango, S.E., Lambie, E.J., and Kimble, J. (1994). The *pha-4* gene is required to generate the pharyngeal primordium of *Caenorhabditis elegans*. Development *120*, 3019–3031.

Mapes, C.J. (1965). Structure and function in the nematode pharynx. I. The structure of the pharynges of *Ascaris lumbricoides, Oxyuris equi, Apectana brevicaudata* and *Panagrellus silusiae*. Parasitology *55*, 269–284.

Mello, C., and Fire, A. (1995). DNA transformation. In *Caenorhabditis elegans*: Modern Biological Analysis of an Organism, H.F. Epstein and D.C. Shakes, eds. (San Diego, CA: Academic Press), pp. 452–482.

Mohler, W.A., Shemer, G., del Campo, J.J., Valansi, C., Opoku-Serebuoh, E., Scranton, V., Assaf, N., White, J.G., and Podbilewicz, B. (2002). The type I membrane protein EFF-1 is essential for developmental cell fusion. Dev. Cell *2*, 355–362.

Nance, J., Lee, J.-Y., and Goldstein, B. (September 26, 2005). Gastrulation in *C. elegans*. *WormBook*, ed. The *C. elegans* Research Community, WormBook. doi/10.1895/wormbook.1.23.1. http://www.wormbook.org.

Neves, A., and Priess, J.R. (2005). The REF-1 family of bHLH transcription factors pattern *C. elegans* embryos through Notch-dependent and Notch-independent pathways. Dev. Cell *8*, 867–879.

Neves, A., English, K., and Priess, J.R. (2007). Notch-GATA synergy promotes endoderm-specific expression of *ref-1* in *C. elegans*. Development *134*, 4459–4468.

Oliphant, L.W., and Cloney, R.A. (1972). The ascidian myocardium: Sarcoplasmic reticulum and excitation-contraction coupling. Z. Zellforsch. *129*, 395–412.

Okkema, P.G., and Fire, A. (1994). The *Caenorhabditis elegans NK-2* class homeoprotein CEH-22 is involved in combinatorial activation of gene expression in pharyngeal muscle. Development *120*, 2175–2186.

Okkema, P.G., Ha, E., Haun, C., Chen, W., and Fire, A. (1997). The *Caenorhabditis elegans NK-2* homeobox gene *ceh-22* activates pharyngeal muscle gene expression in combination with *pha-1* and is required for normal pharyngeal development. Development *124*, 3965–3973.

Petri, B., and Bixel, M.G. (2006). Molecular events during leukocyte diapendesis. FEBS J. *273*, 4399–4407.

Podbilewicz, B., Leikina, E., Sapir, A., Valansi, C., Suissa, M., Shemer, G., and Chernomordik, L.V. (2006). The *C. elegans* developmental fusogen EFF-1 mediates homotypic fusion in heterologous cells and in vivo. Dev. Cell *11*, 471–481.

Portereiko, M.F., and Mango, S.E. (2001). Early morphogenesis of the *Caenorhabditis elegans* pharynx. Dev. Biol. *233*, 482–494.

Priess, J. (2005). Notch signaling in the *C. elegans* embryo. *WormBook*, ed. The *C. elegans* Research Community, WormBook. doi/10.1895/wormbook.1.4.1. http://www.wormbook.org.

Priess, J.R., Schnabel, H., and Schnabel, R. (1987). The *glp-1* locus and cellular interactions in early *C. elegans* embryos. Cell *51*, 601–611.

Samakovlis, C., Manning, G., Steneberg, P., Hacohen, N., Cantera, R., and Krasnow, M.A. (1996). Genetic control of epithelial tube fusion during *Drosophila* tracheal development. Development *122*, 3531–3536.

Sapir, A., Choi, J., Leikina, E., Avinoam, O., Valansi, C., Chernomordik, L.V., Newman, A.P., and Podbilewicz, B. (2007). AFF-1, a FOS-1-regulated fusogen, mediates fusion of the anchor cell in *C. elegans*. Dev. Cell *12*, 683–698.

Schreiber, A.M., Cai, L., and Brown, D.D. (2005). Remodeling of the intestine during metamorphosis of *Xenopus laevis*. Proc. Natl. Acad. Sci. USA *102*, 3720–3725.

Shaw, S.K., Bamba, P.S., Perkins, B.N., and Luscinskas, F.W. (2001). Real-time imaging of vascular endothelial-cadherin during leukocyte transmigration across endothelium. J. Immunol. *167*, 2323–2330.

Sherwood, D.R., Butler, J.A., Kramer, J.M., and Sternberg, P.W. (2005). FOS-1 promotes basement-membrane removal during anchor-cell invasion in *C. elegans*. Cell *121*, 951–962.

Stroeher, V.L., Kennedy, B.P., Millen, K.J., Schroeder, D.F., Hawkins, M.G., Goszczynski, B., and McGhee, J.D. (1994). DNA-protein interactions in the *Caenorhabditis elegans* embryo: Oocyte and embryonic factors that bind to the promoter of the gut-specific *ges-1* gene. Dev. Biol. *163*, 367–380.

Thiery, J.P., and Sleeman, J.P. (2006). Complex networks orchestrate epithelial-mesenchymal transitions. Nat. Rev. Mol. Cell Biol. *7*, 131–142.

Timmerman, L.A., Grego-Bessa, J., Raya, A., Bertran, E., Perez-Pomares, J.M., Diez, J., Aranda, S., Palomo, S., McCormick, F., Izpisua-Belmonte, J.C., and de la Pompa, J.L. (2004). Notch promotes epithelial-mesenchymal transition during cardiac development and oncogenic transformation. Genes Dev. *18*, 99–115.

Developmental Cell
Article

dFezf/Earmuff Maintains the Restricted Developmental Potential of Intermediate Neural Progenitors in *Drosophila*

Mo Weng,[1,2] Krista L. Golden,[2] and Cheng-Yu Lee[1,2,3,*]
[1]Department of Cell and Developmental Biology, University of Michigan Medical School, Ann Arbor, MI, USA
[2]Center For Stem Cell Biology, Life Sciences Institute, University of Michigan, Ann Arbor, MI 48109, USA
[3]Division of Molecular Medicine and Genetics, Department of Internal Medicine, University of Michigan Medical School, Ann Arbor, MI, USA
*Correspondence: leecheng@umich.edu
DOI 10.1016/j.devcel.2009.12.007

SUMMARY

To ensure normal development and maintenance of homeostasis, the extensive developmental potential of stem cells must be functionally distinguished from the limited developmental potential of transit amplifying cells. Yet the mechanisms that restrict the developmental potential of transit amplifying cells are poorly understood. Here we show that the evolutionarily conserved transcription factor dFezf/Earmuff (Erm) functions cell-autonomously to maintain the restricted developmental potential of the intermediate neural progenitors generated by type II neuroblasts in *Drosophila* larval brains. Although *erm* mutant intermediate neural progenitors are correctly specified and show normal apical-basal cortical polarity, they can dedifferentiate back into a neuroblast state, functionally indistinguishable from normal type II neuroblasts. Erm restricts the potential of intermediate neural progenitors by activating Prospero to limit proliferation and by antagonizing Notch signaling to prevent dedifferentiation. We conclude that Erm dependence functionally distinguishes intermediate neural progenitors from neuroblasts in the *Drosophila* larval brain, balancing neurogenesis with stem cell maintenance.

INTRODUCTION

Tissue development and homeostasis often require stem cells to transiently expand the progenitor pool by producing transit amplifying cells. Yet the developmental potential of transit amplifying cells must be tightly restricted to ensure generation of differentiated progeny and to prevent unrestrained proliferation that might lead to tumorigenesis (Morrison and Kimble, 2006; Pontious et al., 2008; Vescovi et al., 2006). Transit amplifying cells are defined by their limited developmental capacity, a feature specified during fate determination (Farkas et al., 2008; Hodge et al., 2008; Sessa et al., 2008). It is unknown whether an active mechanism is required to maintain restricted developmental potential in transit amplifying cells after specification. Here we use *i*ntermediate *n*eural *p*rogenitors (INPs) in developing *Drosophila* larval brains as a genetic model to investigate how restricted developmental potential is regulated in transit amplifying cells.

A fly larval brain hemisphere contains eight type II neuroblasts that undergo repeated asymmetric divisions to self-renew and to generate immature INPs (Figure 1A) (Bello et al., 2008; Boone and Doe, 2008; Bowman et al., 2008). Immature INPs are unstable in nature and are mitotically inactive, and they lack the expression of Deadpan (Dpn) and Asense (Ase) (Figure S1A). Immature INPs commit to the INP fate through maturation, a differentiation process necessary for specification of the INP identity (Figure 1A). INPs express Dpn and Ase, and undergo 8–10 rounds of asymmetric divisions to self-renew and to produce ganglion mother cells (GMCs) that typically generate two neurons (Figure S1A) (Bello et al., 2008; Boone and Doe, 2008; Bowman et al., 2008). While 5–6 immature INPs and 1–2 young INPs are always in direct contact with their parental neuroblasts, the older INPs become progressively displaced from their parental neuroblasts over time (Bowman et al., 2008).

During asymmetric divisions of type II neuroblasts, the basal proteins Brain tumor and Numb are exclusively segregated into immature INPs, and function cooperatively, but nonredundantly, to ensure that immature INPs undergo maturation and commit to the INP fate (Boone and Doe, 2008; Bowman et al., 2008). *brain tumor* or *numb* mutant type II neuroblasts generate immature INPs that fail to mature and do not commit to the INP fate. Instead, *brain tumor* or *numb* mutant immature INPs adopt their parental neuroblast fate, leading to supernumerary type II neuroblasts. Thus, *brain tumor* and *numb* specify the INP fate, and the ectopic expansion of type II neuroblasts in these mutant genetic backgrounds occurs due to failure to properly specify the INP fate. Although Brain tumor is also asymmetrically segregated into GMCs during asymmetric divisions of INPs, the mosaic clones in *brain tumor* mutant INPs contain only differentiated neurons (Bowman et al., 2008). This result indicates that Brain tumor is dispensable for maintaining the restricted developmental potential of INPs. How restricted developmental potential is maintained in INPs is currently unknown.

To identify genes that regulate self-renewal of neuroblasts, we conducted a genetic screen for mutants exhibiting ectopic larval brain neuroblasts (C.-Y.L. and C.Q. Doe, unpublished data). One mutation, *l(2)5138*, specifically resulted in massive expansion of neuroblasts in the brain but did not affect neuroblasts on the

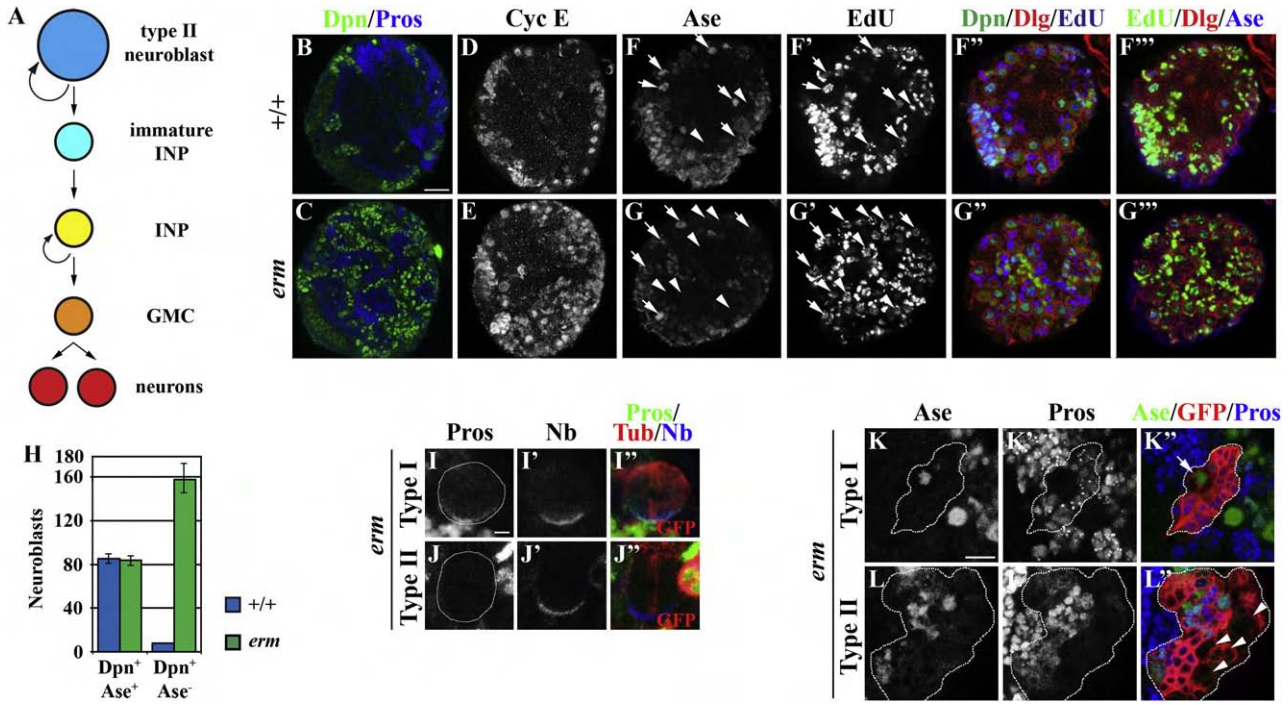

Figure 1. *erm* Mutant Brains Show Ectopic Type II Neuroblasts

(A) A summary of the type II neuroblast lineage.

(B–H) While wild-type (+/+) and *erm* mutant brains contained a similar number of type I neuroblasts ($Dpn^+CycE^+Ase^+EdU^+$; white arrows), *erm* mutant brains contained ectopic type II neuroblasts ($Dpn^+CycE^+Ase^-EdU^+$; white arrowheads). In (H), wild-type brains contained 85 ± 5.2 type I neuroblasts and 8.0 ± 0 type II neuroblasts, whereas *erm* mutant brains contained 83.7 ± 6.4 type I neruoblasts and 159 ± 19.7 type II neuroblasts. Scale bar, 20 μm.

(I and J) In *erm* mutant brains expressing GFP driven by *Ase-Gal4*, Prospero (Pros) always colocalized with Numb (Nb) in metaphase type I neuroblasts (GFP^+; white circle), but never in type II neuroblasts (GFP^-; white circle). Scale bar, 2 μm.

(K and L) *erm* mutant type I neuroblast clones (white circle) always contained a single neuroblast (white arrow), but *erm* mutant type II neuroblast clones (white circle) always contained multiple neuroblasts (white arrowheads).

ventral nerve cord (Figures S1B–S1D). We mapped the *l(2)5138* mutation to the 22B4-7 chromosomal interval that contains the *earmuff* (*erm*) gene (Pfeiffer et al., 2008). The *erm* transcripts are first detected at embryonic stage 4–6 in the specific domain preceding formation of the embryonic brain and remain highly expressed in the brain throughout development (Chintapalli et al., 2007; Pfeiffer et al., 2008). Here, we report that Erm functions to restrict the developmental potential of INPs by promoting Prospero-dependent termination of proliferation and suppressing Notch-mediated dedifferentiation. By restricting their developmental potential, Erm ensures that INPs generate only differentiated neurons during *Drosophila* neurogenesis.

RESULTS

Earmuff Prevents Abnormal Expansion of Neural Progenitors in Type II Neuroblast Lineages

All neuroblasts in *l(2)5138* homozygous mutant brains were proliferative, expressed all known neuroblast markers, and lacked neuronal and glial markers (Figures 1B–1G; Figures S1B–S1D; data not shown). We mapped the *l(2)5138* mutation to the *erm* gene, which encodes a homolog of the vertebrate *F*orebrain *e*mbryonic *z*inc-*f*inger family (Fezf) transcription factors (Hashimoto et al., 2000; Matsuo-Takasaki et al., 2000). The *l(2)5138* mutants contained a single A→T nucleotide change in the *erm* coding region, leading to the substitution of a leucine for a conserved histidine in the third C_2H_2 zinc-finger domain (data not shown). Consistent with its predicted molecular function, ectopic expression of Erm transgenic proteins tagged with a HA epitope at the amino- or carboxyl-terminus driven by neuroblast-specific *Wor-Gal4* was detected in the nuclei of neuroblasts (data not shown). However, the expression of the HA-tagged Erm transgenic protein bearing the identical leucine-to-histidine substitution as in the *l(2)5138* mutant was undetectable, suggesting that the mutant Erm protein is unstable (data not presented). We conclude that *l(2)5138* is a mutant allele of *erm*.

To determine whether *erm* mutant brains have ectopic type I and/or type II neuroblasts, we analyzed the expression pattern of Ase and Prospero (Pros), which are only expressed in type I neuroblasts (Figure S1A) (Bello et al., 2008; Boone and Doe, 2008; Bowman et al., 2008). We found that *erm* mutant brains contained over 20-fold more type II neuroblasts (Dpn^+Ase^-) than wild-type brains, with no significant change in the number of type I neuroblasts (Dpn^+Ase^+) (Figures 1F–1H). Next, we analyzed the localization of Prospero in mitotic neuroblasts in larval brains expressing GFP induced by *Ase-Gal4* (*Ase > GFP*), which mimicked the expression pattern of the endogenous Ase protein (Bowman et al., 2008). In *erm* mutant larval brains, all mitotic type I neuroblasts (GFP^+) showed formation of basal Prospero crescents, but none of the mitotic type II neuroblasts

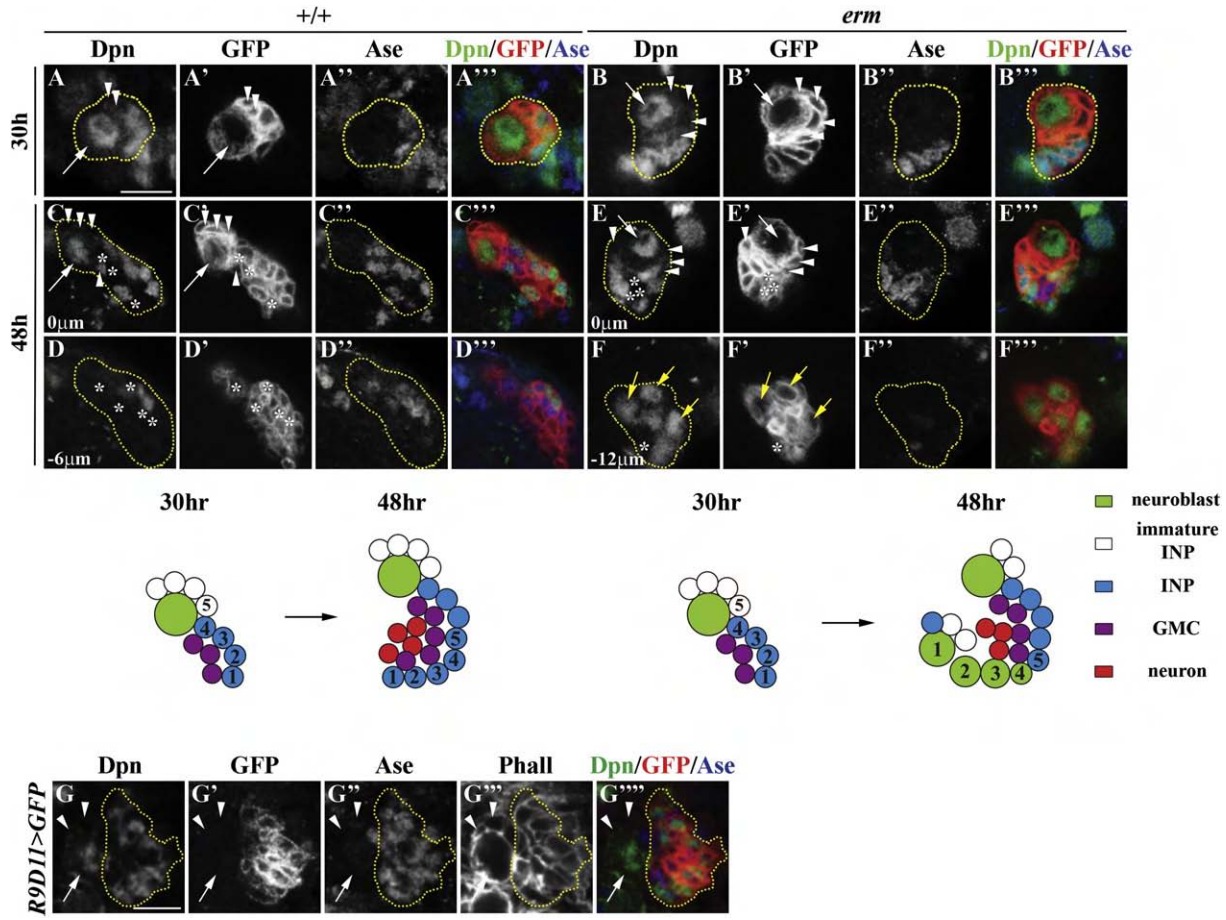

Figure 2. Erm Maintains the Limited Developmental Potential of INPs

(A and B) At 30 hr after clone induction, both wild-type (+/+) and *erm* mutant neuroblast clones (yellow circles) contained a single parental neuroblast (white arrows) directly surrounded by immature INPs (white arrowheads) and 1–2 young INPs (Dpn^+Ase^+).

(C–F) At 48 hr after clone induction, wild-type (+/+) neuroblast clones (yellow circles) contained a single parental neuroblast (white arrows) in direct contact with immature INPs (white arrowheads) and young INPs (Dpn^+Ase^+). Older INPs were away from their parental neuroblasts and were surrounded by GMCs (white asterisks) and neurons (Dpn^-Ase^-). In contrast, the *erm* mutant clones contained ectopic type II neuroblast-like cells ([F], yellow arrows) further from the parental neuroblasts than most INPs and neurons. A summary diagram is shown below.

(G) *R9D11-Gal4* (*Erm-Gal4*) was undetectable in type II neuroblasts (white arrow) and immature INPs (white arrowheads), but was clearly detected in INPs. All scale bars, 10 μm.

(GFP^-) showed the expression of Prospero (Figures 1I and 1J; n = 20). Furthermore, GFP-marked *erm* mutant type II neuroblast clones consistently contained multiple type II neuroblasts, whereas *erm* mutant type I neuroblast clones always contained single type I neuroblasts and neurons (Figures 1K and 1L). We conclude that *erm* mutant brains exhibit an abnormal expansion of type II neuroblasts.

erm Regulates the Developmental Potential of INPs

To determine the cellular origin of ectopic type II neuroblasts in *erm* mutant brains, we analyzed the identity of cells in the GFP-marked clones derived from wild-type or *erm* mutant type II neuroblasts using specific cell fate markers. At 30 hr after clone induction, wild-type and *erm* mutant neuroblast clones appeared indistinguishable, containing single parental neuroblasts (Dpn^+Ase^-; ≥10 μm) in direct contact with 5–6 immature INPs (Dpn^-Ase^-), while most of the INPs (Dpn^+Ase^+; ≥6 μm) were 1 cell or more away from the parental neuroblasts (Figures 2A and 2B). At 48 hr after clone induction, the overall size of both wild-type and *erm* mutant neuroblast clones increased significantly due to an increase in cell number, reflecting continuous asymmetric divisions of the parental neuroblasts. In both wild-type and *erm* mutant clones, the parental neuroblasts remained surrounded by 5–6 immature INPs, while INPs and differentiated neurons ($Dpn^-Ase^-Pros^+$) were found several cells away from the parental neuroblasts (Figures 2C–2F; Figures S2A–S2F). However, *erm* mutant clones contained fewer INPs (16 ± 4; n = 10 brains) than the wild-type clones (21 ± 4; n = 10 brains). Importantly, *erm* mutant clones consistently contained 4–6 smaller ectopic type II neuroblasts (Dpn^+Ase^-; 6–8 μm in diameter) (Figure 2F; Figure S2F). Thus, Erm is dispensable for both the generation and maturation of immature INPs.

Ectopic type II neuroblasts in 48 hr *erm* mutant clones were always several cells away from the parental neuroblasts

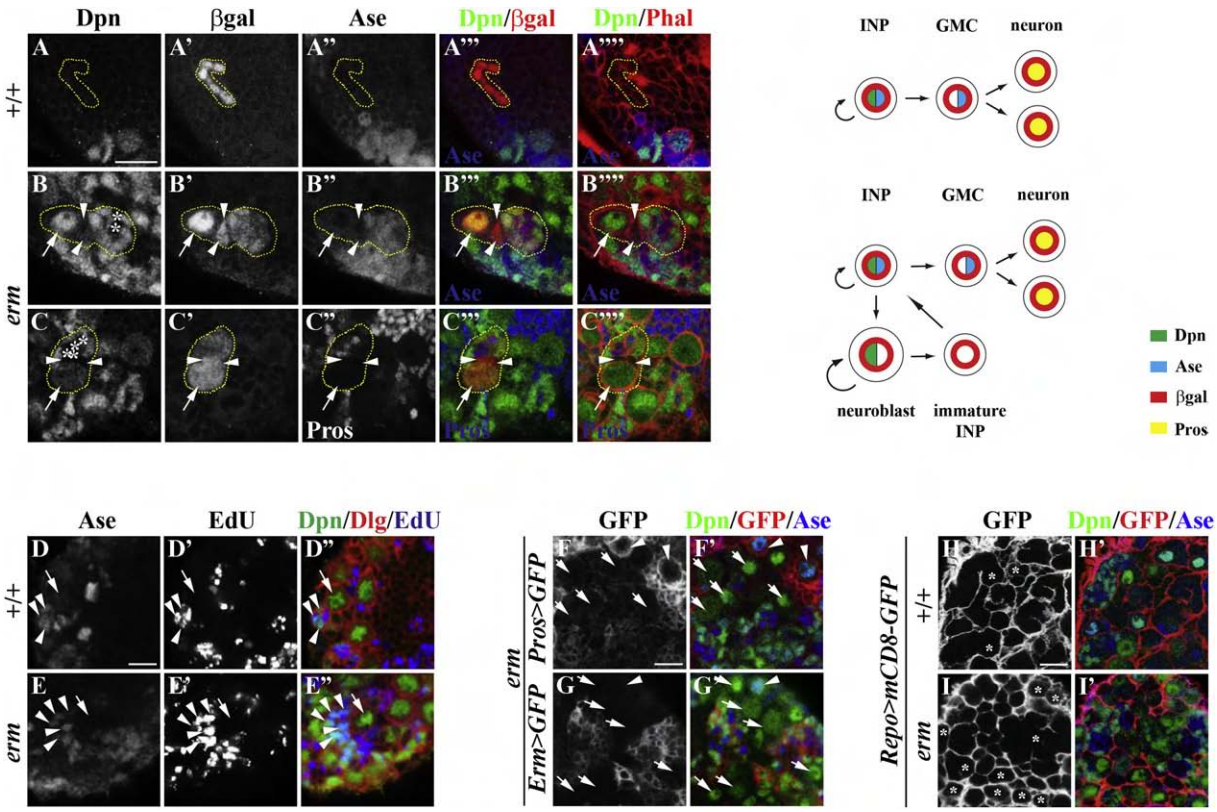

Figure 3. *erm* Suppresses the Dedifferentiation of INPs

(A–C) A wild-type (+/+) INP only generated neurons ($Dpn^{-}Ase^{-}$), but an *erm* mutant INP generated dedifferentiated neuroblasts (white arrows), immature INPs (white arrowheads) and INPs ($Dpn^{+}Ase^{+}$), GMCs ([B], white asterisks), and neurons ([C], white asterisks). A lineage clone is circled in yellow, and a summary diagram is shown on the right.

(D–I) Similar to wild-type type II neuroblasts, ectopic type II neuroblasts in *erm* mutant brains lost incorporated EdU (neuroblasts, white arrows; INPs, white arrowheads) (D and E), did not express *Pros-Gal4* and *Erm-Gal4* (type I neuroblast, white arrowheads; type II neuroblasts, white arrows) (F and G), and established ectopic neuroblast lineages (white asterisks) surrounded by glial membrane (H and I). All scale bars, 10 μm.

(Figure 2F; Figure S2F). This result strongly suggests that ectopic type II neuroblasts in *erm* mutant clones likely originate from INPs and Erm likely functions in INPs. However, we could not assess the spatial expression pattern of the endogenous Erm protein in larval brains due to lack of a specific antibody and low signals by fluorescent RNA in situ (data not shown). Alternatively, we analyzed the expression of the *R9D* series of *Gal4* transgenes in which Gal4 is expressed under the control of overlapping *erm* promoter fragments (Pfeiffer et al., 2008). The expression of *R9D11-Gal4* was clearly detected in INPs, but was undetectable in type II neuroblasts and immature INPs even when two copies of the *UAS-mCD8-GFP* transgenes were driven by two copies of *R9D11-Gal4* at 32°C for 72 hr after larval hatching (Figure 2G; Figure S2G). Consistently, the expression of *Erm-Gal4* was virtually undetectable in *brain tumor* mutant brains that contain thousands of type II neuroblasts and immature INPs (Figure S2H). While the expression of *UAS-erm* induced by the neuroblast-specific *Wor-Gal4* driver led to premature loss of type II neuroblasts, expression of *UAS-erm* driven by *Erm-Gal4* failed to exert any effect on type II neuroblasts (data not shown). Importantly, targeted expression of the fly Erm or mouse Fezf1 or Fezf2 transgenic protein driven by *R9D11-Gal4* restored the function of Erm and efficiently rescued the ectopic neuroblast phenotype in *erm* mutant brains (Figures S2I–S2L). Therefore, *R9D11-Gal4* (*Erm-Gal4*) contains the enhancer element sufficient to restore the Erm function in INPs leading to suppression of ectopic type II neuroblasts in *erm* mutant brains.

erm Mutant INPs Dedifferentiate Back into Type II Neuroblasts

Mutant clonal analyses and overexpression studies strongly suggest that Erm functions to suppress reversion of INPs back into a neuroblast state. Here, we directly tested whether INPs in *erm* mutant brains can dedifferentiate back into type II neuroblasts. We induced βgal-marked lineage clones originating exclusively from INPs via FRT-mediated recombination. We targeted a short pulse of flipase (FLP) expression in INPs by heat-shocking larvae carrying a *UAS-flp* transgene under the control of *Erm-Gal4* and *tub-Gal80^{ts}* at 30°C for 1 hr (see Experimental Procedures for details). At 72 hr after heat shock, INP clones in wild-type brains contained only differentiated neurons ($Dpn^{-}Ase^{-}$) (Figure 3A). In contrast, INP clones in *erm* mutant brains contained one or more type II neuroblasts as well as immature

INPs, INPs, GMCs, and neurons (Figures 3B–3C). This result indicates that while INPs in wild-type larval brains can only give rise to neurons, INPs in *erm* mutant brains can dedifferentiate into type II neuroblasts that can give rise to all cell types found in a normal type II neuroblast lineage. We conclude that Erm functions to maintain the restricted developmental potential of INPs and prevents them from dedifferentiating back into a neuroblast state.

We further assessed whether the dedifferentiated type II neuroblasts in *erm* mutant brains displayed multiple functional characteristics of normal type II neuroblasts.

Apical-Basal Cell Polarity

All mitotic type II neuroblasts in wild-type and *erm* mutant brains showed normal establishment and maintenance of cortical polarity by asymmetrically localizing and segregating atypical Protein Kinase C (aPKC), Pins, Miranda, and Numb (data not shown).

Proliferation Profile

All wild-type and *erm* mutant type II neuroblasts could be labeled with a 3 hr pulse of the thymidine analog EdU (Figures 1F′ and 1FG′), and incorporated EdU can be chased into INPs following a 12 hr EdU-free chase (Figures 3D and 3E).

prospero and earmuff Promoter Activity

While all type I neuroblasts in wild-type and *erm* mutant brains expressed *Pros-Gal4* but lacked *Erm-Gal4* expression, none of the type II neuroblasts in wild-type and *erm* mutant brains showed detectable expression of *Pros-Gal4* or *Erm-Gal4* (Figures 3F and 3G; data not shown).

Formation of Glial Chambers

Individual neuroblast lineages are surrounded by the cortex glial membrane forming distinct chambers (Pereanu et al., 2005). A wild-type brain hemisphere contained eight glial chambers encapsulating eight individual type II neuroblast lineages (Figure 3H). In contrast, an *erm* mutant brain hemisphere contained more than 50 glial chambers, each containing one or more type II neuroblasts and their presumptive progeny (Figure 3I).

Taken together, INPs in *erm* mutant brains dedifferentiate back into apparently normal neuroblasts that can establish ectopic type II neuroblast lineages.

erm Mutant INPs Exhibit Normal Apical-Basal Cortical Polarity

Dysregulation of apical-basal polarity can lead to failure in differentiation and result in ectopic neuroblasts at the expense of GMC formation (Betschinger et al., 2006; Lee et al., 2006a, 2006b, 2006c; Wang et al., 2006). To determine whether the dedifferentiation of INPs in *erm* mutant brains might be due to defects in cortical polarity, we assayed apical-basal polarity by examining the localization of aPKC, Miranda, Prospero, and Numb in larval brains expressing GFP driven by *Ase-GAL4* (*Ase > GFP*). Mitotic INPs (GFP^+) in *erm* mutant brains showed the same asymmetric localization of aPKC, Miranda, Prospero, and Numb as in wild-type brains (Figures 4A and 4B; data not shown). Thus, we conclude that INPs in *erm* mutant brains dedifferentiate while displaying normal cortical polarity.

Erm Restricts Proliferation by Activating Prospero-Dependent Cell Cycle Exit

To determine how Erm maintains the restricted developmental potential of INPs, we performed microarray analyses and found

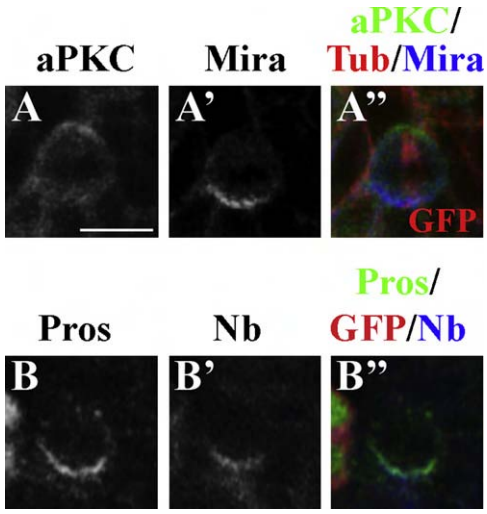

Figure 4. *erm* Mutant INPs Show Normal Apical-Basal Polarity

(A and B) Metaphase INPs in *erm* mutant brains expressing GFP induced by *Ase-Gal4* showed asymmetric localization of aPKC, Miranda (Mira), Pros, and Numb (Nb). The scale bar, 5 μm.

that *prospero* mRNA was drastically reduced in *erm* mutant brains compared to the control brains (M.W. and C.-Y.L., unpublished data). We confirmed that the relative level of *prospero* mRNA was indeed reduced by 60%–70% in *erm* mutant brain extracts by using real-time PCR (data not shown). These data supported that Erm is necessary for proper transcription of *prospero*, and prompted us to test if overexpression of Erm might be sufficient to induce ectopic Prospero expression. We induced a short pulse of Erm expression in brain neuroblasts by shifting larvae carrying a *UAS-erm* transgene under the control of *Wor-Gal4* and *tub-Gal80^{ts}* to from 25°C to 30°C. A 3.5 hr pulse of Erm expression was sufficient to induce nuclear localization of Prospero in larval brain neuroblasts (Figure 5A). Consistent with nuclear Prospero promoting termination of neuroblast proliferation, ectopic expression of Erm induced by *Wor-Gal4* resulted in decreased neuroblasts compared to wild-type brains (Figure 5B). Thus, we conclude that overexpression of Erm can restrict neuroblast proliferation by triggering nuclear localization of Pros.

Our data suggest that Erm might restrict the developmental potential of INPs in part by limiting their proliferation by activating Prospero-dependent cell cycle exit. If so, we predict that overexpression of Erm should induce ectopic nuclear Prospero in INPs and overexpression of Prospero should suppress ectopic neuroblasts in *erm* mutant brains. In wild-type brains, 9.6% of INPs (32/325) showed nuclear localization of Prospero. However, overexpression of Erm driven by *Erm-Gal4* led to nuclear localization of Prospero in 41.5% of INPs (105/253), likely restricting their proliferation potential and resulting in some parental type II neuroblasts surrounded only by differentiated neurons (Figures 5C and 5D). Importantly, ectopic expression of Prospero induced by *Erm-Gal4* efficiently suppressed ectopic neuroblasts and restored neuronal differentiation in *erm* mutant brains (Figures 5E and 5F). Thus, Erm likely restricts the proliferation of INPs by promoting nuclear localization of Prospero. To confirm that

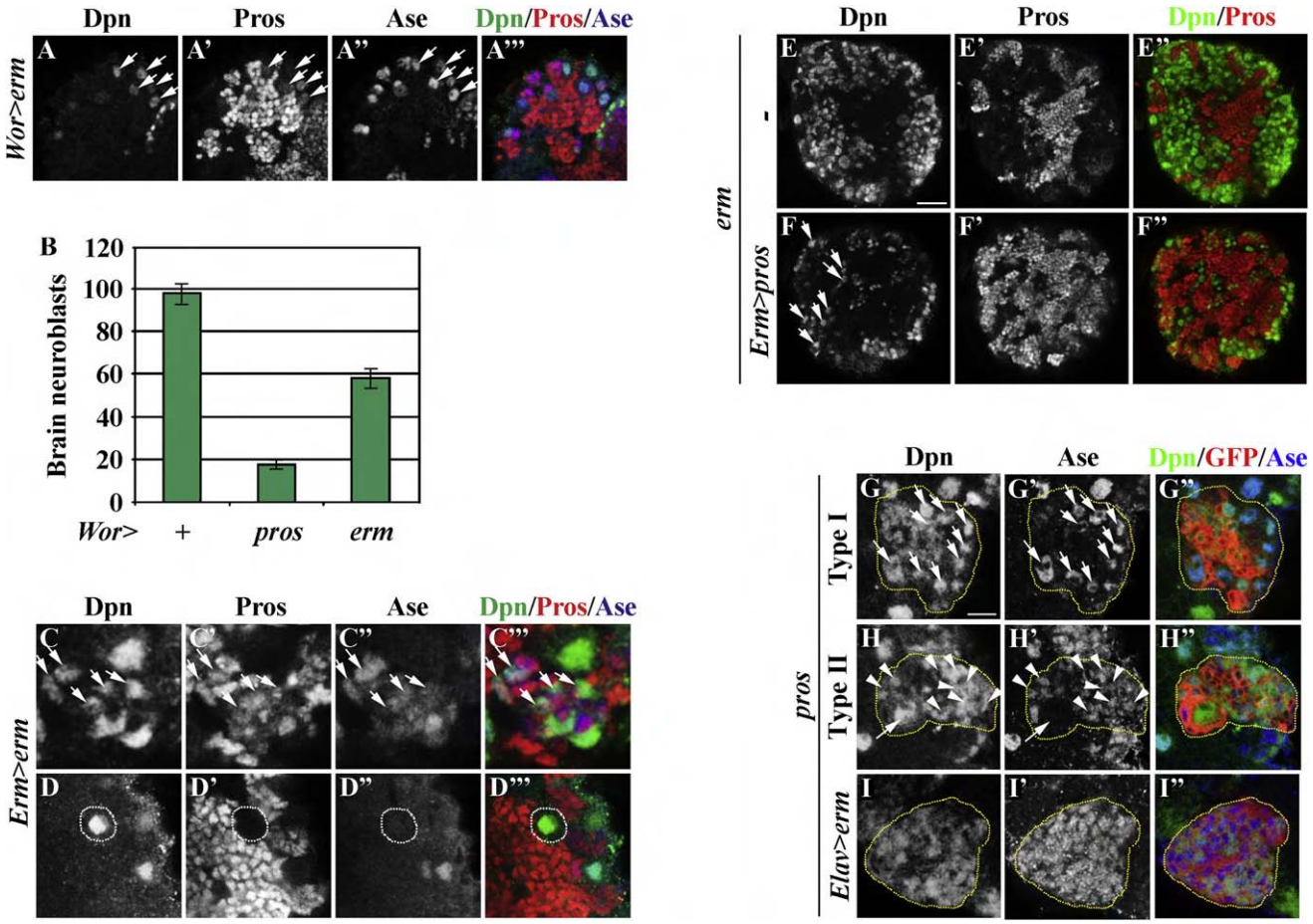

Figure 5. Erm Restricts the Proliferation of INPs by Promoting Nuclear Prospero

(A) A 3.5 hr pulse of Erm expression induced by *Wor-Gal4* was sufficient to trigger Pros localization in neuroblast nuclei (white arrows).

(B) Ectopic expression of Erm (57.9 ± 8.6) or Pros (17.4 ± 4.4 neuroblasts) driven by *Wor-Gal4* was sufficient to terminate neuroblast proliferation prematurely (98.0 ± 8.4 neuroblasts in wild-type brains).

(C and D) Ectopic expression of Erm induced by *Erm-Gal4* triggered a significant increased in INPs that exhibited nuclear Pros (white arrows), likely leading them to exit cell cycle prematurely and resulting in some type II neuroblasts (white circle) surrounded only by neurons. Scale bar, 10 μm.

(E and F) Overexpression of Pros induced by *Erm-Gal4* suppressed ectopic neuroblasts and restored neuronal differentiation in *erm* mutant brains. Scale bar, 20 μm.

(G and H) *pros* mutant type I neuroblast clones contained ectopic neuroblasts (white arrows). *pros* mutant type II neuroblast clones contained a single type II neuroblast (white arrow) but showed dramatic overproliferation of INPs (white arrowheads).

(I) Overexpression of Erm failed to suppress overproliferation of INPs in *pros* mutant type II neuroblast clones. Scale bar, 10 μm.

Prospero indeed functions downstream of Erm to restrict the proliferation of INPs, we performed genetic epistatic analyses. Consistent with previously published results, *prospero* mutant type I neuroblast clones contained ectopic type I neuroblasts (Figure 5G) (Bowman et al., 2008). In contrast, *prospero* mutant type II neuroblast clones exhibited accumulation of ectopic INPs while maintaining single parental neuroblasts (Figure 5H). Furthermore, overexpression of Erm failed to suppress ectopic INPs in *prospero* mutant type II neuroblast clones, consistent with Prospero functioning downstream of Erm (Figure 5I). These results indicate that blocking differentiation is not sufficient to trigger the dedifferentiation of INPs back into type II neuroblasts. Thus, Erm's restriction on the proliferation of INPs is dependent on Prospero function, but its suppression of the dedifferentiation of INPs is independent of Prospero.

Erm Suppresses Dedifferentiation by Antagonizing Notch Signaling

Previous studies showed that overexpression of constitutively active Notch ($Notch^{intra}$) in both type I and II neuroblasts is sufficient to trigger ectopic neuroblasts (Bowman et al., 2008; Wang et al., 2006). Here, we tested whether Erm suppresses the dedifferentiation of INPs by inhibiting Notch signaling. Indeed, knockdown of Notch function by RNAi in *erm* mutant brains led to a dramatic reduction in ectopic type II neuroblasts compared to *erm* mutant brains alone (Figures 6A and 6B). Complementarily, ectopic expression of constitutively active Notch ($Notch^{intra}$) induced by *Erm-Gal4* transforms INPs into ectopic type II neuroblasts (Figure 6C). Thus, reduced Notch function suppresses the dedifferentiation of INPs in *erm* mutant brains whereas ectopic activation of Notch induces the dedifferentiation of INPs. We

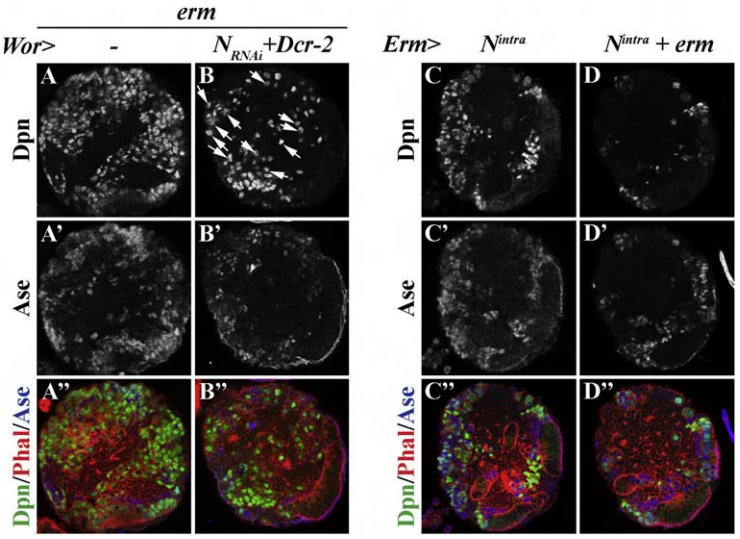

Figure 6. Erm Suppresses the Dedifferentiation of INPs by Negatively Regulating Notch Signaling

(A and B) Knocking down Notch function by RNAi suppressed ectopic neuroblasts (white arrows) in *erm* mutant brains.

(C and D) Ectopic expression of Erm under the control of *Erm-Gal4* suppressed ectopic neuroblasts induced by constitutive activation of Notch signaling. Scale bar, 20 μm.

next tested if Erm suppresses the dedifferentiation of INPs by antagonizing a Notch-activated mechanism. Coexpression of Erm under the control of *Erm-Gal4* is sufficient to suppress ectopic neuroblasts induced by the expression of Notch^{intra} (Figure 6D). Thus, we conclude that Erm can suppress the dedifferentiation of INPs by negatively regulating a Notch-activated signaling mechanism.

DISCUSSION

The limited developmental potential of transit amplifying cells is generally thought to be specified during fate determination (Farkas et al., 2008; Hodge et al., 2008; Sessa et al., 2008). In this study, we report a mechanism that actively maintains the restricted developmental potential of transit amplifying cells after specification of their identity. We show that the evolutionarily conserved transcription factor Erm/Fezf functions to maintain the restricted developmental potential of INPs by limiting their proliferation potential and suppressing their dedifferentiation capacity (Figure 7). Combining proper specification of the transit amplifying cell identity and active maintenance of their restricted developmental potential ensures the generation of differentiated progeny and prevents aberrant expansion of stem cells.

The lineage clones derived from single INPs in erm^1/erm^2 mutant brains contain dedifferentiated neuroblasts, immature INPs, INPs, GMCs, and neurons (Figures 3B and 3C). Several mechanisms could lead to the diversity of cells within the clones. First, INPs in *erm* mutant brains might generate GMCs and neurons initially due to the presence of maternally deposited Erm. However, *erm* transcripts are undetectable in both adult male and female germlines by microarray analyses and in stage 1–3 embryos by RNA in situ (Chintapalli et al., 2007; http://flybase.org/reports/FBgn0031375.html; data not shown). Furthermore, the erm^1/erm^2 allelic combination resulted in little to no zygotic Erm in the brain because the erm^1 mutation likely leads to the production of an unstable Erm protein, whereas the erm^2 mutation deletes the entire *erm* open reading frame (data not shown). Additionally, the ectopic neuroblast phenotype in erm^1/erm^2 mutant brains can be observed as early as 36–48 hr after larval hatching (data not presented). Thus, generation of GMCs and differentiated neurons by INPs in erm^1/erm^2 mutant brains is unlikely due to the maternal effect. Alternatively, *erm* may promote GMC differentiation in the type II neuroblast lineage, and in *erm* mutant brains, GMCs might dedifferentiate back into neuroblasts. If so, we would predict an ectopic accumulation of INPs in similarly staged mosaic clones derived from *erm* mutant type II neuroblasts as compared to wild-type clones. However, 48 hr *erm* mutant single neuroblast clones consistently contained fewer INPs when compared to the wild-type clones (Figures 2C–2F). In addition, blocking GMC differentiation by removing Prospero function resulted in ectopic accumulation of INPs but did not lead to ectopic neuroblast formation (Figure 5H). Therefore, the diversity of cells within *erm* mutant clones is also unlikely due to blocking GMC differentiation. We favor the interpretation that *erm* mutant INPs dedifferentiate into apparently normal neuroblasts that can give rise to all cell types found in a type II neuroblast lineage. Consistently, the dedifferentiated neuroblasts in *erm* mutant brains exhibited

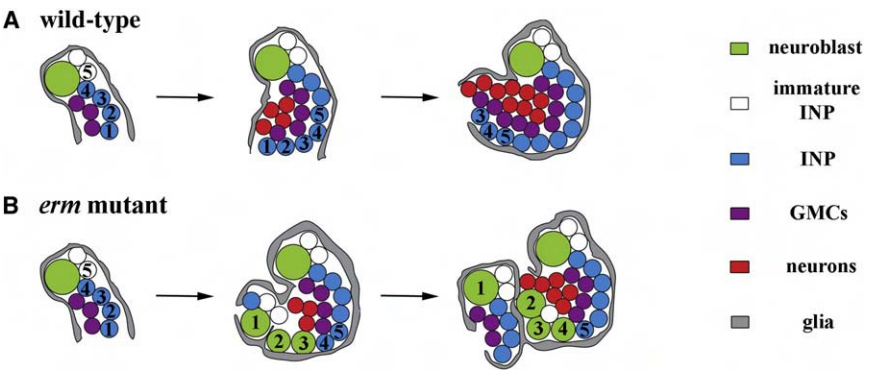

Figure 7. *erm* Maintains the Restricted Developmental Potential of INPs

(A) Wild-type INPs undergo limited rounds of asymmetric divisions to generate neurons prior to exiting from the cell cycle, and they remain in the same glial chamber as their parental type II neuroblasts.

(B) Some *erm* mutant INPs fail to terminate proliferation and dedifferentiate back into their parental type II neuroblast fate. These dedifferentiated neuroblasts can establish ectopic type II neuroblast lineages and form ectopic glial chambers.

normal cortical polarity and proliferation potential (Figures 3 and 4). Furthermore, the dedifferentiated neuroblasts in *erm* mutant brains also lost the expression of *Pros-Gal4* and *Erm-Gal4* and established ectopic type II neuroblast lineages encapsulated by the cortex glial membrane (Figures 3 and 4). Thus, we conclude that Erm likely restricts the developmental potential of INPs by limiting proliferation and suppressing dedifferentiation.

Although mutations in *erm*, *brain tumor*, and *numb* genes all lead to ectopic type II neuroblasts, the proteins appear to regulate INPs at distinct steps in the type II neuroblast lineage (Figure S3). Numb and Brain tumor function cooperatively, but nonredundantly, to ensure that immature INPs undergo maturation and commit to the INP fate (Boone and Doe, 2008; Bowman et al., 2008). While ectopic expression of Numb induces premature differentiation of type II neuroblasts and immature INPs (J. Haenfler, K.L.G., and C.-Y.L., unpublished data), overexpression of Numb is not sufficient to suppress ectopic neuroblasts in *brain tumor* mutant brains (H. Komori and C.-Y.L., unpublished data). Thus, Numb likely promotes differentiation of immature INPs whereas Brain tumor likely prevents immature INPs, which are unstable in nature, from adopting their parental neuroblast fate. More studies will be necessary to discern whether ectopic neuroblasts in *brain tumor* mutant brains arise from dedifferentiation of partially differentiated immature INPs or failure of immature INPs to initiate differentiation. In contrast, immature INPs in *erm* mutant brains mature into functional INPs that exhibit normal cortical polarity and proliferation potential and can generate GMCs and neurons (Figures 2A–2F, 3D, 3E, and 4; Figure S3). Additionally, overexpression of Brain tumor or Numb in INPs was not sufficient to suppress ectopic neuroblasts in *erm* mutant brains (data not shown). Finally, lineage clones derived from single INPs in *erm* mutant brains always contain ectopic type II neuroblasts, multiple immature INPs, INPs, GMCs, and neurons (Figures 3B and 3C). These results indicate that Erm is dispensable for maturation of immature INPs and is not within the genetic hierarchy specifying the INP identity. Instead, Erm maintains the restricted developmental potential of INPs after specification of their identity.

Prospero encodes a homeodomain transcription factor, and nuclear Prospero has been shown to trigger cell cycle exit and GMC differentiation (Choksi et al., 2006; Doe et al., 1991; Maurange et al., 2008). In the wild-type brain, 9.6% of INPs showed nuclear Prospero and were likely undergoing differentiation (data not shown). *prospero* mutant type II neuroblast clones showed ectopic accumulation of INPs but contained single neuroblasts, indicating that blocking differentiation is not sufficient to trigger the dedifferentiation of INPs (Figure 5H). Thus, Prospero restricts the proliferation potential of INPs but does not suppress dedifferentiation of INPs.

While ectopic expression of Prospero in INPs can restore neuronal differentiation in *erm* mutant brains, targeted expression of Erm in neuroblasts or INPs was sufficient to induce rapid nuclear localization of Prospero in these cells and terminate their proliferation (Figure 5). In wild-type brains, Prospero is sequestered in a basal crescent by the adaptor protein Miranda in mitotic neural progenitors (Ikeshima-Kataoka et al., 1997; Shen et al., 1997). Interestingly, mitotic neural progenitors including neuroblasts and INPs transiently overexpressing Erm also showed basal localization and segregation of Miranda and Prospero (data not shown). As such, Erm likely restricts the proliferation potential of INPs by indirectly promoting nuclear localization of Prospero. Therefore, Prospero does not localize in the nuclei of mitotically active INPs, which express Miranda, but does localize in the nuclei of GMCs that do not express Miranda.

How does Erm suppress the dedifferentiation of INPs? Our results show that reduced Notch function can efficiently suppress ectopic neuroblasts in *erm* mutant brains while constitutive activation of Notch signaling induced the dedifferentiation of INPs (Figures 6A–6C). Importantly, coexpression of Erm is sufficient to suppress the dedifferentiation of INPs triggered by expression of constitutively active $Notch^{intra}$ (Figure 6D). Together, these results strongly suggest that Erm prevents the dedifferentiation of INPs by antagonizing a Notch-activated mechanism through interfering with the assembly of the Notch transcriptional activator complex or inhibiting the expression of Notch targets. Intriguingly, the amino terminus of all Fezf proteins contains an engrailed homology 1 domain. This domain can mediate direct interaction with the conserved transcriptional corepressor Groucho that can function as a corepressor of Notch signaling (Cinnamon and Paroush, 2008; Copley, 2005; Jeong et al., 2006; Levkowitz et al., 2003; Shimizu and Hibi, 2009). Additional experiments will be needed to discern how Erm antagonizes Notch-activated dedifferentiation of INPs.

EXPERIMENTAL PROCEDURES

Fly Genetics and Transgenes

A total of six *erm* alleles were recovered from EMS mutagenesis following a standard protocol. erm^2 was generated by a FRT-based high-resolution deletion method and verified by PCR (Parks et al., 2004). The cDNA for *CG31670* was obtained from the *Drosophila* Genome Resource Center, sequenced, and cloned into the *pUAST-HA* vector for germline transformation. Mouse *fezf1* and *fezf2* cDNAs were sequenced (M. Hibi) and cloned into the *pUAST-HA* vector for germline transformation. *Drosophila* cultures were kept at 25°C on standard cornmeal food. Other mutant alleles and transgenes used in this study include $brat^{11}$ (Lee et al., 2006c), $pros^{17}$, *FRT82B* (Lee et al., 2006c), $aPKC^{k06403}$ (Lee et al., 2006b), $pins^{62}$ (Lee et al., 2006b), *UAS-pros* (Hirata et al., 1995), *Wor-gal4* (Lee et al., 2006b), *Ase-gal4* (Zhu et al., 2006), and *R9D-Gal4* lines (Pfeiffer et al., 2008). The $UAS\text{-}Notch_{RNAi}$ lines were obtained from the Vienna *Drosophila* Resource Center. *Oregon R*, *elav-gal4 (C155), hs-flp, UAS-mCD8-GFP, FRT40A, tub-gal80, FRT82B, hs-flp(F38), act-FRT-Stop-FRT-lacZ, UAS-flp, tub-GAL80^{ts}, UAS-dcr-2, UAS-Notch^{intra}, Repo-Gal4* flies were obtained from Bloomington *Drosophila* Stock Center.

Immunofluorescent Staining and Antibodies

Antibody staining was performed as previously described (Lee et al., 2006b). The rabbit Ase antibody was raised against a previously described synthetic peptide (Brand and Perrimon, 1993). Other antibodies used in this study include guinea pig Ase (1:100; J. Knoblich), rat Wor (1:1), rat Dpn (1:1), guinea pig Dpn (1:2500, J. Skeath), mouse Pros (1:100), rat Mira (1:100); guinea pig Mira (1:400), guinea pig Numb (1:3000, J. Skeath); rat Pins (1:500), rabbit Scrib (1:2500), mouse Elav(1:50, DSHB), mouse Dlg (1:100, DSHB), mouse Repo (1:50, DSHB), mouse BrdU (1:50, Roche), rabbit β-gal (1:1000, ICN/Cappel), rat α-Tub (1:100, Sigma), rat mCD8 (1:100, Caltag), rabbit GFP (1:1000, Torreypine), mouse HA (1:1000, Covance), rat HA (1:2000, Roche). Secondary antibodies were from Molecular Probes (details are available upon request). The confocal images were acquired on a Leica SP5 scanning confocal microscope with AOBS.

Edu Pulse-Chase

Larvae were aged for 72 hr after hatching, and were pulse labeled for 3 hr by feeding on the Kankel-White media containing 50 μg/ml EdU (5-ethynyl-2′deoxyuridine) (Lee et al., 2006c). Half of the larvae were processed for staining immediately following the pulse; remaining larvae were transferred to standard media for a 12 hr EdU-free chase. Larvae were dissected and processed for antibody staining as previously described (Lee et al., 2006b). Incorporated EdU was detected by Click-iT fluorescent dye azide reaction as described in the Click-iT product literature (Invitrogen).

Lineage Clonal Analysis

We initially performed genetic clonal analyses of INPs using *Ase-Gal4* by crossing *erm^{1}, Actin-FRT-Stop-FRT-lacZ/CyO, Actin-GFP* flies to *erm^{2}, Ase-Gal4/CyO, Actin-GFP; UAS-flp, tub-Gal80^{ts}* flies. At 24 hr after hatching, *erm^{1}/erm^{2}* larvae were shifted to 31°C for 48 hr to inactivate Gal80^{ts}, allowing FRT-mediated recombination to induce permanently marked lineage clones. The expression level of *Ase-Gal4* is very low (Bowman et al., 2008), allowing us to induce genetic clones at a very low frequency. However, due to the prolonged incubation time at the nonpermissive temperature, clones derived from two neighboring INPs sometimes became overlapped, resulting in appearance of a "large" clone. We repeated this experiment by using *Erm-Gal4*, whose expression level was significantly higher compared to *Ase-Gal4* (M.W. and C.-Y.L., data not shown). We crossed *erm^{1}, Actin-FRT-Stop-FRT-lacZ/CyO, Actin-GFP; Erm-Gal4* flies to *erm^{2}/CyO, Actin-GFP; UAS-flp, tub-Gal80^{ts}* flies. At 24 hr after hatching, *erm^{1}/erm^{2}* larvae were shifted to 31°C for 1 hr to induce positively marked genetic clones derived from single INP. Larvae were returned back to 25°C for 72 hr prior to processing larval brains for antibody staining.

Mutant Clonal Analyses

We induced mosaic clones derived from *erm^{1}* and *pros^{17}* mutant neuroblasts by following a previously established protocol (Lee et al., 2006c; Lee and Luo, 2001).

Overexpression of Notch^{intra}

Overexpression of Notch^{intra} in INPs in larval brains was accomplished by crossing *UAS-Notch^{intra}/CyO, Actin-GFP; tub-Gal80^{ts}* flies to *Erm-Gal4* flies. GFP^{-} larvae were allowed to hatch at 25°C, and were then shifted to 31°C for 72 hr. Larval brains were dissected and processed for antibody staining. Co-overexpression of Erm and Notch^{intra} was carried out following an identical protocol.

Real-Time PCR

Late third instar larval brains were dissected free of surrounding tissues. Total RNA was extracted following the standard Trizol RNA isolation protocol and cleaned by the QIAGEN RNeasy kit. cDNA was transcribed using First Strand cDNA Synthesis Kit for RT-PCR (AMV) (Roche). Quantitative PCR was performed by using SYBR-green. Resulting data were analyzed by the comparative CT method, and the relative mRNA expression is presented.

SUPPLEMENTAL INFORMATION

Supplemental Information includes three figures and can be found with this article online at doi:10.1016/j.devcel.2009.12.007.

ACKNOWLEDGMENTS

We thank Chris Q. Doe in whose lab the *l(2)5138^{1}* was isolated when C.-Y.L was a postdoctoral fellow. We thank Kristin Wildermuth and Caitlin Gamble for the technical assistance in the isolation and the initial phenotypic characterization of the *l(2)5138^{1}* mutant allele. We thank C.Q. Doe, J.A. Knoblich, J.B. Skeath, M. Hibi, and J. Lin for fly stocks, antibody reagents, cDNAs, and advice with real-time PCR. We thank the Bloomington *Drosophila* Stock Center and Vienna *Drosophila* RNAi Center for fly stocks. We thank C.Q. Doe and Sean J. Morrison and the members of the Lee lab for reading the manuscript and providing critical comments. C.-Y.L was initially supported by a Damon Runyon postdoctoral fellowship and is currently supported by Burroughs Wellcome Fund Career Award in the Biomedical Sciences (1006160.01), a Sontag Foundation Distinguished Scientist Award, and the University of Michigan start-up fund.

Received: March 27, 2009
Revised: August 21, 2009
Accepted: December 7, 2009
Published: January 19, 2010

REFERENCES

Bello, B.C., Izergina, N., Caussinus, E., and Reichert, H. (2008). Amplification of neural stem cell proliferation by intermediate progenitor cells in Drosophila brain development. Neural Dev. *3*, 5.

Betschinger, J., Mechtler, K., and Knoblich, J.A. (2006). Asymmetric segregation of the tumor suppressor Brat regulates self-renewal in *Drosophila* neural stem cells. Cell *124*, 1241–1253.

Boone, J.Q., and Doe, C.Q. (2008). Identification of Drosophila type II neuroblast lineages containing transit amplifying ganglion mother cells. Dev. Neurobiol. *68*, 1185–1195.

Bowman, S.K., Rolland, V., Betschinger, J., Kinsey, K.A., Emery, G., and Knoblich, J.A. (2008). The tumor suppressors Brat and Numb regulate transit-amplifying neuroblast lineages in *Drosophila*. Dev. Cell *14*, 535–546.

Brand, A.H., and Perrimon, N. (1993). Targeted gene expression as a means of altering cell fates and generating dominant phenotypes. Development *118*, 401–415.

Chintapalli, V.R., Wang, J., and Dow, J.A.T. (2007). Using FlyAtlas to identify better Drosophila models of human disease. Nat. Genet. *39*, 715–720.

Choksi, S.P., Southall, T.D., Bossing, T., Edoff, K., de Wit, E., Fischer, B.E., van Steensel, B., Micklem, G., and Brand, A.H. (2006). Prospero acts as a binary switch between self-renewal and differentiation in *Drosophila* neural stem cells. Dev. Cell *11*, 775–789.

Cinnamon, E., and Paroush, Z. (2008). Context-dependent regulation of Groucho/TLE-mediated repression. Curr. Opin. Genet. Dev. *18*, 435–440.

Copley, R.R. (2005). The EH1 motif in metazoan transcription factors. BMC Genomics *6*, 169.

Doe, C.Q., Chu-LaGraff, Q., Wright, D.M., and Scott, M.P. (1991). The *prospero* gene specifies cell fates in the *Drosophila* central nervous system. Cell *65*, 451–464.

Farkas, L.M., Haffner, C., Giger, T., Khaitovich, P., Nowick, K., Birchmeier, C., Pääbo, S., and Huttner, W.B. (2008). Insulinoma-associated 1 has a panneurogenic role and promotes the generation and expansion of basal progenitors in the developing mouse neocortex. Neuron *60*, 40–55.

Hashimoto, H., Yabe, T., Hirata, T., Shimizu, T., Bae, Y., Yamanaka, Y., Hirano, T., and Hibi, M. (2000). Expression of the zinc finger gene *fez-like* in zebrafish forebrain. Mech. Dev. *97*, 191–195.

Hirata, J., Nakagoshi, H., Nabeshima, Y., and Matsuzaki, F. (1995). Asymmetric segregation of the homeodomain protein Prospero during Drosophila development. Nature *377*, 627–630.

Hodge, R.D., Kowalczyk, T.D., Wolf, S.A., Encinas, J.M., Rippey, C., Enikolopov, G., Kempermann, G., and Hevner, R.F. (2008). Intermediate progenitors in adult hippocampal neurogenesis: Tbr2 expression and coordinate regulation of neuronal output. J. Neurosci. *28*, 3707–3717.

Ikeshima-Kataoka, H., Skeath, J.B., Nabeshima, Y., Doe, C.Q., and Matsuzaki, F. (1997). Miranda directs Prospero to a daughter cell during Drosophila asymmetric divisions. Nature *390*, 625–629.

Jeong, J.Y., Einhorn, Z., Mercurio, S., Lee, S., Lau, B., Mione, M., Wilson, S.W., and Guo, S. (2006). Neurogenin1 is a determinant of zebrafish basal forebrain dopaminergic neurons and is regulated by the conserved zinc finger protein Tof/Fezl. Proc. Natl. Acad. Sci. USA *103*, 5143–5148.

Lee, T., and Luo, L. (2001). Mosaic analysis with a repressible cell marker (MARCM) for Drosophila neural development. Trends Neurosci. *24*, 251–254.

Lee, C.Y., Andersen, R.O., Cabernard, C., Manning, L., Tran, K.D., Lanskey, M.J., Bashirullah, A., and Doe, C.Q. (2006a). Drosophila Aurora-A kinase

inhibits neuroblast self-renewal by regulating aPKC/Numb cortical polarity and spindle orientation. Genes Dev. *20*, 3464–3474.

Lee, C.Y., Robinson, K.J., and Doe, C.Q. (2006b). Lgl, Pins and aPKC regulate neuroblast self-renewal versus differentiation. Nature *439*, 594–598.

Lee, C.Y., Wilkinson, B.D., Siegrist, S.E., Wharton, R.P., and Doe, C.Q. (2006c). Brat is a Miranda cargo protein that promotes neuronal differentiation and inhibits neuroblast self-renewal. Dev. Cell *10*, 441–449.

Levkowitz, G., Zeller, J., Sirotkin, H.I., French, D., Schilbach, S., Hashimoto, H., Hibi, M., Talbot, W.S., and Rosenthal, A. (2003). Zinc finger protein too few controls the development of monoaminergic neurons. Nat. Neurosci. *6*, 28–33.

Matsuo-Takasaki, M., Lim, J.H., Beanan, M.J., Sato, S.M., and Sargent, T.D. (2000). Cloning and expression of a novel zinc finger gene, Fez, transcribed in the forebrain of Xenopus and mouse embryos. Mech. Dev. *93*, 201–204.

Maurange, C., Cheng, L., and Gould, A.P. (2008). Temporal transcription factors and their targets schedule the end of neural proliferation in *Drosophila*. Cell *133*, 891–902.

Morrison, S.J., and Kimble, J. (2006). Asymmetric and symmetric stem-cell divisions in development and cancer. Nature *441*, 1068–1074.

Parks, A.L., Cook, K.R., Belvin, M., Dompe, N.A., Fawcett, R., Huppert, K., Tan, L.R., Winter, C.G., Bogart, K.P., Deal, J.E., et al. (2004). Systematic generation of high-resolution deletion coverage of the Drosophila melanogaster genome. Nat. Genet. *36*, 288–292.

Pereanu, W., Shy, D., and Hartenstein, V. (2005). Morphogenesis and proliferation of the larval brain glia in Drosophila. Dev. Biol. *283*, 191–203.

Pfeiffer, B.D., Jenett, A., Hammonds, A.S., Ngo, T.T., Misra, S., Murphy, C., Scully, A., Carlson, J.W., Wan, K.H., Laverty, T.R., et al. (2008). Tools for neuroanatomy and neurogenetics in Drosophila. Proc. Natl. Acad. Sci. USA *105*, 9715–9720.

Pontious, A., Kowalczyk, T., Englund, C., and Hevner, R.F. (2008). Role of intermediate progenitor cells in cerebral cortex development. Dev. Neurosci. *30*, 24–32.

Sessa, A., Mao, C.A., Hadjantonakis, A.K., Klein, W.H., and Broccoli, V. (2008). Tbr2 directs conversion of radial glia into basal precursors and guides neuronal amplification by indirect neurogenesis in the developing neocortex. Neuron *60*, 56–69.

Shen, C.P., Jan, L.Y., and Jan, Y.N. (1997). Miranda is required for the asymmetric localization of Prospero during mitosis in Drosophila. Cell *90*, 449–458.

Shimizu, T., and Hibi, M. (2009). Formation and patterning of the forebrain and olfactory system by zinc-finger genes Fezf1 and Fezf2. Dev. Growth Differ. *51*, 221–231.

Vescovi, A.L., Galli, R., and Reynolds, B.A. (2006). Brain tumour stem cells. Nat. Rev. Cancer *6*, 425–436.

Wang, H., Somers, G.W., Bashirullah, A., Heberlein, U., Yu, F., and Chia, W. (2006). Aurora-A acts as a tumor suppressor and regulates self-renewal of Drosophila neuroblasts. Genes Dev. *20*, 3453–3463.

Zhu, S., Lin, S., Kao, C.F., Awasaki, T., Chiang, A.S., and Lee, T. (2006). Gradients of the *Drosophila* Chinmo BTB-zinc finger protein govern neuronal temporal identity. Cell *127*, 409–422.

Available online at www.sciencedirect.com
ScienceDirect
Current Opinion in Neurobiology

Keeping neural progenitor cells on a short leash during *Drosophila* neurogenesis

Mo Weng and Cheng-Yu Lee

The developmental potential of stem cells and progenitor cells must be functionally distinguished to ensure the generation of diverse cell types while maintaining the stem cell pool throughout the lifetime of an organism. In contrast to stem cells, progenitor cells possess restricted developmental potential, allowing them to give rise to only a limited number of post-mitotic progeny. Failure to establish or maintain restricted progenitor cell potential can perturb tissue development and homeostasis, and probably contributes to tumor initiation. Recent studies using the developing fruit fly *Drosophila* larval brain have provided molecular insight into how the developmental potential is restricted in neural progenitor cells.

Address
Center for Stem Cell Biology, Life Sciences Institute, University of Michigan, Ann Arbor, MI 48109, USA

Corresponding author: Lee, Cheng-Yu (leecheng@umich.edu)

Current Opinion in Neurobiology 2010, **21**:1–7

This review comes from a themed issue on
Developmental neuroscience
Edited by Silvia Arber and Graeme Davis

0959-4388/$ – see front matter

DOI 10.1016/j.conb.2010.09.005

Introduction

Restricted developmental potential allows progenitor cells to generate a limited number of terminally differentiated progeny, amplifying the output of stem cells while safeguarding the stem cell pool throughout the natural lifespan of an organism. Expanded progenitor cell potential might result in the formation of aberrant stem-like cells, contributing to developmental defects and possibly tumor initiation. In contrast to stem cells, how progenitor cell potential is restricted remains largely unknown owing to their short-lived nature. The fruit fly *Drosophila* larval brain, which consists of the central brain and optic lobe, possesses well-defined lineages of neural stem cells that generate progenitor cells in a highly reproducible pattern (Figure 1). These lineages provide an excellent *in vivo* system for studying regulation of the progenitor cell potential at a single-cell resolution. Conservation in gene function between flies and mammals suggests that molecular mechanisms that regulate progenitor cell potential in *Drosophila* neural stem cell lineages might be similarly employed during vertebrate neurogenesis.

Central brain neuroblasts generate neural progenitor cells with distinct developmental potential

All neural stem cells in the central brain (called neuroblasts) undergo repetitive asymmetric divisions to self-renew and to generate a neural progenitor cell with limited developmental potential. The cortex of a mitotic central brain neuroblast is highly polarized, and the role of this polarity in neuroblast asymmetric division has been extensively reviewed [1–4]. Discrete protein complexes are assembled in the apical and basal cortical domains. In telophase, the apical protein complexes segregate into the self-renewing neuroblast, whereas the basal protein complexes segregate into the neural progenitor cell. Both genetic and correlative live imaging studies indicate that the apical protein complexes have dual functions: promoting neuroblast identity and targeting the basal protein complexes into the neural progenitor cell. The basal protein complexes function specifically in restricting the neural progenitor cell potential [5]. Two classes of central brain neuroblast lineages (types I and II) can be unambiguously identified based on the progenitor progeny generated and the combination of cell fate markers expressed [6••,7••,8••] (Figure 1). Below, we discuss the functional properties of neural progenitor cells generated in the type I and type II neuroblast lineages and the molecular mechanisms that restrict their developmental potential.

Neuroblasts and neural progenitor cells in the type I lineage

A type I neuroblast divides asymmetrically to generate a self-renewing daughter neuroblast and a neural progenitor cell called a ganglion mother cell (GMC) that divides once to produce two post-mitotic neurons [6••,7••,8••]. During this asymmetric division, the basal proteins Brain tumor and Prospero exclusively segregate into the GMC by binding to the scaffolding protein Miranda, while Numb partitions into the GMC independently of Miranda. The basal proteins remain asymmetrically segregated into GMCs in a telophase *brain tumor* mutant neuroblast, and genetic clones derived from single *brain tumor* mutant neuroblasts always contain one neuroblast and many neurons per clone (Figure 2). Thus, Brain tumor is either dispensable or functionally redundant with other proteins in restricting the GMC potential.

Please cite this article in press as: Weng M, Lee C-Y. Keeping neural progenitor cells on a short leash during *Drosophila* neurogenesis, Curr Opin Neurobiol (2010), doi:10.1016/j.conb.2010.09.005

Figure 1

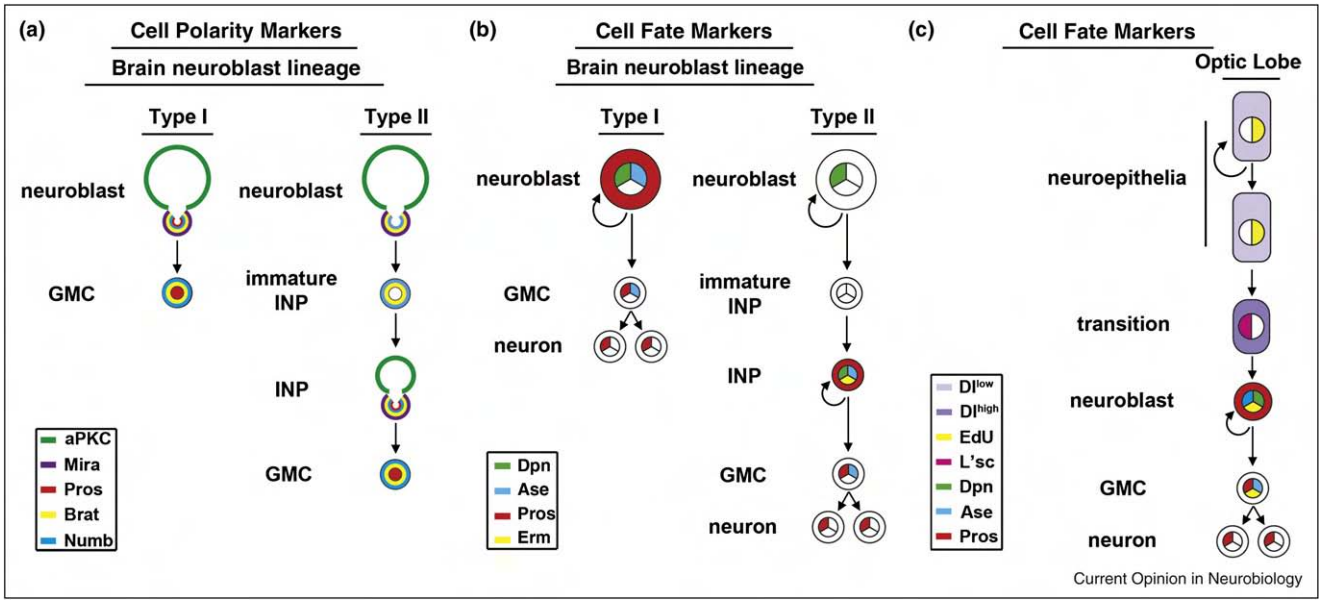

Neural stem cell lineages in the developing *Drosophila* larval brain. **(a)** The apical and basal protein complexes unequally segregate during asymmetric divisions of neural stem/progenitor cells in the type I and type II neuroblast lineage in the larval brain. Abbreviation: aPKC: atypical Protein Kinase C; Mira: Miranda; Pros: Prospero; Brat: Brain tumor. **(b)** The cell fate markers allow unambiguous identification of neural stem/progenitor cells in the type I and type II neuroblast lineage in the larval brain. Abbreviation: Dpn: Deadpan; Ase: Asense; Pros: Prospero; Erm: Earmuff. **(c)** The cell fate markers allow unambiguous identification of neuroepithelial stem cells and progenitor cells in the optic lobe. Abbreviation: Dl: Delta; EdU: 5-ethynyl-2′-deoxyuridine; L'sc: Lethal of scute; Dpn: Deadpan; Ase: Asense; Pros: Prospero.

Figure 2

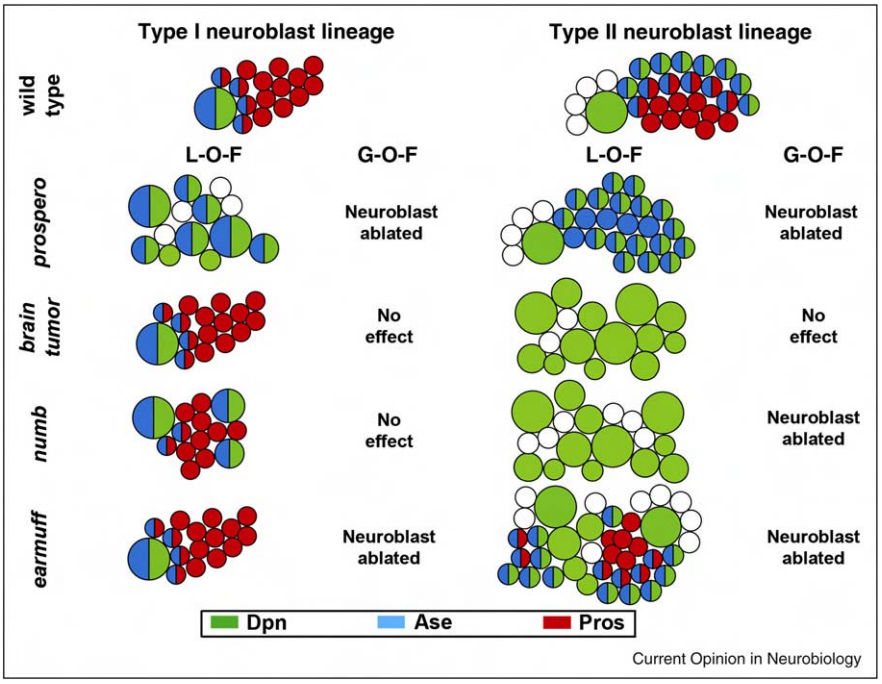

A summary of the identity of cells derived from type I and II neuroblasts lacking or overexpressing key proteins required to restrict the progenitor cell potential. Type I neuroblasts are $Dpn^{+}Ase^{+}$ whereas type II neuroblasts are $Dpn^{+}Ase^{-}$. Abbreviation: L-O-F: loss-of-function; G-O-F: gain-of-function; Dpn: Deadpan; Ase: Asense; Pros: Prospero.

Please cite this article in press as: Weng M, Lee C-Y. Keeping neural progenitor cells on a short leash during *Drosophila* neurogenesis, Curr Opin Neurobiol (2010), doi:10.1016/j.conb.2010.09.005

prospero encodes a homeodomain transcription factor, and plays a key role in specifying neuronal and glial cell types in the developing nervous system [9–12]. Although Prospero is expressed in neuroblasts, it is kept out of neuroblast nuclei by the combination of nuclear exclusion and binding to the scaffolding protein Miranda [13–16]. The Miranda–Prospero complex localizes to the basal cortex of a mitotic neuroblast in metaphase and asymmetrically segregates into the GMC in telophase. Upon completion of cell division, Miranda becomes proteolytically degraded, and Prospero is released from the cortex and localizes to the GMC nuclei [17]. Nuclear Prospero restricts the GMC potential by suppressing genes that promote the neuroblast identity and activating genes that promote differentiation and cell cycle exit [12,18]. While mitotic *prospero* mutant type I neuroblasts exhibit normal apical–basal cortical polarity, *prospero* mutant neuroblast lineage clones contain almost exclusively neuroblasts at the expense of neurons [12,19–22] (Figure 2). Overexpression of Prospero leads to constitutive accumulation of Prospero in neuroblast nuclei, triggering premature loss of neuroblasts. These data indicate that Prospero is necessary and sufficient to restrict the GMC potential.

numb encodes an evolutionarily conserved protein essential for proper neuronal fate specification in the developing nervous system [23–27]. Eighty-five percent of *numb* mutant type I neuroblast lineage clones contain more than one neuroblast per clone despite asymmetric segregation of Miranda into GMCs [8••,28] (Figure 2). Furthermore, mutations that perturb asymmetric segregation of Numb into GMCs lead to formation of ectopic neuroblasts, a phenotype that can be suppressed by overexpression of Numb in neuroblasts [28,29]. Thus, Numb probably restricts the GMC potential independent of Prospero. Fly and mouse studies have shown that Numb suppresses Notch signaling in the developing nervous system, raising the possibility that Numb might restrict the GMC potential by antagonizing Notch signaling. Expression of multiple *Notch* reporters is detectable in neuroblasts but is undetectable in GMCs in the wild-type brain [8••,30]. Additionally, ectopic expression of a constitutively active form of Notch ($Notch_{intra}$) perturbs neuroblast asymmetric divisions, leading to a massive increase in neuroblasts at the expense of neurons [8••,30]. Unlike Prospero, ectopic expression of Numb or knockdown of the *Notch* function by RNA interference is insufficient to trigger premature loss of type I neuroblasts [8••]. Thus, inhibition of the Notch signaling by Numb is necessary but not sufficient to limit the GMC potential.

Neuroblasts and neural progenitors in the type II lineage

A type II neuroblast divides asymmetrically to self-renew and generate an intermediate neural progenitor cell (INP), previously referred to as a transit amplifying GMC, a secondary neuroblast or an intermediate progenitor [6••,7••,8••] (Figure 1). A newly born INP is immature, and is arrested in the G2 phase of the cell cycle and must undergo maturation, during which it acquires restricted developmental potential before resuming proliferation [8]. A mature INP divides asymmetrically several times, each time self-renewing by producing a daughter INP and a GMC. The basal proteins Brain tumor and Numb, inherited from the asymmetrically dividing parental neuroblasts, establish the restricted developmental potential in an immature INP [8••]. Following completion of maturation, the transcription factor Earmuff maintains the INP potential [22••]. These sequential mechanisms play key roles in restricting the INPs potential.

Establishment of the restricted developmental potential in INPs

While a wild-type type II neuroblast clone always contains one neuroblast, 3–5 immature INPs and 20–30 INPs, a *brain tumor* mutant type II neuroblast clone contains almost exclusively neuroblasts [8••] (Figure 2). Interestingly, a mitotic *brain tumor* mutant type II neuroblast shows normal apical–basal cortical polarity and asymmetric segregation of Numb into immature INPs. Thus, ectopic type II neuroblasts in the *brain tumor* mutant brain probably arise from de-differentiation of immature INPs that fail to acquire restricted developmental potential despite inheriting Numb. These data suggest that Brain tumor probably functions parallel to Numb to promote restriction of the INP potential. Overexpression of Brain tumor does not effect the expression of a *Notch* reporter in neuroblasts, and removal of *brain tumor* does not alter binary cell fate determination in the sensory organ precursor lineage, a system highly sensitive to the loss of *Notch* function [8••]. Together, these data strongly suggest that Brain tumor is necessary but not sufficient to restrict the INP potential.

Despite showing normal apical–basal cortical polarity and asymmetric segregation of Brain tumor into immature INPs, *numb* mutant type II neuroblast clones also consist of mostly neuroblasts [8••,28] (Figure 2). Thus, ectopic type II neuroblasts in the *numb* mutant brain might also arise from de-differentiation of immature INPs owing to aberrant activation of the Notch signaling mechanism. Indeed, ectopic expression of $Notch_{intra}$ leads to ectopic type II neuroblasts at the expense of immature INPs, whereas overexpression of Numb or knockdown of the *Notch* function by RNA interference results in the premature loss of type II neuroblasts [8••]. Thus, by antagonizing Notch, Numb is necessary and sufficient to establish the restricted developmental potential in immature INPs. Taken together, Brain tumor and Numb function non-redundantly to establish the INP potential during maturation.

Please cite this article in press as: Weng M, Lee C-Y. Keeping neural progenitor cells on a short leash during *Drosophila* neurogenesis, Curr Opin Neurobiol (2010), doi:10.1016/j.conb.2010.09.005

Maintenance of the restricted developmental potential in INPs

Following maturation, the INP potential requires an active mechanism mediated by the *earmuff* gene for maintenance during limited rounds of asymmetric divisions [22••]. While the number of type I neuroblasts remain unchanged in the *earmuff* mutant brain, the population of type II neuroblasts becomes drastically expanded (Figure 2). Surprisingly, *earmuff* mutant mitotic type II neuroblasts exhibit normal apical–basal cortical polarity and undergo repeated asymmetric divisions to self-renew and to generate immature INPs that mature into INPs. Furthermore, *earmuff* mutant mitotic INPs also exhibit normal cortical polarity and asymmetric segregation of the basal proteins Brain tumor, Prospero and Numb into GMCs that produce differentiated neurons. Thus, it is unlikely that ectopic type II neuroblasts in the *earmuff* mutant brain arise from de-differentiation of immature INPs owing to failure to acquire restricted developmental potential. Analyses of the cell fate markers in lineage clones derived from *earmuff* mutant type II neuroblasts indicate that following maturation, INPs fail to maintain restricted developmental potential and de-differentiate back into type II neuroblasts. Analyses of its promoter expression pattern reveal that *earmuff is* undetectable in type II neuroblasts and immature INPs and instead, is detected in INPs. Additionally, ectopic type II neuroblasts in the *earmuff* mutant brain can be suppressed by restoring the expression of Earmuff in INPs under the control of its own promoter. Thus, Earmuff specifically maintains the INP potential.

One way to maintain the restricted potential of INPs is to limit their proliferation capacity. In the wild-type brain, an INP shows a limited proliferation capacity before exit from cell cycle and terminal differentiation, processes probably regulated by nuclear localization of Prospero [12,31]. While nuclear Prospero is rarely detected in INPs in the wild-type brain, overexpression of Earmuff in neuroblasts or INPs can induce almost a ten-fold increase in the frequency of nuclear Prospero and premature loss of these cells [22••]. Furthermore, INP-specific expression of Prospero can partially suppress the ectopic neuroblast phenotype in the *earmuff* mutant brain. Moreover, *prospero* mutant INPs generate ectopic INPs at the expense of neurons, but do not de-differentiate back into type II neuroblasts [22••]. Thus, a Prospero-dependent mechanism limits INP proliferation and promotes INP differentiation, whereas a Prospero-independent mechanism prevents INPs from acquiring the type II neuroblast identity.

Neuroblast-specific expression of $Notch_{intra}$ leads to ectopic neuroblasts at the expense of GMCs and immature INPs, suggesting that downregulation of Notch might be a general mechanism to restrict the developmental potential in neural progenitor cells. Similarly, ectopic expression of $Notch_{intra}$ in INPs is sufficient to trigger formation of ectopic type II neuroblasts, raising the possibility that *earmuff* might restrict the developmental potential of INPs by antagonizing Notch signaling [22••]. In agreement with this hypothesis, knockdown of *Notch* function by RNA interference partially suppresses the ectopic type II neuroblast phenotype in the *earmuff* mutant brain. Furthermore, overexpression of Earmuff in INPs can suppress the formation of ectopic type II neuroblasts induced by overexpression of $Notch_{intra}$. A recent study demonstrates that the vertebrate homologs of Earmuff can suppress Notch signaling by directly binding to the promoter of a Notch target gene Hes5 during mouse cortical neurogenesis [32•]. Notch signaling plays a crucial role in distinguishing neural stem cell from intermediate progenitors during both embryonic and adult brain neurogenesis [32•,33]. Thus, Earmuff and its vertebrate homologs probably regulate the progenitor cell potential during neurogenesis through antagonizing the Notch signaling.

Optic lobe neuroepithelial stem cells generate two types of neural progenitor cells

Neuroepithelial stem cells in the developing optic lobe initially undergo symmetric divisions to expand the stem cell population, then differentiate into neural progenitors that generate terminally differentiated neurons through limited rounds of asymmetric divisions [34••] (Figure 1). This dynamic mechanism allows rapid generation of a large number of post-mitotic progeny from a relatively small population of stem cells, and is widely used in the context of development and regeneration [35,36]. Failure to properly restrict the developmental potential in neuroepithelial stem cells and their progenitor progeny might contribute to childhood tumors of epithelial origin [37,38]. Thus, understanding how developmental potential is precisely specified in neuroepithelial stem cells and neural progenitor cells will probably provide novel insight into development and tumorigenesis.

The functional property of neuroepithelial stem cells changes dynamically in the outer proliferation center of the developing optic lobe. Before the third larval instar, most neuroepithelial stem cells predominantly undergo symmetric divisions to expand the stem cell population, forming a C-shaped swath flanked with few neuroblasts at the medial edge bordering the central brain. In the third larval instar, neuroepithelial stem cells progressively transition into neuroblasts from the medial edge toward the lateral edge of the optic lobe, leading to narrowing of the neuroepithelia and widening of the neuroblast swath [34••,39,40••]. Neuroblasts in the optic lobe share many parallels with INPs in the central brain, including expression of similar cell fate markers and asymmetric segregation of similar cell polarity proteins. A neuroblast in the optic lobe also undergoes limited rounds of asymmetric divisions to regenerate and to produce a GMC that gives rise to two terminally differentiated progeny [21,34••].

Please cite this article in press as: Weng M, Lee C-Y. Keeping neural progenitor cells on a short leash during *Drosophila* neurogenesis, Curr Opin Neurobiol (2010), doi:10.1016/j.conb.2010.09.005

However, the molecular mechanism that restricts the neuroblast potential in the optic lobe has yet to be investigated and will not be discussed further. Below, we will focus on the molecular mechanism that regulates the neuroepithelial stem cells.

Comparative expression profiling of micro-dissected neuroepithelia and neuroblasts from the optic lobe suggests that the Notch signaling mechanism probably plays a key role in maintaining the neuroepithelial stem cell identity [41••]. Removal of the *Notch* function triggers premature transition from neuroepithelia to neuroblasts, whereas constitutive activation of Notch signaling prevents the transition. Thus, downregulation of Notch signaling is necessary and sufficient for the transition from neuroepithelia to neuroblasts in the larval optic lobe.

How is the Notch signaling spatially and temporally regulated in the developing optic lobe allowing synchronous transition from neuroepithelial stem cells to neuroblasts in a medial-to-lateral manner? Neuroepithelial stem cells become transiently arrested in cell cycle before reaching the transition zone where they lose their epithelial characteristics and assume the stereotypical round neuroblast morphology [42••]. The expression of *delta*, encoding a Notch ligand, is detected at a high level in 1–2 rows of cells that are among those transiently arrested in cell cycle [40••,42••]. Since Delta activates Notch signaling cell non-autonomously and suppresses Notch signaling cell autonomously, overexpression or removal of *delta* leads to both inhibition and acceleration of neuroblast formation. This result suggests that the coordinated change between the level of Delta and the Notch signaling provides the cue that times the transition from neuroepithelia to neuroblasts. Interestingly, the proneural gene *lethal of scute* is also highly expressed in 1–2 rows of cells that are among those transiently arrested in cell cycle [40••,42••]. While removal of the *lethal of scute* function mildly delays the transition of neuroepithelial stem cells to neuroblasts, overexpression of *lethal of scute* suppresses Notch signaling and promotes premature transition. The dynamic integration of Delta and Lethal of scute specifies the transition from neuroepithelia to neuroblasts spatially in the optic lobe by repressing the Notch signaling.

The swath of neuroblasts widens synchronously from the medial edge toward the lateral edge of the developing optic lobe, suggesting that the transition from neuroepithelia to neuroblasts might also be temporally coordinated. Intriguingly, the output of the Janus kinase (Jak/Stat) signaling mechanism coincides with the timing of neuroepithelia transitioning into neuroblasts: Jak/Stat signaling is the highest at the lateral edge and the lowest at the medial edge. Removal of the components in the Jak/Stat signaling mechanism leads to precocious transition of neuroepithelia into neuroblasts, while constitutive activation of the Jak/Stat signaling delays the transition [40••]. In addition, inactivation of the Fat-Hippo signaling mechanism delays the transition from neuroepithelia to neuroblasts, whereas constitutive activation of the Fat-Hippo signaling accelerates the transition at the medial edge of neuroepithelia [42••]. Taken together, the Jak/Stat and the Fat-Hippo signaling mechanisms provide temporal control of the transition from neuroepithelia to neuroblasts. More experiments will be necessary to elucidate whether these two signaling pathways promote the transition through Notch or independent of Notch.

Discussion

The developmental potential in stem cells and progenitor cells must be precisely defined to ensure normal development and prevent accumulation of aberrant stem-like cells. Studies of the neural stem cell lineages in the developing *Drosophila* larval brain have begun to unravel the molecular mechanisms underlying how neural stem cells and neural progenitor cells are functionally distinguished at a single-cell resolution. Accumulating data point to downregulation of the Notch signaling by various mechanisms as a crucial step in establishing the restricted developmental potential in neural progenitor cells. However, additional mechanisms mediated by Brain tumor or Prospero function non-redundantly to the Notch signaling, and play important roles in restricting the developmental potential of neural progenitor cells. Notch also distinguishes neural stem cells from neural progenitor cells in the developing mouse brain [43•,44]. It will be interesting to test whether Brain tumor and Prospero indeed function in parallel of the Notch signaling in restricting the developmental potential in neural progenitor cells, and whether the vertebrate homologs of Brain tumor or Prospero might also play similar roles in regulating neural progenitor cells during mouse cortical neurogenesis. Emerging evidence strongly suggests that the Jak-Stat and Fat-Hippo signaling mechanisms regulate the timing of restricting the developmental potential in neuroepithelial stem cells. It will be important to determine whether these two signaling mechanisms might promote the transition from neuroepithelia to neuroblasts in the developing optic lobe via a Notch-dependent or Notch-independent mechanism.

Acknowledgements

We would like to thank members of the Lee lab for helpful discussion and comments. We would like to acknowledge the editorial support of Jon Kilner, MS, MA (Pittsburgh, PA). M.W. and C.-Y. L. are supported by the Sontag Foundation and NIH (GM092818).

References and recommended reading

Papers of particular interest, published within the annual period of review, have been highlighted as:

- • of special interest
- •• of outstanding interest

1. Gonczy P: **Mechanisms of asymmetric cell division: flies and worms pave the way**. *Nat Rev Mol Cell Biol* 2008, **9**:355-366.

Please cite this article in press as: Weng M, Lee C-Y. Keeping neural progenitor cells on a short leash during *Drosophila* neurogenesis, Curr Opin Neurobiol (2010), doi:10.1016/j.conb.2010.09.005

2. Doe CQ: **Neural stem cells: balancing self-renewal with differentiation**. *Development* 2008, **135**:1575-1587.

3. Knoblich JA: **Mechanisms of asymmetric stem cell division**. *Cell* 2008, **132**:583-597.

4. Wu P-S, Egger B, Brand AH: **Asymmetric stem cell division: lessons from *Drosophila***. *Semin Cell Dev Biol* 2008, **19**:283-293.

5. Cabernard C, Doe CQ: **Apical/basal spindle orientation is required for neuroblast homeostasis and neuronal differentiation in *Drosophila***. *Dev Cell* 2009, **17**:134-141.

6. •• Bello BC, Izergina N, Caussinus E, Reichert H: **Amplification of neural stem cell proliferation by intermediate progenitor cells in *Drosophila* brain development**. *Neural Dev* 2008, **3**:5.
One of the three studies identifies and characterizes the type II neuroblast lineage. Bello *et al.* demonstrate the existence of intermediate progenitor cells in the developing *Drosophila* larval brain, which serve as a novel model to study the mechanism restricting the developmental potential in neural progenitor cells.

7. •• Boone JQ, Doe CQ: **Identification *of Drosophila* type II neuroblast lineages containing transit amplifying ganglion mother cells**. *Dev Neurobiol* 2008, **68**:1185-1195.
One of the three studies identifies and characterizes the type II neuroblast lineage. Boone and Doe demonstrate the existence of transit amplifying GMCs in the developing *Drosophila* larval brain, which serve as a novel model to study the mechanism restricting the developmental potential in neural progenitor cells.

8. •• Bowman SK, Rolland V, Betschinger J, Kinsey KA, Emery G, Knoblich JA: **The tumor suppressors Brat and Numb regulate transit-amplifying neuroblast lineages in *Drosophila***. *Dev Cell* 2008, **14**:535-546.
One of the three studies identifies and characterizes the type II neuroblast lineage. Bowman *et al.* demonstrate the existence of secondary neuroblasts in the developing *Drosophila* larval brain, which serve as a novel model to study the mechanism restricting the developmental potential in neural progenitor cells.

9. Chu-Lagraff Q, Wright DM, McNeil LK, Doe CQ: **The*prospero* gene encodes a divergent homeodomain protein that controls neuronal identity in *Drosophila***. *Development* 1991, **113**:79-85.

10. Manning L, Doe CQ: **Prospero distinguishes sibling cell fate without asymmetric localization in the *Drosophila* adult external sense organ lineage**. *Development* 1999, **126**:2063-2071.

11. Freeman MR, Doe CQ: **Asymmetric Prospero localization is required to generate mixed neuronal/glial lineages in the *Drosophila* CNS**. *Development* 2001, **128**:4103-4112.

12. Choksi SP, Southall TD, Bossing T, Edoff K, de Wit E, Fischer BE, van Steensel B, Micklem G, Brand AH: **Prospero acts as a binary switch between self-Renewal and differentiation in *Drosophila* neural stem Cells**. *Dev Cell* 2006, **11**:775-789.

13. Ikeshima-Kataoka H, Skeath JB, Nabeshima Y, Doe CQ, Matsuzaki F: **Miranda directs Prospero to a daughter cell during *Drosophila* asymmetric divisions**. *Nature* 1997, **390**:625-629.

14. Shen CP, Jan LY, Jan YN: **Miranda is required for the asymmetric localization of Prospero during mitosis in *Drosophila***. *Cell* 1997, **90**:449-458.

15. Matsuzaki F, Ohshiro T, Ikeshima-Kataoka H, Izumi H: **Miranda localizes Staufen and Prospero asymmetrically in mitotic neuroblasts and epithelial cells in early *Drosophila* embryogenesis**. *Development* 1998, **125**:4089-4098.

16. Schuldt AJ, Adams JHJ, Davidson CM, Micklem DR, Haseloff J, Johnston DS, Brand AH: **Miranda mediates asymmetric protein and RNA localization in the developing nervous system**. *Genes Dev* 1998, **12**:1847-1857.

17. Wang H, Cai Y, Chia W, Yang X: ***Drosophila* homologs of mammalian TNF/TNFR-related molecules regulate segregation of Miranda/Prospero in neuroblasts**. *EMBO J* 2006, **25**:5783-5793.

18. Li L, Vaessin H: **Pan-neural Prospero terminates cell proliferation during *Drosophila* neurogenesis**. *Genes Dev* 2000, **14**:147-151.

19. Bello B, Reichert H, Hirth F: **The *brain tumor* gene negatively regulates neural progenitor cell proliferation in the larval central brain of *Drosophila***. *Development* 2006, **133**:2639-2648.

20. Betschinger J, Mechtler K, Knoblich JA: **Asymmetric segregation of the tumor suppressor *brat* regulates self-renewal in *Drosophila* neural stem cells**. *Cell* 2006, **124**:1241-1253.

21. Lee CY, Wilkinson BD, Siegrist SE, Wharton RP, Doe CQ: **Brat is a Miranda cargo protein that promotes neuronal differentiation and inhibits neuroblast self-renewal**. *Dev Cell* 2006, **10**:441-449.

22. •• Weng M, Golden KL, Lee CY: **dFezf/Earmuff maintains the restricted developmental potential of intermediate neural progenitors in *Drosophila***. *Dev Cell* 2010, **18**:126-135.
Weng *et al.* show that following specification of the intermediate neural progenitor cell (INP) identity, their developmental potential requires an active mechanism mediated by Earmuff for maintenance. Earmuff maintains the INP potential by limiting proliferation by promoting nuclear localization of Prospero and suppressing de-differentiation by antagonizing Notch signaling.

23. Uemura T, Shepherd S, Ackerman L, Jan LY, Jan YN: ***numb,* a gene required in determination of cell fate during sensory organ formation in *Drosophila* embryos**. *Cell* 1989, **58**:349-360.

24. Rhyu MS, Jan LY, Jan YN: **Asymmetric distribution of numb protein during division of the sensory organ precursor cell confers distinct fates to daughter cells**. *Cell* 1994, **76**:477-491.

25. Spana EP, Kopczynski C, Goodman CS, Doe CQ: **Asymmetric localization of numb autonomously determines sibling neuron identity in the *Drosophila* CNS**. *Development* 1995, **121**:3489-3494.

26. Spana EP, Doe CQ: **Numb antagonizes Notch signaling to specify sibling neuron cell *fates***. *Neuron* 1996, **17**:21-26.

27. Zhong W, Feder JN, Jiang M-M, Jan LY, Jan YN: **Asymmetric localization of a mammalian numb homolog during mouse cortical neurogenesis**. *Neuron* 1996, **17**:43-53.

28. Wang H, Ouyang Y, Somers WG, Chia W, Lu B: **Polo inhibits progenitor self-renewal and regulates Numb asymmetry by phosphorylating Pon**. *Nature* 2007, **449**:96-100.

29. Wirtz-Peitz F, Nishimura T, Knoblich JA: **Linking cell cycle to asymmetric division: Aurora-A phosphorylates the Par complex to regulate Numb localization**. *Cell* 2008, **135**:161-173.

30. Almeida MS, Bray SJ: **Regulation of post-embryonic neuroblasts by Drosophila Grainyhead**. *Mech Dev* 2005, **122**:1282-1293.

31. Maurange C, Cheng L, Gould AP: **Temporal transcription factors and their targets schedule the end of neural proliferation in *Drosophila***. *Cell* 2008, **133**:891-902.

32. • Shimizu T, Nakazawa M, Kani S, Bae Y-K, Shimizu T, Kageyama R, Hibi M: **Zinc finger genes *Fezf1* and *Fezf2* control neuronal differentiation by repressing *Hes5* expression in the forebrain**. *Development* 2010, **137**:1875-1885.
Shimizu *et al.* show the mouse homologs of Earmuff antagonize Notch signaling by directly binding to the promoter of the *Hes5* gene during cortex neurogenesis.

33. Basak O, Taylor V: **Identification of self-replicating multipotent progenitors in the embryonic nervous system by high Notch activity and Hes5 expression**. *Eur J Neurosci* 2007, **25**:1006-1022.

34. •• Egger B, Boone J, Stevens N, Brand A, Doe C: **Regulation of spindle orientation and neural stem cell fate in the *Drosophila* optic lobe**. *Neural Dev* 2007, **2**:1.
Egger *et al.* show that neuroepithelia in the developing larval optic lobe generate neuroblasts, which in turn generate neurons. This study characterizes symmetric and asymmetric divisions of neuroepithelial cells and neuroblasts.

35. Kriegstein A, Alvarez-Buylla A: **The glial nature of embryonic and adult neural stem cells**. *Annu Rev Neurosci* 2009, **32**:149-184.

36. Farkas LM, Huttner WB: **The cell biology of neural stem and progenitor cells and its significance for their proliferation versus differentiation during mammalian brain development**. *Curr Opin Cell Biol* 2008, **20**:707-715.

Please cite this article in press as: Weng M, Lee C-Y. Keeping neural progenitor cells on a short leash during *Drosophila* neurogenesis, Curr Opin Neurobiol (2010), doi:10.1016/j.conb.2010.09.005

37. Hadjipanayis CG, Van Meir EG: **Brain cancer propagating cells: biology, genetics and targeted therapies**. *Trends Mol Med* 2009, **15**:519-530.

38. Dubuc A, Northcott P, Mack S, Witt H, Pfister S, Taylor M: **The genetics of pediatric brain tumors**. *Curr Neurol Neurosci Rep* 2010, **10**:215-223.

39. Nassif C, Noveen A, Hartenstein V: **Early development of the Drosophila brain: III. The pattern of neuropile founder tracts during the larval period**. *J Comp Neurol* 2003, **455**:417-434.

40. •• Yasugi T, Umetsu D, Murakami S, Sato M, Tabata T: ***Drosophila* optic lobe neuroblasts triggered by a wave of proneural gene expression that is negatively regulated by JAK/STAT**. *Development* 2008, **135**:1471-1480.
Yasugi *et al.* show that conversion of neuroepithelia into neuroblasts in the developing larval optic lobe occurs in a medial-to-lateral manner. These authors demonstrate that the expression of Lethal of scute coincides with the transition from neuroepithelia to neuroblasts, and that the JAK/STAT pathway modulates this transition.

41. •• Egger B, Gold K, Brand A: **Notch regulates the switch from symmetric to asymmetric neural stem cell division in the Drosophila optic lobe**. *Development* 2010, **137**:2981-2987.
Egger *et al.* show that Notch signaling plays a key role in maintaining the identity of neuroepithelia in the developing larval optic lobe. The authors demonstrate that *Notch* loss of function leads to premature conversion of neuroepithelia into neuroblasts.

42. •• Reddy BVVG, Rauskolb C, Irvine KD: **Influence *of fat-hippo* and *Notch* signaling on the proliferation and differentiation of *Drosophla* optic neuroepithelia**. *Development* 2010, **137**:2397-2408.
Reddy *et al.* show that the *Notch* signaling is required for the maintenance of optic lobe neuroepithelia, and *that fat-hippo* signaling pathway regulates the neuroepithelia–neuroblast transition by promoting transient cell cycle.

43. • Mizutani K-i, Yoon K, Dang L, Tokunaga A, Gaiano N: **Differential *Notch* signalling distinguishes neural stem cells from intermediate progenitors**. *Nature* 2007, **449**:351-355.
Mizutani *et al.* identify a population of intermediate neural progenitors that co-exist with neural stem cells in the ventricular zone and show that Notch signaling functionally distinguishes intermediate progenitors from neural stem cells.

44. Corbin JG, Gaiano N, Juliano SL, Poluch S, Stancik E, Haydar TF: **Regulation of neural progenitor cell development in the nervous system**. *J Neurochem* 2008, **106**:2272-2287.

Further reading

Yasugi T, Sugie A, Umetsu D, Tabata T: **Coordinated sequential action of EGFR and Notch signaling pathways regulates proneural wave progression in the Drosophila optic lobe**. *Development* 2010, **137**:3193-3203.

Please cite this article in press as: Weng M, Lee C-Y. Keeping neural progenitor cells on a short leash during *Drosophila* neurogenesis, Curr Opin Neurobiol (2010), doi:10.1016/j.conb.2010.09.005